

General Disclaimer

One or more of the Following Statements may affect this Document

- This document has been reproduced from the best copy furnished by the organizational source. It is being released in the interest of making available as much information as possible.
- This document may contain data, which exceeds the sheet parameters. It was furnished in this condition by the organizational source and is the best copy available.
- This document may contain tone-on-tone or color graphs, charts and/or pictures, which have been reproduced in black and white.
- This document is paginated as submitted by the original source.
- Portions of this document are not fully legible due to the historical nature of some of the material. However, it is the best reproduction available from the original submission.

Copyright 1979
Peter Horvath
All Rights Reserved

ANALYSIS OF LUNAR SEISMIC SIGNALS - DETERMINATION OF INSTRUMENTAL
PARAMETERS AND SEISMIC VELOCITY DISTRIBUTIONS

by

PETER HORVATH

DISSERTATION

Presented to the Faculty of the Graduate School of

The University of Texas at Dallas

in Partial Fulfillment

of the Requirements

for the Degree of

DOCTOR OF PHILOSOPHY

THE UNIVERSITY OF TEXAS AT DALLAS

December 1979

ACKNOWLEDGMENTS

This research was supported by NASA contract NAS-9-14581 and grant NSG-7418. I thank Drs. Gary V. Latham, Yosio Nakamura, H. James Dorman, Mark Landisman, and Ronald W. Ward for critically reviewing the manuscript and offering constructive comments. Dr. Y. Nakamura provided the computer programs for reading the Apollo Passive Seismic Experiments magnetic tapes and for plotting Figures 40 through 43, 46, and 47; Drs. Y. Nakamura and J. Koyama provided data for compiling Table 20, for which I am grateful.

PRECEDING PAGE BLANK NOT FILMED

ANALYSIS OF LUNAR SEISMIC SIGNALS - DETERMINATION OF INSTRUMENTAL
PARAMETERS AND SEISMIC VELOCITY DISTRIBUTIONS

Publication No. _____

Peter Horvath, Ph.D.

The University of Texas at Dallas, 1979

Supervising Professor: Gary V. Latham

Seismographs operated successfully at the Apollo 12, 14, 15, and 16 landing sites for a duration between 5.5 and 8 years. Although the study of the seismic data revealed more about the lunar interior than other data produced by the Apollo Scientific Experiments, the sparse lunar seismic network, the weak seismic sources, the strong scattering of the seismic waves, and occasional noise bursts impose severe limitations on enlarging our knowledge about the velocity distributions in the moon. In order to learn more about the physical state of the moon, much effort has been spent to improve the techniques for identifying direct shear and secondary wave arrivals on the lunar seismograms. In this study, inverse filters were designed to correct for the instrumental response and for near-surface effects and, thus, to facilitate the comparison of the ground motion at the various sites.

The constants of the long-period lunar seismographs were determined from a least-squares inversion of the observed calibration pulses. The noise, especially the digitizing noise, was reduced by using two

positive and two negative calibration pulses. Knowledge of the seismograph parameters permits calculation of the transfer functions for each seismograph and accurate correction of the seismograms for the instrumental response.

The instrumental deconvolution was carried out in the frequency domain after removal of the predictable digitizing errors from the seismograms. The amplitude spectra of the instrument-deconvolved seismic records revealed that other important filtering effects characteristic of each recording site remained in the lunar seismograms. In order to remove these effects, whitening filters were designed by averaging the spectral amplitudes of the largest long-period seismic signals component by component. These average amplitude spectra were shown to be primarily affected by the coupling of the seismometer to the ground and by the near-surface structure. The relative amplifications between the horizontal components were also estimated from these average amplitude spectra.

Average horizontal-to-vertical spectral amplitude ratios computed for a number of major seismic impact signals were compared with spectral ratios calculated for fundamental-mode Rayleigh waves in media consisting of homogeneous, isotropic, horizontal layers. The shear velocities of the best fitting models at the different sites resemble each other and differ from the average for all sites by not more than 20%, except for the bottom layer at station 14. The shear velocities at the various sites increase from 40 m/sec at the surface to about 400 m/sec at depths between 95 and 160 meters. Within this depth range, the velocity-depth functions are well represented by two piecewise linear

segments; although the presence of first order discontinuities cannot be ruled out.

The seismograms corrected for both instrumental response and near-surface effects were found to be comparable at the various sites and were used to obtain readings for the direct shear and secondary wave arrivals. To explore the constraints that direct arrival times could impose on the velocity distributions in the lunar interior, the largest natural impacts and shallow moonquakes were located by two velocity models. The first model consisted of a thicker crust (55 km) and higher compressional and shear velocities (8.1 and 4.6 km/sec, respectively) in the upper mantle, and the second model had a thinner crust (45 km) and lower upper-mantle velocities (7.7 and 4.4 km/sec). The arrival times observed for impacts and shallow moonquakes could not be used to distinguish between these two models because the travel time residuals for both models are similar and are well within the uncertainty of the observed travel times. Although the identification of the secondary arrivals suggests that a velocity discontinuity exists at a depth of about 25 km and that the crust is thinner than 55 km, no conclusive evidence was found for a discontinuity in the mantle or for laterally varying crustal thickness.

TABLE OF CONTENTS

Title - fly	i
Copyright	ii
Title page.	iii
ACKNOWLEDGEMENTS.	iv
ABSTRACT.	v
TABLE OF CONTENTS	viii
LIST OF TABLES.	xi
LIST OF FIGURES	xiii
LIST OF SEISMIC SECTIONS.	xvii
INTRODUCTION.	
1. Research objectives	1
2. Literature review	3
PART 1. DETERMINATION OF THE TRANSFER FUNCTION OF THE LONG- PERIOD LUNAR SEISMOGRAPHS.	
1.1. Introduction.	11
1.2. Description of feedback-controlled lunar seismographs	14
1.3. Computational details for determining the instrumental constants by least-squares fit of the observed and theoretical calibration pulses.	22
1.4. The influence of noise.	28
1.5. Results and discussion.	32
1.6. Conclusion.	34

PART 2. INSTRUMENTAL AND WHITENING DECONVOLUTION OF THE LONG-PERIOD LUNAR SEISMOGRAMS.

2.1. Introduction.	36
2.2. Wavelet-deconvolution techniques.	37
2.3. Instrumental deconvolution of the peaked-mode long-period lunar seismograms	42
2.4. Design of the whitening filters to remove the filtering effects of the near-surface zone.	48
2.5. Some properties of the amplitude spectra of the long-period lunar seismograms.	56
2.6. Summary of Part 2	57

PART 3. NEAR-SURFACE SHEAR WAVE VELOCITIES AS INFERRED FROM THE SPECTRAL AMPLITUDE RATIOS OF THE LONG-PERIOD LUNAR SEISMOGRAMS

3.1. Introduction.	59
3.2. The observed spectral amplitude ratios.	62
3.3. The theoretical spectral amplitude ratios calculated for the fundamental-mode Rayleigh waves	65
3.4. The near-surface velocity distributions	69
3.5. Discussion and conclusions.	73

PART 4. ANALYSIS OF THE LONG-PERIOD LUNAR SEISMIC SIGNALS CORRECTED FOR INSTRUMENTAL RESPONSE AND NEAR-SURFACE EFFECTS

4.1. Introduction.	75
4.2. Direct compressional and shear wave arrivals and locations of major lunar seismic events	76
4.3. Secondary arrivals.	77

	x
4.4. Summary of Part 4	88
CONCLUSIONS	90
APPENDIX: LEAST-SQUARES FIT TO A NON-LINEAR FUNCTION WITH A LINEARIZATION OF THE FITTING FUNCTION.	92
BIBLIOGRAPHY.	95
TABLES.	102
FIGURES	140
SEISMIC SECTION CAPTIONS.	227
VITA.	230
SEISMIC SECTIONS.	Pocket

LIST OF TABLES

Table 1. The lunar seismic network	103
Table 2. Nominal values of the seismograph constants.. . . .	105
Table 3. Description of the calibration pulses	106
Table 4. Seismograph constants obtained in this study.	108
Table 5. Errors in the determination of the seismograph constants (%).	110
Table 6. Absolute values of the relative differences between the amplitude responses of Figure 12 and component 15Z in the peaked mode.	111
Table 7. Absolute values of the relative differences between the amplitude responses of Figure 12 and component 15X in the peaked mode.	112
Table 8. Relative noise for instrumental deconvolution in the peaked mode.	113
Table 9. List of the most energetic long-period lunar seismic events	114
Table 10. Number of time sections classified according to source types and components.	119
Table 11. Relative amplification of the horizontal components (Y/X).	120
Table 12. Structural parameters of the near-surface zone, model 'A'.	121
Table 13. Structural parameters of the near-surface zone, model 'B'.	122

Table 14. Description of the velocity distributions of model 'B' in forms of $\beta = a + bz$ and $\alpha = cz^p$	123
Table 15. Travel times from the Apollo 14 and 16 Active Seismic Experiments.	124
Table 16. Velocity models used in this study with thicker lunar crust and higher lunar mantle velocities.. . . .	125
Table 17. Velocity models used in this study with thinner lunar crust and lower lunar mantle velocities.	126
Table 18. Reference times, origin times, and locations for selected major lunar seismic events.	127
Table 19. Observed and theoretical arrival times for events listed in Table 18	131
Table 20. Arrival times observed by other investigators.	135

LIST OF FIGURES

Figure 1. Compressed time-scale seismic records for the three major types of natural seismic sources.141
Figure 2. Simplified block diagram of the feedback-controlled, direct-digitizing long-period lunar seismographs.143
Figure 3. Average of the positive and the sign-reversed negative calibration pulses in the peaked mode.145
Figure 4. Average of the positive and the sign-reversed negative calibration pulses in the flat mode.147
Figure 5. Schematic flow chart for calculating the seismograph parameters.149
Figure 6. Real and imaginary parts of the partial derivatives of the transfer function to a step of acceleration in the peaked mode151
Figure 7. Real and imaginary parts of the partial derivatives of the transfer function to a step of acceleration in the flat mode153
Figure 8. Partial derivatives of the response to a step of acceleration in the peaked mode155
Figure 9. Partial derivatives of the response to a step of acceleration in the flat mode157
Figure 10. Partial derivatives of the amplitude and phase responses to a step of acceleration in the peaked mode.159
Figure 11. Partial derivatives of the amplitude and phase responses to a step of acceleration in the flat mode.161

Figure 12. Observed and theoretical amplitude and phase responses to a step of acceleration for components 15Z and 15X in the peaked mode.	163
Figure 13. Absolute values of the differences between the observed and theoretical amplitude responses to a step of acceleration for components 15X and 15Z, and the relative errors in relation to the amplitude responses in the peaked mode.	165
Figure 14. Amplitude responses to an impulse of displacement in the peaked mode.	167
Figure 15. Absolute values of the relative differences between the amplitude responses of Figure 12 and component 15Z in the peaked mode	169
Figure 16. Absolute values of the relative differences between the amplitude responses of Figure 12 and component 15X in the peaked mode	171
Figure 17. Schematic flow chart for calculating the waterlevel parameters, the reliable frequency bands, and the relative errors between the observed and theoretical amplitude responses to a step of acceleration	173
Figure 18. Schematic flow chart for calculating the transfer functions of the seismographs and for adjusting the transfer functions with a given waterlevel parameter	175
Figure 19. Schematic flow chart for performing wavelet deconvolution by spectral division.	175

Figure 20. Schematic flow chart for stacking the amplitude spectra of the seismic records corrected for instrumental response in the peaked mode..177
Figure 21. Schematic flow chart for calculating the total transfer function of the instrumental and near-surface effects177
Figure 22. Illustration of the noise of the analog-to-digital converter at station 14179
Figure 23. Sum of the amplitude spectra for the horizontal components (X and Y) of station 12.181
Figure 24. Sum of the amplitude spectra for the horizontal components (X and Y) of station 14.183
Figure 25. Sum of the amplitude spectra for the horizontal components (X and Y) of station 15.185
Figure 26. Sum of the amplitude spectra for the horizontal components (X and Y) of station 16.187
Figure 27. Sum of the amplitude spectra for the vertical components (Z) of stations 12 and 14.189
Figure 28. Sum of the amplitude spectra for the vertical components (Z) of stations 15 and 16.191
Figure 29. Sum of the amplitude spectra for station 12.193
Figure 30. Sum of the amplitude spectra for station 14.195
Figure 31. Sum of the amplitude spectra for station 15.197
Figure 32. Sum of the amplitude spectra for station 16.199
Figure 33. Two examples for instrumental and whitening deconvolution201

Figure 34. Ratio of the average horizontal spectral amplitudes (X to Y).	203
Figure 35. Ratios of the horizontal and vertical spectral amplitudes at station 12	205
Figure 36. Ratios of the horizontal and vertical spectral amplitudes at station 14	207
Figure 37. Ratios of the horizontal and vertical spectral amplitudes at station 15	209
Figure 38. Ratios of the horizontal and vertical spectral amplitudes at station 16	211
Figure 39. Near-surface shear velocity profiles obtained for the Apollo 12, 14, 15, and 16 landing sites.	213
Figure 40. Travel time curves of the refracted compressional waves for station 12	215
Figure 41. Travel time curves of the refracted compressional waves for station 14	215
Figure 42. Travel time curves of the refracted compressional waves for station 15	217
Figure 43. Travel time curves of the refracted compressional waves for station 16	217
Figure 44. Velocity models used in this study for the whole moon	219
Figure 45. Velocity models used in this study for the lunar crust and upper mantle only.	221
Figure 46. Locations of impacts as determined in this study. . .	223
Figure 47. Epicenters of shallow moonquakes as determined in this study	225

LIST OF SEISMIC SECTIONS

(in pocket)

- 'IMPACTS (R,0.4-1.5HZ)' Radial component of ground motion, distance range is 0 to 50°.
- 'IMPACTS (T,0.4-1.5HZ)' Transverse component of ground motion, distance range is 0 to 50°.
- 'IMPACTS (Z,0.4-1.5HZ)' Vertical component of ground motion, distance range is 0 to 50°.
- 'IMPACTS (R,0.4-1.5HZ)' Radial component of ground motion, distance range is 60 to 160°.
- 'IMPACTS (T,0.4-1.5HZ)' Transverse component of ground motion, distance range is 60 to 160°.
- 'IMPACTS(Z,0.4-1.5HZ)' Vertical component of ground motion, distance range is 60 to 160°.
- 'SHALLOW MOONQUAKES (R,0.4-15HZ)' Radial component of ground motion.
- 'SHALLOW MOONQUAKES (Z,0.4-1.5HZ)' Vertical component of ground motion.
- 'DEEP MOONQUAKES (R,0.4-1.5HZ)' Radial component of ground motion.
- 'DEEP MOONQUAKES (T,0.4-1.5HZ)' Transverse component of ground motion.
- 'DEEP MOONQUAKES (Z)' Vertical component of ground motion as recorded with seismographs operated in the peaked mode.

INTRODUCTION

1. Research objectives.

Since most of the information related to the interior of the Earth was obtained either directly or indirectly from the study of the travel times, amplitudes, and apparent velocities of seismic body waves and dispersion of seismic surface waves, it was anticipated that the Apollo passive seismic experiments would provide the seismic velocity distribution in the lunar interior. These velocities as well as other constraints were expected to contribute to the development of models of the composition and temperature distribution in the moon.

Although the first decade of lunar seismology greatly expanded our knowledge concerning the physical state of the interior of the moon, the primary goal of studying the lunar seismograms remained the same. Detailed studies of travel times and amplitudes lead to more and more refined velocity distributions in the moon. Owing to the small number of seismic stations (4) in the Apollo network, these studies required application of some new techniques in order to extract more information from the lunar seismic signals. Improvement in techniques for identification of shear and secondary arrivals, as well as maximum use of amplitude information were obvious needs. This dissertation addresses the problem of designing inverse filters to correct for the effects of instrumental response, coupling of the seismometer to the ground, and near-surface structure, thus making the comparison among the various components of the ground motion at the four lunar seismometer sites possible. This,

as well as conventional filtering techniques, applied in order to decrease the noise contamination of the seismic signals, should result in better identification of seismic phases.

The steps to achieve these goals were as follows.

1. Select the most energetic events from the complete data set
2. Obtain instrumental parameters and transfer functions
3. Remove predictable digitizing errors from the seismograms
4. Correct seismic records for instrumental response
5. Design whitening filters to remove near-surface effects
6. Apply these whitening filters
7. Determine the compressional and shear wave arrival times from the original and deconvolved seismograms
8. Locate the seismic events with these seismic wave arrivals by assuming the compressional and shear velocity distributions in the moon
9. Apply conventional filters to enhance seismic arrivals
10. Make seismic sections and obtain consistent secondary arrivals
11. Refine velocity distributions and determine discontinuities
12. Repeat steps 8 through 11 with the improved velocity models

Although the primary objective is to obtain secondary arrivals and interpret them with respect to the internal structure of the moon, the present analysis may yield other results:

- a.) Quantitative description of the differences among the seismometers
- b.) Estimation of noise; determination of the frequency range in which one may expect to find seismic wave arrivals
- c.) Empirical amplitude ratios of the horizontal components of the ground motion at a given station

- d.) Structural parameters of the near-surface zone
- e.) More precise locations of the seismic events
- f.) Station corrections and quantitative description of lateral heterogeneities

The dissertation is divided into four parts. Part 1 describes how the instrumental parameters and transfer function were obtained. Part 2 deals with inverse filtering, estimation of noise, and designing the whitening filters. The average horizontal-to-vertical spectral amplitude ratios are interpreted in terms of structural properties of the near-surface zone in Part 3. The improved arrival times for the various seismic phases and their implication for the deeper lunar interior are discussed in Part 4. The following section briefly reviews existing studies in lunar seismology.

2. Literature review.

Seismic stations were deployed by the astronauts at the Apollo 11, 12, 14, 15, and 16 landing sites. While station 11 operated for several weeks and station 12 for almost eight years, stations 12, 14, 15, and 16 were operating simultaneously for about five and a half years. This four station network spans the near face of the moon in an approximately equilateral triangle with a separation of about 1100 km between the corners with stations 12 and 14 occupying one of the corners. Each station has one short-period and three long-period seismometers. Table 1 gives the location, orientation, and operational history of these seismometers (e.g., Lauderdale and Eichelman, 1974). Further details on the instrumentation are given in Part 1.

Most of the features of the lunar seismograms were totally unexpected by seismologists, who found these seismograms quite different from those of earthquake seismograms. The long duration, continuous reverberation, emergent body wave beginnings, the almost complete lack of correlation between various displacement components, and the lack of coherently dispersed seismic surface waves were explained by relatively small source magnitudes, intensive scattering, rapidly increasing velocities with depth near the surface, and very low seismic wave attenuation (e.g., Gold and Soter, 1970; Latham et al., 1969 and 1970). The latter three features are related to the lack of volatiles in the heterogeneous, porous material which makes up the outer several kilometers of the moon. An uppermost limit of 20 km is given for the thickness of this scattering zone by Toksöz et al. (1972).

Rayleigh's perturbation theory (Rayleigh, 1945, p. 149) as used by Miles (1960), diffusion theory as used by Wesley (1965), by Latham et al. (1970), and by Warren (1972), as well as experiments by Dainty et al. (1974b) showed that the raypaths of seismic wave arrivals remain unchanged from those predicted by ray theory, although the amplitudes of these arrivals are diminished greatly by intensive scattering. Thus, it was concluded (Toksöz et al., 1974) that conventional travel time and amplitude studies were useful starting points in determining the velocity distribution of the Moon. This work was aided greatly by the availability of artificial impacts of known location and origin time as well as of natural seismic sources.

Classification of natural lunar seismic sources is based upon characteristic envelopes of the whole seismic signal (see Figure 1), upon

the relative strength of the shear wave, and upon the waveform matching of particular signals. Nearly identical seismograms which are repeatedly observed at a given site must be produced by the same source mechanism repeating at the same site. Two types of such matching sources were found: thermal moonquakes and deep moonquakes. Almost all of the natural events can be classified into these two types plus meteoroid impact and shallow moonquake categories.

The thermal moonquakes can be identified by matching the short-period waveforms and by 29.5-day periodicity of occurrence (Duennebier and Sutton, 1974; Cooper and Kovach, 1975; Duennebier, 1976). Each of these signals is recorded at one station only. The source of these signals is believed to be dislocation caused by thermal stress on, or very close to, the surface at distances not greater than several kilometers from the recording site. Most of the repeating waveforms did not change in four to five years, and the source locations are associated to some degree with large rocks and craters (Duennebier, 1976). Thus, it appears that the source of thermal moonquakes is propagation of small cracks in exposed rocks and, possibly, slumping of material along steep slopes (*ibid.*)

The deep moonquakes are the most numerous type of seismic sources in the moon (Latham *et al.*, 1972 and 1973; Lammlein *et al.*, 1974; Lammlein, 1977; Nakamura, 1978). More than 100 different deep moonquake categories were confirmed by their nearly identical long-period waveforms. These signals are less affected by intensive scattering than the meteoroid impact signals and exhibit the best shear wave arrivals noticeable on the lunar seismograms. The deep moonquakes occur at depths between 700 and 1100 km, below which partial melting possibly begins (Nakamura *et al.*, 1973).

The times of occurrence of these deep moonquakes correlate very well with the variation of the tidal forces in the moon. Nakamura (1978) demonstrated that the energy released by deep moonquakes is controlled by the tidal stress field and does not require tectonically accumulated strain energy. The matching waveforms within each source group enabled investigators to improve the signal-to-noise ratio of these signals by simple stacking (Nakamura et al., 1976; Lammlein, 1977; Goins, 1978; Goins et al., 1978).

The most energetic moonquakes are those which originate at shallow depths. The magnitude of the largest ones is estimated to be about 4 on the Gutenberg-Richter scale (Nakamura et al., 1974). Variation of the amplitude of the shallow moonquake signals with distance indicates that shallow moonquakes occur in the upper mantle (Nakamura et al., 1979). Only four to five shallow moonquakes were found yearly. Most likely they are true tectonic moonquakes releasing strain energy which accumulates as the moon cools.

The similarity of the envelope characteristics of the natural impacts to those of artificial impacts distinguishes impacts from moonquakes. The shear wave arrivals are usually buried in the scattered wave train. The energies and distributions of meteoroid impacts both in space and in time were studied by Latham et al. (1973), Duennebier and Sutton (1974b), Duennebier et al. (1975), and Dorman et al. (1978).

Petrologic and mineralogic studies, laboratory measurements of the returned samples, and active seismic experiments resulted in the determination of the velocity distributions and the composition of the uppermost few kilometers of the moon. The low velocities and their large

gradients with depth (e.g., Cocper et al., 1974) were attributed to the presence of porous, brecciated material and to the absence of volatiles in this zone (Gangi, 1972; Talwani et al., 1973; Todd et al., 1973; Tittman et al., 1974). The compressional velocity is about 100 m/sec at the surface and reaches 4 to 5 km/sec at depths of 1.5 to 2 km. The near-surface velocities and densities are described in greater detail in Part 3.

The velocity distribution in the deeper crust was determined from the study of artificial impact signals. Since the shear wave arrivals are obscured by intensive scattering, Toksöz et al., (1972 and 1974) assumed the ratio of the compressional and shear velocities to be 1.7. At depths greater than a few kilometers the compressional velocity increases slowly, attaining values of about 6.1 km/sec at 20 km (ibid). The lower crust, defined as the layer below this depth, has a rather homogeneous compressional velocity of about 6.8 km/sec.

The transition between the upper and lower crust is by no means considered to have been uniquely defined. Possible refracted wave arrivals (Toksöz et al., 1972 and 1974) and peg-leg multiples (Goins, 1978; Goins et al., 1978) indicate that there is a first-order discontinuity at a depth of 20 to 25 km. This first-order discontinuity could be the consequence of compositional changes from a basaltic upper crust to gabbroic anorthosite in the lower crust (Mizutani and Newbigging, 1973; Wang et al., 1973). A second-order velocity discontinuity would not require compositional changes but implies the closing of impact-induced microcracks in the basaltic crust (Todd et al., 1973). The crust was possibly formed by large scale igneous differentiation early in the history of the moon. The

highland soils were derived from a suite of highly feldspathic rocks (Reid, 1974). This feldspathic material is believed to represent the initial crust which was cratered by impacts and was flooded by basalts in maria. This sequence of events implies the existence of a first-order discontinuity above the feldspathic layer only in mare areas (Dainty et al. 1974). Goins (1978) identified peg-leg multiples from a depth of about 20 km also at highland areas. If this interpretation is correct, the compositional change should not be restricted to mare areas and should be the result of the original crustal differentiation, and the 20-km discontinuity also should have remained undisturbed by impacts in later times.

The thickness of the crust is given at 55 to 60 km under stations 12 and 14 in most studies published since the beginning of lunar seismic investigation. New arrival times by Koyama and Nakamura (1979) for the compressional wave read from two artificial impact records at station 12 indicate a crustal thickness of about 45 km. Peg-leg multiples from the base of the crust (Dainty et al., 1977; Goins, 1978) imply a crustal thickness of either 60 or 90 km at station 15 and of about 75 km at station 16.

The velocities in the lunar mantle have been determined by a process of successive approximation starting with a homogeneous sphere beneath the crust. The average velocities between depths of 60 and 920 km were determined by Toksöz et al. (1974) as 8.0 and 4.2 km/sec for the compressional and shear waves, respectively. Lamlein et al. (1974) and Lamlein (1977) used a model of linearly decreasing velocities in the mantle: 8.1 and 4.7 km/sec at a depth of 60 km and of 8.0 and 4.3 km/sec at 800 km for the compressional and shear waves, respectively. Nakamura et al. (1974b) showed

that the differences between the arrival times of the shear and compressional waves require a drop in the shear wave velocity at a depth of about 300 km. They later refined the velocity distributions in the mantle by using more events and by analyzing the decay of the shear wave amplitude as a function of distance (Nakamura et al., 1976). They showed that a continuous decrease of the velocities with depth satisfies both the travel time data and the shear wave amplitude data. A discontinuity at a depth of about 300 km was also indicated by reflected compressional wave arrivals (Voss et al., 1976) and by converted shear wave arrivals (Nakamura et al., 1974b; Latham et al., 1977). Indications for lateral variations of the seismic velocities in the upper mantle were found by Nakamura et al. (1977).

Goins (1978) and Goins et al. (1978) inverted the observed arrival times for a two-layer mantle. Compressional and shear velocities of 7.7 and 4.45 km/sec were determined in the upper mantle and 7.54 and 4.25 km/sec in the lower mantle. Although the bounds given on these velocities permit the velocities to be constant in the mantle, their final model consists of continuously decreasing velocities in the upper mantle and of a first-order discontinuity at a depth between 400 and 480 km. This discontinuity was determined by reflected arrivals on sections of polarization-filtered seismic records (Dainty et al., 1976; Goins et al., 1978; Goins, 1978). The latest results by Koyama and Nakamura (1979) also indicate small negative velocity gradients in the entire mantle. The mantle velocities at a depth of 45 km were found to be 7.85 and 4.31 km/sec for the compressional and shear waves, respectively.

Although the bounds on the velocities of the deeper lunar interior

are rather large (Nakamura et al., 1976; Goins, 1978), the various upper mantle velocities are consistent with a composition of olivine-pyroxene (ibid.). Small negative velocity gradients can be attributed to the increase of temperature with depth and to compositional change caused by increasing pyroxene or iron content (Nakamura et al., 1976). The increased attenuation, especially of shear waves, and the deep moonquake activity in the lower mantle support the hypothesis that the temperature increase itself can account for the velocity distributions.

The complicated waveforms of the lunar seismic signals and low coherency among the different components of the ground motion make convincing identification of reflected or converted arrivals quite difficult. These secondary arrivals are needed to clarify the discontinuities and to narrow the bounds on the velocities of the lunar interior. The major tool for searching for secondary arrivals has been the particle motion filter. Although the application of these filters assumes that the horizontal seismographs are matched, Jarosch (1977) concluded that the method seems to work in spite of the mismatch among the instrumental responses and of the small angle of incidence for most body wave arrivals at the free surface. Goins (1978) scaled the signal amplitudes of the three components to the same level before applying the particle motion filters. Although this normalization may also lead to incorrectly rotated transverse and radial components, Goins (1978) also concluded that it is a reasonable approach.

PART 1. DETERMINATION OF THE TRANSFER FUNCTION OF THE LONG-PERIOD LUNAR SEISMOGRAPHS.

1.1. Introduction.

A seismograph measures the relative motion between the frame of the seismometer and the mass of the pendulum. The relation between this motion and the ground displacement, velocity, or acceleration can be described by an integral equation, a differential equation, or the equivalent Laplace transform equation. These equations are functions of frequency and of certain controlled parameters of the seismograph.

It is often useful to obtain the actual ground motion from the seismic signal. This process is called instrumental deconvolution. In order to calculate the ground motion with reasonable accuracy, one has to answer two basically different groups of questions.

1. What are the characteristic equations of the system? What is the accuracy of the solution to these equations under the specified conditions? Are the assumptions used in deriving the solution reasonable approximations to the actual operating conditions? What is the noise introduced by the instrumentation? Do significant changes occur in the instrumental constants during operation?

2. What is the reliable frequency band for a meaningful deconvolution, that is, what is the accuracy of the deconvolution process? How do errors in the instrumental response and in the digitizing process propagate? What is the signal-to-noise ratio of the seismic records?

Answers to the first group of questions are independent of the

seismic records and come from the design, testing, and calibration of the seismographs. Part 1 answers these questions for the long-period lunar seismometers. The second group of questions is related to the deconvolution process itself and is discussed in Part 2.

If the Laplace transform or Fourier transform equation is used to solve the integral or differential equations then the function which describes the seismograph is called the transfer function whose inverse Laplace or Fourier transform is the impulse response (Bath, 1973, p. 234). The transfer function or the impulse response can be obtained in the following ways:

1. The empirical method involves Fourier analysis of the output of the system for an input which is equivalent to a known ground motion and is produced by some electrical or mechanical technique. This output is termed the calibration pulse or signal. Shaking table experiments (Silverman, 1939; Kelly, 1939), sine wave simulators (Murphy et al., 1954), application of the Maxwell impedance bridge (Willmore, 1959), and tapping tests (Matumoto, 1958; MacElwane and Sohon, 1932) are some examples for this technique.

2. The theoretical method consists of deriving the impulse response or transfer function analytically. The impulse response can be obtained as a solution of the equations of motion (Chakrabarty, 1949; Chakrabarty and Choudhury, 1964; Landisman et al., 1959). The transfer function may be derived by applying electrical network theories (Neugeberger, 1970; Kollar and Russell, 1966; Dopp, 1964; Hagiwara, 1958; Sutton and Latham, 1964). These methods require knowledge of the values of the instrumental constants.

The first technique does not yield the impulse response if the input is not an impulse in the desired domain (displacement, velocity, or acceleration). In this case, additional numerical integration or differentiation is needed to derive the impulse response from the calibration pulse. These operations introduce additional numerical noise, which would obscure the comparison of the various seismometers and would reduce the width of the frequency band for a reliable instrumental deconvolution. For example, if the input is obtained from a tapping test (MacElwane and Sohon, 1932, p. 111) then the impulse-displacement response of the seismograph is the twice-differentiated calibration pulse. If Lagrangian interpolation polynomials are used to obtain the derivatives, numerical noise can severely limit the passband. Increasing either the number of points used for the interpolation polynomials or the noise level of the pulse will narrow the frequency band for a predetermined signal-to-noise ratio for the instrument-deconvolved seismic records.

To decrease such noise and thus to broaden the reliable frequency band, and to learn more about the seismograph, it is desirable to combine the empirical and theoretical methods. First, the instrumental constants are determined from the calibration pulse, and then these constants are used in the analytical description of the impulse response of the transfer function. Espinosa et al. (1962) showed that the instrumental parameters can be determined by comparing the calibration pulse with a set of theoretically calculated responses at several points only. Mitchell and Landisman (1969) used the numerical least-squares technique for an electromagnetic seismograph.

They calculated the theoretical transfer function with a formula given by Hagiwara (1958), and transformed it into the time domain with the fast Fourier transform algorithm. Their experiments showed that this method was superior to the direct Fourier analysis of the pulse in yielding the values of the seismograph constants and in approximating the true transfer or response function in the presence of noise. The least-squares method was improved by deriving explicit expressions for the theoretical impulse response in the time domain (Jarosch and Curtis, 1973) and also by including the scale factor between the observed and theoretical calibration pulses (*ibid.*) and the origin time of the observed calibration pulse (Mitronovas and Wielandt, 1975; Mitronovas, 1976) in the inversion.

In the present analysis, the least-squares technique is used to determine the instrumental constants and the transfer functions of the direct-digitizing, feedback-controlled, long-period lunar seismographs. These lunar seismographs are described briefly in the next section; Section 1.3. provides computational details. The influence of noise and the results of these calculations are discussed in the final sections.

1.2. Description of feedback-controlled lunar seismographs.

The Apollo lunar seismic stations have a sensor unit and a central station electronics module. Each sensor unit consists of one short-period vertical component seismometer (SPZ) with a resonant period of 1 second, three closely matched, orthogonal, long-period seismometers (LP) with resonant periods of about 15 sec, and uncaging, leveling, and

temperature control devices. In the short-period instrument, a moving magnet mass is suspended from the frame with a LaCoste spring. By its movement, this magnet induces voltage in a coil, which is fixed to the frame. This voltage is therefore proportional to the relative velocity between the frame and the suspended mass. A LaCoste type spring is also used for the suspension of the mass in the vertical long-period seismometer (Z), while the horizontal sensors (X and Y) employ a swinging-gate system. Since the relative motion between the mass and the frame of the long-period seismometers is measured by capacitor-type displacement transducers, the electrical output is proportional to the relative displacement between the mass and frame. Long-term stability of the instruments is accomplished by feedback circuits, which can be switched between the normal (flat) and the modified (peaked) modes of operation. In the latter mode, the feedback filter is bypassed and the transfer function was sharply peaked at a period of about 2.2 sec.

The filtered and amplified signals of all four seismometers, as well as the feedback signal (also called the tidal output), and the output from the temperature sensor unit were digitized in 10-bit words and multiplexed in the central electronics unit. The 10-bit words were transmitted through a shift register in frames of 0.60375 seconds each. These frames comprise four samples from each of the LP components, 28 (station 15 only) or 29 SPZ samples, and alternately the two horizontal tidal samples or the vertical tidal sample and the output of the temperature sensor. Although the SPZ at station 12 never worked and occasionally a few of the other components functioned erratically,

most of the sensors operated normally for approximately 5.5 to 8 years until the time of the turn-off of the lunar passive seismic network on September 30, 1977. More detailed descriptions of the instrumentation are given elsewhere (e.g., Sutton and Latham, 1964; Earth Sciences, a Teledyne Company, 1968; Latham et al., 1969 and 1970; Lauderdale and Eichelman, 1974).

The calibration of all twelve LP seismographs was accomplished periodically by commands (e.g., Latham et al., 1969 and 1970). A suddenly applied electrical current, I , through the damping coil at time $t=t'$ produces a force, which is equivalent to a step of ground acceleration (Sutton and Latham, 1964; Kollar and Russell, 1966; Jarosch and Curtis, 1973):

$$m y_a(t) = m \frac{dy_v(t)}{dt} = m \frac{dy_d^2(t)}{dt^2} = \mu I H(t-t'), \quad \text{or} \quad m \frac{dy_a(t)}{dt} = \mu I \delta(t-t') \quad (1A)$$

where y is the ground motion and subscripts a , v , and d denote acceleration, velocity, and displacement, respectively; μ is the damping coil constant; H is the Heaviside step function, δ is the Dirac delta or impulse function and m is the seismometer mass. The relative displacement measured between the mass of the long-period pendulum and the frame of the seismometer is the calibration pulse, $C(t)$, which is proportional to the response to a unit step of acceleration, $R_0(t)$.

The response to a unit impulse of acceleration, $R_1(t)$, is

given by applying the differentiation and integration theorems of convolution

$$\frac{m}{\mu I} C(t) = R_0(t) = H(t) * R_1(t) = \delta(t) * \int_0^t R_1(x) dx \quad (1B)$$

where * stands for convolution, x is a dummy variable, and the system was assumed to be causal. From (1B)

$$\frac{dR_0(t)}{dt} = R_1(t) \quad (1C)$$

The responses to a unit impulse of velocity or unit impulse of displacement, $R_2(t)$ and $R_3(t)$, respectively, are obtained by the definition of the responses,

$$y_a(t) * R_1(t) = y_v(t) * R_2(t) = y_d(t) * R_3(t) \quad (1D)$$

and by the differentiation and integration theorems of convolution,

$$y_a(t) * R_1(t) = y_a(x) dx * \frac{dR_1(t)}{dt} = y_v(t) * \frac{dR_1(t)}{dt} = y_d(t) * \frac{d^2 R_1(t)}{dt^2} \quad (1E)$$

Relations among $R_k(t)$'s described by equations (1B) through (1E) can be summarized by

$$\frac{m}{\mu I} \frac{d^k C(t)}{dt^k} = R_k(t), \quad k=0,1,2,3 \quad (1F)$$

$$\text{or } \frac{dR_k(t)}{dt} = R_{k+1}(t), \quad k=0,1,2 \quad (1G)$$

Equations (1F) and (1G) can be expressed in the frequency domain as follows

$$\frac{m}{\mu I} (j\omega)^k \bar{C}(\omega) = T_k(\omega), \quad k=0,1,2,3 \quad (2A)$$

$$j\omega T_k(\omega) = T_{k+1}(\omega), \quad k=0,1,2 \quad (2B)$$

where ω is the angular frequency, $j=\sqrt{-1}$, and $\bar{C}(\omega)$ and $T_k(\omega)$ are the Fourier transforms of $C(t)$ and $R_k(t)$, respectively,

$$\bar{C}(\omega) = \int_{-\infty}^{\infty} C(t) \exp(-j\omega t) dt \quad (2C)$$

$$T_k(\omega) = \int_{-\infty}^{\infty} R_k(t) \exp(-j\omega t) dt \quad (2D)$$

If the seismograph responds linearly to the ground motion, the Fourier transform of the calibration pulse for the long-period lunar seismographs can be approximated analytically by using the equivalent electric current analog shown in Figure 2 (Sutton and Latham, 1964; Earth Sciences, a Teledyne Company, 1968) as follows

$$\frac{m}{\mu I} \bar{C}^c(\omega) = T_0^c(\omega) = \begin{cases} - \frac{j\omega^{-1} K_1 G(\omega) F_d(\omega)}{1 + K_1 K_2 G(\omega) F_d(\omega) F_f(\omega)} K K_3 F_a(\omega) F_d(\omega) & (3A) \\ - \frac{j\omega^{-1} K_1 G(\omega) F_d(\omega)}{1 + K_1 K_2 G(\omega) F_d(\omega)} K K_3 F_a(\omega) F_d(\omega) & (3B) \end{cases}$$

where superscript c denotes calculated values,

$$G(\omega) = \frac{1}{-\omega^2 + 2\beta\omega_0 j\omega + \omega_0^2} \quad (3C)$$

is the transfer function of the seismometer if the input is considered to be frame acceleration and the output is the displacement between the seismometer mass and the frame (Sutton and Latham, 1964),

$$F_d(\omega) = \frac{\omega_d}{\omega_d + j\omega} \quad (3D)$$

is the transfer function of the demodulator low-pass filter,

$$F_f(\omega) = \frac{\omega_f}{\omega_f + j\omega} \quad (3E)$$

is the transfer function of the feedback low-pass filter,

$$F_a(\omega) = \frac{j\omega}{\omega_a + j\omega} \quad (3F)$$

is the transfer function of the high-pass filter in the output amplifier,

$$F_1(\omega) = \left[\frac{\omega_1^2}{-\omega^2 + 2\cos\frac{\pi}{8}\omega_1 j\omega + \omega_1^2} \right]^2 \left[\frac{\omega_1^2}{-\omega^2 + 2\cos\frac{3\pi}{8}\omega_1 j\omega + \omega_1^2} \right]^2 \quad (3G)$$

is the transfer function of the output low-pass antialias filter, and $K, K_1, K_2, K_3, \beta, \omega_0, \omega_d, \omega_f, \omega_a,$ and ω_1 are defined in Table 2. Equations (3A) and (3B) are valid when the feedback circuit is operated in the flat mode and the peaked mode, respectively.

The transfer functions to an impulse of acceleration, velocity, or displacement, $T_k^C(\omega)$ ($k=1,2,3$), can be calculated from equations (2) and (3)

$$T_k^C(\omega) = (j\omega)^k \{R(\omega) + jI(\omega)\} = \omega^k A(\omega) \exp\{j(F(\omega) - k\frac{\pi}{2})\} \quad (4A)$$

where $R(\omega)$ and $I(\omega)$ are the real and imaginary parts of the calculated transfer function to a step of acceleration, $A(\omega)$ and $F(\omega)$ are the calculated amplitude and phase spectra of the response to a step of acceleration

$$T_0^C(\omega) = R(\omega) + jI(\omega) = A(\omega) \exp\{jF(\omega)\} \quad (4B)$$

$$A(\omega) = \sqrt{R(\omega)^2 + I(\omega)^2}, \quad F(\omega) = \tan^{-1}\{I(\omega)/R(\omega)\} \quad (4C)$$

The nominal values for the seismograph constants used in equations (3) and in Figure 2 are listed in Table 2. The nominal responses to a step of acceleration calculated with the inverse Fourier transform of equations (3) differ from the observed calibration pulses shown in Figures 3 and 4 for the peaked mode and the flat mode, respectively. In these figures, the positive and sign-reversed negative pulses were averaged. The averaging and the determination of the beginning of these calibration pulses are discussed in the following section. These pulses were taken during the relatively quiet lunar nights when the instrument temperatures were $125 \pm 0.5^{\circ}\text{F}$ and the background noise was lower than that during the lunar days. Table 3 gives the dates when these calibration pulses were recorded and summarizes the visually obtained properties of these pulses.

There are significant differences among the amplitudes of the pulses for the different components. Some of the differences in the amplitudes are attributed to the different currents applied through the damping coils. Although the current level was set to provide about one-fourth full scale output or 256 digital units (DU) in the flat mode (Earth Sciences, a Teledyne Company, 1968), all of the calibration pulses in the peaked mode, except for component 15Z, are much smaller (13 to 20 DU) because the effective stiffness of the suspension is increased in the peaked mode. The larger calibration pulse for component 15Z in both modes is primarily due to an undetermined failure in setting the calibration current. The calibration pulse for component 12Z looks similar to the others in the peaked mode but differs from the others in the flat mode.

To estimate the effects of temperature on the response of the lunar long-period seismographs and the long-term drift, the maximum amplitudes, durations, and time intervals between successive peaks were compared for calibration pulses taken in the peaked mode between 1971 and 1975. In the flat mode, the times of the zero crossings were compared instead of the time intervals between successive peaks for calibration pulses recorded in 1975 and 1976.

The changes in most calibration pulses for a given component were within the seismic background noise level except in the peaked-mode calibration pulses for component 15Z. For these pulses, the time intervals between successive peaks remained unchanged and the maximum amplitudes were 14% lower at 137°F than at 125°F. Most of the differences can be explained by a smaller calibration current and/or output gains at 137°F than at 125°F. In the following sections, those calibration pulses are analyzed which were taken during the lunar nights, when the temperature was $125 \pm 0.5^\circ\text{F}$, and the signal-to-noise ratio was highest.

1.3. Computational details for determining the instrumental constants by least-squares fit of the observed and theoretical calibration pulses.

The least-squares scheme, described in the Appendix, can be constructed either in the time domain or in the frequency domain. The former scheme fits the calibration pulse with the calibrated response to a step of acceleration. In the latter scheme, either the calculated amplitude or the calculated complex transfer function serves as a fitting function to the Fourier transform of the observed

calibration pulse. The schematic flow chart of the computer program is shown in Figure 5. The first method is preferred to the second one because it involves numerical operations on the calculated transfer function instead of the observed calibration pulse and because the observed-minus-calculated (O-C) curve is measured in digital units. Since this scheme requires the calculation of the inverse Fourier transform of the partial derivatives, and thus, longer computational time, it was used only to investigate the effects of noise and to judge the goodness of the fit.

In order to understand the limitations of this numerical technique and to interpret the results correctly, I shall discuss the iterational process in some detail (see Figure 5 and Appendix).

The first step in the iterational loop requires the calculation of the transfer function to a step of acceleration. The nominal values of the seismograph constants, listed in Table 2, were used for the first iteration. If the sampling interval in the time domain is τ ($\tau=0.15094$ seconds for the long-period lunar seismograms) and the number of points to be calculated in the time domain is N (N was an integral power of 2, because the fast Fourier transform was used), then the Nyquist angular frequency, ω_{Nq} , and the sampling interval in the angular frequency domain, σ , are

$$\omega_{Nq} = \frac{\pi}{\tau} = 2\pi \cdot 3.3126 \text{ sec}^{-1} \quad \text{and} \quad \sigma = \frac{2\omega_{Nq}}{N} = \frac{2\pi}{N\tau} \quad (5)$$

The transfer function was evaluated at angular frequencies of $\omega = m\sigma$ ($m=0,1,2,\dots,N/2-1$) according to equations (3) and (4). The analytical

expressions for the partial derivatives of the transfer function with respect to the instrumental parameters were evaluated according to formulas derived from equations (3):

$$\frac{\partial T_0(\omega)}{\partial a_1} = \frac{T_0(\omega)}{a_1} \quad (6A)$$

$$\frac{\partial T_0(\omega)}{\partial a_2} = - \frac{T_0(\omega)G(\omega)ja_3\omega}{D(\omega)} \quad (6B)$$

$$\frac{\partial T_0(\omega)}{\partial a_3} = - \frac{T_0(\omega)G(\omega)}{D(\omega)}(2a_3+a_2j\omega) \quad (6C)$$

$$\frac{\partial T_0(\omega)}{\partial a_4} = \frac{T_0(\omega)}{a_4D(\omega)} \frac{j\omega}{a_4+j\omega} \quad (6D)$$

$$\frac{\partial T_0(\omega)}{\partial a_5} = - \frac{T_0(\omega)}{a_5+j\omega} \quad (6E)$$

$$\frac{\partial T_0(\omega)}{\partial a_6} = \frac{2T_0(\omega)}{a_6} \left[\frac{-2\omega^2+j\omega 2\cos\frac{\pi}{8}a_6}{a_6^2-\omega^2+j\omega 2\cos\frac{\pi}{8}a_6} + \frac{-2\omega^2+j\omega 2\cos\frac{3\pi}{8}a_6}{a_6^2-\omega^2+j\omega 2\cos\frac{3\pi}{8}a_6} \right] \quad (6F)$$

$$\frac{\partial T_0(\omega)}{\partial a_7} = - \frac{T_0(\omega)G(\omega)F_d(\omega)F_f(\omega)}{D(\omega)} \quad (6G)$$

$$\frac{\partial T_0(\omega)}{\partial a_8} = - \frac{T_0(\omega)a_7G(\omega)F_d(\omega)}{a_8D(\omega)} \frac{j\omega}{a_8+j\omega} \quad (6H)$$

$$\text{where } D(\omega) = 1 + a_7F_f(\omega)F_d(\omega)G(\omega) \quad (6I)$$

Parameters a_m ($m=1,2,\dots,7$ or 8) are given in Table 2 and $F_f(\omega)$ is taken as unity in the peaked mode and $\partial T_0(\omega)/\partial a_8$ applies in the flat mode only. The real and imaginary parts of the partial derivatives are shown in Figures 6 and 7. The theoretical calibration pulse and its partial derivatives were calculated by the inverse Fourier transform of equations (3) and (6) when the time domain was used for fitting (see Figures 8 and 9). When the amplitude spectra were fitted, the amplitude and phase responses to a step of acceleration were obtained from (3) and (4), while the partial derivatives (see Figures 10 and 11) were calculated with formulas derived from (4):

$$\frac{\partial A(\omega)}{\partial a_m} = \frac{R(\omega) \frac{\partial R(\omega)}{\partial a_m} + I(\omega) \frac{\partial I(\omega)}{\partial a_m}}{\sqrt{R(\omega)^2 + I(\omega)^2}}, \quad m=1,2,\dots,7 \text{ or } 8 \quad (7A)$$

$$\frac{\partial F(\omega)}{\partial a_m} = \frac{R(\omega) \frac{\partial I(\omega)}{\partial a_m} - I(\omega) \frac{\partial R(\omega)}{\partial a_m}}{R(\omega)^2 + I(\omega)^2}, \quad m=1,2,\dots,7 \text{ or } 8 \quad (7B)$$

As seen from Figures 6 through 11, some of the partial derivatives are practically identical. The linearly dependent partial derivatives cannot be used in the least-squares scheme (see Appendix). In fact, the iteration did not converge if partial derivatives with respect to parameters a_2 , a_3 , and a_4 were used simultaneously in the peaked mode. Similarly, only one partial derivatives could be used from parameters a_2 and a_8 , from a_4 and a_6 , and from a_5 and a_7 in the

flat mode. Beside the seismograph parameters, the exact origin time of the calibration pulse was also unknown and had to be determined in the least-squares scheme, which required calculation of the partial derivative of the calibration pulse with respect to time. The time derivative is similar to the partial derivative with respect to a_6 in the peaked mode and with respect to a_4 and a_6 in the flat mode.

The value of a_4 was fixed in both modes of operation because its effect on the calibration pulse is negligible. The nominal value of a_6 was also accepted as the correct one because shifting the beginning of the calibration pulse by one sample changes a_6 by about 25%. In the peaked mode, only the product of the damping constant and the free frequency of the pendulum can be determined because ω_0^2 is much smaller than are the other terms in the denominator of equation (3C) at those frequencies where the amplitude response is significant. I assumed $2\pi/\omega_0=15$ sec in the peaked mode in order to determine one constant from a_2 and a_3 . Finally, in the flat mode, a_3 and a_7 were adjusted to permit comparison of the calculated values for a_7 in the two modes of operation. Also, the pendulum constants are more readily affected by unusual conditions than are the electrical constants.

The next step involves the calculation of an approximate scale factor, c , which relates the observed points, y_i , and the theoretical function, $y(x)$, such that (compare to equation (A3) in the Appendix):

$$\sum_{i=1}^M (y_i - cy(x_i))^2 = \text{minimum with respect to } c \text{ only,} \quad (8)$$

where x and y are either the time and the calibration pulse or the frequency and the transfer function (amplitude or complex spectrum), and M is the number of points to be fitted. c is given by the calibration parameters (μ , I , and m , see equations (1A), (1D), (3A), and (3B)):

$$c = \frac{\mu I}{m} \quad (9)$$

Equation (8) yields

$$c = \frac{\sum_{i=1}^M y_i y(x_i)}{\sum_{i=1}^M y(x_i)^2} \quad (10)$$

The sample number k closest to the origin time of the calibration pulse was calculated by the formula

$$\sum_{i=1}^{M-k+1} \{C((i+k-1)\tau) - cR_0^C(i\tau)\}^2 = \text{minimum with respect to } k, \quad (11)$$

except when the amplitude spectra was used in the least-squares scheme. This criterion cannot be applied in the flat mode because the relative change between two consecutive amplitudes of the calibration

pulse is smaller, thus the minimum expressed by (11) is much less affected by the improper beginning in the flat mode than in the peaked mode.

Next, the difference between the observed and calculated functions, termed O-C error or O-C vector, and the root mean square (RMS) error were calculated according to equations (A2E) and (A3) of the Appendix. The following steps were straightforward: check for convergence, scale the theoretical function, and calculate the inverse Fourier transform of the partial derivatives if needed. Finally, the adjustments were calculated according to (A3) of the Appendix with subroutine 'LLSQ' of the IBM Scientific Subroutine Package (IBM Application Program, 1970). Before the iteration was repeated, the adjustments in the origin time of the calibration pulse was checked; if it was more than half of the sampling interval then the first sample of the observed calibration pulse was changed accordingly.

This iteration process converged very fast; after 3 to 5 iterations the adjustments were of the order of 10^{-5} , and after 5 to 7 iterations the RMS error started increasing because the limit of resolution was reached.

1.4. The influence of noise.

Special attention should be given to the effects of noise in the determination of the seismograph parameters because the signal-to-noise ratio is rather small for most calibration pulses. Noise in the calibration pulse may force the least-squares scheme to adjust

an instrumental parameter incorrectly when the product of the needed adjustment to this parameter and the partial derivative of the spectrum of the calibration pulse with respect to this parameter changes with frequency in the same way as the noise spectrum. The following error sources will be discussed in some detail:

- a) Digitizing noise and instrumental nonlinearity
- b) Instrumental noise except nonlinearity
- c) Ground noise
- d) Numerical noise

a) The lunar seismometers used truncation-type analog-to-digital converters (Gold and Rader, 1969, p. 99). The digitizing errors can be important for the calibration pulses in the peaked mode because the signal amplitudes were only 13 to 20 digital units (DU). Instrumental nonlinearity did not affect the largest calibration pulses significantly as demonstrated in connection with the numerical noise by the satisfactory fit obtained between the observed and calculated calibration pulses for station 15. The positive and the negative calibration pulses of 13 to 20 DU are slightly different from each other in the peaked mode and the negative calibration pulses resulted in higher values for the damping constant, for the scale factor, and for $2\pi/\omega_a$ than did the positive calibration pulses. From these results, I conclude that the sum of the positive and the sign-reversed negative pulses must be used for determining the seismograph parameters, which also results in cancelling the d.c. level caused by digitization. In the flat mode, the digitizing errors and the nonlinear effects of the instrument are less important than

either the seismic ground or instrumental noise.

b) and c). The instrumental noise is described in the literature in great detail (e.g., Byrne, 1961; Sutton and Latham, 1964). My purpose was to determine the effects of the instrumental and seismic ground noises on the accuracy of the determination of the seismometer constants. The high frequency noise, which is caused by the amplifier-transducer noise, does not affect the calculations because the instrumental response is low at high frequencies. Studies by Byrne (1961) and Sutton and Latham (1964) showed that the feedback and thermal noises increase with period and are inversely proportional to the square root of the mass of the pendulum. Since the mass of the lunar seismometers is very small (0.75 kg for the long-period instruments), most of the long-period noise can be attributed to these noises, especially to the thermal noise. This long-period noise and the seismic ground noise influence the determined values of a_5 and, to a lesser extent, the scaling factor in the peaked mode (see the partial derivatives in Figures 8 and 10). Since the noise is about 1 DU in the peaked mode, the seismic ground noise cannot be separated from the errors of digitization. In the flat mode, the long-period ground noise influences all five partial derivatives used in the least-squares process since the corresponding constants can be determined best from the long-period portion of the calibration pulse spectra, where the amplitudes of the partial derivatives are largest. The damping constant is more sensitive than the other constants to noise at periods of 15 to 25 seconds. The rest of the parameters are influenced by the noise at longer periods (see Figures 9 and 11).

d). The numerical noises are introduced by the finite number of samples used in the fast Fourier transform, by the simplification of the model from which the theoretical transfer functions are calculated, and by the rounding errors. These numerical errors were investigated in the time domain using calibration pulses for station 15. The O-C values for the calibration pulse for the vertical component in the peaked mode were less than 1 DU for most of the 379 points used (10 points had values between 1 and 1.2, another 10 between 1.48 and 2), if the sampling interval in the angular frequency domain was $\sigma = \omega_{Nq}/4096$. When the sampling interval in the angular frequency domain was increased, the O-C values increased, but the calculated constants, except a_5 , remained essentially the same. a_5 increased by 5% or so with each doubling of the sampling interval in the angular frequency domain up to $\sigma = \omega_{Nq}/512$. These observations reflect the sensitivity of a_5 to long-period noise (see Figures 8 and 10) and the long duration of the calibration pulse (Table 2). In the flat mode, however, the RMS errors for the horizontal components did not decrease for sampling interval in the angular frequency domain smaller than $\sigma = \omega_{Nq}/512$ and the O-C values were comparable with the estimated noise in Table 3 (7.1 DU for 15X and 9.2 DU for 15Y). These results show that although the O-C values are affected by the length of the fast Fourier transform, 1024 samples in the time domain are sufficient for obtaining the instrumental constants in both operating modes.

1.5. Results and discussion.

In the previous sections, I discussed the limitations inherent in calculating the constants of the long period lunar seismographs. They can be summarized as follows:

1. The d.c. level can be suppressed and the signal-to-noise ratio can be improved by averaging the positive and sign-reversed negative calibration pulses (I refer to this sum as a set of pulses).

2. The transfer function and its derivatives should have at least 512 complex points.

3. The computation is faster in the frequency domain.

4. The nominal value of 0.72 sec for $2\pi/\omega_1$ is acceptable as the best estimate because its determined value is sensitive to the origin time of the calibration pulse.

5. The nominal value of 100 sec for $2\pi/\omega_a$ is acceptable as the correct one in both operating modes because its derived value is strongly influenced by long-period noise in the peaked mode and by K_1K_2 in the flat mode.

6. In the flat mode, long-period noise affects every partial derivative very strongly.

7. The scale factor, the origin time of the calibration pulse, the product of K_1 and K_2 , and the product of β and ω_0 can be calculated in the peaked mode.

8. In the flat mode, the scale factor, the origin time of the calibration pulse, the product of K_1 and K_2 which is influenced by ω_a , the damping constant, and the free frequency of the pendulum which is

influenced by ω_f can be adjusted.

9. β and the scale factor are over- and underestimated using the negative and the positive pulses, respectively, in the peaked mode.

Table 4 lists the average of the constants determined from the sum of two sets of calibration pulses (one from 1972 and another from 1975) in the peaked mode and for one set of pulses (from 1976) in the flat mode. The nominal values for those constants which cannot be calculated are also given in Table 4. Since the determined values for $\omega_0\beta$ and K_1K_2 are different in the peaked and in the flat modes, K_f' and β_f' were calculated from the constants. K_f' would be 1 and β_f' would be β_f if the noise were negligible and the partial derivatives with respect to every seismograph parameter were linearly independent. Relative amplifications were also calculated assuming the amplification to be 1.0 for component 15X, whose calibration pulse possesses a relatively low noise level in the flat mode (see Table 3) and whose determined constants are closest to the averages of the constants in both modes. The errors in the determination of the seismograph constants were calculated by taking the maximum of the differences between the values given in Table 4 and the values determined from one positive and one negative pulse only. These errors, as well as the relative differences in the damping coefficients, in K_1K_2 , and in the scale factors, are given in Table 5 and correlate strongly with the estimated noise in the flat mode (see Table 3). The noise and the relative errors are larger for the horizontal components than for the vertical ones.

Although the noise and the choice of the seismograph constants

to be adjusted in the least-squares scheme influences the determined values of the seismograph constants, the transfer functions of the seismographs can be calculated with good accuracy. The good fit between the peaked-mode calculated and observed amplitude and phase responses to a step of acceleration is shown in Figures 12 and 13 for 15X and 15Z. It should be noted that the relatively large O-C values at long periods are caused by the finite length of the Fourier transform (see Section 1.3.).

The peaked-mode amplitude responses to an impulse of displacement, which were calculated with the constants of Table 4, with $KK_1K_3=1$ DU/cm, and with equations (2)-(4), are shown in Figure 14. Tables 6 and 7 and Figures 15 and 16 give the absolute values of the relative differences between these individual amplitude responses and the amplitude response of components 15X and 15Z. These relative differences are the relative errors which could be made in the deconvolution process by using the transfer function of 15Z, which was determined with the smallest errors, and of 15X, which represents the average of the transfer functions. As seen from Figures 15 and 16, the errors are most sensitive to K_1K_2 which can be determined with the best accuracy in the peaked mode. The maxima of the errors generally exceed 10%, which corresponds to the largest determined difference between the average and the individual damping constants (see the curve for 14Z in Figure 15).

1.6. Conclusions.

Although precise seismograph constants cannot be calculated from

the calibration pulses, a theoretical transfer function whose inverse Fourier transform fits each individual calibration pulse best can be determined for each seismograph. The results allow one to deconvolve the records with instrumental response having errors of less than 10%, but do not permit to compare the absolute amplitudes among the various components. Therefore, any studies using the amplitudes of the seismic records should be based on sound experimental and/or statistical investigations of the individual amplification factors. More precise determination of the transfer functions can be obtained by stacking the calibration pulses, by studying the long-period noises in the flat mode for the vertical and horizontal components separately, and by merging the calibration pulses of peaked and flat modes into the same least-squares scheme. It is also possible that a satisfactory explanation can be found for some of the irregularities in the operation of the seismographs and that the temperature effects on the free period and damping coefficient of the seismometer can be determined by stacking the calibration pulses for different time intervals.

PART 2. INSTRUMENTAL AND WHITENING DECONVOLUTION OF THE LONG-PERIOD LUNAR SEISMOGRAMS.

2.1. Introduction.

The first part of this dissertation dealt with the long-period lunar seismographs. The theoretical transfer function of these instruments was determined individually by a least-squares process. This was necessary in order to correct the seismic records for instrumental response in the peaked mode because the calibration pulses of the various components exhibit certain differences but are generally too small to be used directly for calculating the actual ground motion. The instrumental deconvolution may increase the noise at those frequencies where the instrumental response is low in comparison to the noise. It is therefore necessary to control the noise at these frequencies. Different deconvolution and quality control techniques are reviewed in the following section. Then, the most suitable technique is used to remove the instrumental effects from the long-period lunar seismic signals recorded in the peaked mode. For signals recorded in the flat mode, the influence of instrumental response can be ignored by comparison with local site effects and noise, because the instrumental response is nearly constant in the frequency band of interest. Section 2.4. shows that the amplitude spectra of the ground motion are characteristic of each recording site. These near-surface effects were removed by inverse filters derived from the average spectral amplitudes of the ground motion. These inverse filters are termed whitening filters, because they were designed to diminish

dominant peaks in the amplitude spectra. The application of these whitening filters permits the comparison of the various seismic records without the strong instrumental and near-surface effects.

2.2. Wavelet-deconvolution techniques.

The seismic signals carrying information about the transmission properties of the medium are modified by the source, the receiver, and the local structure at the recording site. The mathematical model for describing these modifications consists of the convolution of the response functions of the different linear physical processes. This type of model permits correction for any of these effects if its response function is given.

The convolution equation for a linear system is given by

$$r(t) = w(t)*g(t) + n(t) \quad (12)$$

where t is the time variable, $w(t)$ is the impulse response of a system whose input and output are $g(t)$ and $r(t)$, respectively, $n(t)$ is additive noise, and $*$ represents the convolution operation. If $w(t)$ is the impulse response of the seismograph, then $g(t)$ is the ground motion, and $r(t)$ is the seismogram.

An inverse filtering process can be defined as a process of calculating $g(t)$ from $r(t)$ and $w(t)$. This process is called wavelet deconvolution and can be carried out either in the time domain or in the frequency domain. In the time domain, the standard wavelet deconvolution is performed by the Wiener or optimum least-squared filtering

(Robinson and Treitel, 1967).

The frequency domain deconvolution can be performed after taking the Fourier transform of equation (12) (functions denoted by lower-case and capital letters are Fourier transform pairs):

$$R(\omega) = W(\omega)G(\omega) + N(\omega) \quad (13)$$

The Fourier transform of the calculated input, $\bar{G}(\omega)$, is obtained by spectral division:

$$\bar{G}(\omega) = \frac{R(\omega)}{\bar{W}(\omega)} = \frac{R(\omega)\bar{W}^*(\omega)}{|\bar{W}(\omega)|^2} \quad (14)$$

where superscript * denotes complex conjugate, and $\bar{W}(\omega)$ is the Fourier transform of the wavelet used and may differ from that of the true wavelet, $W(\omega)$:

$$\bar{W}(\omega) = W(\omega) + M(\omega) \quad (15)$$

or in the time domain

$$\bar{w}(t) = w(t) + m(t) \quad (16)$$

The error $m(t)$ will contribute to the total error of the deconvolution.

The relation between the Fourier transforms of the actual and calculated inputs is obtained from equations (13) - (16):

$$G(\omega) = \bar{G}(\omega) \frac{1 - N(\omega)/R(\omega)}{1 - M(\omega)/\bar{W}(\omega)} = \bar{G}(\omega) \{1 - \rho(\omega)\} \quad (17A)$$

where $\rho(\omega)$ is the relative difference between the calculated and actual inputs:

$$\rho(\omega) = \frac{\bar{G}(\omega) - G(\omega)}{\bar{G}(\omega)} = 1 - \frac{1-N(\omega)/R(\omega)}{1-M(\omega)/\bar{W}(\omega)} \quad (17B)$$

If $M(\omega)=0$ for all frequencies, then (17B) becomes

$$\rho(\omega) = \frac{N(\omega)}{R(\omega)} \quad (17C)$$

The absolute values of the relative errors can be estimated from (17B) if $|N(\omega)| \ll |R(\omega)|$ and $|M(\omega)| \ll |\bar{W}(\omega)|$:

$$|\rho(\omega)| < \frac{|M(\omega)|}{|\bar{W}(\omega)|} + \frac{|N(\omega)|}{|R(\omega)|} = \frac{|M(\omega)|}{|\bar{W}(\omega)|} + \frac{|N(\omega)|}{|\bar{G}(\omega)||\bar{W}(\omega)|} \quad (17D)$$

Although equation (14) is satisfactory in the noiseless case ($|M(\omega)|=0$ and $|N(\omega)|=0$ for all frequencies), $|\rho(\omega)|$ is large (see equation (17D)) at those frequencies where $|\bar{W}(\omega)|$ becomes small in comparison with $|N(\omega)|/|G(\omega)|$ (Rice, 1962). Therefore, it is necessary to control the signal-to-noise ratio of the calculated input at these frequencies. This quality control can be achieved by suppressing either the noise, $N(\omega)$, or the amplitudes of $1/\bar{W}(\omega)$. The latter process will be discussed in the following paragraphs.

One can add white noise to the wavelet, $\bar{w}(t)$, before the ground motion is calculated. This process is called whitening and is a standard procedure in least-squares filtering. The equivalent process

in the frequency domain is called γ -Fourier filtering, which modifies the power spectrum in the denominator of (14) by adding a term proportional to the signal or to the noise level (Deregowski, 1971):

$$\bar{G}(\omega) = \frac{R(\omega)\bar{W}^*(\omega)}{|\bar{W}(\omega)|^2 + \lambda E_n} \frac{E_s + E_n}{E_s} = \frac{(1+\gamma)R(\omega)\bar{W}^*(\omega)}{|\bar{W}(\omega)|^2 + \gamma E_s} \quad (18A)$$

where $E_s = \int_{-\infty}^{\infty} |\bar{W}(\omega)|^2 d\omega$ (18B)

$$E_n = \int_{-\infty}^{\infty} |G(\omega) - \bar{G}(\omega)|^2 d\omega \quad (18C)$$

$$\frac{\lambda}{\gamma} = \frac{E_s}{E_n} \quad (18D)$$

It can be easily shown (ibid.) that this process increases the central auto-correlation value of the wavelet $\bar{w}(t)$ by the factor $(1+\gamma)$, just as the whitening does, where γ is the ratio of the energy of the added white noise to the energy of the wavelet.

One can avoid changing $R(\omega)/\bar{W}(\omega)$ at those frequencies where the signal-to-noise ratio is acceptable by introducing a minimum wavelet amplitude or waterlevel (Helmberger and Wiggins, 1971; Clayton and Wiggins, 1976), which is expressed as the fraction of the maximum wavelet amplitude, $|\bar{W}(\omega)|_{\text{Max}}$:

$$\text{minimum wavelet amplitude} = k|\bar{W}(\omega)|_{\text{Max}} \quad (19A)$$

where k is called the waterlevel parameter. Expression (19A) is used in the denominator of (14) at those frequencies where the wavelet amplitudes are low:

$$\bar{G}(\omega) = \frac{R(\omega)\bar{W}^*(\omega)}{\{\max\{|\bar{W}(\omega)|, k|\bar{W}(\omega)|_{\text{Max}}\}\}^2} \quad (19B)$$

The noise also can be suppressed by determining the frequency band, $(\omega_{\text{min}}, \omega_{\text{Max}})$, in which the signal-to-noise ratio is acceptable and by introducing constant amplitudes outside this band:

$$\bar{G}(\omega) = \begin{cases} R(\omega)/\bar{W}(\omega), & \text{if } \omega_{\text{min}} \leq \omega \leq \omega_{\text{Max}} \quad (20A) \\ R(\omega_{\text{min}})/\bar{W}(\omega_{\text{min}}), & \text{if } \omega < \omega_{\text{min}} \quad (20B) \\ R(\omega_{\text{Max}})/\bar{W}(\omega_{\text{Max}}), & \text{if } \omega_{\text{Max}} < \omega \quad (20C) \end{cases}$$

The amplitudes of the calculated input can also be zeroed outside this band (Plesinger et al., 1970):

$$\bar{G}(\omega) = \begin{cases} R(\omega)/\bar{W}(\omega), & \text{if } \omega_{\text{min}} \leq \omega \leq \omega_{\text{Max}} \quad (21A) \\ 0, & \text{if } \omega < \omega_{\text{min}} \text{ or } \omega_{\text{Max}} < \omega \quad (21B) \end{cases}$$

Although there is not much practical difference between (20) and (21) in case of large signal-to-noise ratio, (20) is closer to reality, since the input seldom is a band-limited signal.

All of these techniques for quality control involve the estimation of the signal-to-noise ratio, that is $\rho(\omega)$ or its inverse Fourier transform. This estimation leads to the percentage of white noise to be added to the wavelet, the value of γ in the γ -Fourier filter, the waterlevel, or the reliable frequency band, and it requires the estimation of $n(t)$ and $m(t)$ or $N(\omega)$ and $M(\omega)$. The reliable frequency band can also be defined by trial and error; the spectral amplitudes of the calculated input would increase at those frequencies where the $|1/\bar{W}(\omega)|$ becomes small in relation to the noise (Plesinger et al., 1970).

2.3. Instrumental deconvolution of the peaked-mode long-period lunar seismograms.

As shown in the previous section, the noise in the calculated ground motion should be suppressed. This noise depends on the noise level of the recorded seismograms to be corrected for instrumental response and may be estimated from the difference between the observed and theoretical calibration pulses. In this section, I describe how the calibration pulses were used to estimate the reliable frequency band for instrumental deconvolution of the peaked-mode long-period lunar seismograms.

The simplest and most rapid way to estimate the signal-to-noise ratio of the calibration pulse is by inspection of its phase spectrum (see Figure 12 for components 15X and 15Z). Oscillations of the phase

spectrum of the observed calibration pulses increase with decreasing signal-to-noise ratio. The phase spectra of the peaked-mode calibration pulses are oscillatory at frequencies higher than about 1.3 Hz (1.6 Hz for component 15Z) (see Figure 12). Near this frequency the amplitude of the noise is about that of the signal. The lower limit for the reliable frequency band was estimated assuming the additive noise to be white, i.e., the signal-to-noise ratios are about the same at those frequencies where the signal amplitudes are the same. Thus, the lower limit is the frequency where the amplitude response of the seismograph is about the same as that at the upper limit and is about 0.28 Hz for most components and about 0.17 Hz for component 15Z.

The estimate for the reliable frequency band for instrumental deconvolution was refined by calculating the residuals between the theoretical and observed calibration pulses (Kulhanek and Lima, 1970, used an analytically calculated amplitude spectrum to estimate digitizing errors). The lower curves of Figure 13 show the absolute value of the differences between the amplitude spectra of the observed and theoretical calibration pulses in the peaked mode. The Fourier transforms of the observed and the calculated calibration pulses $\bar{C}(\omega)$ and $\bar{C}^c(\omega)$, respectively, are given from equations (1), (2), (3), (9), and (13):

$$\bar{C}(\omega) = c(j\omega)^{-3}W(\omega) + N_c(\omega) \quad (22A)$$

$$\bar{C}^c(\omega) = c(j\omega)^{-3}\bar{W}(\omega) \quad (22B)$$

where $N_c(\omega)$ is the additive noise in the observed calibration pulse. The difference between the Fourier transforms of the calculated and observed calibration pulses, $\delta\bar{C}(\omega)$, is given by equations (22A), (22B), and (15):

$$\delta\bar{C}(\omega) = \bar{C}^c(\omega) - \bar{C}(\omega) = c(j\omega)^{-3}M(\omega) - N_c(\omega) \quad (23A)$$

And the absolute value of the difference is

$$|\delta\bar{C}(\omega)| \leq c\omega^{-3}|M(\omega)| + |N_c(\omega)| \quad (23B)$$

Since $M(\omega)$ and $N(\omega)$ were assumed to be random, and $\delta\bar{C}(\omega)$ was found to be random,

$$c\omega^{-3}|M(\omega)| \ll |N_c(\omega)| \quad (23C)$$

With (23C), (23B) becomes

$$|\delta\bar{C}(\omega)| = |N_c(\omega)| \quad (23D)$$

Figure 13 also gives the absolute values of the relative errors defined as the ratio of the observed-minus-calculated values to the theoretical amplitude spectra of the calibration pulse. Table 8 lists the upper limit for the frequency band in which the relative errors are less than 0.4, 1.0, and 2.5. These relative errors were used to estimate the relative difference between the observed and calculated ground

motions. If the primary source of noise is the digitizing process and the transducer-amplifier system (see Section 1.4.), then the noise is signal-independent and

$$N(\omega) \approx N_c(\omega). \quad (24A)$$

(17D) can be simplified assuming $|M(\omega)| \approx 0$ and using (24A) and (23D):

$$|\rho(\omega)| \approx \frac{|\delta C(\omega)|}{|R(\omega)|} \quad (24B)$$

This equation can be freed from $R(\omega)$ if $g(t)$ is assumed to be a stationary random time sequence. This is an acceptable assumption at those frequencies where the noise amplitudes are comparable to the signal amplitudes. This assumption means that

$$\frac{|\bar{C}(\omega)|}{|R(\omega)|} \approx \epsilon \approx \frac{\int |C(t)| dt}{\int |r(t)| dt} \quad (25A)$$

(25A) gives the simplest error estimation using (24B);

$$|\rho(\omega)| = \frac{|\delta \bar{C}(\omega)|}{|\bar{C}(\omega)|} \epsilon \quad (25B)$$

The least-squares technique of fitting the calibration pulse with the theoretically calculated pulse also yielded relative noise parameters, such as the maximum and the average of the residuals in the frequency band of 0 to ω_{Nq} divided by the amplitude spectrum of the

calibration pulse at the peak frequency. The schematic flow chart for calculating these values is shown in Figure 17. These relative noise parameters can be used as waterlevels if they were corrected for the amplitudes and the noise of the records which may be different from those of the calibration pulse (compare with equation (25B)). Since most of the long-period lunar seismograms are weaker and noisier than the calibration pulse for component 15Z and are more energetic than the calibration pulses for the other components, two waterlevel parameters were chosen: 0.03 for seismograms with amplitudes larger than 30 to 50 digital units and not too noisy and 0.1 for the smaller signals. The reliability of these waterlevels was tested by deconvolving some of the records with different waterlevel parameters before the routine processing. These trial deconvolutions showed that the above choices were satisfactory except for the very noisy records.

The noises which are easily spotted and classified by inspection are the following:

1. Most of the "glitches" are those impulsive-type noises in the peaked mode which look like distorted calibration pulses and can be described rather accurately by the following empirical formula

$$c_1 C(t) + c_2 \frac{dC(t)}{dt} = c_1 \int \{c_1 \bar{w}(t) dt + c_2 \bar{w}(t)\} (dt)^2 \quad (26)$$

where c_1 and c_2 are constants, $C(t)$ is the theoretical or observed calibration pulse, C is given by equation (9), and $\bar{w}(t)$ is the impulse-displacement response of the seismograph. The times of occurrence of

these glitches correlate strongly with temperature changes near the station. A glitch was easily removable by the model described by equation (26) if the power spectrum of the seismic signal was stronger at frequencies above the peak frequency of the seismometer than at the peak frequency. However, if there were many overlapping glitches and the seismic signal was strong near the peak frequency of the seismograph response, removing the glitches by fitting the seismograms with equation (26) distorted the signals considerably. This distortion was caused by not having been able to resolve the exact beginnings of the individual glitches.

Other techniques, such as the prediction error operation (Wiggins and Miller, 1972) and adaptive filters (Sims and D'Mello, 1978), were not tried in this study. They also would distort the signal, because the distortion increases rapidly with the unpredictability of the glitches in comparison to the unpredictability of the signal (Wiggins and Miller, 1972).

2. Bit-holds and bit-jumps of the analog-to-digital converter were observed only at station 14. These types of digitizing errors are illustrated in Figure 22. It is clear from Figure 22 that the bit-holds cannot be removed from the seismograms and that the bit-jumps can be removed without any information loss. The correction for bit-jumps was done by checking six-minute sections of the seismograms for missing levels of digitization.

3. Most of the spikes were also removed from the seismograms by checking the changes in signal amplitudes in windows of few seconds.

The instrumental deconvolution was carried out in the frequency domain as the schematic flow chart of the computer program shows in Figure 19. After a time section of the seismogram was corrected for bit-jumps and for spikes, the d.c. level was removed, and cosine-bell tapers were applied at both ends of the time section. The Fourier transform of this tapered signal was divided by the peaked-mode complex transfer function of the seismograph according to (19). The transfer functions were adjusted with the waterlevels by a separate computer program whose schematic flow chart is shown in Figure 18. The instrumental deconvolution was completed by taking the inverse Fourier transform. The amplitude spectra of the deconvolved records reveal that other important filtering effects characteristic of each recording site remained in the lunar seismograms. These filters cause most of the amplitude spectra to deviate systematically from a rather uniform spectrum and prevent an easier comparison of the different seismograms. The removal of these effects is discussed in the following section. Naturally the approach cannot be deterministic, as correcting the seismograms for the instrumental response, and should rely on statistical means.

2.4. Design of the whitening filters to remove the filtering effects of the near-surface zone.

In addition to the effects of the peaked-mode instrumental response, the following major processes also influence the observed amplitude spectra of the long-period lunar seismograms.

1. Source effects

2. Propagation effects, e.g., frequency-dependent attenuation.
3. Noises, e.g. spikes and glitches
4. Near-surface effects, e.g., large velocity gradients,
lateral inhomogeneities
5. Coupling between the seismometer and the ground.

Although all of these effects are important in shaping the lunar seismograms, the filtering effects of the near-surface zone and the poor coupling are considered to be primarily responsible for most of the differences observed among the signals recorded by the various components (Lammlein et al., 1974; Nakamura et al., 1975; Mark and Sutton, 1975). Apart from scaling the signal amplitudes of all three long-period components of the ground motion to the same level (Goins, 1978) the seismograms were not corrected in the past for these effects.

Since no deterministic way is available to reduce these filtering effects one must resort to statistical methods. Ideally, the statistical approach would mean choosing a set of events for each similar group of sources such that the hypocenters are evenly distributed in space and the noise level is rather low. It would also mean combining the amplitude spectra properly within each group; that is, the statistical combination of the individual amplitude spectra would result in cancellation of all influences except those attributed to the near surface and the source effects.

Initially, I selected 65 of the largest events from the complete seismic data set. These 65 events include 40 impacts (8 artificial and 32 natural), 10 shallow moonquakes, and 15 deep moonquakes. At least one time section of 2048 samples (309 seconds) was chosen from each

record starting just before the beginning of the seismic signal. For signals from some distant events, another section of the same length, following the first by 3 or 4 minutes, was also selected. These 65 events and the beginnings of the approximately five-minute sections are listed in Table 9. The first letter of the code in this table refers to the type of source: A to deep moonquakes, H to shallow moonquakes (also called high frequency teleseismic events), C to impacts. The two digit numbers following the first letter are used to denote source locations for deep moonquakes and are arbitrary sequence numbers for shallow moonquakes and impacts; A46 was reclassified as A01 by Nakamura (1978). The artificial impact records are distinguished from the natural impact records by using a letter and a number following the first letter. The letter denotes the source (L for Lunar Module and S for Saturn IV booster), the number is the second digit of the Apollo mission number (12, 14, etc.). 'WL' is the waterlevel parameter in percent used in the peaked-mode instrumental deconvolution process (see Section 2.3.). 'Com' gives information about the various components for each station, such that integers 1, 2, or 3 imply that the X, Y, or Z component, respectively, did not operate properly for that event and thus no signal can be seen; the letters X, Y, or Z are used to denote those time sections whose amplitude spectra peaked in the frequency band of approximately 0.3-2 Hz. Since this selection eliminated those time sections which possess inadequate signal-to-noise ratios, sections marked with X, Y, and Z were used for designing the whitening filters.

Table 10 lists the number of time sections used in this study by components and by event types. Those listed in Table 10 as 'Good'

met the above signal-to-noise ratio criterion; those in column 'Noisy' were not used to design the whitening filters. Table 10 also lists the number of time sections which were recorded in the flat mode.

To obtain the relative magnifications for the various components at each station, the same events should be chosen for each component. Since the small number of time sections meeting the above signal-to-noise ratio criterion does not permit this, it was necessary to compromise by selecting the same events for the horizontal components only, except for the few events listed in Table 9. The present selection of events permits rotation of the horizontal components into radial and transverse directions and particle-motion studies.

It was also likely that unbiased statistical analysis cannot be performed with the small number of events within each of these event types. It was reasonable, nevertheless, to expect that the seismic records can be corrected for the average near-surface effects at each site if the other effects, such as the spectral density functions of the individual sources and the propagation effects along the various raypaths, produced smaller alterations in the spectral amplitudes than the near-surface effects. To test this supposition, amplitude spectra of time sections from the three major source types were combined at each site as weighted arithmetical averages.

$$\bar{X}_s(n\sigma) = \frac{1}{N_{SH}} \sum_{i=1}^{N_{SH}} c_i X_{si}(n\sigma) \quad (27A)$$

$$\bar{Y}_s(n\sigma) = \frac{1}{N_{sH}} \sum_{i=1}^{N_{sH}} c_i Y_{si}(n\sigma) \quad (27B)$$

$$\bar{Z}_s(n\sigma) = \frac{1}{N_{sZ}} \sum_{i=1}^{N_{sZ}} c_i Z_{si}(n\sigma) \quad (27C)$$

where $n = 0, 1, 2, \dots, 1023$; superscript s denotes the source types, X_{si} , Y_{si} , and Z_{si} are the amplitude spectra of the individual time sections, recorded in the peaked mode and corrected for the instrumental response, \bar{X}_s , \bar{Y}_s , and \bar{Z}_s are the average of the N_{sH} and N_{sZ} number of individual amplitude spectra, σ is the sampling interval in the angular frequency domain ($\sigma = 2\pi \cdot 0.003235 \text{ sec}^{-1}$), and c_i are individual weight factors.

The flow chart of the computer program for calculating spectral amplitude averages according to equations (27) is shown in Figure 20. The averaging can be done after the individual amplitude spectra have been smoothed and, if desired, weighted. The smoothing will not be considered at this point since the associative law holds for summing and smoothing with moving averages in rectangular windows. When no weighting is applied to the individual spectral amplitudes ($c_i = 1$), the seismic records with larger amplitudes have greater weight in the average amplitude spectrum than the weaker records. When the energies or the amplitudes of the sections are scaled to the same level before summation, the individual amplitude spectra are treated with approximately the same weight, except that a noisier record contribute less in the frequency band of interest than the records with good signal-to-noise

ratio if the noise is stronger outside this band. Weighting does not permit derivation of relative magnification ratios for the two horizontal components at a particular site, but allows an empirical reliability test for the consistency of the shapes of the determined average amplitude spectra.

In addition to this test for the consistency of the average amplitude spectra, subsets were selected within the most numerous groups. The average amplitude spectra of these different groups are similar to each other for a given component except in certain frequency bands in which noise, discussed in the following section, is obviously present, and except for impact signals which are most affected by distance dependent attenuation. Based upon the similarity among the average amplitude spectra of the different groups and upon the similarity between the amplitude spectra of two consecutive five-minute sections, I conclude that the five minute sections starting at about the beginning of the seismic signals adequately defines the statistical properties of the amplitude spectra. The average amplitude spectra obtained by simple addition of the amplitude spectra for the different components and source types are shown in Figures 23 through 28.

Although there are some differences among the average amplitude spectra of the different source types, I stacked these spectra for every component because the number of sections is small for some of these groups and I wanted to derive only one whitening filter for each component. These average amplitude spectra are shown in Figures 29 through 32 after they were smoothed with moving averages in a rectangular window of 17 samples (0.055 Hz). Figures 29 through 32 also show the average

horizontal amplitude spectra at each station defined as

$$\text{HOR}(n\sigma) = \sqrt{\bar{X}(n\sigma)^2 + \bar{Y}(n\sigma)^2}, \quad n=0,1,2,\dots,1023 \quad (28)$$

where \bar{X} and \bar{Y} are the average amplitude spectra for components X and Y, respectively.

These average amplitude spectra can be considered as the amplitude spectra of the near-surface effects for an average source and attenuation. The whitening filters can be obtained from the smoothed average amplitude spectra assuming the filters to be either zero phase or minimum phase. In the latter case, the filter is causal and the phase spectrum can be calculated with the Hilbert transform of the logarithm of the amplitude spectrum. The minimum-phase assumption contradicts the fact that the signal was dominated by scattered surface waves and the zero-phase assumption violates causality. However, I adopted the assumption of zero phase in calculating the whitening filters because the true phase spectra of the direct shear and secondary arrivals were not expected to be determined from the amplitude spectra of the long time-sections (five-minute sections were required to describe the average spectral properties of the scattered surface waves). To avoid the undesirable sidelobes of a rectangular window, the average amplitude spectra were smoothed with moving averages over a 0.109 Hz window which was cosine tapered at both ends around the central frequency of the window. Thus, the amplitude spectra of the whitening filters differ slightly from those of Figures 29 through 32.

To reduce the numerical errors, the zero phase whitening filters

were multiplied by the complex transfer function of the seismograph and equation (20) was used to stabilize the inverse filtering process in the peaked mode. (Figure 21 shows the flow chart of the computer program). The reliable frequency band was chosen to be (0.2 Hz, 1.5 Hz). The upper limit of this band could have been slightly higher for a few of the largest signals. Seismic signals recorded in the flat mode were also corrected with the whitening filters. This inverse filtering process did not require suppression of the noise because the whitening filters contained some noise thought to be white. The whitening filters in the peaked mode could have been designed such they also included the instrumental effects. Although this approach would have eliminated the necessity of determining the transfer function of the seismographs, it would not have yielded information of the seismographs, of the near-surface structure, and of the noise, and would not have permitted correction of the flat-mode seismograms for the near-surface effects.

Although the zero-phase nature of the whitening filters caused the seismic arrivals to be observed slightly earlier, the inverse filters diminished the sharp peaks in the amplitude spectra considerably. Tests conducted in the time domain also showed that the inverse filters made the comparison among the different components possible. This is demonstrated in Figure 33 with the deconvolved Y components of ground motion at stations 14 and 16. The knowledge of the average amplitude spectra also permits derivation of the average relative amplification between the horizontal components, which is discussed in the following section.

2.5. Some properties of the amplitude spectra of the long-period lunar seismograms.

The average amplitude spectra derived in the preceding sections permitted empirical determination of the relative amplitude ratios between the horizontal components of the long-period lunar seismographs.

The ratios of the average horizontal amplitude spectra (X/Y) of all sections with good signal-to-noise ratio are shown in Figure 34 after they were smoothed with moving averages in a rectangular window of 17 samples (0.055 Hz). The relative average amplifications calculated for two frequency bands are listed in Table 11. Although the X/Y ratios at some frequencies differ from the average by as much as 30% and might indicate the presence of lateral inhomogeneities, the differences among the amplifications at the different stations are primarily attributed to the coupling between the seismometer and ground. The cable connecting the sensor unit to the central electronics unit is thought to be the most important factor in the coupling (Lamlein et al., 1974). This cable comes out at an angle of about 30° to the positive Y direction and possibly acts like a fourth leg. Sharp increases in the amplitude spectra at the peak frequency of the amplitude responses of the horizontal components at station 16 are also interpreted to be a result of this mechanical effect.

At certain frequencies most of the time sections show unusually high amplitudes which are associated with noise. The large amplitudes at less than 0.2 Hz correspond to the frequency content of the glitches as mentioned in Section 2.3. They can be buried in the signal

and unnoticed in the seismograms recorded in the peaked mode. These glitches are abrupt ground motions caused by thermal expansion of the temperature insulating shroud and of the soil surrounding the seismometer.

Other types of instrumental noises, such as bit-jump and bit-hold errors of the analog-to-digital converter and spikes, were discussed in Section 2.3. Some of the long-period signals show a spectral peak at the frequency of 1.6563 Hz or half of the Nyquist frequency, which corresponds to one data frame (see Section 1.2. for details about instrumentation) and is probably caused by varying reference voltage in the analog-to-digital converter. Other noises of possibly instrumental origin are present in the seismic records from stations 12 and 14 at periods of 3-4 seconds. Station 12 seismograms also show a spectral peak at periods of 8-10 seconds. Both of these noises are attributed to the on/off switching of the temperature control unit. The mechanism of this interaction is unknown.

2.6. Summary of Part 2.

This part of the dissertation has described the methods used for correcting the long-period lunar seismograms for instrumental response. To control the noise, waterlevel parameters of 0.10 for most seismograms and of 0.03 for seismograms with good signal-to-noise ratio were determined from the analysis of the signal-to-noise ratio of the calibration pulses. The instrument-corrected seismic records were used to determine the whitening filters for each component in order to reduce the characteristic near-surface effects and to make uniform

filtering of the different seismic records possible. These filters, which can be considered to be the amplitude spectra for an average source and propagation character, work satisfactorily. Although the zero-phase nature of the whitening filters causes the seismic arrivals to be observed slightly earlier, the sharp spectral peaks of the long-period lunar seismograms are diminished considerably. The rather white nature of the amplitude spectra permits comparison of the seismograms from different stations as described in Part 4. The average spectral amplitudes were also used to derive relative amplitude ratios between the horizontal components.

PART 3. NEAR-SURFACE SHEAR WAVE VELOCITIES AS INFERRED FROM THE SPECTRAL AMPLITUDE RATIOS OF THE LONG-PERIOD LUNAR SEISMOGRAMS.

3.1. Introduction.

In the preceding part of this dissertation, the amplitude spectra of the most energetic long-period seismograms were studied in 309-second sections. Although the amplitude spectra depend on the source depth and distance, they are similar in two consecutive sections of the signals. The average amplitude spectra calculated for the three major types of sources at a given site also show a high degree of consistency. These observations suggest that the average amplitude spectra may be interpreted in terms of near-surface effects. This interpretation is important because other information on the physical properties of the near-surface zone is very limited.

Similar compressional velocities of 92 to 114 m/sec were obtained for the topmost layer, the regolith, by active seismic experiments at the Apollo 14, 16, and 17 sites (Cooper et al., 1974) and by analyzing the signals from the Lunar Module lift-off at the Apollo 11, 12, 14, and 15 sites (Nakamura et al., 1975). Cooper et al. (1974) characterized the regolith as a rather homogeneous layer of differing thicknesses at the different sites (8.5, 12.2, and 4.0 m at stations 14, 16, and 17 respectively) and determined the compressional velocities to be about 300 m/sec for the underlying material at all three sites. The results of the seismic profiling experiment at the Apollo 17 site gave velocities of 495, 960, and 4700 m/sec at depths of 32, 390, and 1385 m (Cooper et al., 1974). The last two velocities are less certain

because the few arrivals measured at distances greater than 1.1 km had to be corrected for topography. Although the velocities were given as stepwise increases with depth, the investigators recognized the possibility of a continuous increase of the velocities with depth. In fact, the travel times and amplitudes at the Apollo 14 and 16 sites were re-interpreted in terms of a power-law velocity variation with depth, $v(z) = 110z^{1/6}$ m/sec, where z is the depth in meters down to 10 meters (Gangi, 1978).

These low velocities and their rapid increase with depth were shown by laboratory measurements to be reasonable for porous, brecciated material with no volatile content. Measurements by Stesky and Renton (1977) on lunar soil samples under low loads yielded velocities appropriate for the uppermost 100 m and suggest that the compressional velocities and the Poisson's ratio did not depend strongly on the density of the soil samples. The Poisson's ratio is about 0.46 at near-zero pressure and is rather constant at 0.40-0.43 in the pressure range of 0.2 to 5 bars. The compressional velocity increases from 250 m/sec at the near-zero pressure to 750 m/sec at 5 bars. Laboratory measurements on Apollo 17 rock powders by Talwani et al. (1973 and 1974) yielded compressional velocity gradients between 0.5 and 0.1 (km/sec)/km at confining pressures of 0 to 0.5 kbars, and 10 to 20 times less at higher pressures of up to 2.5 kbars. The velocities and their gradients are higher for the "light mantle material", which is a product of a variety of breccias, than those for the "dark mantle material", which has a composition similar to that of mare basalt samples (Talwani et al., 1974).

Soil densities were measured in the laboratory (Carrier et al., 1973; Stesky and Renton, 1977) and by soil mechanics experiments in situ (e.g., Mitchell et al., 1972; Houston et al., 1974). The results, which were summarized by Heiken (1975), show widely varying densities of less than 1 to more than 2 g/cm³. Sutton and Duennebier (1970) obtained densities of 1.1 to 1.5 g/cm³ at the landing sites of Surveyor spacecraft by modeling the influence of the soil on spacecraft vibrations.

The ratios of the horizontal to vertical long-period spectral amplitudes were studied by Nakamura et al. (1975) and by Mark and Sutton (1975). The former group obtained the thickness and the shear velocity of the regolith from the maximum of the spectral amplitude ratios, assuming that it was produced by quarter-wavelength interference of shear waves trapped in the regolith. An average shear velocity of 37 m/sec was found in a layer of 4.4, 3.7, and 4.4 meters thick at the Apollo 11, 12, and 15 landing sites, respectively. Mark and Sutton (1975) fitted the spectral ratios of a few impact records with spectral ratios calculated theoretically for the fundamental-mode Rayleigh waves. They found that the shear velocities increase from about 35 m/sec at the surface to about 400 m/sec at a depth of 120 m under stations 12 and 15. It was also shown that the velocity stratification obtained at the Apollo 14 site by Cooper et al. (1974) results in a theoretical infinite value near the peak of the observed spectral ratio curve.

In this part of the dissertation I also used the spectral ratio technique, modeling the observed amplitude ratios with ellipticities calculated for the fundamental-mode Rayleigh waves, to obtain the shear velocity distributions at the Apollo 12, 14, 15, and 16 landing sites.

First, the spectral amplitude ratios for many of the largest events are shown to be similar at a given site. Then, the average spectral amplitude ratio curves are fitted with theoretical curves. A discussion of the velocity distributions thus obtained concludes this part of the dissertation.

3.2. The observed spectral amplitude ratios.

The spectral amplitude ratios, \bar{R} , were calculated from the average spectral amplitudes (see equations (27) and (28)) according to the following relation

$$\bar{R}(n\sigma) = \frac{\text{HOR}(n\sigma)}{\bar{Z}(n\sigma)} = \frac{\sqrt{\bar{X}(n\sigma)^2 + \bar{Y}(n\sigma)^2}}{\bar{Z}(n\sigma)}, \quad n=0,1,2,\dots,1023 \quad (29)$$

where \bar{X} , \bar{Y} , and \bar{Z} are the average amplitude spectra calculated from the spectral amplitudes of all time sections having adequate signal-to-noise ratios. These spectral ratios are shown as the top curve of Figures 35 through 38 after they were smoothed with moving averages in a rectangular window of 17 frequency samples. If the attenuation and source effects were the same for the vertical and horizontal components and the same events were used, then these average spectral ratios would be free of such effects. Since the events used in calculating the average horizontal and vertical amplitude spectra (see Tables 9 and 10) are different, the spectral ratios calculated by (29) may include effects other than those of near-surface origin and may be distorted at least by

a scale factor. To test the importance of these effects on the spectral ratios and to obtain the correct values for these ratios, the spectral ratios were calculated according to the following equation for those time sections which met the signal-to-noise ratio criterion described in Section 2.4.

$$R_i(n\sigma) = \frac{\sqrt{X_i'(n\sigma)^2 + Y_i'(n\sigma)^2}}{Z_i'(n\sigma)}, \quad n=0,1,2,\dots,1023 \quad (30)$$

where R_i are the individual spectral ratios, X_i' , Y_i' , and Z_i' are the spectral amplitudes in the horizontal and vertical directions after they were smoothed with Hamming-Tukey smoothing coefficients (Bath, 1974, p. 179). To obtain a better estimate for the spectral ratios, these individual spectral ratios were averaged for each source type:

$$R_s(n\sigma) = \frac{1}{N_s} \sum_{i=1}^{N_s} R_i(n\sigma), \quad n=0,1,2,\dots,1023 \quad (31)$$

where subscript s stands for the source type and N_s is the number of sections. The flow chart for calculating these average spectral ratios is given in Figure 20, and the average spectral ratios are shown as the lower three curves of Figures 35 through 38.

As seen from these figures, the average spectral ratio curves calculated by (29) and (31) are very similar at a given station, except those at station 15 and that for deep moonquakes at station 12. At

station 15, the dominant peak in the average spectral amplitude ratio curve is apparently shifted toward lower frequencies with increasing source depth, while at station 12, there is no dominant peak in the spectral ratio curve for deep moonquakes. The moonquake signals are generally smaller than those of impacts, and stations 12 and 15 have smaller horizontal amplitudes than stations 14 and 16. Since the spectral amplitude ratios are dominated by the noise at those frequencies where the signal amplitudes and/or the instrumental sensitivities are low in comparison with the noise level, the apparent source dependency of the spectral ratios may be attributed to the use of less energetic signals recorded by the very sharply peaked seismometers at the least sensitive stations. Indeed, the spectral ratio curves of the largest moonquakes are much more like those of impacts than those of weak moonquakes.

Thus, the spectral ratios at a given station are generally independent of the source depth and distance. Furthermore, the spectral ratios of the two different sections of the signals from the distant events are quite similar. The hypothesis that spectral ratios are determined primarily by the physical parameters of the near-surface zone fits these facts very well. Scattering and ground coupling may also influence the spectra ratio curve.

The problem of comparing the measured spectral ratios for the isotropically arriving scattered surface waves with theoretical ratios for plane Rayleigh waves was solved by introducing a multiplying factor of $2\sqrt{2}/\pi=0.9$ to equation (30) (Mark and Sutton, 1975). However, I omitted this factor because the relative amplifications among the

components are not precisely known (see Part 1 of this dissertation) and imperfect coupling between the seismometer and the ground is also suspected of causing certain irregularities, such as the sharp increase of the station 16 spectral amplitudes at 0.45 Hz (see Section 2.5.). Since the signal amplitudes of the Y component of ground motion are about 1.7 times larger than those of the X component for station 16, (see Section 2.5.), and since the sharp peak of the spectral ratio curve at about 0.45 Hz corresponds to the peak magnification of the Y component operated in the peaked mode, the observed spectral ratios at around this frequency were excluded from the frequency band in which the observations should be fitted with theoretical curves. The lower limit for this frequency band is the frequency at which the long-period noise is sufficiently small and is about 0.3 Hz for all stations. The higher limit is the frequency where the horizontal-to-vertical spectral ratio becomes that of the noise, i.e., 2.3, 1.6, 2.1, and 1.7 Hz for stations 12, 14, 15, and 16, respectively.

3.3. The theoretical spectral amplitude ratios calculated for the fundamental-mode Rayleigh waves.

Assuming the vertical velocity variations to be much larger than the lateral ones, the near-surface structure was modeled as a series of homogeneous, isotropic, horizontal layers. The validity of this model can be partially tested by calculating the ratio of the average X and Y amplitude spectra for all sections having good signal-to-noise ratio. The X/Y spectral amplitude ratios were discussed in Section 2.5. and are shown in Figure 34. Some of these ratios differ from the average

(listed in Table 11 for two frequency bands) by as much as 30%, and follow a pattern similar to the horizontal-to-vertical spectral amplitude ratios near the dominant peak of the horizontal-to-vertical spectral ratios. These variations may indicate a tilt in the particle motion ellipse, which may be produced by anelastic effects of the medium (Boore and Toksöz, 1969), by the presence of anisotropy, by lateral inhomogeneities, or by ground coupling effects (e.g., a rocking motion of the instrument). Variations of the X/Y spectral ratios are not considered to be dominant effects.

Assuming a horizontally layered medium, the ratio of the horizontal and vertical axes of the particle motion ellipse, also called ellipticity of the Rayleigh type surface waves, was calculated theoretically with the Haskell matrix technique (Haskell, 1953). Since the distribution of energy among the different Rayleigh modes is unknown, I also assumed that Rayleigh waves of the fundamental mode dominates the ground motion in the frequency band of interest. Disregarding the possible contribution of body waves, Love waves and higher-mode Rayleigh waves appears to be justified quantitatively by the good agreement between the results presented here and those from refraction experiments, as described in the following section. Some additional qualitative arguments can also be given. The long time-windows used and the similarity between the spectral ratios in two consecutive five-minute windows support the assumption that the contribution of the body waves is negligible. If the energy of Love waves varied with frequency in the same way as the energy of the horizontal ground motion of Rayleigh waves, then the observed spectral ratios would differ from those

calculated for Rayleigh waves by a scale factor only. The low velocities and large velocity gradients near the surface, as well as heterogeneities concentrated near the surface, support the assumption that higher-mode Rayleigh waves may be neglected because surface sources produce fundamental-mode surface waves primarily and because the conversion from fundamental-mode surface waves to higher-mode waves is small in a scattering medium (Malin, 1978). To emphasize the contribution of the fundamental-mode Rayleigh waves and to use the most energetic events, only signals from meteoroid impacts were used.

The densities and the velocities should satisfy certain constraints established by other investigations, which were reviewed in Section 3.1. In order to simplify the comparison among the different sites and to handle as few variables as possible, I varied the thickness and the shear velocity of the layers and kept the compressional-to-shear velocity ratios and densities identical in the corresponding layers at all sites. These restrictions are also justified by the fact that the theoretical ellipticities of the fundamental-mode Rayleigh waves in the 0.3-2.3 Hz band are most sensitive to shear velocities and least to compressional velocities and densities. Since the theoretically calculated ellipticities are invariant to a common scale factor simultaneously applied to the thicknesses and velocities (Haskell, 1953), the shear or compressional velocity must be fixed at a given depth in order to obtain unique solutions. A compressional velocity of 104 m/sec in the regolith, which is the average of the observations at the four sites, was used to fix this scale factor. Moreover, the density of the superficial layer also was fixed because the theoretically calculated

ellipticities are affected by the density ratios only. Finally, it was also my objective that the theoretical models consisted of as few layers as were necessary to model the spectral amplitude ratios.

Two different compressional-to-shear velocity ratio and density profiles were assumed for calculating the theoretical ellipticities. In the first model, model 'A', which is similar to the model of Mark and Sutton (1975), the compressional-to-shear velocity ratios are higher and the densities are lower in the four uppermost layers than in model 'B'. Average spectral ratio curves for impacts were fitted with theoretical curves by adjusting the thicknesses and the velocities of the layers of the model. These adjustments were made by examining the partial derivatives of the theoretical ellipticities with respect to these variables (a least-squares iterative scheme was also tried, but the infinities in the calculated ellipticities caused the iteration to diverge). The fit in the frequency band of interest was judged by eye on plots having linear frequency and amplitude scales, such as those of Figures 35 through 38. The spectral ratios calculated for the final models are shown in Figures 35 through 38 as a dot-dash line for model 'A' and a dashed line for model 'B'.

The structural parameters of these models are given in Tables 12 and 13. The agreement between the theoretical and observed ratio curves is reasonably good except at high frequencies, where noise dominates the spectra, and at the low frequency end of the spectral ratio curves for stations 14 and 16. The sharp increase in the station 16 spectral ratios at 0.45 Hz is attributed to a rocking motion of the seismometer, as was discussed earlier. The decrease below 0.8 Hz at station 14

could not be modeled without the introduction of infinities in the theoretical curves.

3.4 The near-surface velocity distributions.

The discontinuities introduced to facilitate the theoretical calculations do not necessarily represent actual interfaces. Although I cannot rule out the presence of discrete layers, such as the regolith, the velocities of models 'A' and 'B', which are remarkably similar, may be interpreted as varying continuously with depth. Figure 39 shows the shear velocity distributions of model 'B'. This model, which possesses smaller compressional-to-shear velocity ratios and higher densities, is preferred to model 'A' because its theoretical spectral ratio curves fit the observed curves more closely, the velocities at the various sites differ less from one another, and the theoretical arrival times of the compressional waves (Figures 40 through 44) are closer to the first arrivals from the Lunar Module lift-offs (Nakamura et al., 1975) at stations 12, 14, and 15.

All model 'B' velocity distributions are similar and differ from the average for all sites by not more than 20%, except for the bottom layer at station 14. The velocities at stations 14 and 15 are almost the same down to about 50 meters, below which the velocities are much higher at site 14 than at 15. The thicknesses of the layers having the same velocities are about 20% larger at station 15 than at 12 in the uppermost 41 meters, below which the shear velocities are about the same at these sites. The velocities at station 16, except for the topmost layer, which is fixed, are lower than those at any other station.

If the calculated velocities are taken as the averages in any layer and are assigned to the center of this layer, marked with crosses in Figure 38, then a piecewise linear increase of the shear velocities with depth in two segments, as shown with dashed line in Figure 38, describes the shear velocities of model 'B' rather well. Each segment of these continuous shear velocities, β , is described as

$$\beta = a + bz \quad (32)$$

where z is depth in meters, and a and b are constants, which were determined by least squares and are listed in Table 14. Table 14 also lists the depths where the gradient, b in equation (32) changes, i.e., where a second-order discontinuity occurs. Although these depths and a in (32) are affected by the same scale factor which was used to fix the compressional velocity of the regolith, the value of b in (32) is not affected by the choice of the surface velocity.

The shear velocities obtained by Mark and Sutton (1975) are higher in the uppermost 80 to 100 meters than those of models 'A' and 'B' at station 12. The differences are attributed to the way the fit was obtained. The details of the spectral ratio curve at short periods, which are controlled by the physical parameters of the shallower layers, weigh little if fitted on plots of the logarithm of the spectral amplitude ratios versus period, as was done by Mark and Sutton (1975). They specified the velocities and the density at site 12 down to 413.5 meters, which was not necessary in this study. Their velocities are closer to those of models 'A' and 'B' at station 15 than at 12.

Although power-law functions were found to fit the shear

velocities of model 'B' rather poorly, the compressional velocity, α , can be described adequately by a power-law function in the uppermost 10 to 13 meters:

$$\alpha = cz^p \quad (33)$$

where z is depth in meters, and c and p are constants, which were also determined by least squares and are listed in Table 14. The exponent in (33) is also invariant to the scale factor applied to fix the compressional velocities at the surface. Table 14 also lists the number of layers, where this power-law fit is adequate, and the average compressional velocities in these layers.

Compressional velocities of model 'B' agree very well with those obtained from the seismic signals of the Lunar Module lift-offs (Nakamura et al., 1975). The first arrivals at stations 14 and 15 are within 10 msec of the theoretical arrival times of refracted compressional waves calculated for model 'B' (Figures 41 and 42) and within 80 msec at station 12 (Figure 40).

The average compressional velocity calculated with Gangi's (1978) power-law formula is about 134 m/sec in the uppermost 10 m which is close to those found in this study at stations 14 and 16 (see Table 14). From equation (33) the travel times, t , of the compressional wave arrivals at distance x is

$$t = t_0(x/x_0)^{1-p} \quad (34A)$$

where t_0 is the travel time at distance x_0 (Gangi, 1978). Obtaining p

from the best fitting power-law models, $p=1/3$ (Table 14), and using the first arrival from the Lunar Module lift-off at station 14, $t_0=670$ msec and $x_0=178$ meters (Nakamura et al., 1975),

$$t = 21.2 \cdot x^{2/3} \text{ msec} \quad (34B)$$

where x is in meters. Table 15 compares the travel times calculated for various velocity models with those observed from the Apollo 14 and 16 stacked data. As seen in Table 15, travel times calculated with equation (34B) agree best with the observed ones.

The compressional velocities of models 'A' and 'B' increase more smoothly with depth than those obtained by Cooper et al. (1975) at the Apollo 14, 16, and 17 sites. They obtained a compressional velocity of 4.7 km/sec at a depth of 1385 m at site 17. If the gradient of the shear velocity for the bottom zone (see Table 14) is extended to a depth of a few kilometers and the compressional-to-shear velocity ratio is assumed to be the same (2.0), then the extrapolated compressional velocities are much higher than theirs between depths of 0.1 and 1.0 km and reach 4.7 km/sec at depths of 1250 to 1500 meters at stations 12, 15, and 16. The differences at depths less than 1 km are attributed to the large uncertainties in the travel time data of the seismic profiling experiments at distances of 1.1 to 3 km. The linear extrapolation of the compressional velocity of model 'B' at station 14 yields a value of 4.7 km/sec at a depth of 790 m. These comparisons suggest the velocity gradients of Table 14 may be correct in the uppermost one or two kilometers at all sites except at 14, where the velocity gradient obtained in this study

should decrease with depth.

The unusually high velocities at depths between 50 and 100 meters at station 14 also can be supported by the following argument. If the spectral peaks observed at 0.85 Hz for the horizontal component of the ground motion and at 1.6 to 1.7 Hz for the vertical component (see Figure 30) were caused by resonance of the shear and compressional waves in a layer, respectively, then the peak frequencies must be proportional to the velocities in this layer and, therefore the layer must have an average compressional-to-shear velocity ratio of about 2.0. Since the compressional-to-shear velocity ratio was found to be much higher than 2.0 in the regolith (see Section 3.1), the spectral peaks of the ground motion at station 14 must be explained by a deep velocity discontinuity.

3.5 Discussion and conclusion.

Results from this study indicate that processes acting at the surface of the moon have produced a surface zone of remarkably uniform physical properties. Although the presence of discrete layering is not ruled out by these results, the obtained layered velocity-depth functions can be well fitted with two piecewise linear segments. Continuous velocities, thus derived, are characterized by two zones; a thin (10 to 25 m thick) superficial zone of high velocity gradient, overlying a zone of decreased velocity gradient extending to a depth of at least 150 to 200 m, the maximum depth accessible to the method.

Based on the velocities of these two zones, except the bottom zone at site 14, the sites fall into two groups. At the older sites

(14 and 16), the shear velocities of the piecewise linear model and the average compressional velocities in the uppermost 10 to 13 meters are lower, and the uppermost layers of the layered models are thicker than at the younger sites (12 and 15). The velocities are lower at site 16 than at the other sites. The lower velocities at the older sites may simply reflect longer exposure to meteoroid bombardment at these sites.

The velocity gradients of the bottom zone at station 14 are significantly higher than those at the other three sites. The higher velocities under station 14 at depths between 50 and 100 meters may be those of an older surface layer preserved by deposition of the Fra Mauro formation 4 billion years ago, i.e., at the time of the Imbrium impact. Alternatively, the higher velocities may correspond to the basal portion of the Fra Mauro Formation itself, indurated by sintering at the time of deposition.

In conclusion, the observed horizontal-to-vertical spectral amplitude ratios were shown to be characteristic of each site and were fitted with the theoretically calculated spectral ratios. Owing to differences between the spectra of the two horizontal components of ground motion, the limitations caused by using only the fundamental mode Rayleigh waves for ellipticity modeling, and disregarding lateral inhomogeneities, this technique may not be used to model fine details of the structure. The results should be interpreted as representing gross velocity distributions as shown by the rather good fit of the piecewise linear shear velocity models to the obtained layered models.

PART 4. ANALYSIS OF THE LONG-PERIOD LUNAR SEISMIC SIGNALS CORRECTED FOR INSTRUMENTAL RESPONSE AND NEAR-SURFACE EFFECTS.

4.1. Introduction

In the first two parts of this dissertation, I described how inverse filters were designed to remove the instrumental response and the near-surface effects from the long-period lunar seismograms. The application of these inverse filters resulted in comparable seismic signals from the various seismographs. (See Section 2.4. and Figure 33). It was expected that the seismic signals containing no dominant spectral peaks would yield better-defined direct shear and secondary wave arrivals than those derivable from the original, uncorrected seismograms. There are large uncertainties in the seismic event locations and in the velocity distributions (see Section 2.) because the small number of seismic stations (4), the small seismic sources, and the intensive scattering produced few seismic arrivals which can be observed on the lunar seismograms with uncertainty less than a few seconds; most first arrivals are emergent and most direct shear and secondary arrivals are buried in the scattered wavetrain.

Identification of direct shear wave arrivals is important in order to narrow the bounds on the velocity distributions for the lunar interior and on the source location. The recognition of secondary arrivals may clarify the depths of velocity discontinuities in the lunar interior. Velocity discontinuities were identified at depths of 20 to 25 km in the crust (Toksöz et al., 1974; Goins, 1978; Goins, et al., 1978), at depths of 45 to 90 km for the bottom of the crust

(Latham et al., 1972; Toksöz et al., 1974; Dainty et al., 1977; Goins, 1978; Koyama and Nakamura, 1979), and at depths of 300 to 480 km in the mantle (Nakamura et al., 1974b and 1976; Voss et al., 1976; Latham et al., 1977; Goins, 1978; Goins et al., 1978). Well-constrained first-order discontinuities would narrow the bounds on the average velocities in the upper mantle. The determined values of the velocities in the upper mantle vary from 8.1 to 7.75 km/sec for the compressional waves and from 4.7 to 3.7 km/sec for the shear waves. The velocity gradients determined for the mantle also vary widely (e.g., Latham et al., 1973; Dainty et al., 1974; Nakamura et al., 1974b and 1976; Goins et al., 1978; Koyama and Nakamura, 1979).

To search for secondary arrivals, I located the seismic events with assumed velocity distributions, and then seismic record sections were made for the three source types, impacts, shallow moonquakes, and deep moonquakes. Seismic sections of the radial, transverse, and vertical components of ground motion were examined for consistent sets of secondary arrivals, as discussed in Section 4.2. The difficulties in locating the seismic events are presented in the following section. The most important question to be answered is whether the compressional and shear wave arrivals are satisfactory to distinguish among the possible velocity distributions in the lunar interior; primarily, whether they are able to resolve the thickness of the crust and the average mantle velocities.

4.2. Direct compressional and shear wave arrivals, and locations of major lunar seismic events.

The sparse array, strong scattering, emergent beginnings, unrecognizable shear wave arrivals from surface sources, and occasional glitches impose severe limitations on the number of locatable seismic events. Furthermore, rather large differences occur in the observed arrival times for stations 12 and 14, which are relatively close to each other. These differences are partially attributed to the different amplifications of the near-surface zones at stations 12 and 14, and to the facts that the short-period vertical seismometer at station 12 did not work normally and that the long-period vertical seismometer at station 14 only operated intermittently. Thus, most of the first arrivals were read from the long-period vertical component for station 12, and from either the short-period vertical component or the horizontal components for station 14. The number of reliable direct body wave arrivals observable for a seismic event is further limited by the facts that impacts produce weak shear waves and that moonquakes tend to produce weak compressional waves. The amplitudes of the seismic wave arrivals, especially those from impacts, are further obscured by intensive scattering.

The emergent beginnings and obscured shear wave arrivals resulted in different estimates for the arrival times, as read by different investigators (see Table 20). The observed-minus-calculated arrival times, the residuals, may not be distributed randomly for emergent arrivals. This contradicts the assumptions involved in finding the locations of the seismic events by minimizing the residuals in the least-squares sense (e.g., James et al., 1969). To increase the reliability of the observed arrival times, I read the direct shear wave

arrivals from the long-period seismic records and ignored the emergent first arrivals when better-defined arrivals could be observed at other stations. This should lead to increased stability of the least-squares solutions of the locations (*ibid.*). The direct shear arrivals were read using both the original seismograms and the seismic records corrected for the instrumental response and near-surface effects. Preliminary seismic sections containing records filtered with a three-pole Butterworth filter in various frequency bands were also used to aid the search for consistent sets of direct shear arrivals. Generally, it was easiest to read the direct shear arrivals from deconvolved seismic records filtered in a frequency band of 0.3 to 0.5 Hz and rotated into the transverse direction. The seismic sections and the rotation of the horizontal components of ground motion are described in the following section.

As described in Section 2.4., from the complete data set I initially selected 65 large events (see Table 9). I expected to obtain the locations of these events with residuals less than a few seconds. Two different velocity models were used to locate these events. These two models are given in Tables 16 and 17 and are shown in Figures 44 and 45. Velocities in Table 16 correspond to those published by Nakamura *et al.*, (1976); velocities in Table 17 are similar to those of Koyama and Nakamura (1979), Goins *et al.* (1978), and Goins (1978). These velocity models were only working models; they were used to locate the seismic events and to calculate theoretical arrival times for reflected and converted seismic waves.

As seen from Figures 44 and 45, the velocities are continuous,

except at depths of 25, 60 or 45, 200, 425 and 1350 km. The continuous velocities were obtained by Mohorovičić's relation (Bullen, 1965, Chapter 7):

$$v(r) = v_i (r/r_i)^a \quad (35A)$$

where v is the velocity inside a spherical shell at radius r , v_i is the velocity at the outside radius of the shell, r_i . If the velocity is v_{i+1} at a radius $r=r_{i+1}$ (where $r_i \geq r \geq r_{i+1}$), then

$$a = \frac{\ln(v_{i+1}/v_i)}{\ln(r_{i+1}/r_i)} \quad (35B)$$

Tables 16 and 17 specify two compressional and two shear velocities at certain depths. The velocities change abruptly at such depths, which represent first-order discontinuities, where reflection and/or conversion can take place.

If the angle of incidence is i_i at radius r_i , then the radius of the deepest point of the downgoing ray, R_i , is

$$R_i = r_i (\sin i_i)^{1/(1-a)} \quad (35C)$$

If the seismic ray traverses this shell only once, then the contributions of this shell to the travel time and distance, T_i and D_i , respectively, are

$$T_i = \begin{cases} \frac{2}{1-a} \frac{r_i}{v_i} \cos i_i & , \text{ if } R_i \geq r_{i+1} \quad (35D) \\ \frac{1}{1-a} \left[\frac{r_i}{v_i} \cos i_i - \frac{r_{i+1}}{v_{i+1}} \cos i_{i+1} \right] & , \text{ if } R_i \leq r_{i+1} \quad (35E) \end{cases}$$

$$D_i = \begin{cases} \frac{2}{1-a} \left[\frac{\pi}{2} - i_i \right] & , \text{ if } R_i \geq r_{i+1} \quad (35F) \\ \frac{1}{1-a} [i_{i+1} - i_i] & , \text{ if } R_i \leq r_{i+1} \quad (35G) \end{cases}$$

where i_{i+1} is calculated from the following relation

$$\frac{r_i \sin i_i}{v_i} = \frac{r_{i+1} \sin i_{i+1}}{v_{i+1}} \quad (35H)$$

The travel times and distances for the upgoing rays are given by (35E) and (35G), respectively, and i_i is calculated from (35H) since i_{i+1} is known.

Some of the weak impacts listed in Table 9 could not be located without having large residuals. Table 18 lists those events which could be located with residuals of a few seconds or less. The origin times and locations in Table 18 are based upon the observed arrival times in Table 19 and upon the velocity distributions in Table 17. Table 19 also lists the calculated arrival times. I assumed surface sources for events classified as impacts and a source depth of 80 km for shallow moonquakes

because the focal depths could not be resolved (e.g., Nakamura et al., 1979). Figures 46 and 47 give the epicenters of the impacts and of the shallow moonquakes, respectively. I also attempted to locate the deep moonquakes, but the observed arrival times led to residuals of up to 10 to 15 seconds. Therefore, I did not list the observed arrival times for the compressional waves in Table 19, and I decided to use those deep-moonquake locations which were published by Lammllein (1977). Although Lammllein's locations may not be consistent with the observed shear wave arrival times in Table 19, the seismic record sections for deep moonquakes may be used to search only for those seismic wave arrivals which are converted at or reflected from a discontinuity closer to the surface than to the source.

I also decided to use events H07, H08, H09, C02, and C03, which were recorded at two stations only. For these events, the locations in Table 18 are preferred to those in the footnote of Table 18. The seismograms of H01 and H07, as well as of C01 and C02, are very similar at a given station. The first several seconds of the seismograms of C03 and C04 also show some degree of similarity. Finally, the locations for H08 and H09 are near mare areas like those for other shallow moonquakes located in this study. The locations and origin times for the artificial impacts were determined by spacecraft navigation and are given by Lauderdale and Eichelman (1974), except for event CS6, which had to be located by seismological methods because the tracking signal was lost before impact.

The origin times, locations, and residuals calculated for natural impacts and shallow moonquakes with the velocities in Table 16

(source depth of 100 km was assumed for shallow moonquakes) are very similar to those calculated with the velocities in Table 17. Since most residuals are within the uncertainties in the observations, the arrival times of the direct compressional and shear waves from natural lunar seismic sources cannot be used to distinguish between these two velocity models. The uncertainties in the observations were estimated by the differences in the arrival times as read by the different investigators (see Table 20). For artificial impacts from distances between 11.2 and 35.7⁰, the residuals calculated with the velocities in Table 17 are a few seconds smaller than those calculated with the velocities in Table 16. Thus, the distances for aligning the seismic records in the sections and the arrival times for reflected and converted seismic waves were calculated with the velocities in Table 17, as discussed in the following section.

One important result of the locations obtained in this study is that two shallow moonquakes, H01 and H07, occurred at the same source region almost two years apart. This finding provides further evidence that shallow moonquakes are true tectonic quakes (Nakamura et al., 1979).

4.3. Secondary arrivals.

It was expected that secondary arrivals would be recognized most readily when the true ground motions could be compared among the various sites. Thus, the seismograms were corrected for instrumental response and near-surface effects, were filtered and were rotated into the radial, R, and transverse, T, directions according to

$$R(t) = -X(t)\cos \alpha - Y(t)\sin \alpha \quad (36A)$$

$$T(t) = X(t)\sin \alpha - Y(t)\cos \alpha \quad (36B)$$

where $X(t)$ and $Y(t)$ are the deconvolved and filtered X and Y components of ground motion as the function of time, t , and α is the angle from the positive X axis of the seismometer to the direction toward the source from the station (positive is clockwise). α 's are listed in Table 18 under the column 'Azimuth'. R is positive away from the source, T is positive to the right looking from the source.

Seismic sections were made for the three major source types, artificial, shallow moonquakes, and deep moonquakes, by aligning the radial, transverse, and vertical components of ground motion according to the distance between the source and the station (see Table 18), and using the arrival times of either the direct compressional or the direct shear wave (see Table 19). The seismic record sections given in the pocket consist of seismic records filtered with a three-pole Butterworth filter (Bath, 1973, p. 260) having high-pass and low-pass frequency cut-offs at 0.4 and 1.5 Hz, respectively. The signal amplitudes on these seismic record sections are positive toward increasing distances. The seismic records are identified by a sequence number, a four-character word, and a scale factor used for scaling the amplitudes of the seismic records by division (see also Seismic Section Captions).

If one of the components was not working normally (see Table 9),

then the corresponding seismic record was zeroed. This process resulted in plotting one horizontal component of ground motion on both the radial and transverse sections when the other one was zeroed. No seismic record was plotted when either both horizontal components or the vertical component were missing. The glitches were also zeroed, and the seismic record was not plotted at those times when the amplitudes were clipped. Since some of the seismic records are shifted slightly along the distance axis for clarity of the sections, a line is drawn between the correct distance (see Table 18) and the beginning of the record, which is marked by a small tickmark. The background noise may be estimated for impact and shallow-moonquake seismic records from that portion of the record which lies between this tickmark and the compressional wave arrival.

Other seismic record sections, not included in the pocket, were also made using cut-off frequencies other than 0.4 and 1.5 Hz in order to compare the seismic signals in various frequency bands. The lengths of the seismic records were also varied in order to compare various parts of the seismic records. Polarization filters were also used for enhancing rectilinear motions, as discussed below.

Low coherency among the displacement components of ground motion and weak onsets of seismic arrivals in comparison with the amplitudes of the ambient signal make the identification of direct shear and secondary arrivals difficult. To enhance the rectilinear motion, thus to reduce the number of possible readings for direct shear and secondary wave arrivals, polarization filters were designed by Voss et al., (1976), Jarosch, (1977), Dainty et al. (1977), Goins (1978),

and Goins et al. (1978). The practical and theoretical difficulties in applying the polarization filters for the long-period lunar seismograms are significant. In addition to the low coherency among the various ground motion components and to the strongly scattered body wave arrivals, unknown relative magnification among the seismographs, almost vertically arriving body waves, missing or very small vertical components of ground motion, and the fact that the polarization filters also pass signals which are energetic only on one component made the application of the polarization filters doubtful. In fact, the polarization filters did not aid the identification of secondary arrivals, because most arrival times read from the polarization-filtered seismic record sections coincided with the increase in the signal amplitudes only on one component of the ground motion.

Apart from the increase of the signal amplitudes, no criterion could be set to read any set of secondary arrivals. Theoretical travel times were calculated for many possible reflected and converted seismic waves and were compared with the times where the signal amplitudes increase. Uncertainties in the distances and in the arrival times at which the seismic records are aligned were estimated to result in seismic waves arriving up to several seconds earlier or later than predicted by theoretical calculations. Possible variations in the velocities and the fact that the source depths for moonquakes cannot be determined accurately additionally complicate the identification of the converted and reflected seismic wave arrivals.

The most energetic reflections are normally those from the free surface, which may be important in the impact and shallow moonquake

seismograms. The theoretical arrival times for shear waves reflected once, twice, and thrice from the free surface (SS, 3S, and 4S, respectively) were calculated with the model in Table 17 and are given on the impact sections. No consistent increases in the signal amplitudes were found at arrival times predicted for compressional waves reflected from the free surface. The most impulsive arrivals observed for SS are at distances 4 to 5.3° , for 3S are between 6.5 and 9° , and for 4S are between 9 and 12° (see the transverse component of ground motion). These arrivals indicate that the direct shear wave arrivals are rather energetic between 2 and 3° , which, according to models in Tables 16 and 17, corresponds to an abrupt increase in the shear velocities at a depth between 20 and 30 km (see Bullen, 1965, Chapter 7). Possible peg-leg shear wave multiples in the upper crust, corresponding to the theoretical travel time curve S25, also suggest a velocity discontinuity at a depth of about 25 km. Peg-leg shear wave multiples in the whole crust, corresponding to the theoretical travel time curve S45, appear to be recognizable at distances of 70 to 90° . The direct shear waves are also slightly more impulsive at distances greater than 70° than between 50 and 70° . The increased impulsiveness of the shear wave arrivals at distances of 70 to 90° indicates that the shear wave velocities decrease at a smaller rate below 200 km than above this depth. The absence of recognizable shear waves at distances greater than 90° may be the result of either increasing attenuation or an increasingly negative shear wave velocity gradient at depths from 400 to 450 km.

Although the minimum distance at which surface reflections

can be observed increases with increasing source depth, the SS arrivals do not constrain the depths of shallow moonquakes because no consistent SS arrivals were recognized on the shallow-moonquake sections. The amplitudes of some of the shallow-moonquake signals increase at arrival times predicted for peg-leg multiples in the upper crust and in the whole crust (see curves S25 and S45 on the transverse component).

S to P conversions at the 25 and 45 km discontinuities can also be observed at about 5 and 8 seconds before the direct shear arrival on some of the vertical seismic records for deep moonquakes. Latham et al. (1970) explained high frequency trains of waves beginning on the horizontal components at the Apollo 14 site about 8 sec after the direct compressional waves as shear waves converted at a depth of approximately 25 km. Based upon models of Tables 16 and 17 and upon similar arrivals at 4.5 to 5 seconds after the first arrivals, I interpret the arrivals following the first arrivals and preceding the shear wave arrivals by 4 to 5 and 8 to 9 seconds as seismic waves converted at depths of approximately 25 and 45 km, respectively. The depths of discontinuities where these conversions take place cannot be constrained by more than 3 and 5 km, respectively, because the uncertainties of these observations are about 1 second.

Seismic arrivals preceding the direct shear wave arrivals by 20 to 30 seconds were observed by Latham et al. (1974) and by Nakamura et al. (1974b) on the vertical seismograms from deep moonquakes. According to velocity distributions in Table 17, these seismic arrivals can be identified as conversion of the shear wave to a compressional wave at a depth slightly greater than 200 km (see the theoretical arrival time

curve for the shear-to-compressional wave conversion at the 200 km discontinuity on the deep-moonquake seismic record sections.)

Beside the high-frequency trains following the first arrivals by about 8 seconds, which are most characteristic at site 14, no station dependency of any of the above discussed secondary arrivals was found.

4.4. Summary of Part 4.

In this part of the dissertation, the study of the long-period lunar seismograms corrected for instrumental response and near-surface effects has been described. It was my objective to identify consistent sets of direct shear and secondary wave arrivals, and thus to constrain the velocities in the lunar mantle and the depths of the velocity discontinuities. Two velocity models, one with a thicker crust (55 km) and higher upper mantle velocities (8.1 and 4.6 km/sec) and the other with a thinner crust (45 km) and lower upper mantle velocities (7.7 and 4.4 km/sec), were used to locate the natural impacts and the shallow moonquakes and to obtain the travel time residuals. Although most residuals for both models are within the uncertainty of the observed arrival times, the model with thinner crust and lower upper mantle velocities is preferred because it gives smaller residuals for the arrival times observed for artificial impacts at distances between 11° and 36° . Seismic sections were made of the radial, transverse, and vertical components of ground motion in order to search for consistent sets of secondary arrivals. The only criterion for reading the secondary arrivals was the increase of the signal amplitudes. The velocities and the depths of the

velocity discontinuities cannot be severely constrained by secondary arrivals. However, based upon the amplitudes of the shear wave arrivals reflected from the free surface and upon the arrival times of converted waves, it is likely that the crust is thinner than 55 km and that a first-order discontinuity separates the upper and lower crust at a depth of about 25 km. Also, some indications were found for a first- or a second-order discontinuity at a depth of about 200 km.

CONCLUSIONS

The small number of lunar seismic stations (4), the small magnitudes of seismic sources, and strong scattering imposed severe limitations on locating the natural seismic events and on deriving structural information about the lunar interior from the available seismic data. Since these conditions cannot be improved for the time being, it was necessary to correct for those effects which influenced the detection of seismic signals. In this study, inverse filters were designed to correct for the instrumental response, for the coupling of the seismometer to the ground, and for the near-surface structural effects. By removing the predictable digitizing errors and by applying these inverse filters, the calculated ground motions were found to be more comparable at the various recording sites than were the recorded ground motions. The deconvolved signals permit reading the shear wave arrivals with smaller uncertainty than is possible from the original seismograms, and thus yield better-constrained locations. However, no conclusive set of secondary arrivals could be recognized on the seismic sections made for impact, shallow-moonquake, and deep-moonquake records. Although this study of the long-period seismic signals did not result in severe constraints on the structure of the lunar interior, the transfer function of the long-period seismographs and the near-surface velocities were derived from the analysis of the calibration pulses and of the horizontal-to-vertical spectral amplitude ratios of the long-period lunar seismograms, respectively.

The finding of consistent sets of secondary arrivals remains the

most important goal for the analysis of the lunar seismic signals in the future. Beside further limiting the number of impacts and shallow moonquakes to only the largest of those used in this study, stacked deep-moonquake seismic signals should be used as the continuation of this work.

APPENDIX: LEAST-SQUARES FIT TO NON-LINEAR FUNCTION WITH A
LINEARIZATION OF THE FITTING FUNCTION.

If the observations y_i at x_i ($i=1,2,\dots,M$) are to be fitted with a function $y(x,a_1,a_2,\dots,a_n)$, which is the function of the independent variable x and of the parameters a_j ($j=1,2,\dots,n$) then the method of linear least squares can be used to determine the optimum values for the parameter increments δa_j . First, the fitting function is expanded to first order in a Taylor's expansion as a function of the parameters:

$$y(x) = y_0(x) + \sum_{j=1}^n \frac{\partial y_0(x)}{\partial a_j} \delta a_j \quad (A1)$$

where $y_0(x) = y(x, a_1^0, \dots, a_n^0)$,

$$\frac{\partial y_0(x)}{\partial a_j} = y_{0j}(x) = \left[\frac{\partial y(x, a_1, \dots, a_n)}{\partial a_j} \right]_{\left\{ a_k \right\}_{k=1}^n = \left\{ a_k^0 \right\}_{k=1}^n}$$

and $\left\{ a_k^0 \right\}_{k=1}^n$ are the starting values for the set of parameters.

The partial derivatives, $y_{0j}(x)$, may be calculated either analytically or numerically from the analytical expression of the fitting function.

The differences between the observed and calculated values are given by

$$y_i - y(x_i) = y_i - y_0(x_i) - \sum_{j=1}^n y_{0j}(x_i) \delta a_j, \quad i=1,2,\dots,M$$

The last equation can be abbreviated by a matrix equation:

$$\underline{b} - \underline{A}\underline{x} = \underline{r} \quad (A2A)$$

where once-underlined lower-case letters indicate column vectors, and twice-underlined capital letter denotes a matrix:

$$\underline{b} = \begin{vmatrix} y_1 - y_0(x_1) \\ \vdots \\ y_M - y_0(x_M) \end{vmatrix} \quad (A2B)$$

is the observed-minus-calculated column vector,

$$\underline{A} = \begin{vmatrix} y_{01}(x_1) & \dots & y_{0n}(x_1) \\ \vdots & & \vdots \\ y_{01}(x_M) & \dots & y_{0n}(x_M) \end{vmatrix} \quad (A2C)$$

is the matrix of the partial derivatives,

$$\underline{x} = \begin{vmatrix} \delta a_1 \\ \vdots \\ \delta a_n \end{vmatrix} \quad (A2D)$$

is the parameter increment or adjustment column vector, and

$$\underline{r} = \begin{bmatrix} y_1 - y(x_1) \\ \vdots \\ y_M - y(x_M) \end{bmatrix} = \begin{bmatrix} r_1 \\ \vdots \\ r_M \end{bmatrix} \quad (\text{A2E})$$

is the residue or error column vector.

The unknown vector, \underline{x} , is calculated by minimizing the sum of the squared residues, that is the mean-square error, E ,

$$E = \|\underline{r}\|^2 = \sum_{i=1}^M r_i^2 = \|\underline{b} - \underline{A}\underline{x}\|^2 = \text{minimum} \quad (\text{A3})$$

M must be equal to or greater than n , and the column vectors of matrix \underline{A} must be linearly independent. This process can be repeated with the new values of the parameters ($a_j + \delta a_j$, $j=1,2,\dots,n$) as long as the iteration converges, that is as long as the mean-square error decreases.

BIBLIOGRPHY

- Báth M. (1973) Spectral Analysis in Geophysics. Elsevier Scientific Publishing Company, Amsterdam-Oxford-New York, 563 pp.
- Boore D. M. and Toksöz M. N. (1969) Rayleigh wave particle motion and crustal structure. Bull. Seismol. Soc. Am. 59, p. 331-346.
- Bullen K. E. (1965) An introduction to the theory of seismology. Cambridge, 381 pp.
- Byrne C. J. (1961) Instrument noise in seismometers. Bull. Seismol. Soc. Am. 51, p. 69-84.
- Carrier W. D. III, Mitchell J. K., and Mahmood A. (1973) The relative density of the lunar soil. Proc. Lunar Sci. Conf. 4th, p. 2404-2411.
- Chakrabarty S. K. (1949) Response characteristics of electromagnetic seismographs and their dependence on the instrumental response. Bull. Seismol. Soc. Am. 39, p. 205-218.
- Chakrabarty S. K. and Choudhury S. N. R. (1964) Response characteristics and electromagnetic seismographs. Bull. Seismol. Soc. Am. 54, p. 1445-1458.
- Clayton M. R. and Wiggins R. A. (1976) Source shape estimation and deconvolution of teleseismic body waves. Geophys. J. Roy. Astr. Soc. 47, p. 131-177.
- Cooper M. R. and Kovach R. L. (1975) Energy, frequency, and distance of moonquakes at the Apollo 17 site. Proc. Lunar Sci. Conf. 6th, p. 2863-2879.
- Cooper M. R., Kovach R. L., and Watkins J. A. (1974) Lunar near-surface structure. Rev. Geophys. Space Phys. 12, p. 291-307.
- Dainty A. M., Toksöz M. N., Solomon S. C., Anderson K., and Goins N., (1974) Constraints on lunar structure. Proc. Lunar Sci. Conf. 5th, p. 3091-3114.
- Dainty A. M., Toksöz M. N., Anderson K., Pines P. J., Nakamura Y. and Latham G. V. (1974b) Seismic scattering and shallow structure of the moon in Oceanus Procellarum. The Moon 9, p. 11-29.
- Dainty A. M., Toksöz M. N., and Stein S. (1976) Seismic investigation of the lunar interior. Proc. Lunar Sci. Conf. 7th, p. 3057-3075.
- Dainty A. M., Goins N. R., and Toksöz M. N. (1977) Crustal structure of the moon from deep events (abstract). Earthquake Notes 48, p. 11-12.

- Deregowski S. M. (1971) Optimum digital filtering and inverse filtering in the frequency domain. Geophys. Prosp. 19, p. 729-768.
- Dopp S. (1964) Application of communication network theory to the electromagnetic seismograph. Bull. Seismol. Soc. Am. 54, p. 1479-1489.
- Dorman J., Evans S., Nakamura Y., and Latham G. (1978) on the time varying properties of the lunar seismic meteoroid population. Proc. Lunar Sci. Conf. 9th, p. 3615-3626.
- Duennebier F. (1976) Thermal movement of the regolith. Proc. Lunar Sci. Conf. 7th, p. 1073-1086.
- Duennebier F. and Sutton G. H. (1974) Thermal moonquakes. J. Geophys. Res. 79, p. 4351-4363
- Duennebier F. and Sutton G. H. (1974b) Meteorid impacts recorded by the short-period component of Apollo 14 lunar seismic station. J. Geophys. Res. 79, p. 4365-4374.
- Duennebier F., Dorman J., Lammlein D., Latham G., and Nakamura Y. (1975) Meteorid flux from passive seismic experiment data. Proc. Lunar Sci. Conf. 6th, p. 2417-2426.
- Earth Sciences, a Teledyne Company (1968) Final Technical Report for ALSEP Passive Seismic Experiment Subsystem Program. Report no. 640-0768-0057.
- Espinosa A. F., Sutton G. H., Miller H. J. (1962) A transient technique for seismograph calibration. Bull. Seismol. Soc. Am. 52, p. 767-779.
- Gangi A. F. (1972) The lunar seismogram. The Moon 4, p. 40-48.
- Gangi A. F. (1978) A comparison of two types of velocity models for the lunar crust: smooth, continuous and stepwise layered. Final report, NASA Grant NSG-7189, Texas A&M University.
- Goins N. R. (1978) Lunar seismology: The internal structure of the Moon. Ph. D. dissertation. M. I. T.
- Goins N. R., Toksöz M. N., and Dainty A. M. (1978) Seismic structure of the lunar mantle: an overview. Proc. Lunar Sci. Conf. 9th, p. 3575-3588.
- Gold B. and Rader C. M. (1969) Digital processing of signals. McGraw-Hill Company, New York, 269 pp.
- Gold T. and Soter S. (1970) Apollo 12 seismic signal: indication of a deep layer of powder. Science 167, p. 1071-1075.

- Hagiwara T. (1958) Note on the electromagnetic seismograph. Bull. Earthq. Res. Inst. 36, p. 139-164.
- Haskell N. A. (1953) The dispersion of surface waves on multilayered media. Bull. Seismol. Soc. Am. 43, p. 17-34.
- Heiken G. (1975) Petrology of lunar soil. Rev. Geophys. Space. Phys. 13, p. 567-587.
- HelMBERGER D. and Wiggins R. A. (1971) The upper mantle structure of Midwestern United States. J. Geophys. Res. 76, p. 3229-3245.
- Houston W. N., Mitchell J. K., and Carrier W. D. (1974) Lunar soil density and porosity. Proc. Lunar Sci. Conf. 5th, p. 2361-2364.
- IBM Application Program (1970) System/360 Scientific Subroutine Package (360A-CM-03X) Programmer's Manual. Publication number GH20-0205-4. IBM, New York, 454 pp.
- James D. E., Sacks L. S., Lazo E. L., and Aparicio P. G. (1969) On locating local earthquakes using small networks. Bull. Seismo. Soc. Am. 59, p. 1201-1212.
- Jarosch H. S. (1977) The use of surface reflections in lunar seismograms. Bull. Seismol. Soc. Am. 67, p. 1647-1659.
- Jarosch H. S. and Curtis A. R. (1973) A note on the calibration of the electromagnetic seismograph. Bull. Seismol. Soc. Am. 63, p. 1145-1155.
- Kelly D. (1939) A reaction type shaking table. Geophysics 4, p. 69-75.
- Kollar F. and Russell R. D. (1966) Seismometer analysis using current analog. Bull. Seismol. Soc. Am. 56, p. 1193-1205.
- Koyama J. and Nakamura Y. (1979) Re-examination of the lunar seismic velocity structure (abstract). In Lunar and Planetary Science X, p. 685-687.
- Kulhanek O. and Klima K. (1970) The reliable frequency band for amplitude spectra corrections. Geophys. J. Roy. Astr. Soc. 21, p. 235-242.
- Lammlein D. (1977) Lunar seismicity and tectonics. Phys. Earth Planet. Inter. 14, p. 224-273.
- Lammlein D. R., Latham G. V., Dorman J., Nakamura Y., Ewing M. (1974) Lunar seismicity, structure, and tectonics. Rev. Geophys. Space Phys. 12, p. 1-21.
- Landisman M., Sato Y., and Ewing M. (1959) The distortion of pulselike earthquake signals by seismographs. Geophys. J. Roy. Astr. Soc. 2, p. 101-115.

- Latham G. V., Ewing M., Press F., Sutton G., Dorman J., Toksöz N., Wiggins R., Nakamura Y., Derr J., and Duennebieer F. (1969) Passive seismic experiment. Apollo 12 Prel. Sci. Reports, NASA SP-214, p. 143-161.
- Latham G. V., Ewing M., Press F., Sutton G., Dorman J., Nakamura Y., Toksöz N., Wiggins R., and Kovach R. (1970) Passive seismic experiment. Apollo 14 Prel. Sci. Reports, NASA SP-235, p. 39-53.
- Latham G. V., Ewing M., Dorman J., Lammllein D., F. Press, Toksöz N., Sutton G., Duennebieer F., and Nakamura Y. (1972) Moonquakes and lunar tectonism. The Moon 4, p. 373-382.
- Latham G. V., Ewing M., Dorman J., Nakamura Y., Toksöz N., Press F., Sutton G., Lammllein D., and Duennebieer F. (1972b) Passive seismic experiment. Apollo 15 Prel. Sci. Reports, NASA SP-289, P. 8-1-25.
- Latham G. V., Ewing M., Dorman J., Nakamura Y., Press F., Toksöz N., Sutton G., Duennebieer F., and Lammllein D. (1973) Lunar structure and dynamics - results from the Apollo passive seismic experiment. The Moon 7, p. 396-420.
- Latham G. V., Nakamura Y., Dorman J., Duennebieer F., Ewing M., and Lammllein D. (1977) Results from the Apollo Seismic Experiment. Proc. Soviet-Amer. Conf. Cosmochem. NASA SP-370, P. 389-401.
- Lauderdale W. W. and Eichelman W. F. (editors) (1974) Apollo Scientific Experiments Data Handbook. NASA Technical Memorandum, TM X-58131.
- MacElwane J. B. and Sohon F. W. (1932) Introduction to theoretical seismology. John Wiley and Sons, Inc., New York, Part II, 149 pp.
- Malin P. E. (1978) A first order scattering solution for modeling lunar and terrestrial seismic codas. Ph. D. Dissertation, Princeton Univ.
- Mark N. and Sutton G. H. (1975) Lunar shear velocity structure at Apollo sites 12, 14, and 15. J. Geophys. Res. 80, p. 4932-4938.
- Matumoto T. (1958) Calibration of an electromagnetic seismograph by means of frequency analysis. Bull. Earthquake Res. Inst. 36, P. 54-64.
- Meissner R., Voss J., and Kaestle H. J. (1973) A_1 moonquakes, problems of determining their epicenters and mechanism. The Moon 6, p. 292-303.
- Miles J. W. (1960) Scattering of elastic waves by small inhomogeneties. Geophysics 25, p. 642-648.
- Mitchell B. J. and Landisman M. (1969) Electromagnetic seismograph constants by least-squares inversion. Bull. Seismol. Soc. Am. 59, p. 1335-1348.

- Mitchell J. K., Carrier W. D. III, Houston W. N., Scott R. F., Bromwell L. G., Durgunoglu H. T., Hovland J. J., Treadwell D. D., and Costes N. C. (1972) Soil mechanics. NASA Spec. Publ. SP-315, p. 8-1-8-29.
- Mitronovas W. (1976) Accuracy in the phase determination of LP electromagnetic seismographs based on transient calibration pulse. Bull. Seismol. Soc. Am. 66, p. 97-104.
- Mitronovas W. and Wielandt E. (1975) High-precision phase calibration of long-period electromagnetic seismographs. Bull. Seismol. Soc. Am. 65, p. 411-424.
- Mizutani H. and Newbigging E. I. (1973) Elastic velocities of Apollo 14, 15 and 16 rocks. Proc. Lunar Sci. Conf. 4th, p. 2601-2609.
- Murphy L. M., Wilson R. M., Burgess L. R., and Pearce T. H. (1954) Response curves of an electromagnetic seismograph by sine-wave simulator method. Bull. Seismol. Soc. Am. 44, p. 7-19.
- Nakamura Y., (1978) A₁ moonquakes: source distribution and mechanism. Proc. Lunar Sci. Conf. 9th, p. 3589-3607.
- Nakamura Y., Lammlein D., Latham G., Ewing M., Dorman J., Press F., and Toksöz N. (1973) New seismic data on the state of the deep lunar interior. Science 181, p. 49-51.
- Nakamura Y., Dorman J., Duenebier F., Ewing M., Lammlein D., and Latham G. (1974) High frequency teleseismic events. Proc. Lunar Sci. Conf. 5th, p. 2883-2890.
- Nakamura Y., Dorman J., Duenebier F., Lammlein D., and Latham G. V. (1974b) Deep lunar interior inferred from recent seismic data. Geophys. Res. Lett. 1, p. 137-140.
- Nakamura Y., Dorman J., Duenebier F., Lammlein D., and Latham G. V. (1975) Shallow lunar structure determined from the passive seismic experiment. The Moon 13, p. 57-66.
- Nakamura Y., Duenebier F., Latham G. V., and Dorman J. (1976) Structure of the lunar mantle. J. Geophys. Res. 81, p. 4818-4824.
- Nakamura Y., Latham G. V., Dorman H. J., Horvath P., and Ibrahim, A. K. (1977) Seismic indication of broad-scale heterogeneities in the lunar interior: A preliminary report. Proc. Lunar Sci. Conf. 8th, p. 487-498.
- Nakamura Y., Latham G. V., Dorman H. J., Ibrahim A. K., Horvath P. (1979) Shallow moonquakes: depth, distribution and implications as to the present state of the lunar interior. Proc. Lunar Sci.

Conf. 10th (in press).

Neugebauer H. J. (1970) Application of electric network theory in seismometry. Assemblee Generale de la Comission Seismologique Europeene 12th (Proceedings).

Plesinger A., Schick R., and Zuern W. (1970) Stability problems in the approximation of true ground motion. Assemblee Generale de la Comission Seismologique Europeene 12th (Proceedings).

Rayleigh L. (1945) Theory of Sound. Dover, New York. Vol. II, pp. 504.

Reid A. M. (1974) Rock types present in lunar highland soils. The Moon 9, p. 141-146.

Rice R. B. (1962) Inverse convolution filters. Geophysics 27, p. 4-18.

Robinson, E. A. and Treitel S. T. (1967) Principles of digital Wiener filtering. Geophys. Prosp. 15, p. 311-333.

Silverman D. (1939) The frequency response of electromagnetically damped and reluctance type seismometers. Geophysics 4, p. 53-68.

Sims C. S. and D'Mello M. R. (1978) Adaptive deconvolution of seismic signals. IEEE Trans. Geosci. Electr. GE-16, p. 99-103.

Stesky R. M. and Renton B. (1977) Compressional and shear velocities in powdered rock under low loads. Proc. Lunar Sci. Conf. 8th, p. 1225-1233.

Sutton G. H. and Duennbier F. K. (1970) Elastic properties of the lunar surface from Surveyor spacecraft data. J. Geophys. Res. 75, p. 7439-7444.

Sutton G. H. and Latham G. V. (1964) Analysis of a feedback controlled seismometer. J. Geophys. Res. 69, p. 3865-3882.

Talwani P., Nur A., and Kovach R. L. (1973) Compressional and shear wave velocities in granular materials to 2.5 kilobars. J. Geophys. Res. 78, p. 6899-6909.

Talwani P., Nur A., and Kovach R. L. (1974) Implications of elastic wave velocities for Apollo 17 powders. Proc. Lunar Sci. Conf. 5th, p. 2919-2926.

Tittman B. R., Hously R. M., Alers G. A., and Cirilin E. H. (1974) Internal friction in rocks and its relationship to volatiles on the Moon. Proc. Lunar Sci. Conf. 5th, p. 2913-2918.

- Todd T., Richter D. A., Simmois G., and Wang H. (1973) Unique characterization of lunar samples by physical properties. Proc. Lunar Sci. Conf. 4th, p. 2639-2662.
- Toksöz M. N., Press F., Anderson K., Dainty A., Latham G., Ewing M., Dorman J., Lamlein D., Nakamura Y., Sutton G., and Duennebier F. (1972) Velocity structure and properties of the lunar crust. The Moon 4, p. 490-504.
- Toksöz M. N., Dainty A. M., Solomon S. C., and Anderson K. (1974) Structure of the moon. Rev. Geophys. Space Phys. 12, p. 539-567.
- Voss J., Weinrebe W., Schildknecht F., and Meissner R. (1976) Filter processes applied to scattering parts of lunar seismograms for identifying the 300 km discontinuity of the lunar grid system. Proc. Lunar Sci. Conf. 7th, p. 3133-3142.
- Wang H., Todd T., Richter D., and Simmons G. (1973) Elastic properties of plagioclase aggregates and seismic velocities in the moon. Proc. Lunar Sci. Conf. 4th, p. 2663-2672.
- Warren N. Q. (1972) Q and structure. The Moon 4, p. 430-441.
- Wesley J. P. (1965) Diffusion of seismic energy in the near range. J. Geophys. Res. 70, p. 5099-5106.
- Wiggins R. A. and Miller S. P. (1972) New noise reduction technique applied to long-period oscillations from the Alaskan earthquake. Bull. Seismol. Soc. Am. 62, p. 471-479.
- Willmore P. L. (1959) The application of the Maxwell impedance bridge to the calibration of electromagnetic seismographs. Bull. Seismol. Soc. Am. 49, p. 99-114.

Table 1. The lunar seismic network.¹⁾

Station	Installation	Location (degrees)		Azimuths ²⁾	Total number of days ³⁾	
		Latitude	Longitude (degrees)		in peaked	in flat mode
11	July 21, 1969	0.68 N	23.42 E	0.		21 ⁴⁾
12	Nov. 19, 1969	3.04 S	23.42 W	180.	2055 ⁷⁾	817 ^{5,6)}
14	Feb. 5, 1971	3.65 S	17.48 W	0.	2288 ⁸⁾	
15	July 31, 1971	26.08 N	3.66 E	0.	1615	638 ⁶⁾
16	Apr. 21, 1972	8.97 S	15.51 E	-25.5	1350	638 ⁶⁾

- 1) The network was turned off on September 30, 1977.
- 2) The listed azimuths are the directions of the ground motion which give positive signals on one of the horizontal components (X) and no signal on the other (Y). Azimuths are measured clockwise from North. The direction of the ground motion which gives positive signals on Y is 90° clockwise from the direction listed.
- 3) Only those days were excluded from this count when the signal was lost for at least one full day. This happened at station 14 only between March 1 and March 5, 1975, between January 18 and February 19, 1976, between March 17 and May 20, 1976, between June 8 and June 10, 1976, between October 9 and November 12, 1976, and between July 30 and August 4, 1977.
- 4) Station 11 was turned off for the lunar night between August 2 and August 17, 1969.
- 5) Station 12 was operating in the flat mode between November 19 and November 22, 1969, and between October 14, 1974 and April 9, 1975.

Table 1. (continued)

- 6) Stations 12, 15, and 16 were operating in the flat mode between June 28, 1975 and March 27, 1977.
- 7) The short-period vertical seismometer at station 12 never worked properly.
- 8) The long-period vertical seismometer at station 14 did not work properly most of the time.

Table 2. Nominal values of the seismograph constants.

Constant	Nominal value	Parameter ¹⁾
A/D converter transfer function	$K = 0.2049 \text{ DU/mV}$	
Displacement transducer transfer f.	$K_1 = 5000 \text{ V/cm}$	
Output gain	$K_3 = 31.6 \text{ at } 0 \text{ dB}^{2)}$	$a_1 = K_1 K_3$
Pendulum damping constant	$\beta = 0.85$	$a_2 = 2\beta$
Pendulum free period	$2\pi/\omega_0 = 15 \text{ sec}$	$a_3 = \omega_0$
Demodulator low pass cutoff frequ.	$\omega_d = 47.62 \text{ sec}^{-1}$	$a_4 = \omega_d$
Output high pass cutoff period	$2\pi/\omega_a = 100 \text{ sec}$	$a_5 = \omega_a$
Output low pass cutoff period	$2\pi/\omega_1 = 0.72 \text{ sec}$	$a_6 = \omega_1$
Coil-magnet transfer function	$K_2 = 0.0016 \text{ gal/V}$	$a_7 = K_1 K_2$
Feedback low pass cutoff period	$2\pi/\omega_f = 6300 \text{ sec}$	$a_8 = \omega_f$

1) As referred to in the text and in the figures.

2) The attenuator had four settings with 10dB increments from 0 dB to 30 dB (0 dB was used most of the time).

Table 3. Description of the calibration pulses.¹⁾

Comp	Peaked mode ²⁾ (1974, day 175)			Flat mode (1976, day 149)						
	Maxima (DU's)	Length ³⁾ (sec)	Maxima (DU's)	Minima (DU's)	Zero crossing (sec)	Length ³⁾ (sec)	Minima (DU's)	Zero crossing (sec)	Length ³⁾ (sec)	Noise (DU's)
12X	14.5	45	257.0	7.6	-49.0	43.0	24.0	150	15	
12Y	14.5	42	236.0	7.0	-40.5	42.0	22.5	60	28	
12Z	15.5	43	361.0	9.8	-189.5	34.3	22.2	110	9	
14X	14.5	35	Station 14 is unstable in flat mode							
14Y	16.0	35								
14Z ⁴⁾	14.5	45								
15X	15.5	40	281.5	7.6	-54.5	45.0	23.1	160	7	
15Y	15.5	40	304.0	8.0	-67.0	39.4	21.5	120	11	
15Z	124.0	80 ⁵⁾	511.5 ⁶⁾		-345.0	44.0	23.6	210	6	
16X	19.5	45	318.0	7.4	-64.0	41.0	23.4	110	11	
16Y	13.5	40	263.5	7.7	-56.0	40.0	21.2	60	16	
16Z	19.0	50	338.5	7.5	-71.0	38.0	20.6	100	11	

- 1) Quantities were measured from the average of the positive and the sign-reversed negative calibration pulses (see Figures 3 and 4).
- 2) The noise was about 1 digital unit (DU) for all calibration pulses in the peaked mode, except for component 16Y and for the positive calibration pulse for component 15Z, for which the noise was 2 DU's.
- 3) Length refers to the approximate duration of the calibration pulse,

Table 3. (continued)

that is the time difference between the beginning of the calibration pulse and the return to the background noise level.

- 4) Calibration pulse of 1971 day 170 was used for component 14Z.
- 5) The positive calibration pulse follows 56 seconds after the negative one, while the signal from the negative pulse is still about 2 DU's above the noise level.
- 6) The amplitudes of the calibration pulse are clipped.

Table 4. Seismograph constants obtained in this study. 1)

Comp	Peaked mode ($2\pi/\omega_{op}=15\text{sec}$)					Flat mode ($2\pi/\omega_f=6300\text{sec}$)					K_f'	$\beta_f' = \frac{\beta_p}{\omega_{of}\omega_{op}}$
	C_p	β_p	a_{7p}	Peak ²⁾	freq. period	C_f	β_f	$\frac{2\pi}{\omega_{of}}$ sec	a_{7f} gal/cm	$\frac{a_{7p}}{a_{7f}}$		
12X	0.92	0.726	7.04	0.430	2.32	0.85	0.670	14.9	6.06	1.16	0.731	
12Y	0.95	0.763	7.50	0.443	2.26	0.81	0.602	14.2	6.43	1.17	0.723	
12Z	0.93	0.704	6.87	0.424	2.36	0.87	1.07	21.6	7.43	0.92	1.01	
14X	0.97	0.742	7.73	0.450	2.22	Station 14 is unstable in flat mode						
14Y	1.10	0.739	8.48	0.469	2.13							
14Z	0.93	0.719	7.69	0.450	2.22	cal pulse is clipped						
15X	1.0	0.715	7.61	0.446	2.24	1.0	0.691	14.5	6.49	1.17	0.692	
15Y	1.03	0.678	8.10	0.459	2.18	0.99	0.732	15.6	7.31	1.11	0.705	
16X	1.13	0.717	6.46	0.414	2.42	1.04	0.721	15.4	5.94	1.09	0.736	
16Y	0.91	0.726	8.12	0.459	2.18	0.85	0.691	15.4	7.36	1.10	0.742	
16Z	1.22	0.669	7.46	0.440	2.27	1.12	0.680	15.2	7.84	0.95	0.678	
Median		0.717-	7.61-							1.10-	0.723-	
		0.719	7.68	0.446	2.24		0.691 ⁴⁾	15.2 ⁴⁾	6.49 ⁴⁾	1.11	0.731	
Average		1.01 ³⁾	0.714	7.56	0.444	2.25	0.94	0.684 ⁴⁾	15.0 ⁴⁾	6.78 ⁴⁾	1.08	0.752

1) Table 2 lists the symbols used; C's are relative amplifications,

Table 4. (continued)

$C = (ca_p)/(ca_f \text{ for component 15X})$ (see equation (10)). Subscripts p and f refer to the peaked mode and the flat mode, respectively.

Nominal values for ω_a , ω_d , and ω_f are given in Table 2.

- 2) Determined from the amplitude responses to an impulse of displacement; frequency is in Hz and period is in seconds.
- 3) Constant of 15Z was not used for calculating this value.
- 4) Constant of 12Z was not used for calculating this value.

Table 5. The errors in the determination of the seismograph constants.¹⁾

	Peaked mode (%)			Flat mode (%)				$\frac{\beta_f - \beta_f'}{\beta_f}$	$1 - K_f'$	$\frac{C_p - C_f}{C_f}$
	C_p	β_p	a_{7p}	C_f	β_f	$\frac{2\pi}{\omega_{of}}$	a_{7p}			
12X	1	3	1	6	3	3	6	-0.08	-0.16	0.08
12Y	1	1	1	3	1	2	5	-0.17	-0.17	0.17
12Z	1	5	1	1	1	1	3	0.06	0.08	0.07
14X	1	3	2							
14Y	6	3	1							
14Z	2	6	1							
15X	5	4	1	1	1	1	2	-0.01	-0.17	0
15Y	3	1	1	1	1	2	3	-0.04	-0.11	0.04
15Z	1	1	1							
16X	1	2	1	7	4	3	10	-0.02	-0.09	0.09
16Y	3	3	2	2	4	1	8	-0.07	-0.10	0.07
16Z	3	6	1	1	1	1	2	0.01	0.05	0.09

¹⁾ Tables 2 and 4 give the symbols used.

Table 6. Absolute values of the relative differences between the amplitude responses of Figure 12 and component 15Z in the peaked mode.

Comp	Scale ¹⁾	Frequency (Hz)											
	factor	0.2	0.3	0.4	0.45	0.5	0.6	0.7	0.8	0.9	1.0	1.1	1.2
12X	0.93	33.37	38.66	51.69	7.40	7.51	8.70	13.45	15.75	16.94	17.73	18.22	18.58
12Y	0.82	25.23	26.02	23.99	0.00	7.00	17.25	19.38	20.29	20.74	21.03	21.21	21.33
12Z	0.85	34.43	41.78	62.88	12.51	13.44	4.08	9.53	12.22	13.63	14.58	15.17	15.60
14X	0.87	13.69	13.00	8.05	0.04	10.83	14.54	14.74	14.76	14.76	14.74	14.74	14.73
14Y	0.95	6.52	10.51	24.16	18.56	35.32	18.78	12.73	10.03	8.68	7.81	7.27	6.89
14Z	0.91	9.92	9.62	6.79	0.00	6.73	9.67	9.97	10.06	10.10	10.12	10.13	10.14
15X	0.91	11.29	11.53	10.54	0.00	3.87	8.37	9.21	9.55	9.72	9.83	9.89	9.94
15Y	1.03	9.06	11.17	18.46	7.71	14.59	3.52	0.59	0.73	1.39	1.82	2.08	2.27
16X	0.79	55.56	69.67	98.12	21.68	18.19	5.62	13.65	17.75	19.94	21.42	22.36	23.05
16Y	0.95	1.03	3.58	13.14	7.48	20.62	12.72	9.77	8.38	7.68	7.22	6.93	6.73
16Z	0.98	6.03	7.48	12.79	1.03	5.93	0.97	0.45	1.12	1.46	1.69	1.84	1.94

¹⁾The scale factors are the ratios of the maximum of the amplitude responses of each component (see Figure 12) to that of component 15Z. The amplitude responses of Figure 12 were divided by the scale factors.

Table 7. Absolute values of the relative differences between the amplitude responses of Figure 12 and component 15X in the peaked mode.

Comp	Scale ¹⁾	Frequency (Hz)											
	factor	0.2	0.3	0.4	0.45	0.5	0.6	0.7	0.8	0.9	1.0	1.1	1.2
12X	0.92	19.54	24.44	36.54	7.70	10.15	0.02	3.62	5.31	6.25	6.87	7.24	7.53
12Y	0.91	12.24	12.74	11.57	0.26	3.42	7.91	9.05	9.52	9.76	9.91	10.01	10.08
12Z	0.94	20.74	27.68	46.78	12.64	15.59	4.11	0.24	2.28	3.44	4.17	4.66	5.02
14X	0.96	1.78	0.86	2.82	0.40	6.39	5.31	4.68	4.38	4.21	4.10	4.03	3.98
14Y	1.05	16.23	20.31	32.03	18.70	29.38	9.41	2.93	0.26	1.15	2.01	2.57	2.97
14Z	1.00	1.32	1.84	3.54	0.08	2.54	1.11	0.61	0.38	0.26	0.18	0.13	0.09
15Y	1.14	18.33	20.57	26.41	7.71	8.70	4.48	7.96	9.39	10.14	10.60	10.90	11.12
15Z	1.10	10.15	10.35	9.34	0.00	4.34	7.73	8.44	8.72	8.86	8.95	9.00	9.04
16X	0.87	40.02	53.61	75.64	21.68	19.48	2.54	4.21	7.48	9.36	10.56	11.37	11.95
16Y	1.04	11.12	13.81	21.75	7.48	15.24	4.01	0.44	1.07	1.88	2.37	2.70	2.93
16Z	1.08	4.70	3.50	2.44	1.03	9.53	8.62	8.01	7.70	7.52	7.41	7.33	7.27

¹⁾The scale factors are the ratios of the maximum of the amplitude responses of each component (see Figure 12) to that of component 15X. The amplitude responses of Figure 12 were divided by the scale factors.

Table 8. Relative noise for instrumental deconvolution in the peaked mode.

Component	Freq. (Hz) where the s/n is			Relative noise ¹⁾	
	2.5	1.0	0.5	Maximum	Average
all but 15Z	1.1-1.3	1.4-1.5	1.6-1.7	0.10-0.18	0.02-0.03
15Z	1.5	1.7	1.9	0.04	0.01

- 1) The maximum or the average of the residuals between the amplitude spectrum of the calculated and observed calibration pulses in the frequency band of 0 to ω_{Nq} divided by the amplitude spectrum of the calculated calibration pulse at the peak frequency (see Table 4).

Table 9. List of the most energetic long-period lunar seismic events.¹⁾

Event	Station 12			Station 14			Station 15			Station 16			
Yr:day	Code	Com	WL	Hr:mn:sec	Com	WL	Hr:mn:sec	Com	WL	Hr:mn:sec	Com	WL	Hr:mn:sec
71:051	A01	XYZ	10	15:07	XYZ	10	15:07	no records			no records		
75:086	A01	flat		18:47	1	3							
75:113	A01	Z	3	11:54	1	3	11:54	XYZ	3	11:55	XYZ	3	11:55
75:304	A01	flat		6:34	1	3	6:34	flat		6:37	flat		6:35
73:148	A14	weak			weak			weak			XYZ	10	18:56
72:145	A16	weak			weak			weak			Z	10	9:24
73:001	A17	XYZ	10	11:34	XY3	10	11:34	XYZ	10	11:32	XYZ	3	11:34
74:116	A20	XYZ	10	9:20	XY3	10	9:20	XYZ	10	9:19	XYZ	3	9:19
72:341	A33	weak			weak			weak			XYZ	3	13:29
											XYZ	3	13:32
72:138	A34	weak			weak			XYZ	10	23:33	XYZ	10	23:33
74:166	A42	1 Z	10	13:21	XY3	10	13:21	XYZ	10	13:22	XYZ	10	13:23
74:084	A44	XYZ	10	14:33	XY3	10	14:32	XYZ	10	14:31	XYZ	10	14:32
73:243	A46	XYZ	10	0:04	XY3	10	0:04						
74:343	A46							XYZ	10	23:49	XYZ	10	23:46
77:107	A73	weak			weak			weak			XYZ	10	17:13
69:324	CL2	flat		22:17	no records			no records			no records		
71:038	CL4	Z	3	0:45		10	0:45	no records			no records		
71:215	CL5	weak			weak			XYZ	3	3:03	no records		
70:105	CS3		3	1:09	no records			no records			no records		
71:035	CS4	XYZ	3	7:41	no records			no records			no records		
71:210	CS5	XYZ	3	20:59	Z	3	20:59	no records			no records		

Table 9. (continued)

Event	Station 12			Station 14			Station 15			Station 16		
Yr:day Code	Com	WL	Hr:mn:sec	Com	WL	Hr:mn:sec	Com	WL	Hr:mn:sec	Com	WL	Hr:mn:sc
72:110 CS6		3	21:02	XYZ	3	21:02	XYZ	3	21:04	no records		
72:345 CS7	XYZ	3	20:33		3	20:33	XYZ	10	20:35	X2Z 10 20:34		
72:134 C01		3	8:47		3	8:47	XYZ	3	8:48	XYZ 3 8:48		
71:143 C02	XYZ	3	22:20	XYZ	3	22:20	no records			no records		
71:163 C03	XYZ	3	10:51	XYZ	3	10:51	no records			no records		
71:193 C04	XYZ	3	18:08	XYZ	3	18:08	XYZ	3	18:08	no records		
72:199 C05	XYZ	3	21:57:45	XYZ	3	21:57:45	XYZ	3	21:56:45	Z 3 21:57:15		
	XYZ	3	22:01	XYZ	3	22:01	XYZ	3	22:00	YZ 3 22:00		
72:213 C06	XYZ	10	18:11		3	18:10	XYZ	10	18:08	3 18:11		
72:324 C07	XYZ	10	18:26	XYZ	10	18:25	XYZ	10	18:24	10 18:25		
73:113 C08		10	13:56	X	3	13:56		Z	10	13:55	Z 10 13:55	
73:262 C09		10	9:32		3	9:32		Z	10	9:34	XYZ 10 9:32	
											XYZ 10 9:35	
73:269 C10	XYZ	10	20:53	XYZ	10	20:50	XYZ	10	20:48	X2Z 10 20:49		
74:038 C11	Z	10	6:21	XYZ	10	6:21	XYZ	10	6:22	10 6:21		
74:181 C12	XYZ	10	17:44		3	17:44	weak			weak		
74:187 C13	Z	10	14:17	XYZ	10	14:17	XYZ	10	14:14	Z 10 14:16		
74:305 C14	flat, weak			XYZ	10	11:44		Z	10	11:45	Z 10 11:43	
										Z 10 11:46		
74:325 C16	flat	13.18		XYZ	10	13:18	XYZ	10	13:18	XYZ 10 13:15		
74:343 C17	flat, weak			XYZ	10	9:32	XYZ	10	9:33	XYZ 10 9:29		
74:349 C18	flat	9:08		XYZ	3	9:07	XYZ	10	9:10	XYZ 10 9:09		

Table 9. (continued)

Event	Station 12	Station 14	Station 15	Station 16
Yr:day Code Com WL Hr:mn:sec	Com WL Hr:mn:sec	Com WL Hr:mn:sec	Com WL Hr:mn:sec	Com WL Hr:mn:sc
75:064 C20	flat, weak	1 3 10 21:53	XYZ 10 21:54	Z 10 21:51
75:085 C22	flat, weak	1 3 10 12:04	XYZ 10 12:07	Z 10 12:06
75:102 C23	XYZ 10 18:16	1Y3 10 18:16	XYZ 10 18:15	XYZ 3 18:14 XYZ 3 18:18
75:124 C25	Z 3 10:05	1 3 3 10:05	XYZ 3 10:06	Z 3 10:05
77:107 C26	XY3 10 23:35	XYZ 10 23:35	XYZ 10 23:37	Z 10 23:36
77:179 C27	Z 10 22:25:30	3 10 22:26	XYZ 10 22:27	X Z 10 22:27
76:025 C28	flat 16:09	123	flat 16:11	flat 16:11:45
76:109 C29	flat 8:46	123	flat 8:47	flat 8:48
76:121 C30	flat 11:54	123	flat 11:55	flat 11:52
76:137 C31	flat, weak	123	flat, weak	flat 12:47
76:240 C32	flat, weak	weak	flat, weak	flat 4:31
77:007 C33	flat, weak	weak	flat, weak	flat 3:49
77:153 C34	weak	weak	weak	XYZ 10 14:26
76:319 C35	flat 23:16	123	flat 23:17	flat 23:18:30
77:256 C36	20:33	3 20:34	weak	weak
73:171 H01	XYZ 10 20:24	XY3 10 20:24:48	Z 10 20:26	Z 10 20:27:30
74:192 H02	Z 10 0:52	3 10 0:52	Z 10 0:50	XYZ 10 0:50
	Z 10 0:56	XY3 10 0:56	Z 10 0:54	XYZ 10 0:54
75:003 H03	flat 1:46	XY3 3 1:46:30	Z 3 1:46:30	3 1:47
		XY3 3 1:50:30	Z 3 1:50:30	3 1:50
75:012 H04	flat 3:19	Y3 10 3:19	XYZ 10 3:17	XYZ 10 3:20

Table 9. (continued)

Event	Station 12			Station 14			Station 15			Station 16		
Yr:day Code	Com	WL	Hr:mn:sec	Com	WL	Hr:mn:sec	Com	WL	Hr:mn:sec	Com	WL	Hr:mn:sec
73:072 H06	XYZ	10	8:01	X23	10	8:01	12Z	10	8:02:30	XYZ	10	8:01
	XYZ	10	8:05	23	10	8:05	12Z	10	8:05	XYZ	10	8:05
71:192 H07	XYZ	10	13:27	Z	10	13:28	no records			no records		
71:140 H08	XYZ	10	17:28	XYZ	10	17:28	no records			no records		
	Z	10	17:32	XYZ	10	17:32	no records			no records		
71:107 H09	XYZ	10	7:04:45	XYZ	10	7:04:45	no records			no records		
	XYZ	10	7:08:45	XYZ	10	7:08:45	no records			no records		
76:066 H10	flat		10:15	XY3	10	10:15	flat	10:14		flat		10:16
76:068 H11	flat		14:43	XY3	10	14:43	flat	14:45		flat		14:43:45

1)

Yr:dy;Hr:mn:sec is the beginning of the 309 minute time sections.

Code is the event designation as used in the text, in the seismic sections, and in Tables 18, 19, and 20. The first letter of the code is the type of source; A is deep moonquake, C is impact, H is shallow moonquake. The two-digit numbers are arbitrary sequence numbers for natural impacts and shallow moonquakes and are source locations for deep moonquakes. The artificial impacts are denoted by the letter C followed by a letter, giving the source (L is for Lunar Module and S is for Saturn IV booster), and by a number, giving the second digit of the mission number. WL is the waterlevel parameter (in %) used for instrumental deconvolution. Com is 1, 2, or 3 if the X, Y, or Z component, respectively, did not operate

Table 9. (continued)

properly at the time of the event, and X, Y, or Z are used to denote those time sections which were recorded in the peaked mode and were used for computation of the whitening filters. 'flat' indicates that the long-period seismographs were operated in the flat mode at the time of the event and the seismograms of all three components were used in the seismic sections. 'weak' indicates that the signal amplitudes were too small to be used in this study.

Table 10. Number of time sections classified according to source type and to components.

	Deep moonquakes		Shallow moonquakes		Impacts		Total					
	Peaked	Flat	Peaked	Flat	Peaked	Flat	Peaked	Flat				
	Good	Noisy	Good	Noisy	Good	Noisy	Good	Noisy				
12X	5	2	2	7	3	4	14	10	7	26	15	13
12Y	5	2	2	7	3	4	14	10	7	26	15	13
12Z	7		2	10		4	18	5	7	35	5	13
14X	6	1		11	4		16	7		33	12	
14Y	6	3		11	2		16	11		33	16	
14Z	1			5			5			11		
15X	7		1	1	5	2	21	3	4	29	8	7
15Y	7		1	1	5	2	21	3	4	29	8	7
15Z	7		1	8		2	24		4	39		7
16X	11	1	1	5	3	2	11	14	7	27	18	10
16Y	11	1	1	5	3	2	11	12	7	27	16	10
16Z	12			6	2	2	22	3	7	40	5	10

1) The number of time sections listed in column 'Good' were recorded in the peaked mode and were used for computation of the whitening filters, in column 'Noisy' were not so used. The number of time sections listed in column 'Flat' were recorded in the flat mode and were used in the seismic record sections.

Table 11. Relative amplification of the horizontal components $(Y/X)^1$

Sta	Deep moonquakes		Shallow quakes		Impacts		Total	
	0.2-1.5	0-2.5	0.2-1.5	0-2.5	0.2-1.5	0-2.5	0.2-1.5	0-2.5
12	1.02	0.99	1.02	0.93	0.98	0.91	0.98	0.92
14	1.49	1.29	1.14	1.21	1.23	1.21	1.21	1.21
15	1.30	1.27	1.26	1.13	1.40	1.27	1.40	1.26
16	1.39	1.21	1.36	1.27	2.07	2.00	1.80	1.70

¹⁾ Average amplifications in two frequency bands, 0.2 to 1.5 Hz and 0 to 2.5 Hz.

Table 12. Structural parameters of the near-surface zone; model 'A'.¹⁾

ρ	α/β	Station 12		Station 14		Station 15		Station 16	
		z	β	z	β	z	β	z	β
1.5	2.9	1.2	36	2.9	36	1.7	36	4.4	36
1.6	2.7	4.1	62	5.0	49	6.2	62	9.9	56
1.7	2.4	11.3	96	8.6	68	13.0	96	25.1	96
1.8	2.2	19.5	136	18.0	98	25.4	136	49.6	136
1.9	2.0	41.1	204	28.1	117	59.3	204	104.6	204
1.9	2.0	84.3	226	64.4	183	104.6	283	168.4	283
1.9	2.0	127.5	340	86.4	277	149.9	340		
1.95	2.0	-	430	-	360	-	480	-	400

¹⁾ ρ is density in g/cm^3 , z is depth in meters, α and β are compressional and shear velocities in m/sec.

Table 13. Structural parameters of the near-surface zone; model 'B'.¹⁾

ρ	α/β	Station 12		Station 14		Station 15		Station 16	
		z	β	z	β	z	β	z	β
1.8	2.6	1.9	40	3.2	40	2.8	40	5.1	40
1.85	2.5	7.5	68	5.5	55	9.5	68	10.9	62
1.9	2.25	10.3	93	9.5	76	12.8	93	27.1	106
1.9	2.16	18.7	135	19.0	109	22.8	135	51.5	150
1.95	2.08	33.6	167	30.3	131	40.7	167	111.2	227
1.95	2.06	80.1	205	70.8	204	74.2	205	178.5	313
2.0	2.0	135.9	302	95.5	309	141.2	302	-	440
2.0	2.0	-	395	-	400	-	395	-	-

¹⁾ ρ is density in g/cm^3 , z is depth in meters, α and β are compressional and shear velocities in m/sec.

Table 14. Description of the velocity distributions of model 'B' in the forms of $\beta = a + bz$ and $\alpha = cz^p$. ¹⁾

Station	Top zone			Bottom zone		Power law		N	$\bar{\alpha}$
	a	b	h	a	b	c	p		
12	33.7	6.9	16.1	118	1.7	106	0.31	3	159
14	29.6	6.1	10.1	62	2.9	89	0.32	3	134
15	31.7	5.7	19.2	107	1.8	93	0.34	3	156
16	29.8	4.1	25.2	95	1.5	75	0.35	2	126

¹⁾ β and α are the shear and compressional velocities, respectively, in m/sec, z is depth in m, a , b , c , and p are constants, h is the depth in m where the gradient (b) changes its value, N is the number of uppermost layers in which the power law adequately describes the compressional velocities, and $\bar{\alpha}$ is the average velocity in the zone consisting of these layers.

Table 15. Travel times from the Apollo 14 and 16 Active Seismic Experiments. ¹⁾

x	t_m	$t_{1/6}$	t_{14}	t_{16}	$t_{1/3}$
4.57	55	51.7	44.0	40.1	58.3
9.14	91	92.1	87.9	80.2	92.6
13.71	123	129.1	131.9	120.3	121.5
18.29	151	164.2	175.8	160.4	147.1
27.43	206	230.1	245.0	240.6	192.9

¹⁾ x is the separation of the geophones in m (Gangi, 1978, Table III), t_m is measured from the Apollo 14 and 16 stacked data in msec (ibid.), $t_{1/6}$ is calculated for the self-compacting-powder model: $t_{1/6} = 14.57 \times x^{5/6}$ msec (ibid.), t_{14} is calculated for the Apollo 14 layered model in msec (ibid.), t_{16} is calculated for the Apollo 16 layered model in msec (ibid.), $t_{1/3}$ is calculated for the 1/3 power law model: $t_{1/3} = 21.2 \times x^{2/3}$ msec.

Table 16. Velocity models used in this study with thicker lunar crust and higher lunar mantle velocities.¹⁾

Depth (km)	Compr. vel. (km/sec)	Shear vel. (km/sec)
0.0	0.1	0.05
0.25	1.0	0.5
1.0	2.1	1.2
5.0	4.1	2.4
9.0	5.0	2.9
17.0	5.9	3.4
25.0	6.4	3.7
	6.6	3.8
55.0	6.8	3.9
	8.1	4.6
200.0	8.0	4.5
	7.9	4.4
425.0	7.8	4.2
	7.8	3.9
1350.0	7.9	3.7
	8.0	2.0
1738.0	8.0	2.0

¹⁾ First-order discontinuities are at those depths where two compressional and two shear velocities are given. The velocities between the depths listed in this table are continuous and are given by equations (35).

Table 17. Velocity models used in this study with thinner lunar crust and lower mantle velocities.¹⁾

Depth (km)	Compr. vel. (km/sec)	Shear vel. (km/sec)
0.0	0.1	0.05
0.25	1.0	0.5
1.0	2.1	1.2
5.0	4.1	2.4
9.0	5.0	2.9
17.0	5.9	3.4
25.0	6.4	3.6
	6.6	3.9
45.0	6.8	4.0
	7.7	4.4
200.0	7.6	4.35
	7.6	4.25
425.0	7.6	4.20
	7.6	4.10
1350.0	7.6	3.80
	7.6	3.50
1738.0	7.6	3.50

¹⁾ First-order discontinuities are at those depths where two compressional and two shear velocities are given. The velocities between the depths listed in this table are continuous and are given by equations (35).

Table 18. Reference times, origin times, and locations for selected major lunar seismic events.¹⁾

Code	Reference time		Origin (sec)	Epicenter (degree) ²⁾		Distances (degrees) ³⁾				Azimuths (degrees) ^{3,4)}			
	yr:day	hr:mn		Latitude	Longitude	12	14	15	16	12	14	15	16
CL2	69	324 22 17	17.7	3.94 S	21.21 W	2.4				67.8			
CL4	71	38 45	25.7	3.42 S	19.67 W	3.7	2.2			-84.1	-84.1		
CL5	71	215 3 04	-23.0	26.36 N	0.25 E			3.1				-94.0	
CS3	70	105 1 10	-19.0	2.75 S	27.86 W	4.5				93.6			
CS4	71	35 7 41	-4.6	8.09 S	26.00 W	5.7				26.8			
CS5	71	210 20 59	-17.1	1.51 S	11.80 W	11.7	6.1			-97.3	69.5		
CS6	72	110 21 02	-2.4	2.33 N	24.02 W	5.4	8.9	35.7		173.6	-47.7	127.2	
CS7	72	345 20 33	-17.7	4.21 S	12.30 W	11.2	5.2	34.0	28.0	-83.6	96.4	-151.	-56.5
C01	72	134 8 47	-20.0	1.40 N	16.76 W	8.0	5.1	31.5	33.8	-124.	8.2	-138.	-48.2
C02	71	143 22 20	-22.5	0.65 N	17.23 W	7.2	4.3			-121.	3.3		
C03	71	163 10 51	-98.5	32.42 N	29.04 W	35.9	37.7			171.9	-16.1		
C04	71	293 18 08	-108.	30.70 N	28.58 W	34.1	36.0	28.6		172.1	-16.4	-73.2	
C05	72	199 21 56	-335.	31.50 N	148.90 E	150.6	149.3	113.5	131.3	-167.	23.2	32.0	81.0
C06	72	213 18 08	-4.3	33.90 N	3.92 W	41.3	39.7	10.2	46.7	-155.	17.8	-38.2	-126.
C07	72	324 18 24	-160.	61.18 N	16.27 W	64.3	65.2	40.5	77.4	178.5	-4.7	-21.7	6.3

Table 18. (continued)

Code	Reference time		Origin (sec)	Epicenter (degree)		Distances (degrees)				Azimuths (degrees)				
	yr:day	hr:mn		Latitude	Longitude	12	14	15	16	12	14	15	16	
C16	74	325	13 16	-29.3	6.14 S	21.77 E	45.1	39.2	36.7	6.8	-84.4	95.2	148.9	91.4
C23	75	102	18 14	-55.0	3.20 N	34.37 E	58.2	52.3	37.3	22.4	-95.7	83.1	122.7	83.4
C25	75	124	10 05	-362.	35.00 S	131.70 W	103.1	107.4	140.9	126.2	52.9	-129.	-114.	-121.
C26	77	107	23 35	-166.	20.09 S	61.00 W	40.5	45.5	77.9	74.4	62.1	-115.	-120.	-83.0
C28	76	025	16 09	-148.	5.45 S	72.51 W	49.0		80.1	87.2	85.		-101.	-69.6
C30	76	121	11 52	21.7	9.04 S	12.10 E	35.8		36.4	3.4	-78.2		165.9	-71.3
C31	76	137	12 47	-8.2	10.48 S	9.83 E	33.8		37.1	5.8	-75.6		169.9	-80.1
C35	76	319	23 16	-216.	19.37 N	89.01 W	68.2		83.9	106.6	112.3		-71.4	-46.8
C36	77	256	20 34	-13.7	1.43 S	22.61 W	1.8	5.6			-153.		-66.7	
H01	73	171	20 24	-160.	20.01 S	72.41 W	50.7	55.9	87.0	85.0	66.5	-112.	-114.	-84.0
H02	74	192	50	-185.	19.12 N	73.54 E	97.6	92.2	64.2	63.7	-109.	71.0	80.3	88.9
H03	75	3	1 46	-237.	28.47 N	92.45 W	73.3	78.7	82.7	110.0	121.3	-59.7	-61.5	-37.1
H04	75	12	3 17	-161.	59.59 N	53.65 E	86.1	83.8	47.8	75.0	-150.	28.8	31.6	44.4
H06	73	72	8 01	-275.	84.98 S	110.50 W	86.7	86.6	118.0	84.0	5.0	-175.	-175.	-150.
H07	71	192	13 28	-201.	20.16 S	72.16 W	50.5	55.7			66.2	-112.		

Table 18. (continued)

Code	Reference time			Origin (sec)	Epicenter (degree)		Distances (degrees)				Azimuths (degrees)			
	yr:day	hr:mn			Latitude	Longitude	12	14	15	16	12	14	15	16
H08	71	140	17 29	-168.	39.44 N	18:62 W	42.7	43.1			-175.	-1.5		
H09	71	107	07 05	-247.	49.45 N	28.69 E	69.0	66.4			-147.	30.8		
H10	76	66	10 14	-91.6	49.22 N	26.01 W	52.3	53.4	32.6	68.6	177.8	-7.6	-40.0	-2.3
H11	76	68	14 43	-46.0	18.13 S	11.83 W	18.9	15.5	46.7	28.1	-36.2	159.5	-160.	-86.4
A01	75	113	11 54 ⁵⁾		10.80 S	31.30 W	11.0	15.5	50.2	46.1	44.8-118.	-133.	-70.9	
A14	73	143	18 58		22.50 S	35.30 W				50.5				-86.3
A16	72	145	09 24		5.90 N	6.80 E				17.2				-5.1
A17	73	001	11 33		33.50 N	33.10 W	37.7	40.0	32.6	62.7	166.7	-20.5	-68.0-19.2	
A20	74	116	09 20		20.80 N	27.00 W	24.1	26.2	28.6	51.3	171.8	20.5	-94.1-28.5	
A28	71	288	06 29		7.00 N	24.20 E		42.9				75.7		
A33	72	341	13 30		7.10 N	1.05 E				90.6				108.4
A34	72	138	23 33		7.50 N	6.70 W			21.0	27.6			-150.	-28.5
A42	74	166	13 21		23.10 N	45.70 W	34.0	38.4	44.7	67.9	141.4	-44.5	-82.7-35.0	
A44	74	084	14 33		61.70 N	16.80 E		70.4		70.7		16.5		26.1
A08	77	107	17 15		26.30 N	32.40 W				48.5				-91.8

Table 18. (continued)

- 1) Origin times and locations of C and H events were obtained by using arrival times listed in Table 19 and the velocity distributions given in Table 17. Source depths were assumed to be 0 km for C events and 80 km for H events. Locations of A events are from Lamlein et al. (1977) and were used for calculations of the distances and azimuths only.
- 2) Alternate locations of those events which had arrival times observed at two stations only are as follows:

Code	Latitude (°)	Longitude (°)
C02	7.91 S	18.09 W
C03	36.30 S	37.25 W
H07	24.06 N	67.29 W
H08	45.38 S	29.81 W
H09	62.61 S	23.93 E

- 3) No distance and azimuth are given if there was no long-period seismogram available at a given station or if the seismic signal was not used in the seismic sections.
- 4) Azimuth is the angle from the positive X axis of the seismometer to the direction toward the source from the station (see Table 1 for the orientation of the long-period seismometers). Positive is clockwise.
- 5) Reference time of the seismic signal at station 14 is 71:051; 11:54.

Table 19. Observed and theoretical arrival times for events listed in Table 18.¹⁾

Code	Station 12				Station 14				Station 15				Station 16			
	P _{obs}	P _{cal}	S _{obs}	S _{cal}	P _{obs}	P _{cal}	S _{obs}	S _{cal}	P _{obs}	P _{cal}	S _{obs}	S _{cal}	P _{obs}	P _{cal}	S _{obs}	S _{cal}
CL2	38.0	37.6	55.5	52.8												
CL4	51.5	52.0	67.5	72.3	44.5	44.5	60.0	59.0								
CL5									-0.5	0.5	24.5	28.3				
CS3	10.0	10.8	34.0	34.8												
CS4	31.0	31.1	56.0	55.9												
CS5	41.0	40.6	87.5	85.0	19.5	20.0		47.1								
CS6	31.5	31.5	56.5	56.5	47.0	47.0	86.0	81.0	150.0	147.0	259.0	258.8				
CS7	39.0	39.2	79.0	81.7	14.3	15.4	44.0	39.6	134.5	125.6		232.8	105.0	103.1		193.4
C01	25.0	25.5	55.0	57.6	12.5	12.5	36.5	36.6	114.0	114.0	216.0	214.3	121.5	122.4		228.9
C02	19.5	19.5	50.0	50.2	6.5	6.5	28.0	28.0								
C03	52.0	51.7	164.0	164.0	58.5	58.5	176.0	176.0								
C04	35.5	35.5	143.0	142.9	41.5	42.4		155.0	15.0	15.0	107.0	107.1				
C05	114.5	114.5		508.3	123.5	113.1		505.1	55.0	55.0		380.5	89.0	88.9		451.0
C06		<u>165.9</u>		293.2	160.0	160.0		282.9	51.0	51.0	88.0	88.0		<u>185.6</u>		327.8
C07	90.0	91.4	286.0	282.2	94.5	94.5	292.0	288.0	7.0	7.0	132.0	132.2	131.5	133.7		363.2

Table 19. (continued)

Code	Station 12				Station 14				Station 15				Station 16			
	P _{obs}	P _{cal}	S _{obs}	S _{cal}	P _{obs}	P _{cal}	S _{obs}	S _{cal}	P _{obs}	P _{cal}	S _{obs}	S _{cal}	P _{obs}	P _{cal}	S _{obs}	S _{cal}
C16	149.0	<u>155.1</u>	294.0	293.1	132.0	133.2	252.0	254.8	124.0	124.0	239.0	238.7	11.0	11.0	40.5	40.5
C23	171.5	<u>175.8</u>	350.0	348.8	157.0	155.2	313.0	312.4	100.5	100.5	210.0	216.8	44.5	44.5	124.0	118.9
C25	2.0	4.1	304.9	14.5	14.5	325.8	76.5	76.5	455.4	53.5	53.5	405.8				
C26	6.0	1.5	141.0	126.6	19.5	20.0	160.0	158.9	130.0	130.0	361.0	361.0	119.0	119.0	340.0	
C28	50.0	50.0	196.0	198.4					154.0	154.0	90.7	175.0	175.0	430.3		
C30		<u>171.7</u>	284.0	284.0					<u>174.7</u>	286.0	287.5	46.5	46.5	64.5	65.3	
C31		<u>134.4</u>	241.0	241.0					<u>146.4</u>	262.0	262.1	27.5	27.5	54.0	53.8	
C35	49.0	49.0	251.4	67.0					98.0	98.0	345.0	344.6	158.5	158.5	467.8	
C36	3.0	3.0	16.0	15.8	21.0	21.0	46.6								267.1	
H01		<u>35.7</u>	182.0	182.0	54.0	54.0	215.0	215.0	156.0	<u>151.7</u>	399.7	<u>146.1</u>	388.7			
H02		<u>155.4</u>	434.4	128.0	141.2	404.1	57.0	57.0	242.0	242.0	55.5	55.5	240.0	239.3		
H03	34.0	34.0	245.7	51.0	50.6	275.0	276.5	62.5	62.4	298.6	133.0	133.0	442.3			
H04		<u>147.7</u>	393.4	140.0	140.9	380.1	24.0	24.0	161.0	162.7	<u>114.7</u>	331.0	331.0			
H06	34.0	35.3	282.6	35.0	35.0	282.1	109.0	111.3	438.1	27.5	27.5	266.0	267.3			
H07		-5.7	140.0	140.0	12.5	12.5	173.0	173.0								

Table 19. (continued)

Code	Station 12				Station 14				Station 15				Station 16			
	P _{obs}	P _{cal}	S _{obs}	S _{cal}	P _{obs}	P _{cal}	S _{obs}	S _{cal}	P _{obs}	P _{cal}	S _{obs}	S _{cal}	P _{obs}	P _{cal}	S _{obs}	S _{cal}
H08		<u>-1.1</u>	123.5	123.5	0.0	0.0	126.0	126.0								
H09	10.0	10.0	210.0	210.0	1.5	1.5	192.0	192.0								
H10		<u>109.7</u>	262.5	260.6	113.5	113.5	267.5	267.4	38.5	38.5	132.5	135.9		<u>164.5</u>		363.3
H11		<u>32.8</u>		91.7	20.0	20.0	69.0	69.4	139.5	135.3	271.0	271.0	66.0	67.1	150.0	151.8
A01			106.				116.				213.				192.	
A14															22.5	
A16															170.	
A17			29.				29.				50.				107.5	
A20			27.				30.				37.				105.5	
A28							38.									
A33															218.5	
A34											39.				52.5	
A42			58.5				71.				93.				170.5	
A44							26.5								51.	
A08															4.	

Table 19. (continued)

- 1) Reference times are listed in Table 17. Arrival times are given for those signals only which were used in the seismic sections. The seismic records of C and H events are aligned in the sections according to either the observed or, if underlined, the calculated arrival times of the compressional waves. The seismic records of A events are aligned according to the observed shear-wave arrivals.

Table 20. Arrival times observed by other investigators.¹⁾

a) Artificial impacts									
Event Sta.		Latham <u>et al.</u> (1972b)		Toksoz <u>et al.</u> (1974)		Koyama & Naka- mura (1979) ²⁾		Jarosch (1977)	
Code		P	S	P	S	P	S	P	S
CL4	12	-0.8	3.2	-2.0			3.4		
	14	-1.0	-3.3	-0.3		0.3		0.5	-2.4
CL5	15	-0.5		-0.5			-9.7		-10.3
CS3	12	0.4	-2.5	-1.0		0.0	-3.3	-0.2	
CS4	12	0.1	-4.9			0.2	-3.1	0.2	1.0
CS5	12	-2.6		-2.6		1.0	-2.1	4.6	1.4
	14	0.0	43.4*	-0.5		0.1	44.9*	1.1	37.5*
CS7	12					0.2	2.2	3.4	-3.3
	14					0.5	-6.2	0.1	-16.7
	15								210.9*
	16							-0.8	185.2*

b) Meteoroid impacts

Event Sta.		Nakamura <u>et al.</u> (1977)		Goins (1978)		Koyama & Naka- mura (1979) ²⁾	
		P	S	P	S	P	S
CO1	12	0.2		0.2	7.7	0.3	
	14	-0.2	0.5	0.0	0.3	-0.1	0.5
	15	0.1	4.0	0.3	1.0	0.4	1.0
	16	-1.3	220*	-0.9		-1.1	222.5*

Table 20. (continued)

C05	12	-0.5		0.5		-0.5	
	14	0.4	630*	0.3		0.5	630*
	15	4.7	380*	-8.7		-8.5	380*
	16	-0.2	530*	-12.3		-12.9	530*
C06	12	195.1*		196.4*		196.1*	338*
	14	16.4	280*	18.1		17.5	307*
	15	1.9	2.0	0.3	7.5	2.0	2.0
	16	192*	320*	199.5*		193*	331*
C07	12			-2.4			
	14	0.1	8.0	-0.2	-1.8		
	15	15.1	-2.0	14.3			
	16	-1.1	360*	-0.2			
C16	12	13.1					
	14	9.8	18.0				
	15	0.0	1.0				
	16	0.1	9.5				
C23	12	0.1		0.3	-58.0	0.2	2.0
	14		-13.0	1.0		1.0	7.0
	15	0.3	10.0	0.3		0.3	10.0
	16	-0.2	-4.0	0.1	6.5	-0.1	-4.0
C25	12	0.3		-0.7		0.3	282*
	14	0.4	320*	1.0		1.6	320*
	15	1.2	510*	1.0	4.0	1.3	416*
	16	0.3	460*	0.1		0.3	375*

Table 20. (continued)

C26	12		0.9		0.6	37.0
	14		-1.2		-0.5	38.5
	15		-2.1		-1.8	
	16		7.5		0.5	
C28	12		1.1	-2.5		
	15		0.5	372.2*		
	16		-4.3			

c) Shallow moonquakes

Event	Sta.	Nakamura <u>et al.</u> (1979) ²⁾		Goins (1978)		Koyama & Naka- mura (1979) ²⁾		Lammlein (1977) ³⁾	
		P	S	P	S	P	S	P	S
H01	12	56.0*	-2.0	55.0*	3.3	56.0*	5.5	0.0	
	14	13.0	4.0	12.5		13.0	-7.5	17.0	165.3
	15	148*	360*	145.7*		147.5*	346*	98.0*	316.5
	16	191*	430*	198.5*	412.5*		422.5*		
H02	12	139*	459*	138.5*		138.7*	417*	167.2	
	14	1.0	439*	-2.7		0.6	407*	153.4	
	15	1.0	13.0	-0.5		0.5	21.0	85.0	184.5
	16	4.5	30.0	-5.2		4.5	30.0	81.8	179.5
H03	12	0.0		-0.4	269*	-0.5	256*	0.0	217.2
	14	0.0	5.0	0.3		0.2	10.0	17.8	
	15	-1.5	300*	-2.0		-1.4	315*	29.0	
	16	2.0	510*	-5.5	453*	2.0	510*	100.6	

Table 20. (continued)

H04	14	-2.0	368*			-2.5	356*		
	15	-4.0	1.0			6.0	1.0	0.0	130.9
	16	125*	0.0			125*	0.0	94.4	295.2
H06	12	0.0	267*	0.1	272*	0.2	267*	6.5	239.3
	14	-1.0	280*	0.9		0.5	272.5*		
	15	-9.0	465*	-9.3		-9.0	398.5*	71.0	
	16	-0.5	4.0	0.3	-6.6	0.5	2.6	0.0	230.9
H07	12	-2.0*	0.0						126.8
	14	10.0	-8.0					0.0	151.3
H08	12	0.0*	-0.5						123.3
	14	0.0	-2.0					0.0	123.8
H09	12	0.0	2.0					7.0	207.7
	14	0.5	-10.0					0.0	192.2
H10	12	118*	0.5	110.8*	-0.5	110.8*	0.5		
	14	-0.5	0.5	-0.2	1.2	-0.5	0.5		
	15	-0.5	-8.5	0.7	3.3	-0.5	-2.5		
	16	168*	347*		346*	161*	355*		
H11	12			98.8*					
	14	2.0	0.0	4.2	1.3	2.0	0.0		
	15	10.5	-5.0	10.0	-5.9	9.5	-5.0		
	16	-6.0	-16.0	3.9		-6.0	-16.0		

1) Differences between arrival times read by other investigators and used

Table 20. (continued)

in this study (see Table 19) are given in seconds. Arrival times read only by other investigators are marked with * and were measured from the reference times given in Table 18.

- 2) Observed arrival times were used in the publications but were unpublished; the arrival times were provided by the first authors.
- 3) Only relative arrival times were given by Lammlein (1977).

Figure 1. Compressed time-scale seismic records for the three major types of natural seismic sources (from Nakamura et al., 1974).

PRECEDING PAGE BLANK NOT CM ME

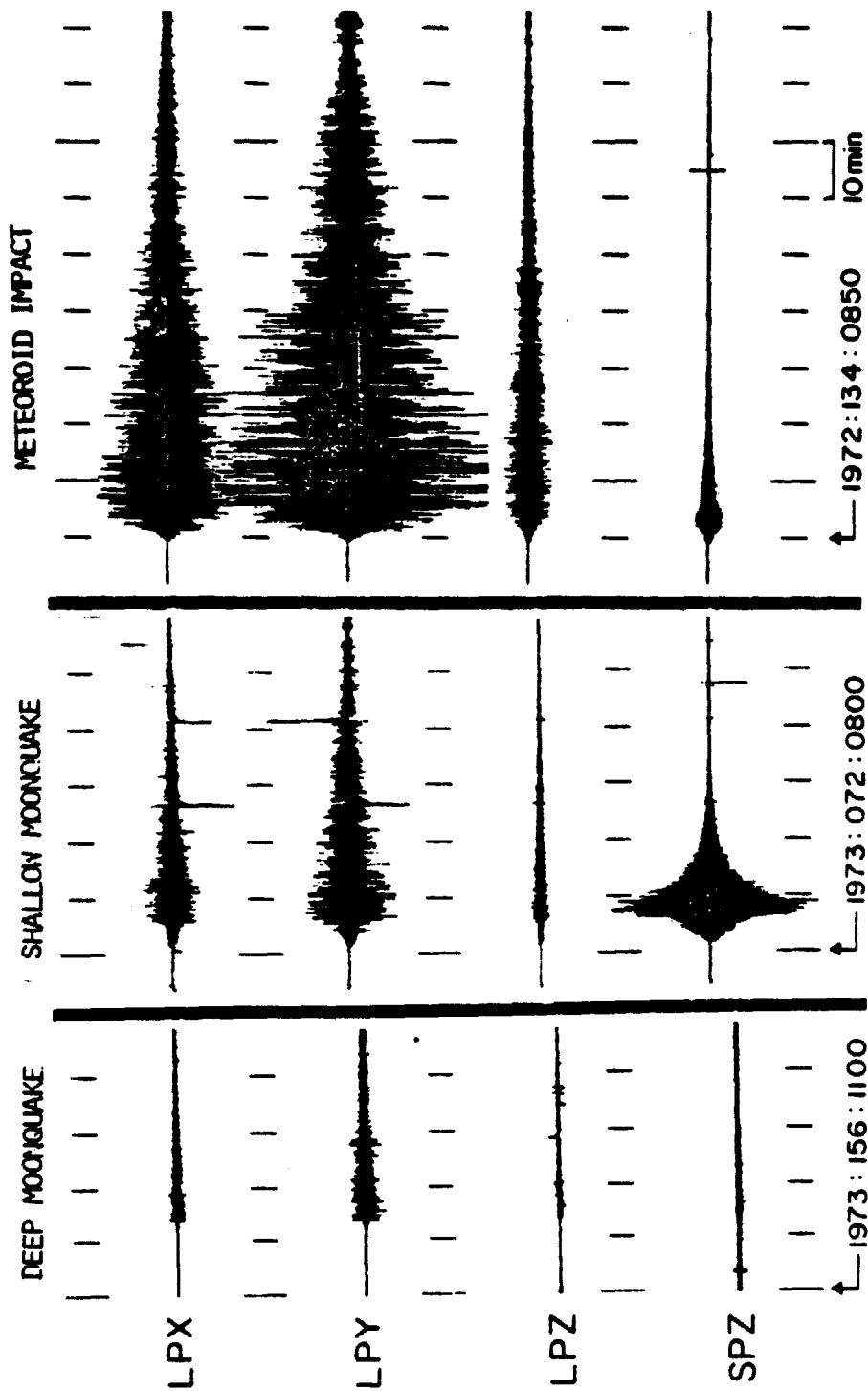


FIGURE 1.

ORIGINAL PAGE
OF POOR QUALITY

Figure 2. Simplified block diagram of the feedback controlled,
direct digitizing long-period lunar seismographs.

FIGURE 2.

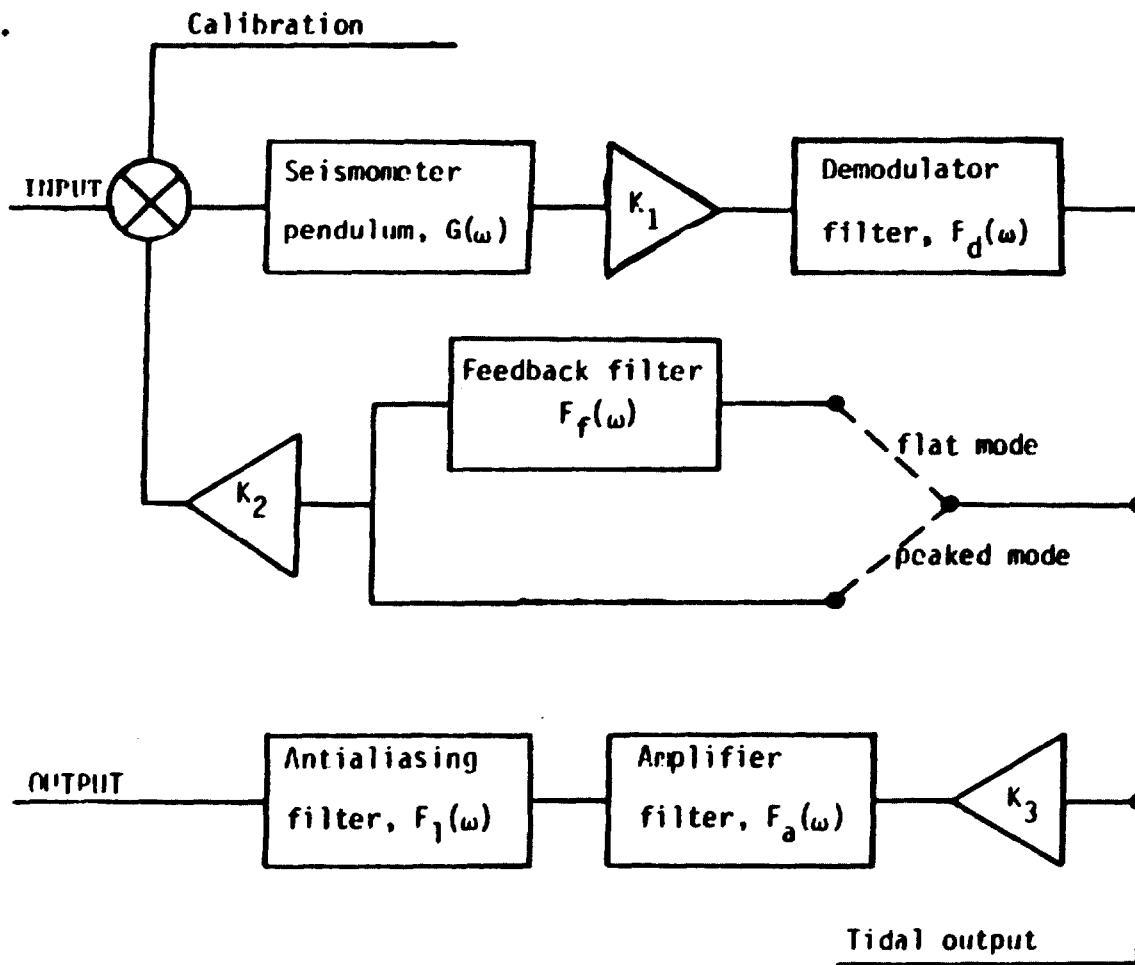


Figure 3. Average of the positive and the sign-reversed negative calibration pulses in the peaked mode. The maxima of the calibration pulses are given in Table 3. The minima are 0.

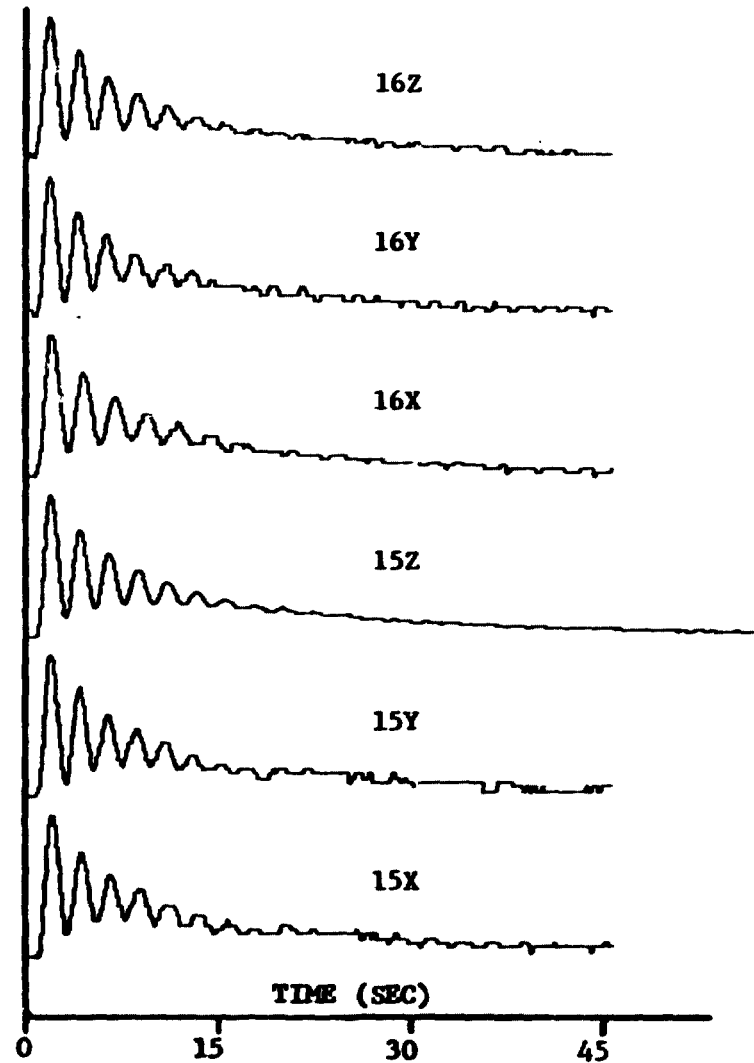
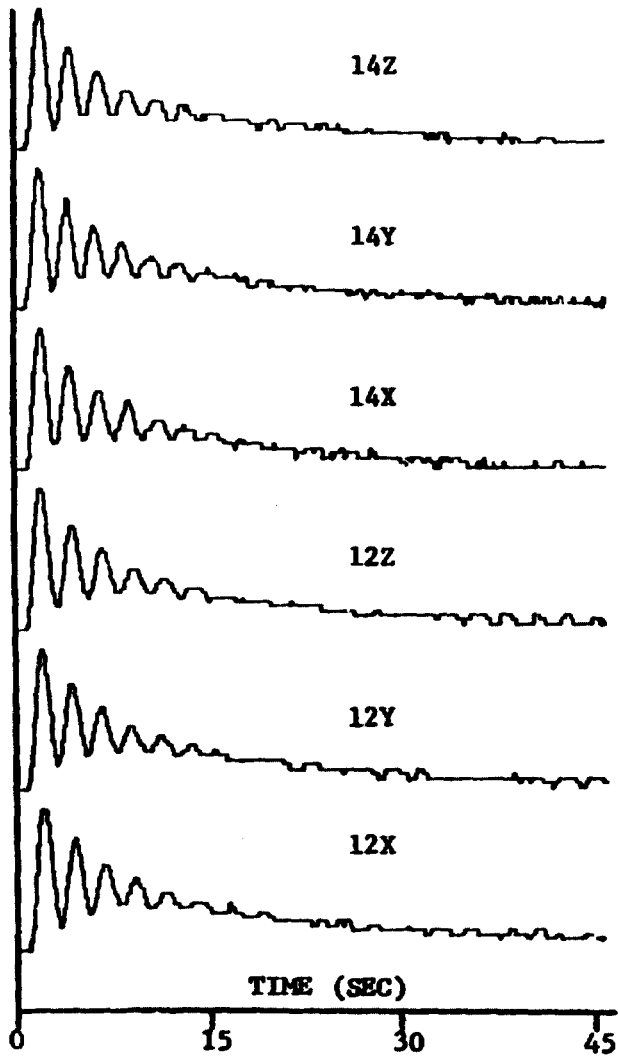


FIGURE 3.

Figure 4. Average of the positive and the sign-reversed negative calibration pulses in the flat mode. See Figure 3 for explanation; the minima are also given in Table 3.

FIGURE 4.

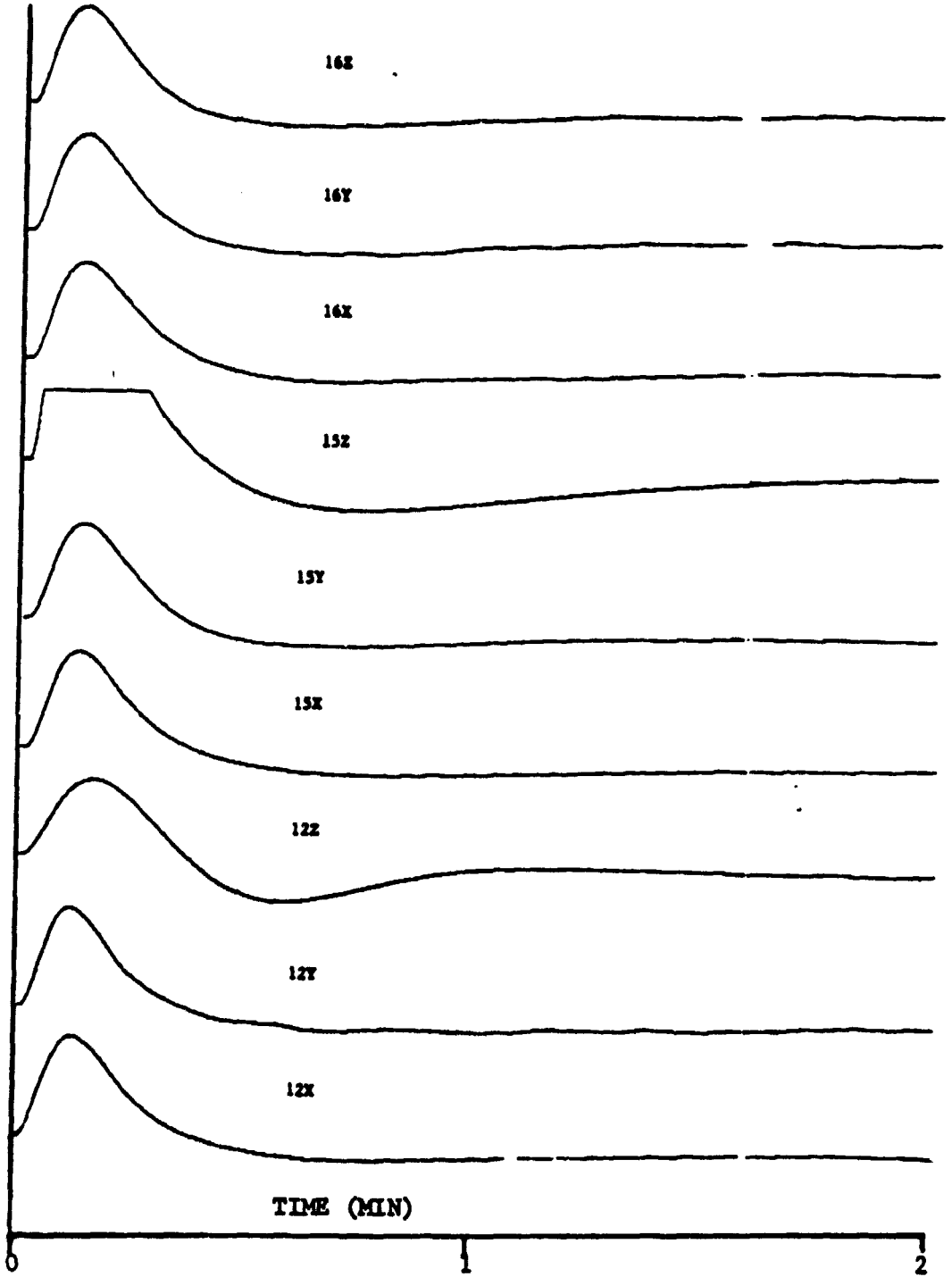


Figure 5. Schematic flow chart for calculating the seismograph parameters.

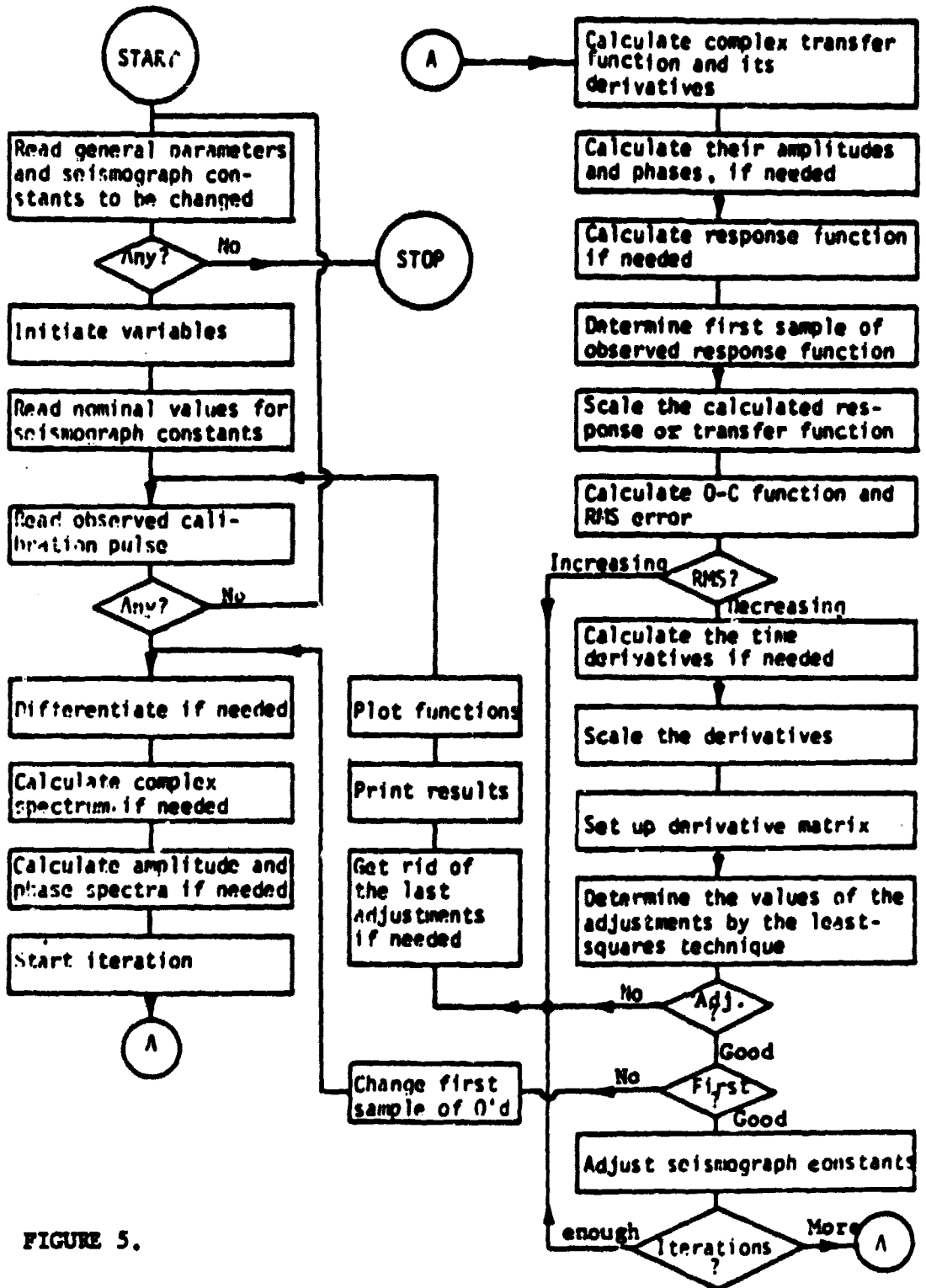


FIGURE 5.

Figure 6. Real and imaginary parts of the partial derivatives of the transfer function to a step of acceleration in the peaked mode. The parameters, a_i , and their units are listed in Table 2. The calculations were carried out with seismograph constants obtained for component 15X (see Table 4) and with $KK_1K_3=10$ DU/cm. The minima and maxima are given in $\text{DUsec}^3/\text{cm/unit}$ of each parameter.

FIGURE 6.

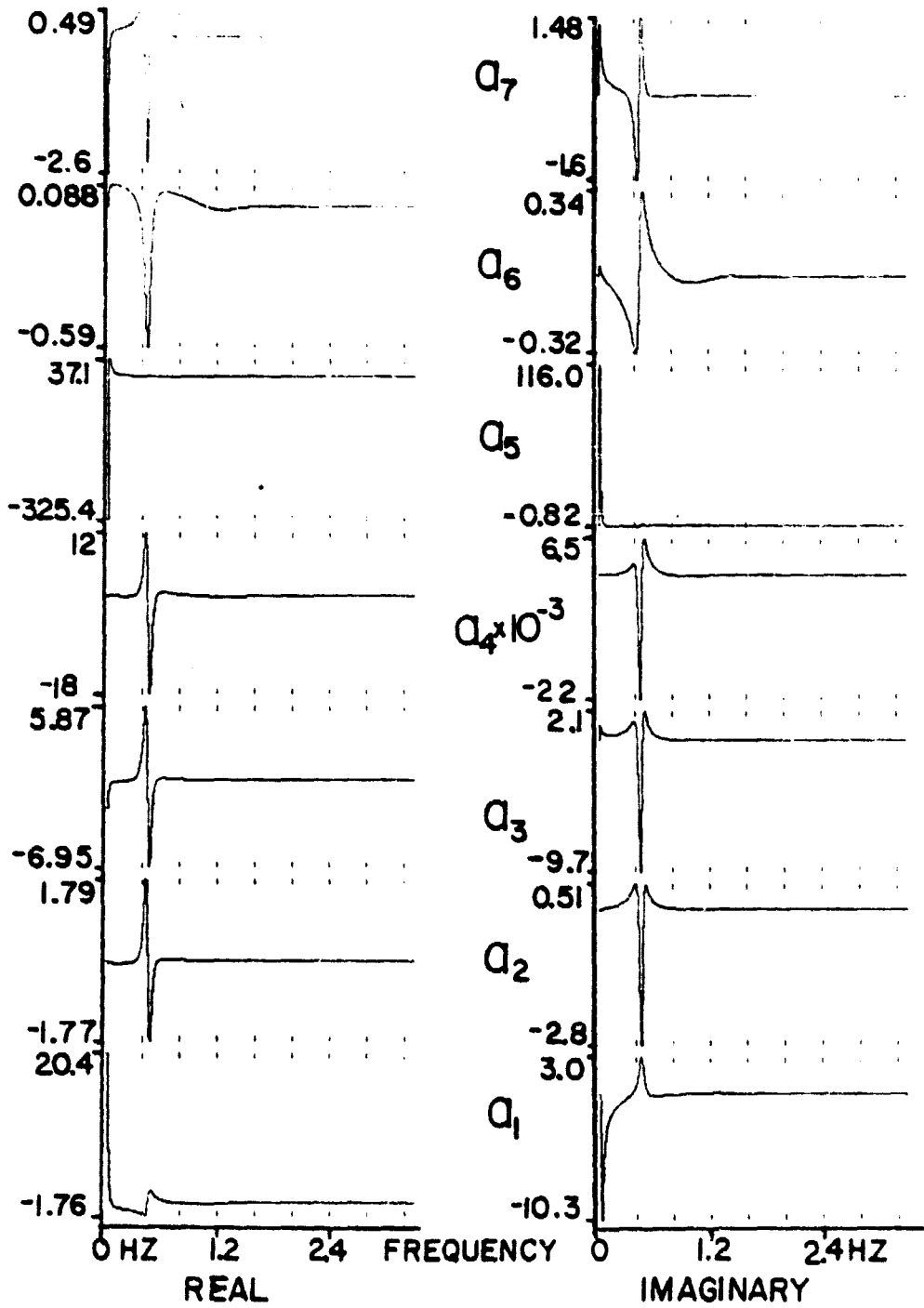


Figure 7. Real and imaginary parts of the partial derivatives of the transfer function to a step of acceleration in the flat mode. See Figure 6 for explanation.

FIGURE 7.

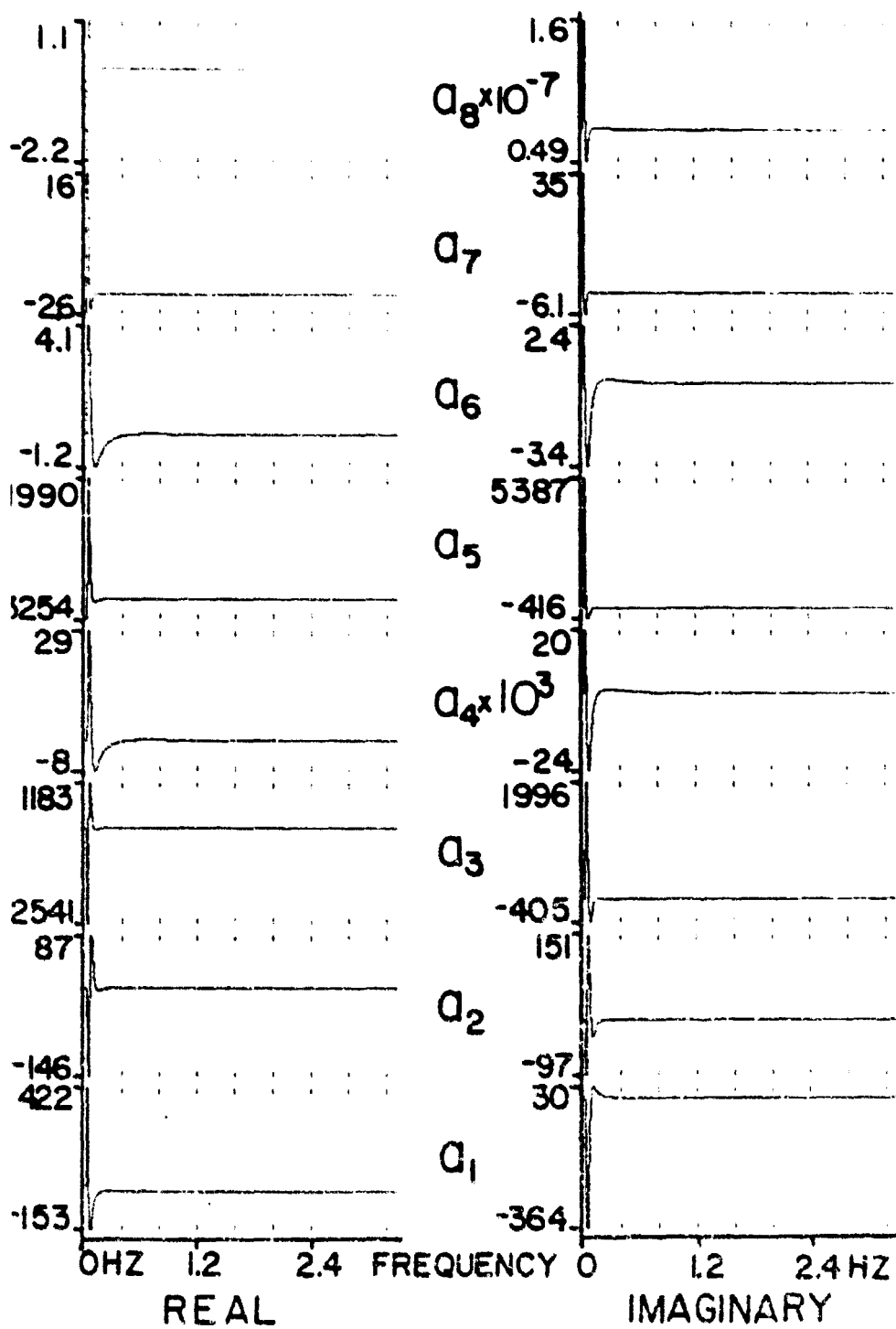


Figure 8. Partial derivatives of the response to a step of acceleration in the peaked mode. See Figure 6 for explanation. The minima and maxima are given in $\text{DUsec}^2/\text{cm/unit}$ of each parameter.

FIGURE 8.

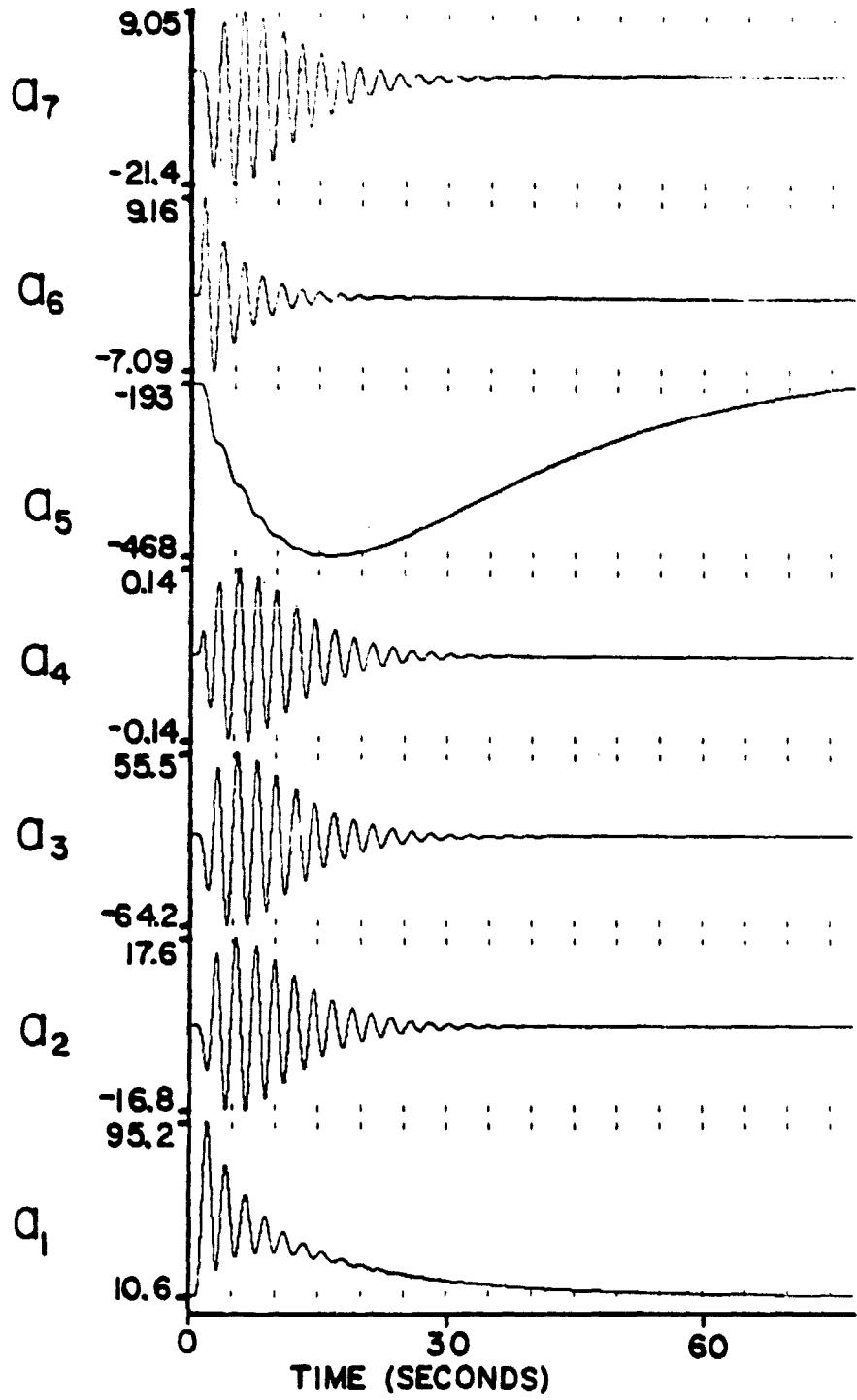


Figure 9. Partial derivatives of the response to a step of acceleration in the flat mode. See Figure 8 for explanation.

FIGURE 9.

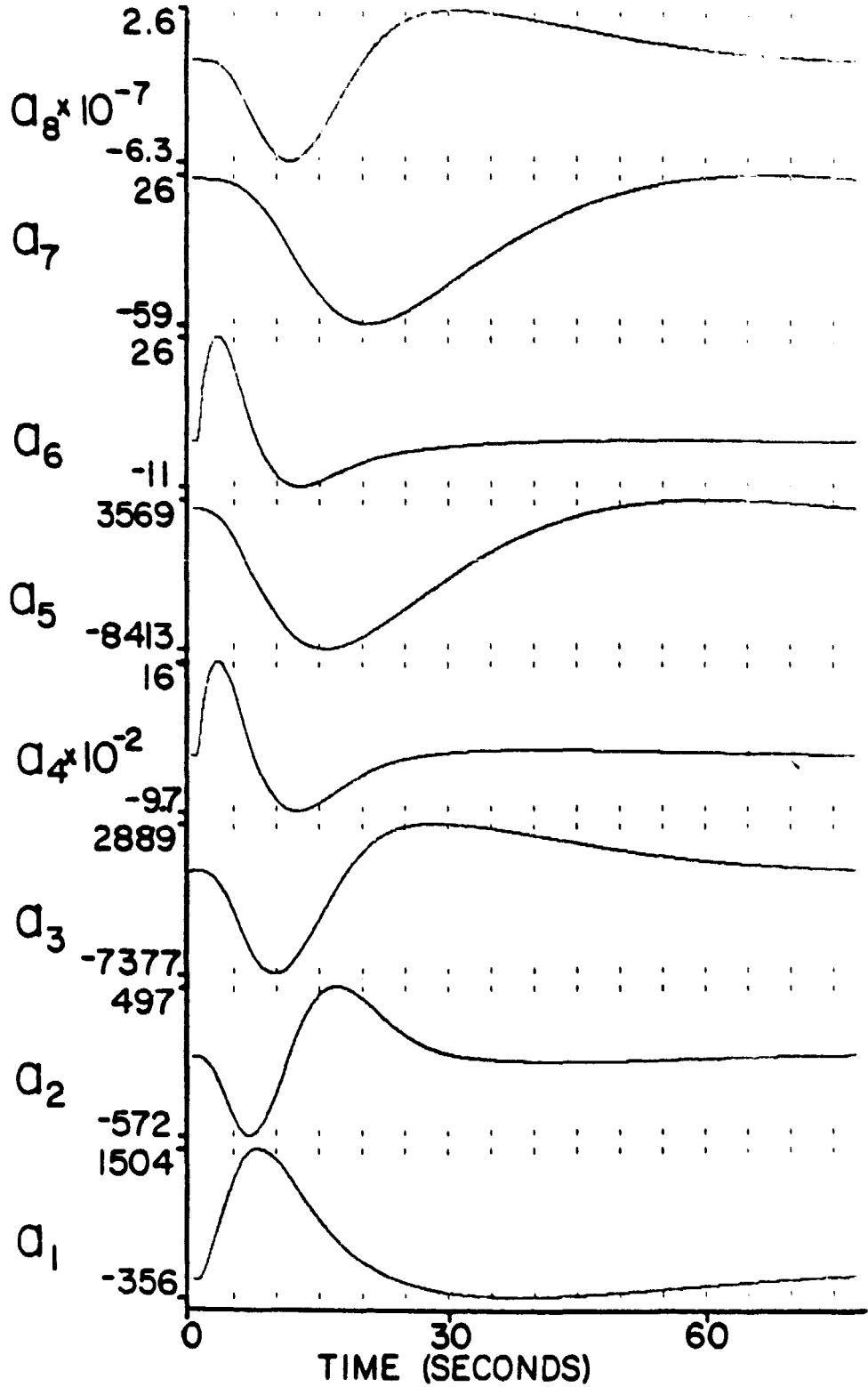


Figure 10. Partial derivatives of the amplitude and phase response to a step of acceleration in the peaked mode. See Figure 6 for explanation. The minima and maxima are given in $\text{DUsec}^3\text{cm/unit}$ of each parameter for the amplitude spectra and in radian/unit of each parameter for the phase spectra.

FIGURE 10.

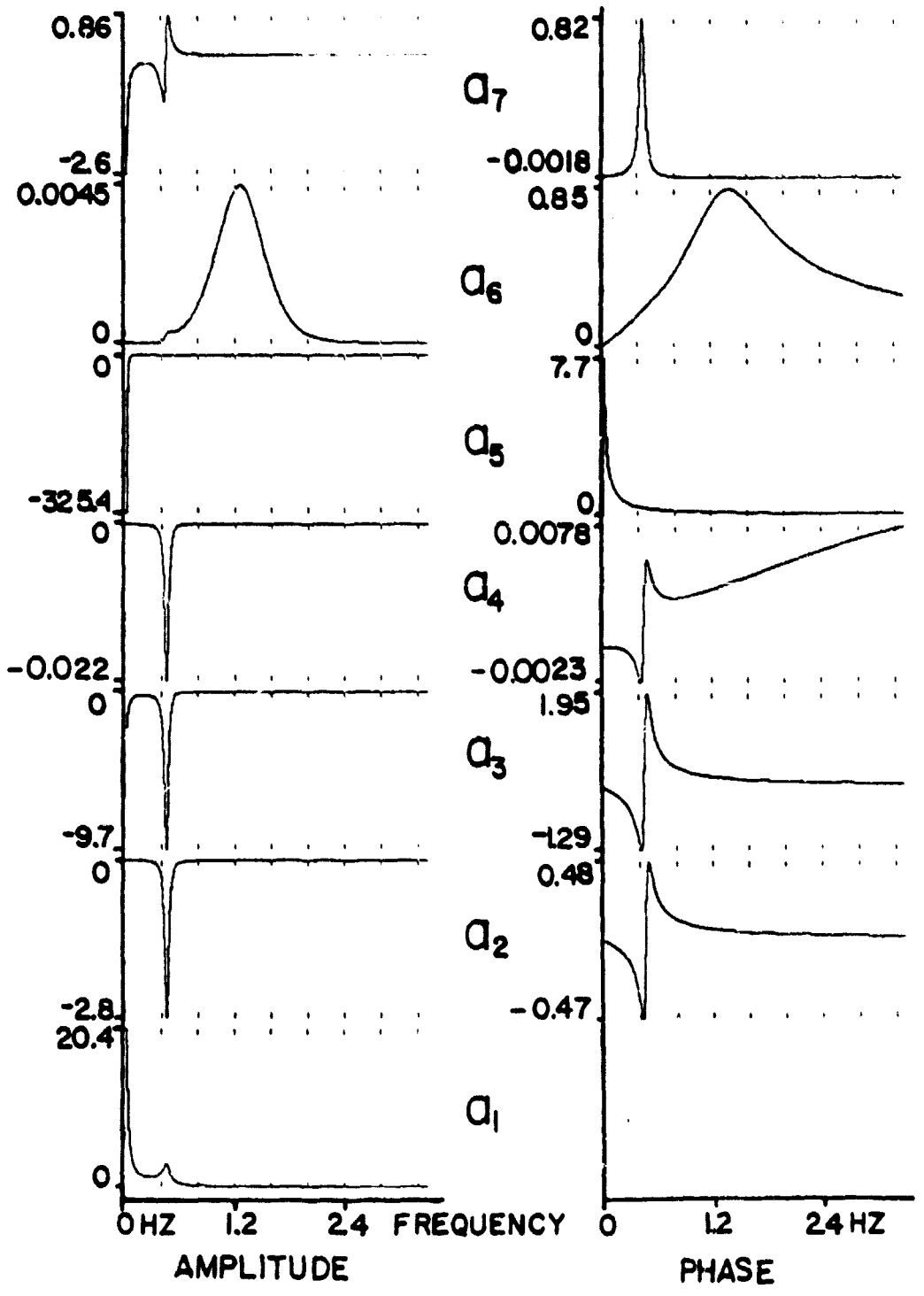


Figure 11. Partial derivatives of the amplitude and phase responses to a step of acceleration in the flat mode. See Figure 10 for explanation.

FIGURE 11.

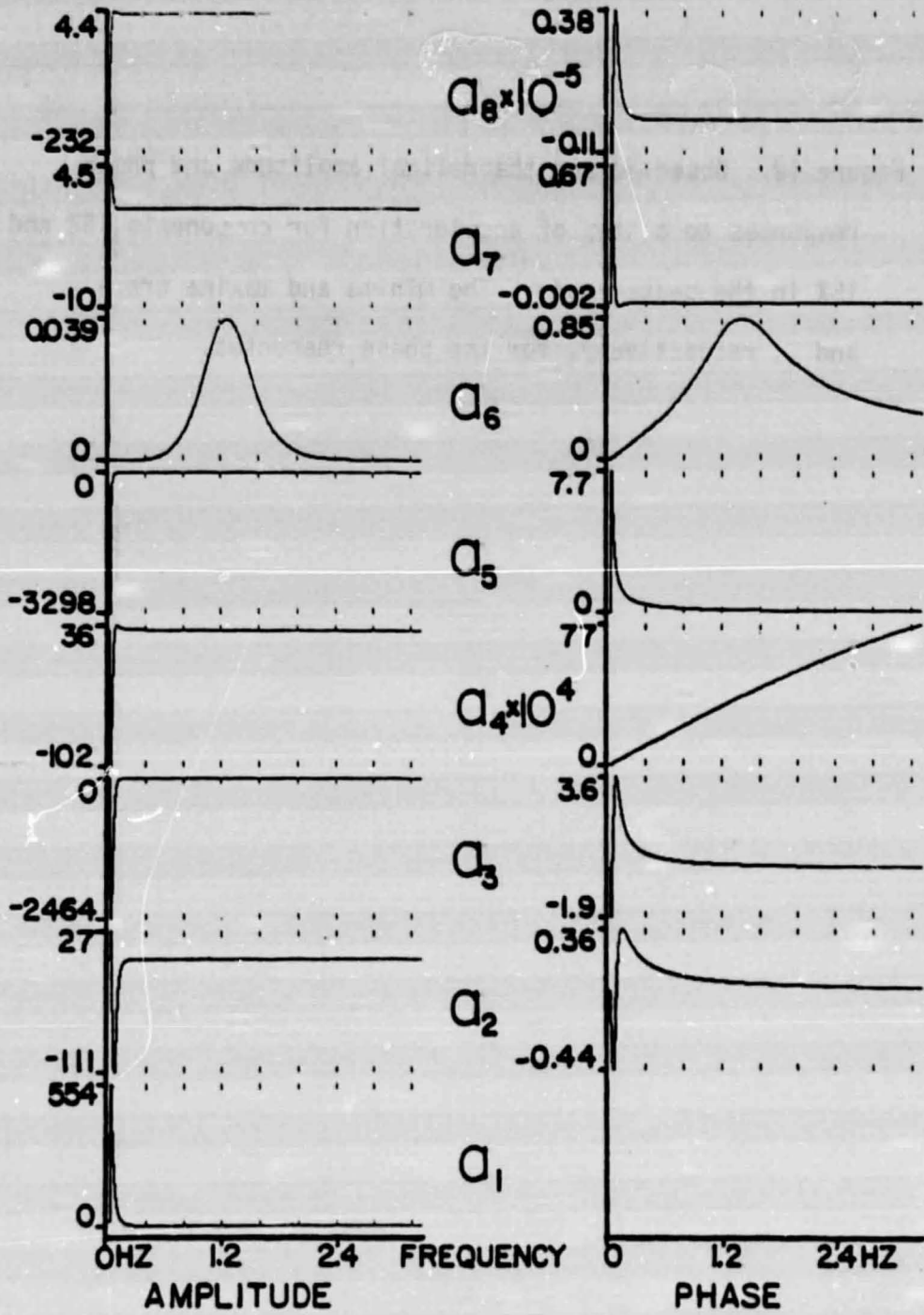


Figure 12. Observed and theoretical amplitude and phase responses to a step of acceleration for components 15Z and 15X in the peaked mode. The minima and maxima are - and , respectively, for the phase responses.

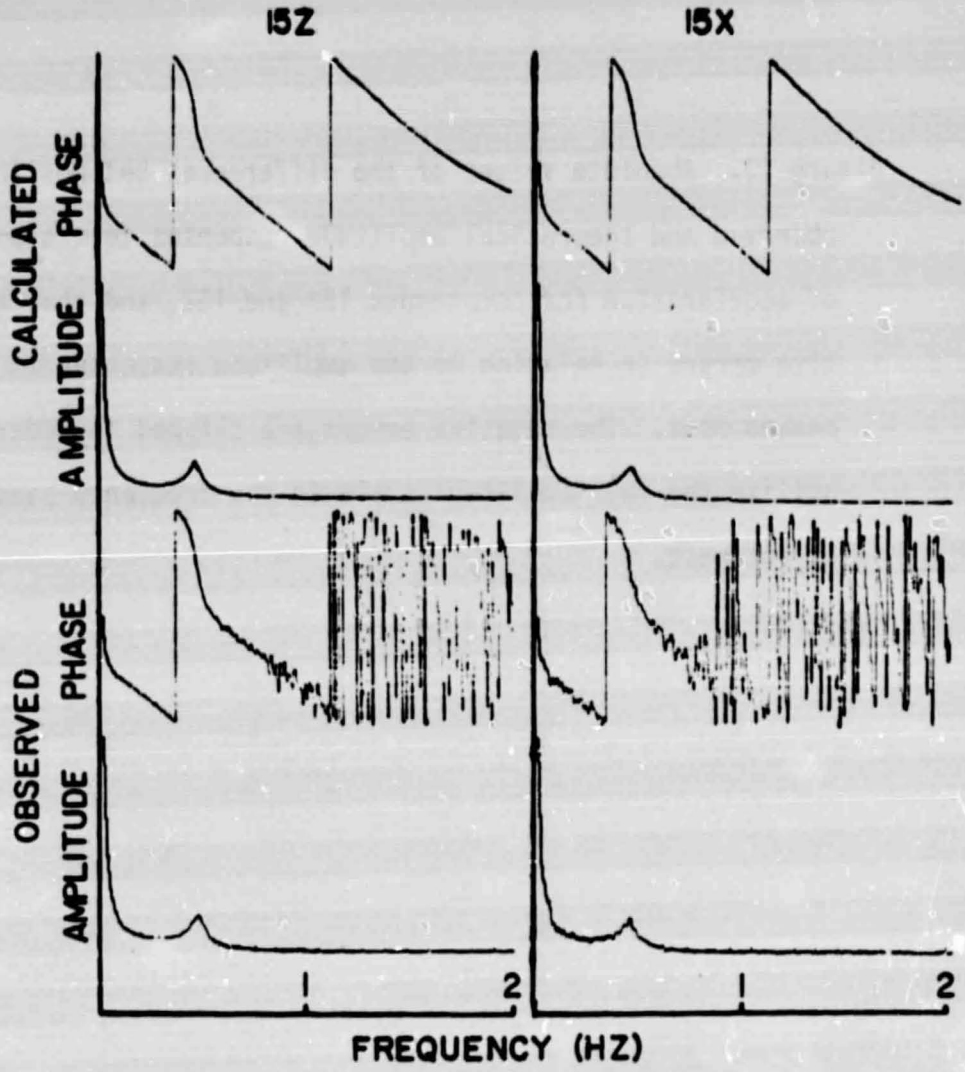


FIGURE 12.

Figure 13. Absolute values of the differences between the observed and theoretical amplitude responses to a step of acceleration for components 15X and 15Z, and the relative errors in relation to the amplitude responses in the peaked mode. The relative errors are clipped in order to utilize the full amplitude scale in the frequency band of interest.

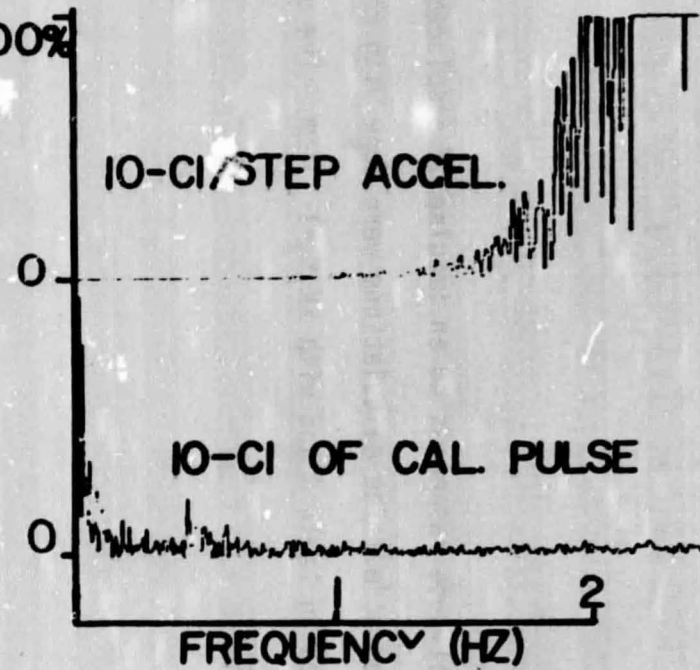
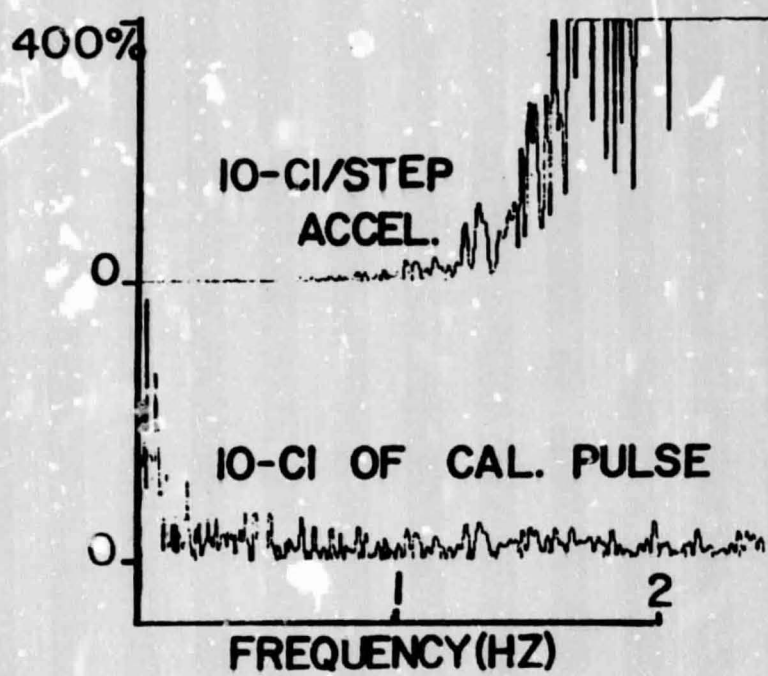


FIGURE 13.

Figure 14. Amplitude responses to an impulse of displacement in the peaked mode. The calculations were done with constants listed in Table 4 and with $KK_1K_3=1$ DU/cm. The units are DUsec/cm.

AMPLITUDE RESPONSES

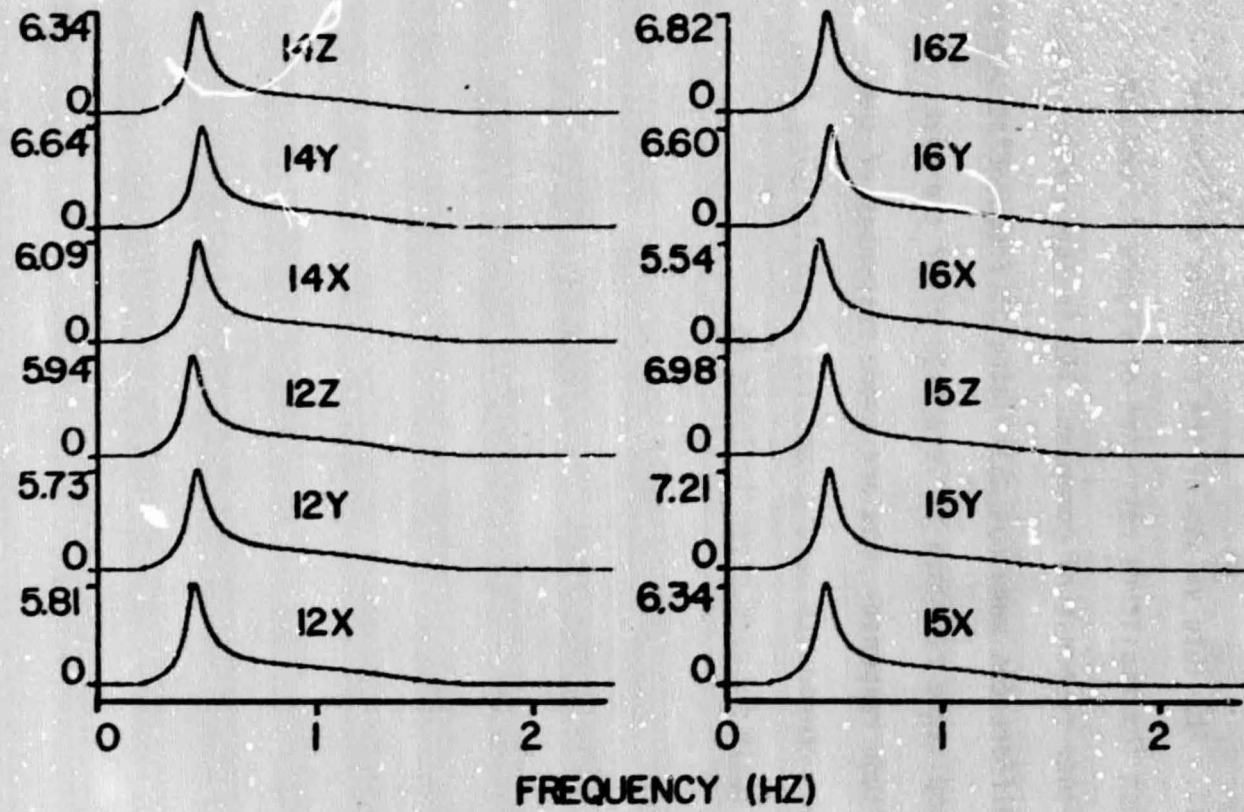


FIGURE 14.

Figure 15. Absolute values of the relative differences between the amplitude responses of Figure 12 and the amplitude response of component 15Z in the peaked mode. The differences were not calculated at frequencies where the amplitude response is less than 3% of the peak amplitude response. The amplitude responses of the various components were normalized by multiplying them with scale factors given in Table 6.

DEVIATION IN AMPLITUDE RESPONSE RELATIVE TO 15Z
(PEAKED MODE)

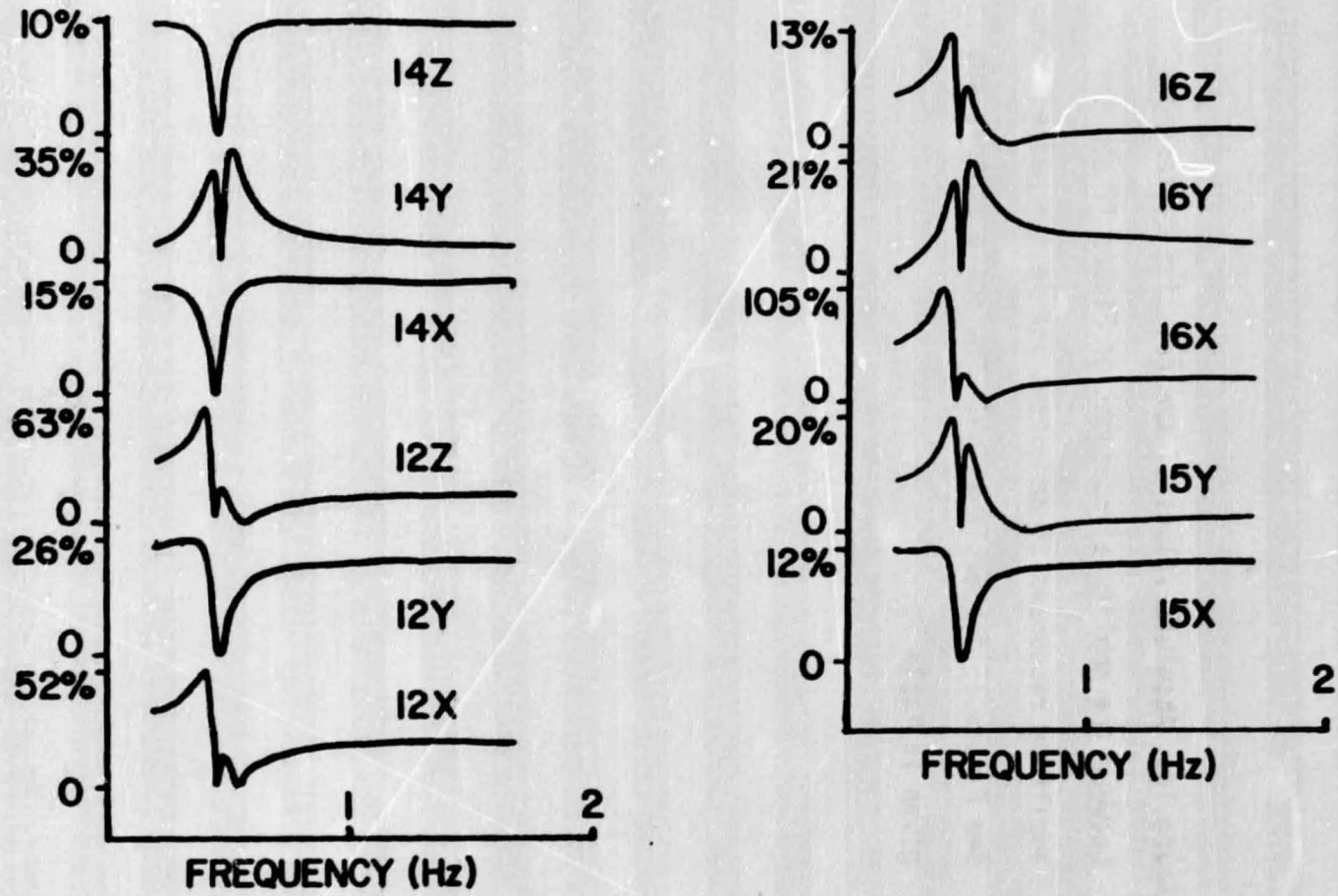


FIGURE 15.

Figure 16. Absolute values of the relative differences between the amplitude responses of Figure 12 and the amplitude responses of component 15X in the peaked mode. See Figure 15 for explanation. The scale factors are given in Table 7.



DEVIATION IN AMPLITUDE RESPONSE RELATIVE TO 15X
(PEAKED MODE)

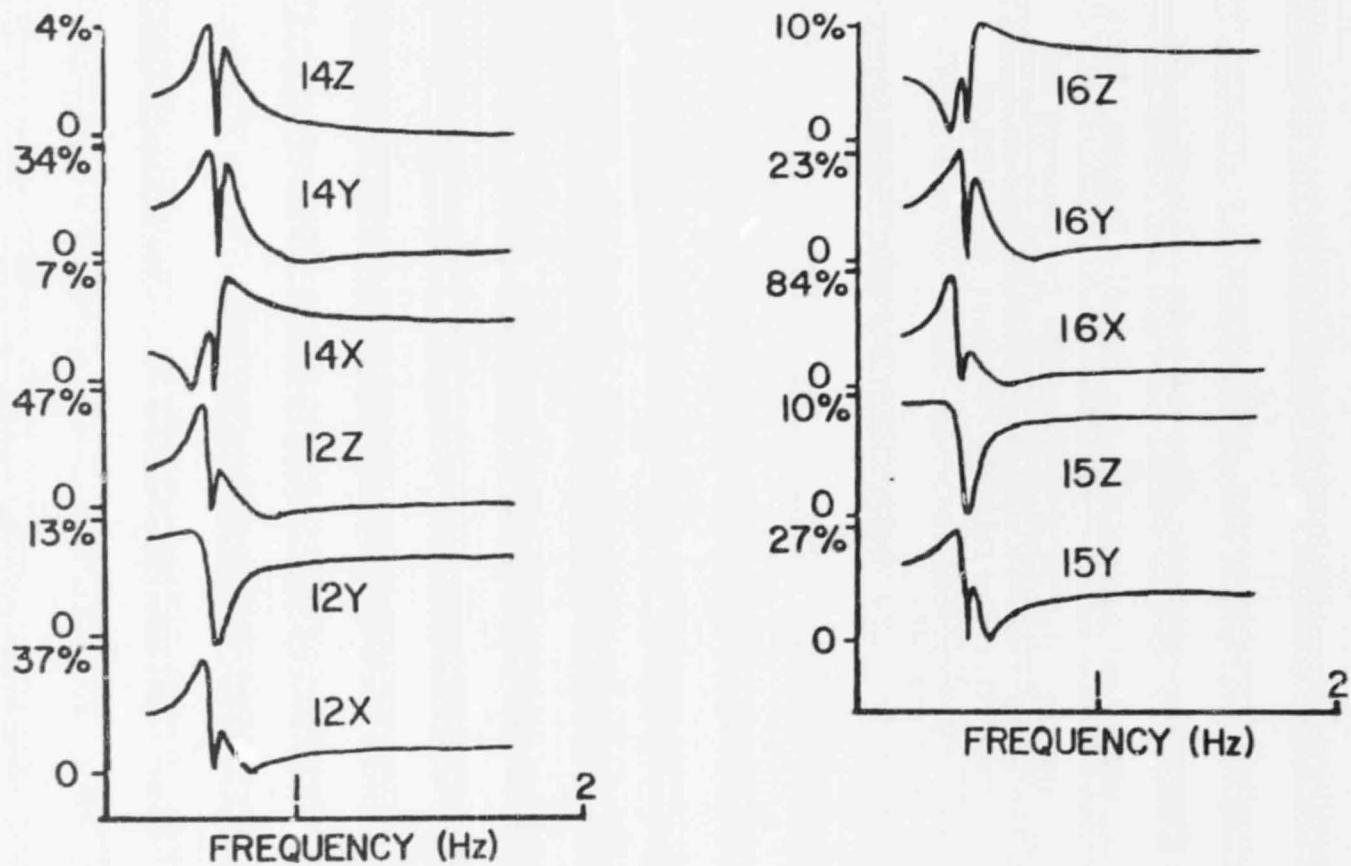


FIGURE 16.

Figure 17. Schematic flow chart for calculating the waterlevel parameters, the reliable frequency bands, and the relative errors between the observed and theoretically amplitude responses to a step of acceleration.

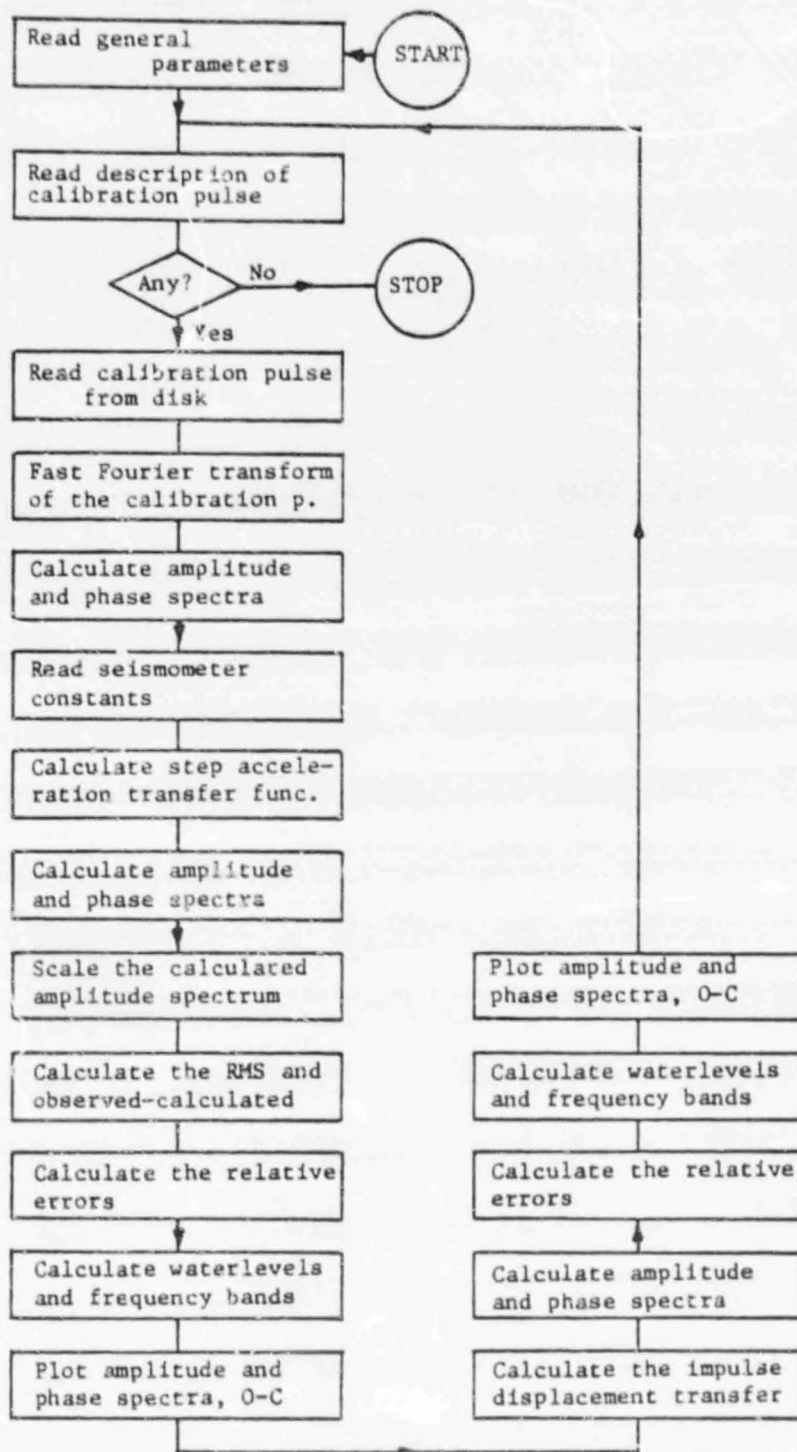


FIGURE 17.

Figure 18. Schematic flow chart for calculating the transfer functions of the seismographs and for adjusting the transfer functions with a given waterlevel parameter.

Figure 19. Schematic flow chart for performing wavelet deconvolution by spectral division.

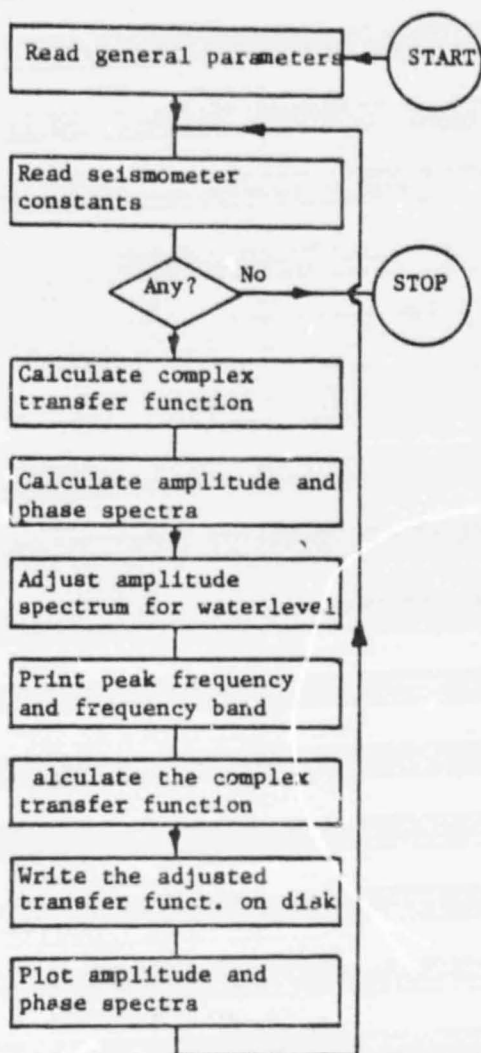


FIGURE 18.

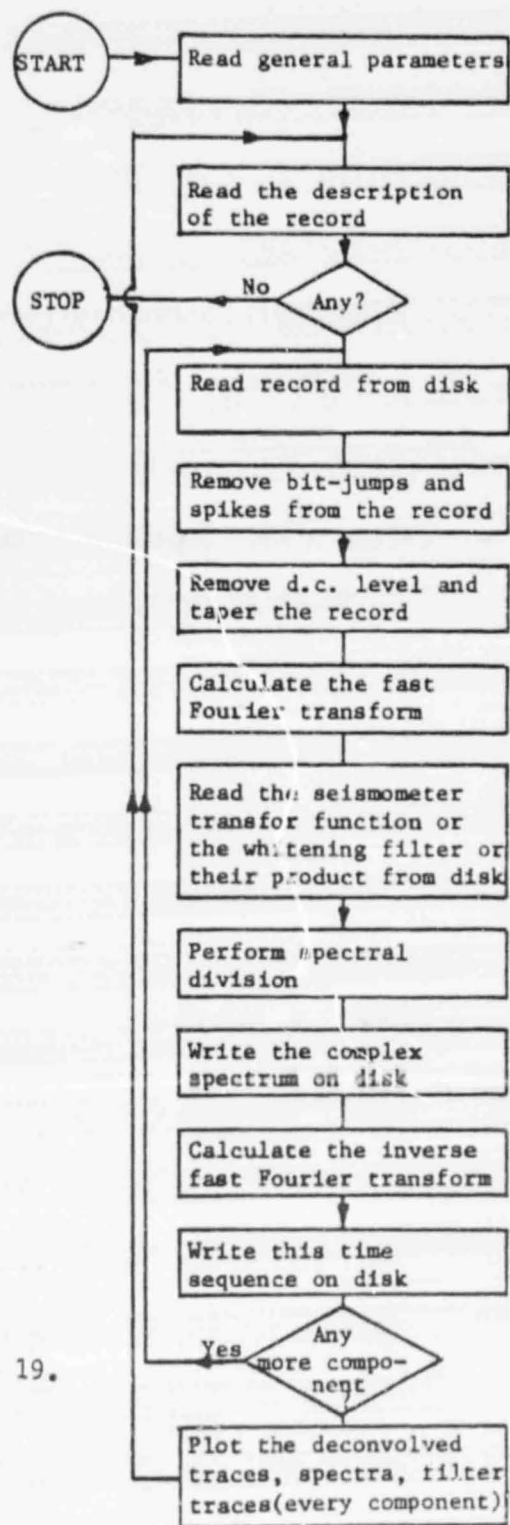


FIGURE 19.

Figure 20. Schematic flow chart for stacking the amplitude spectra of the seismic records corrected for instrumental response in the peaked mode.

Figure 21. Schematic flow chart for calculating the total transfer function of the instrumental and near-surface effects.

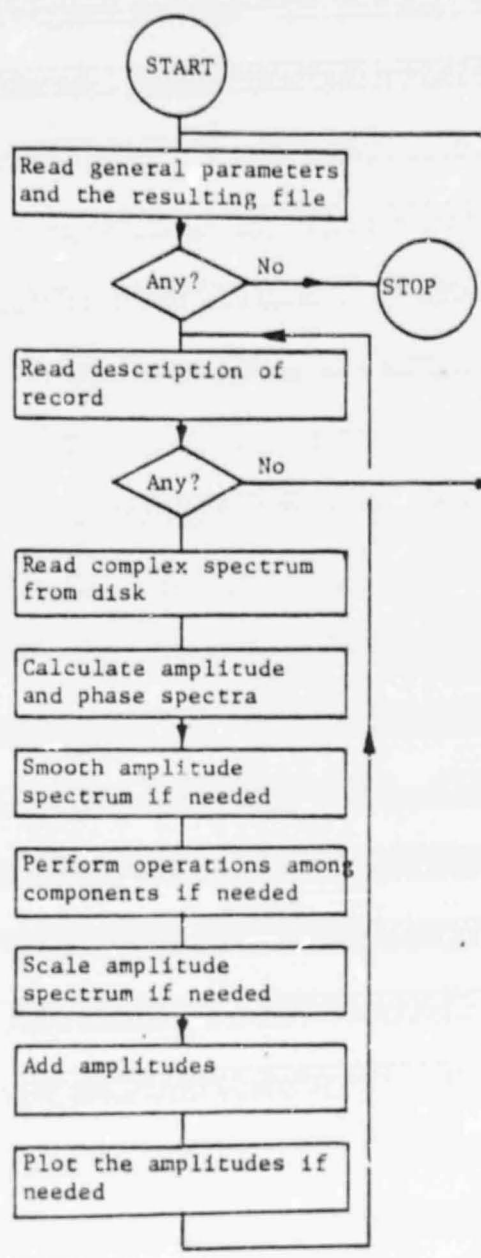


FIGURE 20.

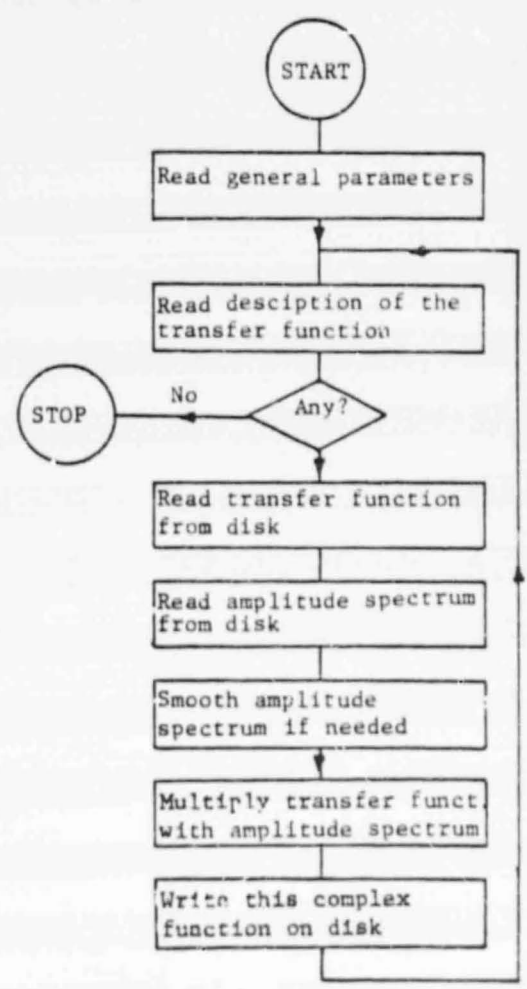
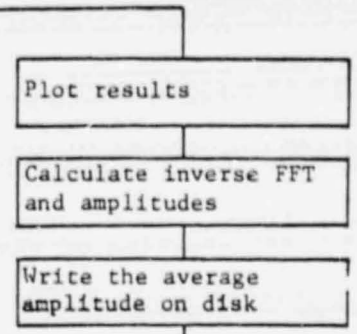


FIGURE 22.

Figure 22. Illustration of the noise of the analog-to-digital converter at station 14.

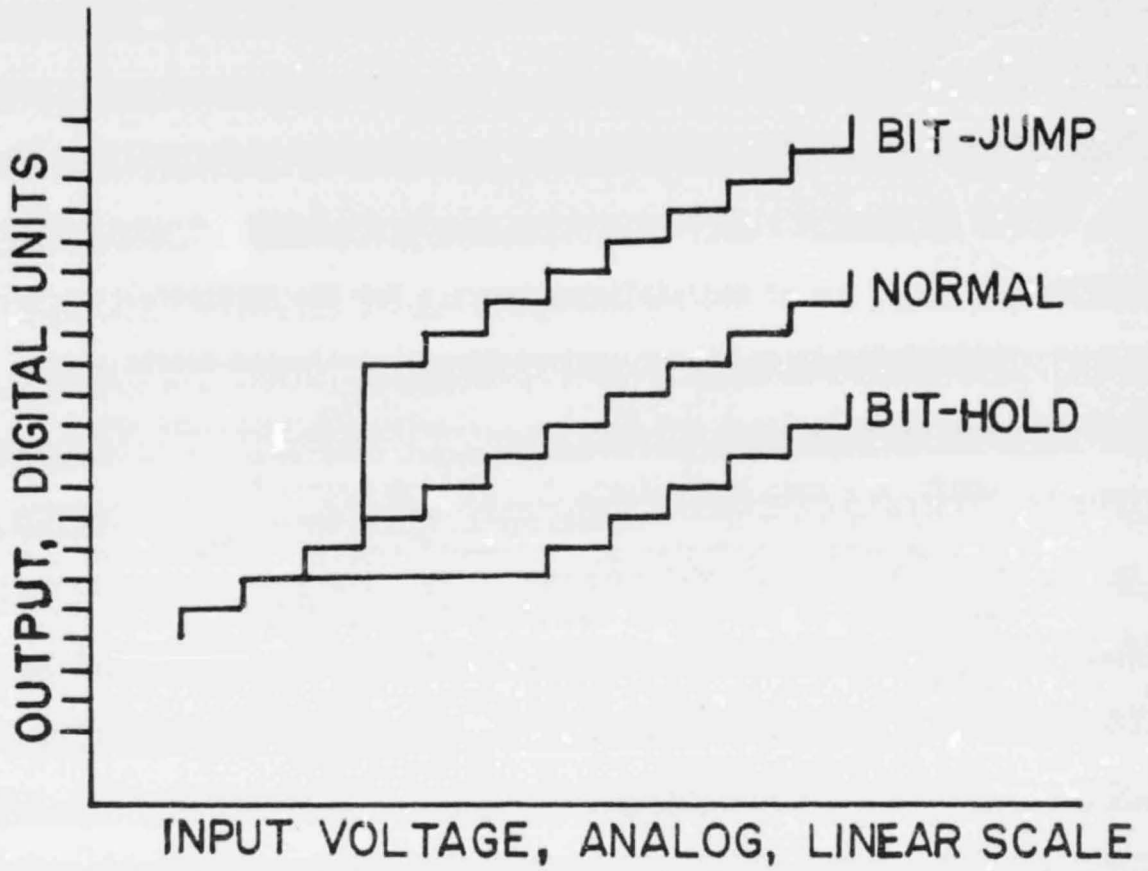


FIGURE 22.

Figure 23. Sum of the amplitude spectra for the horizontal components (X and Y) of station 12. The selected events are listed in Tables 8 and 9. The following abbreviations are used: A - deep moonquakes, H - shallow moonquakes, C - impacts (artificial and meteoroid impacts). The minima and maxima of the curves are given in parantheses. Units are DUsec.

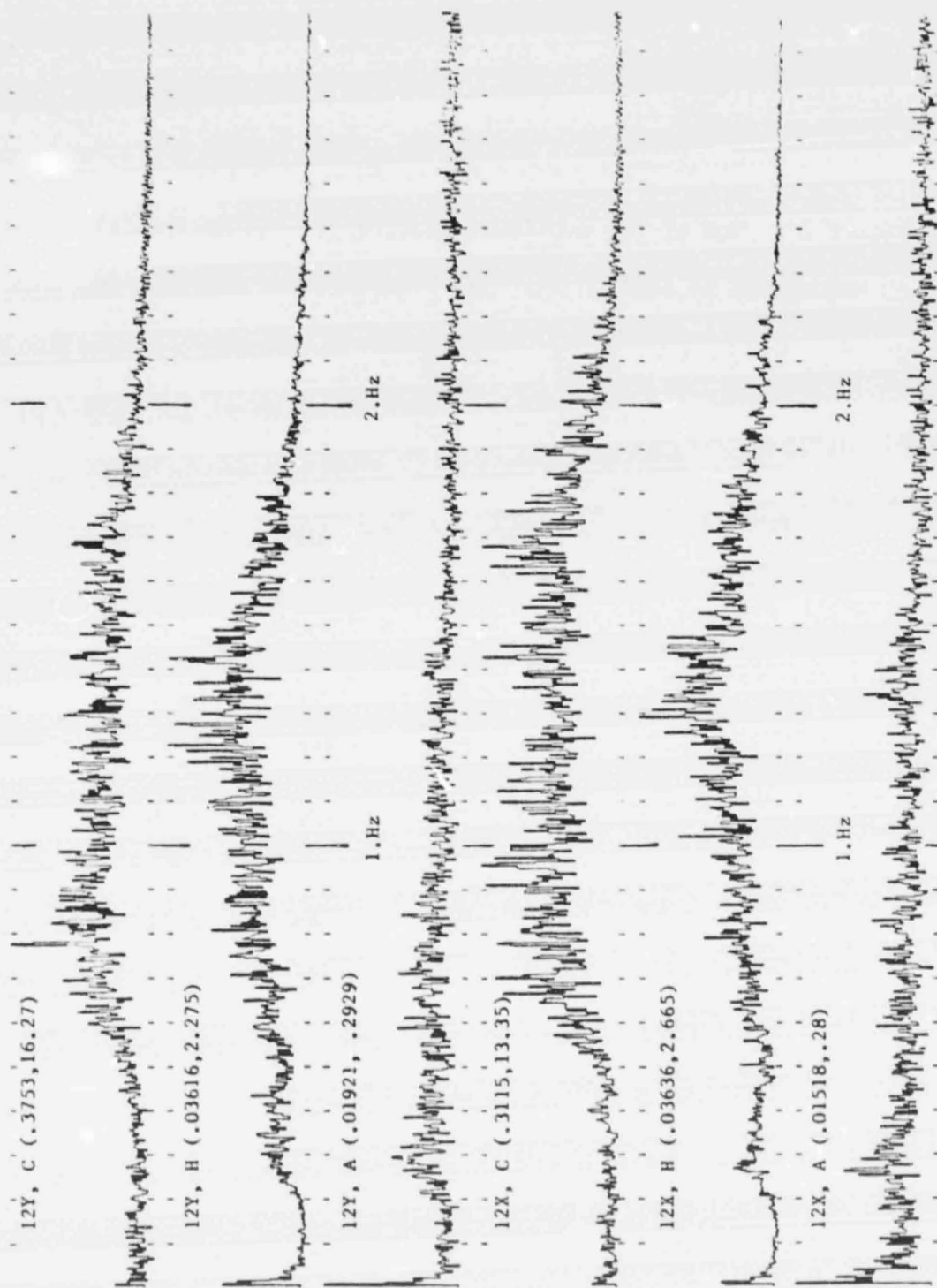


FIGURE 23.

Figure 24. Sum of the amplitude spectra for the horizontal components of station 14. See Figure 23 for explanation.

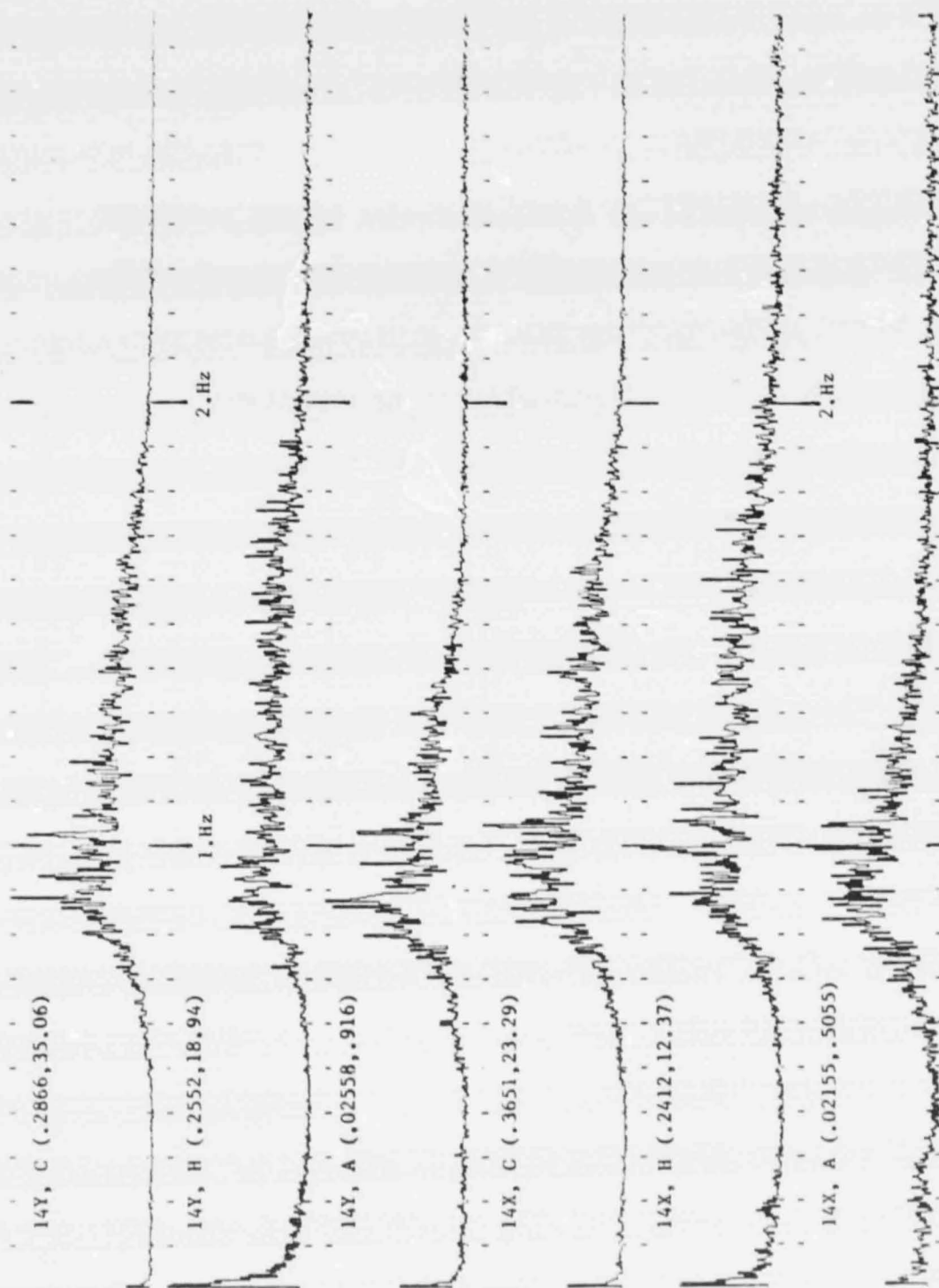


FIGURE 24.

Figure 25. Sum of the amplitude spectra for the horizontal components of station 15. See Figure 23 for explanation.

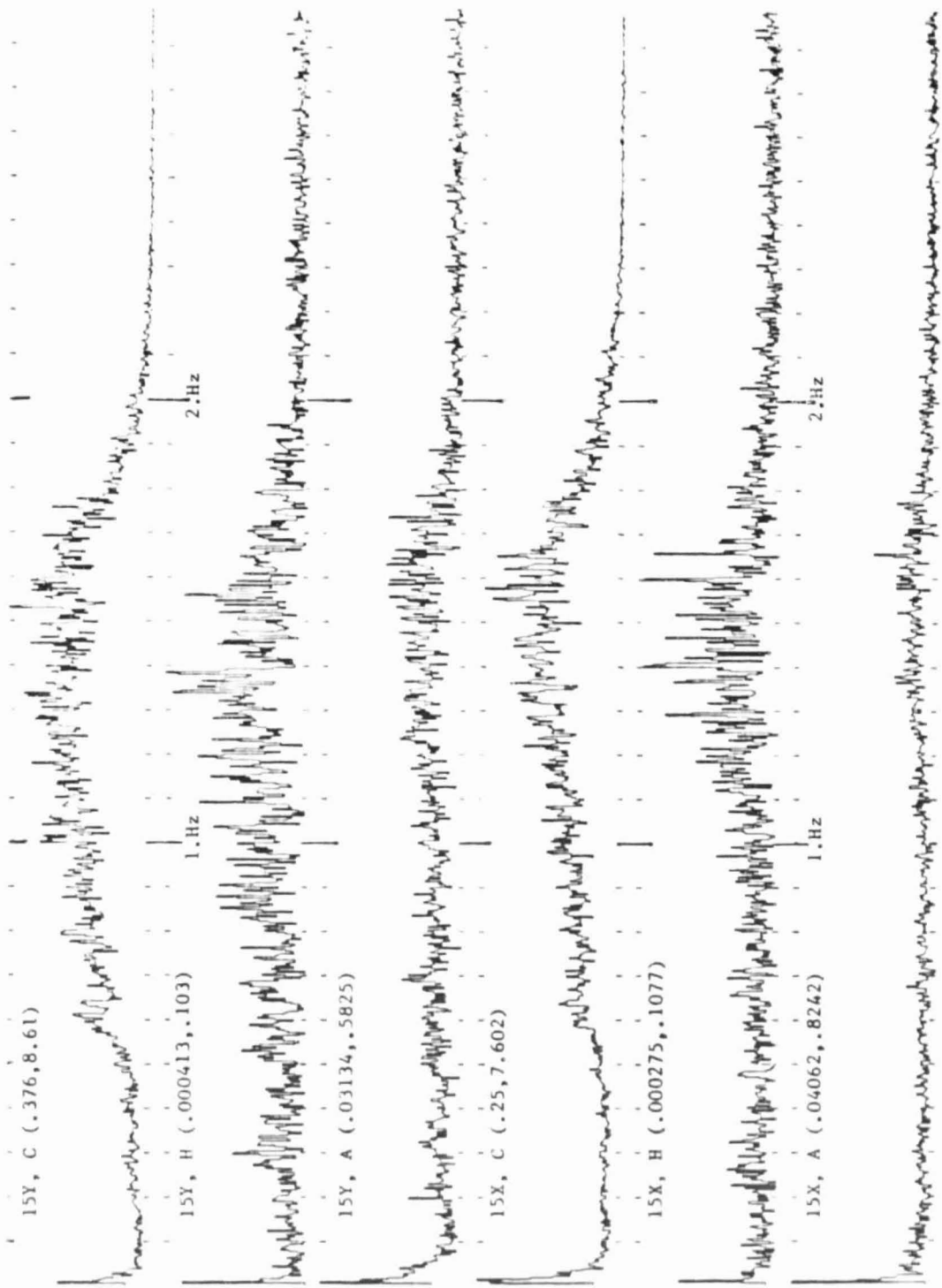


FIGURE 25.

Figure 26. Sum of the amplitude spectra for the horizontal components of station 16. See Figure 23 for explanation.

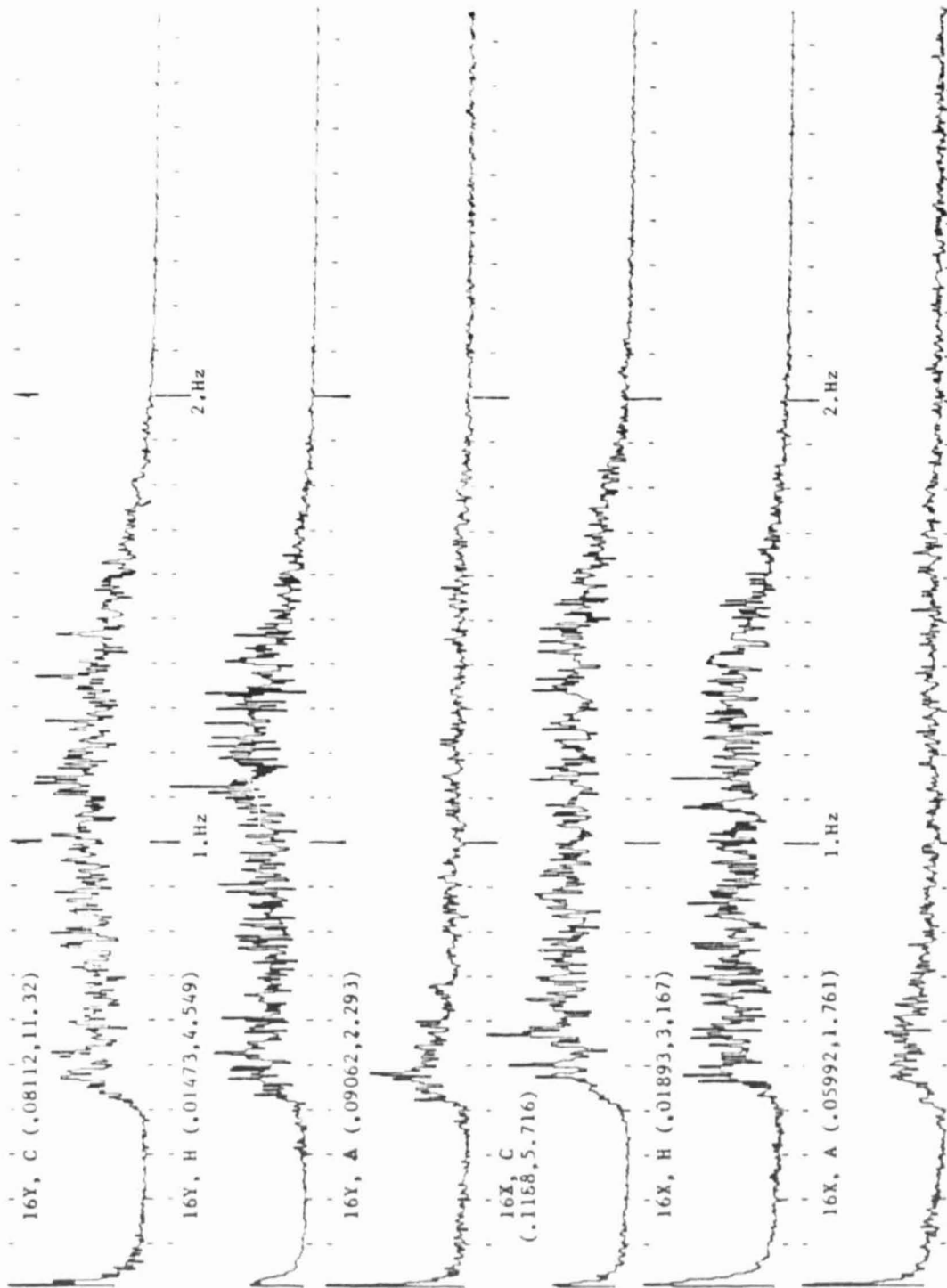


FIGURE 26.

Figure 27. Sum of the amplitude spectra for the vertical components (Z) of stations 12 and 14. See Figure 23 for explanation.

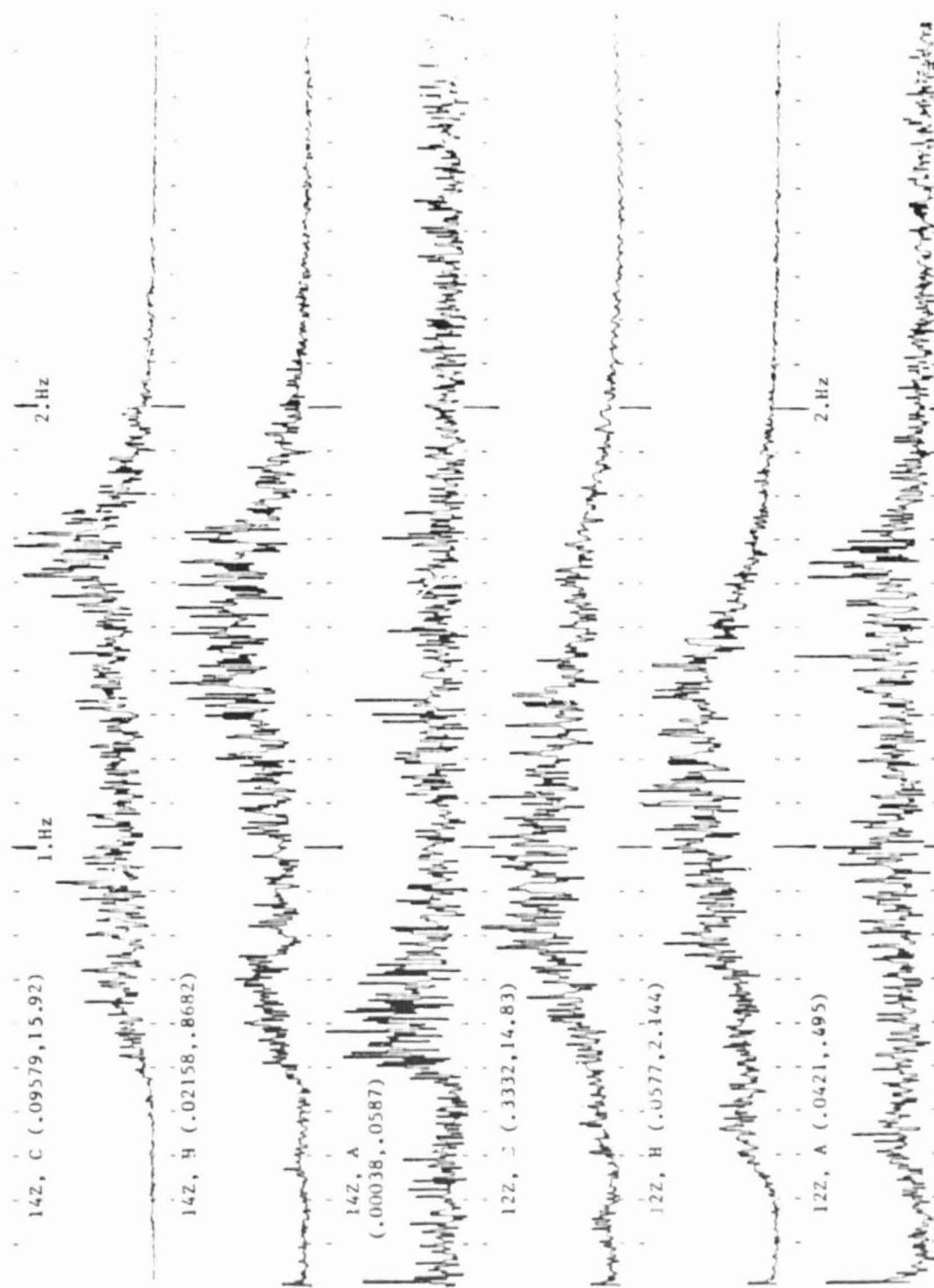


FIGURE 27.

Figure 28. Sum of the amplitude spectra for the vertical components of stations 15 and 16. See Figure 23 for explanation.

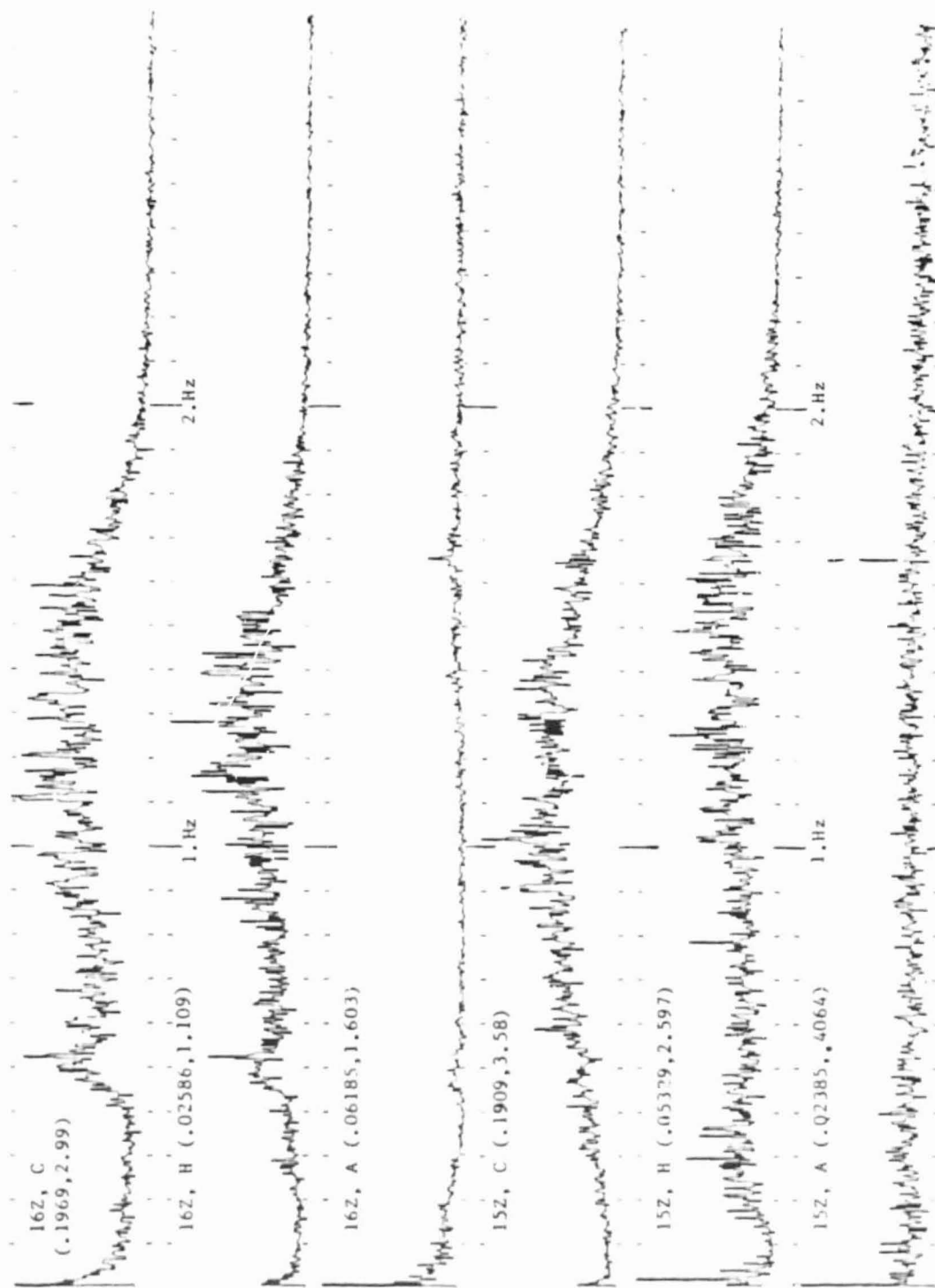


FIGURE 28.

Figure 29. Sum of the amplitude spectra for station 12. HOR is the horizontal component calculated with equation (28). The amplitudes are smoothed with moving averages in a rectangular window of 0.055 Hz.

AMPLITUDE SPECTRA AT STATION I2

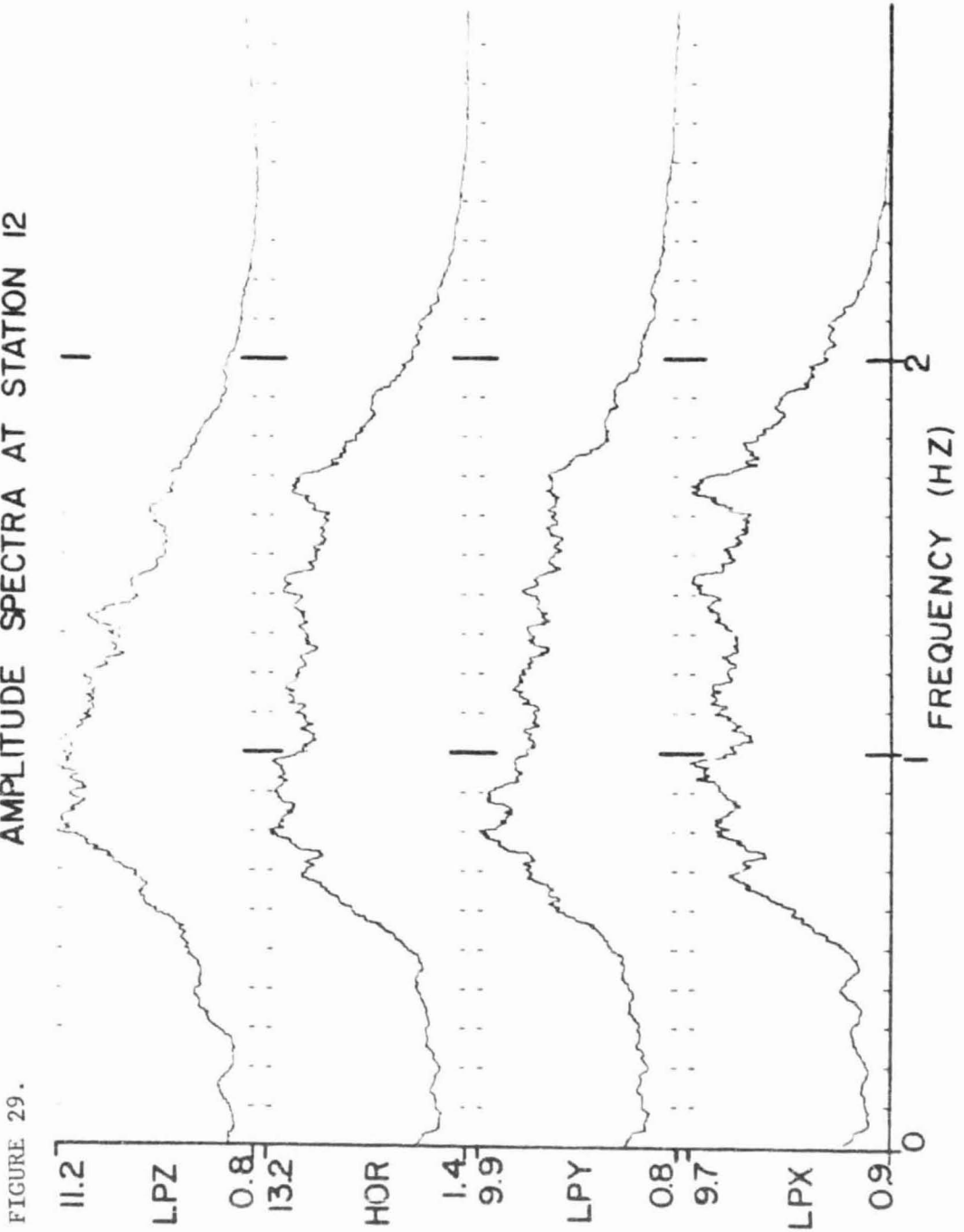


FIGURE 29.

Figure 30. Sum of the amplitude spectra for station 14. See
Figure 29 for explanation.

FIGURE 30. AMPLITUDE SPECTRA AT STATION 14

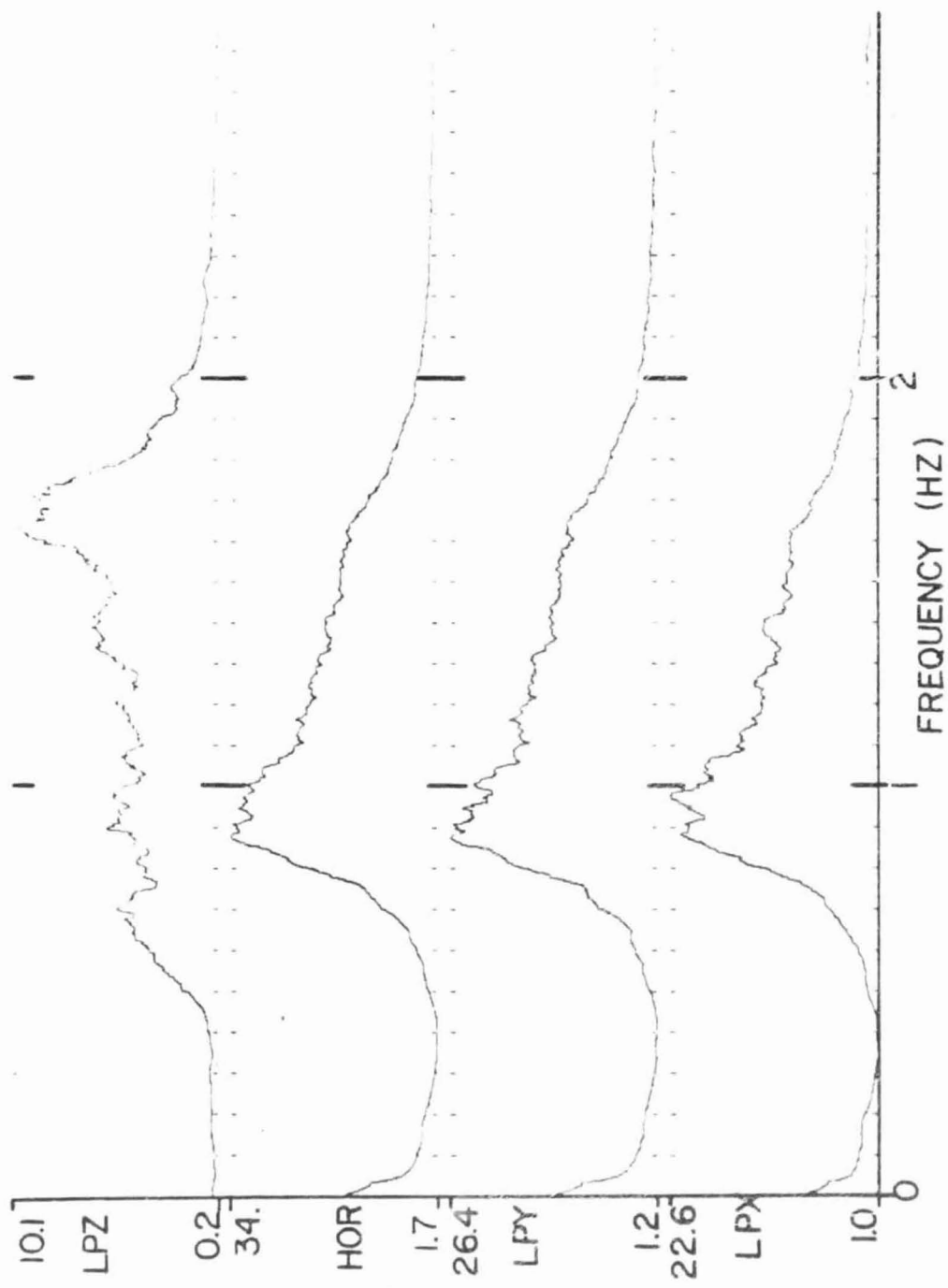


Figure 31. Sum of the amplitude spectra for station 15. See Figure 29 for explanation.

FIGURE 31.

AMPLITUDE SPECTRA AT STATION 15

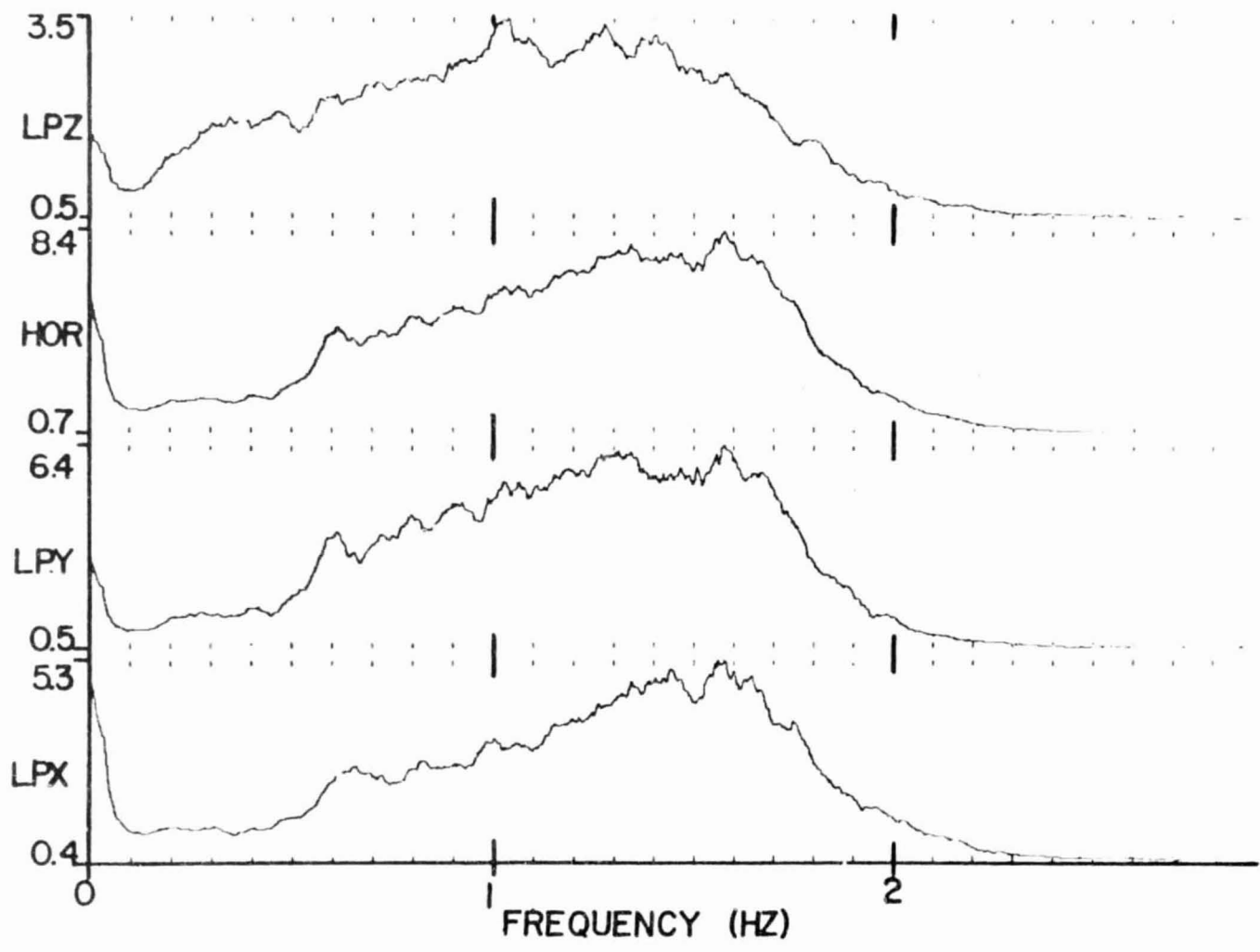


Figure 32. Sum of the amplitude spectra for station 16. See Figure 29 for explanation.

FIGURE 32.

AMPLITUDE SPECTRA AT STATION 16

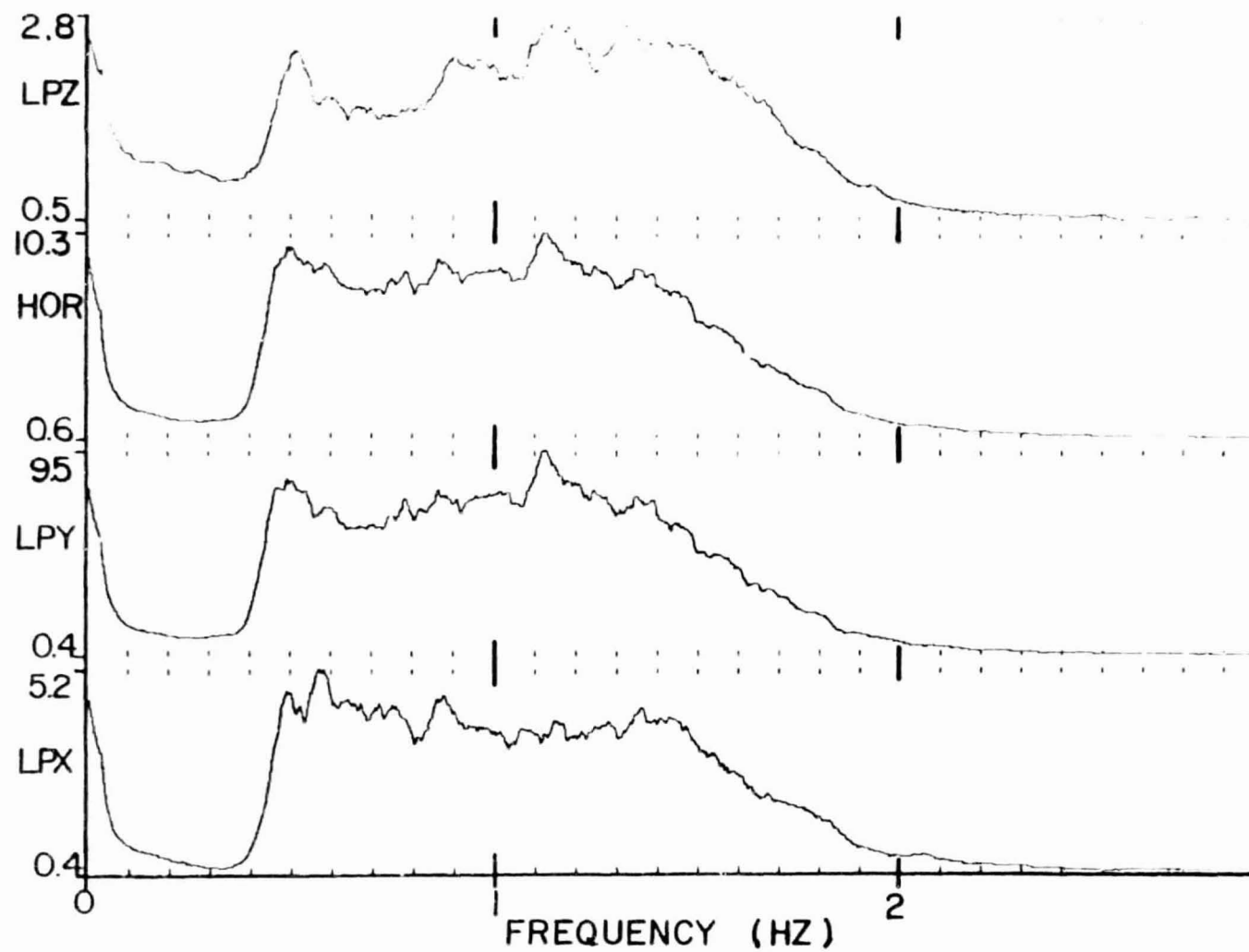


Figure 33. Two examples for instrumental and whitening deconvolution. The P wave arrival times at which the records are aligned are given in Table 19.

FIGURE 33.

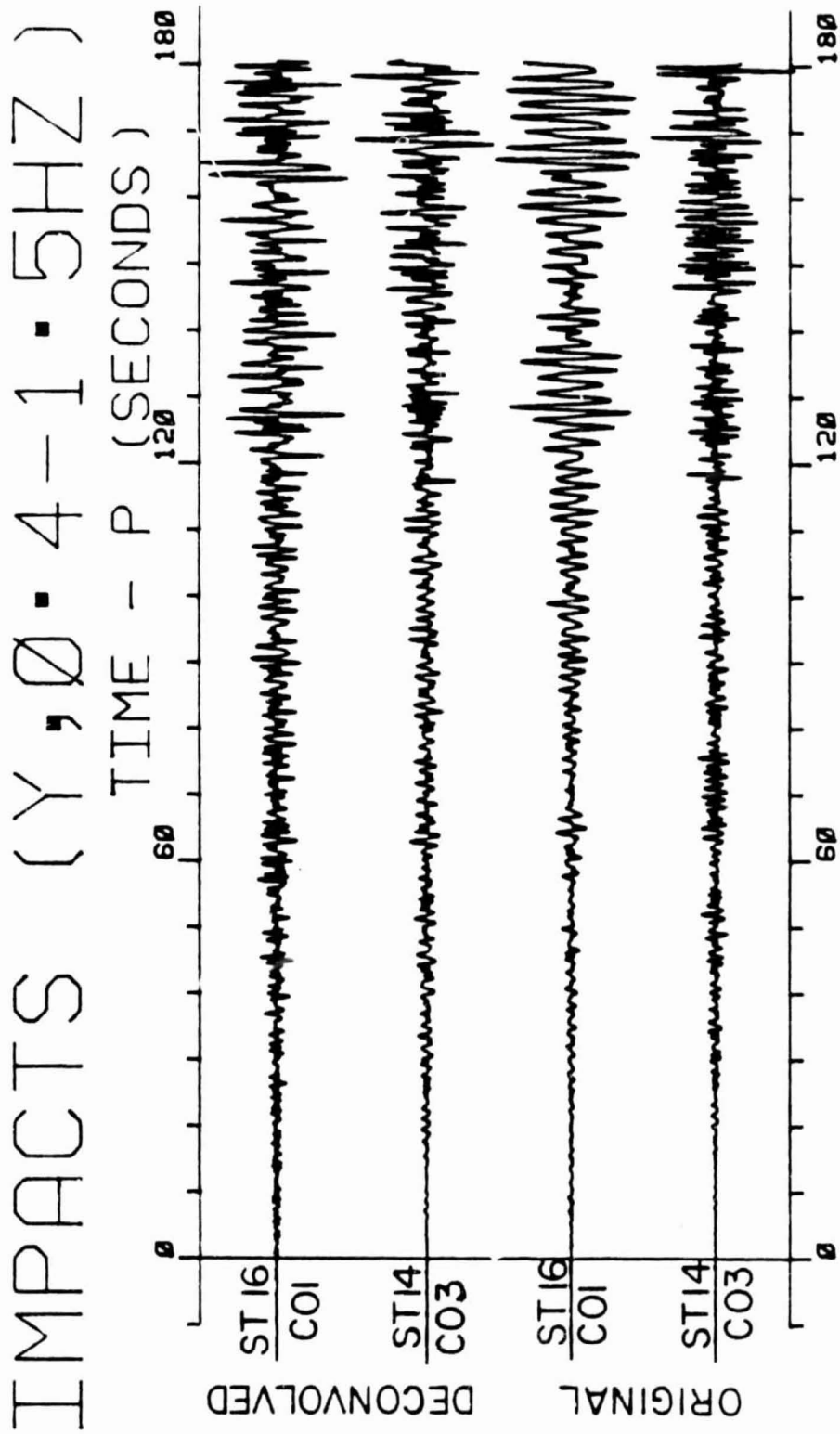


Figure 34. Ratio of the average horizontal spectral amplitudes
(X to Y). See Figure 29 for explanation.

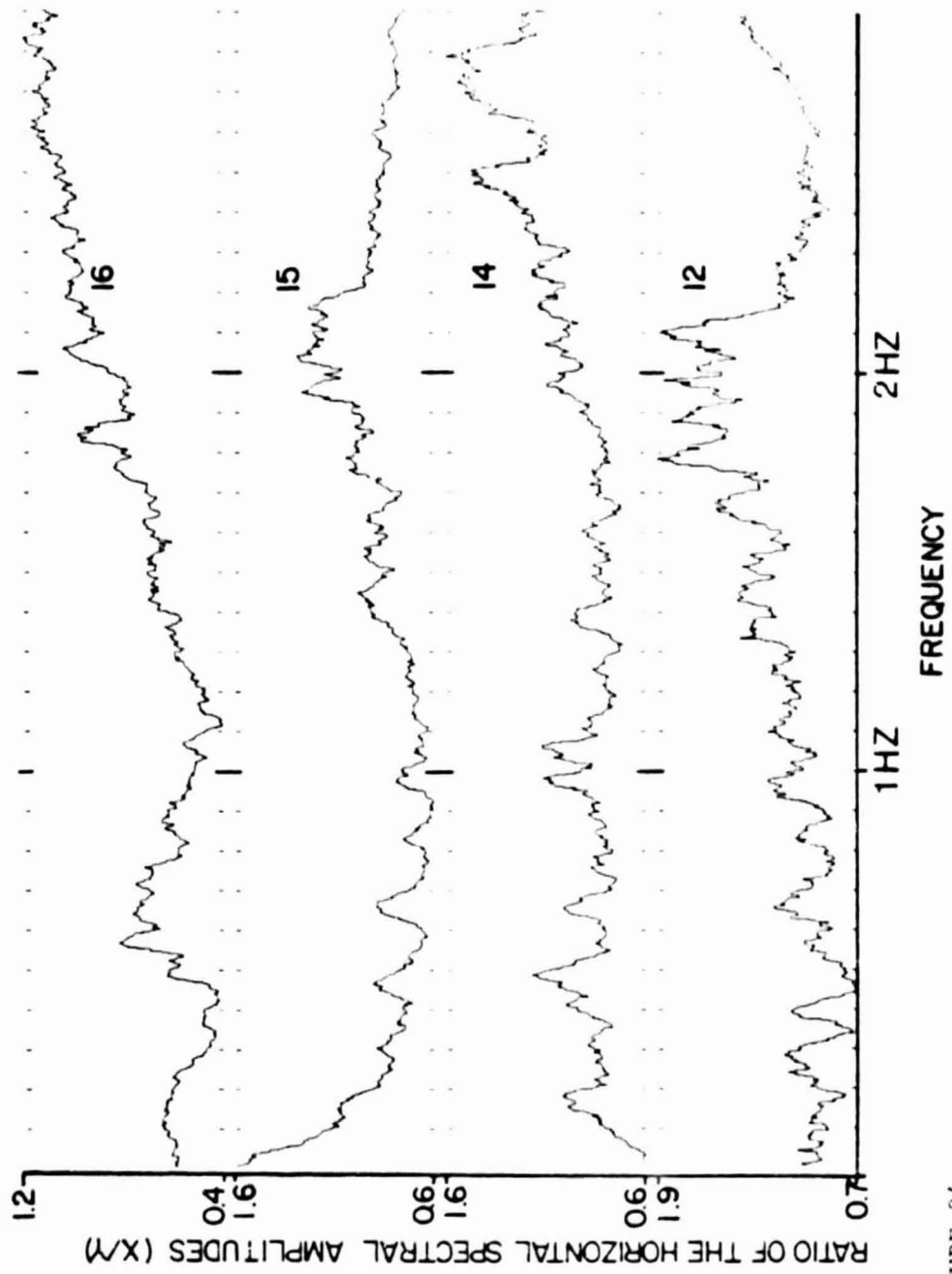


FIGURE 34.

Figure 35. Ratios of the horizontal and vertical spectral amplitudes at station 12. The ratios were calculated individually and were averaged for deep moonquakes (A), shallow moonquakes (H), and impacts (C). Curve 'Total' is the spectral ratio curve calculated from the average spectral amplitudes (see Figures 29 through 32). The amplitudes are clipped at long periods in order to utilize the full amplitude scale in the frequency band of interest. The average ratios were smoothed with moving averages in a window of 0.55 Hz. The dot-dash and the dashed curves are the theoretical curves calculated for models 'A' and 'B', given in Tables 12 and 13, respectively.

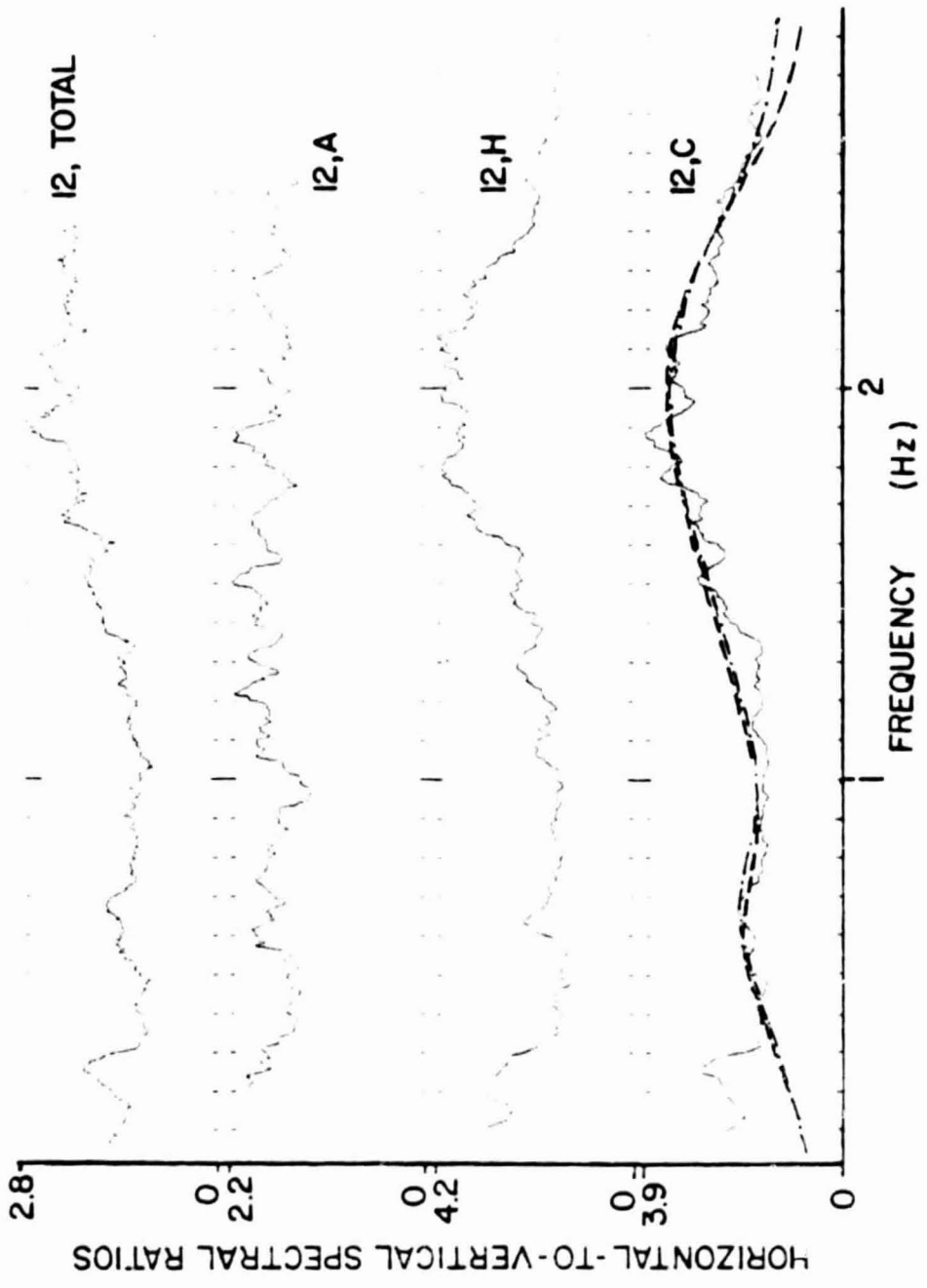


FIGURE 35.

Figure 36. Ratios of the horizontal and vertical spectral amplitudes at station 14. See Figure 34 for explanation.

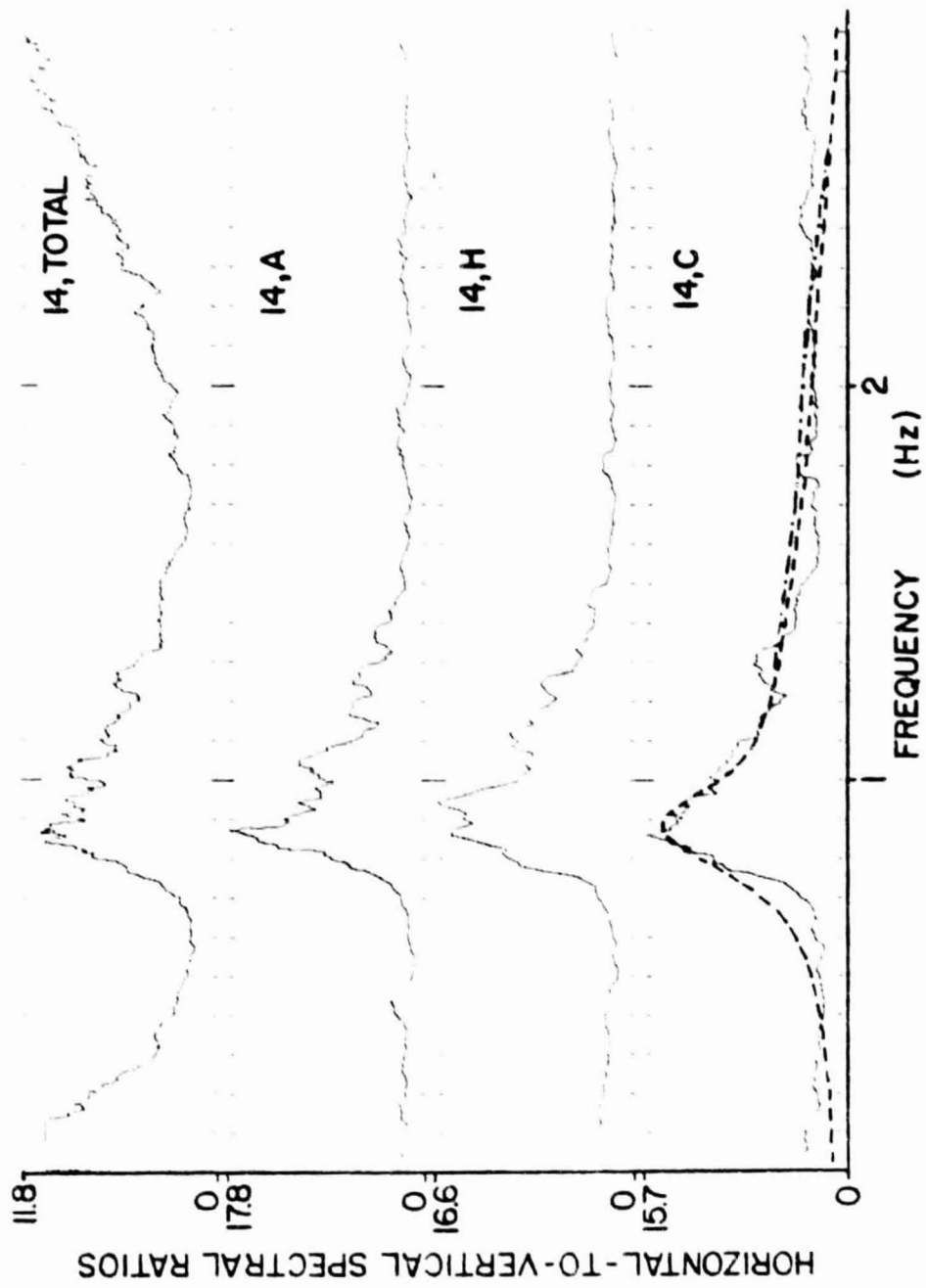


FIGURE 36.

Figure 37. Ratios of the horizontal and vertical spectral amplitudes at station 15. See Figure 34 for explanation.

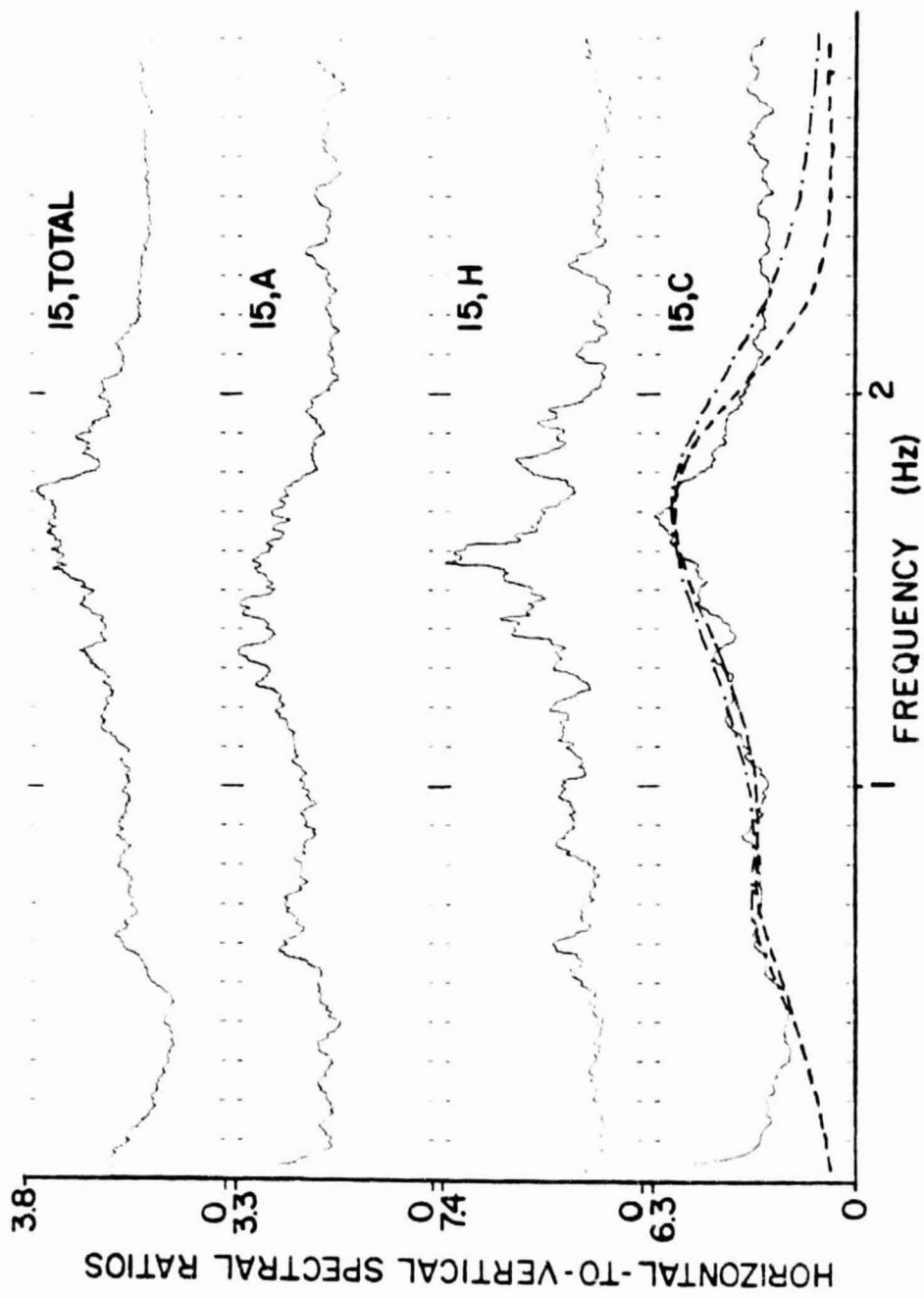


FIGURE 37.

Figure 38. Ratios of the horizontal and vertical spectral amplitudes at station 16. See Figure 34 for explanation.

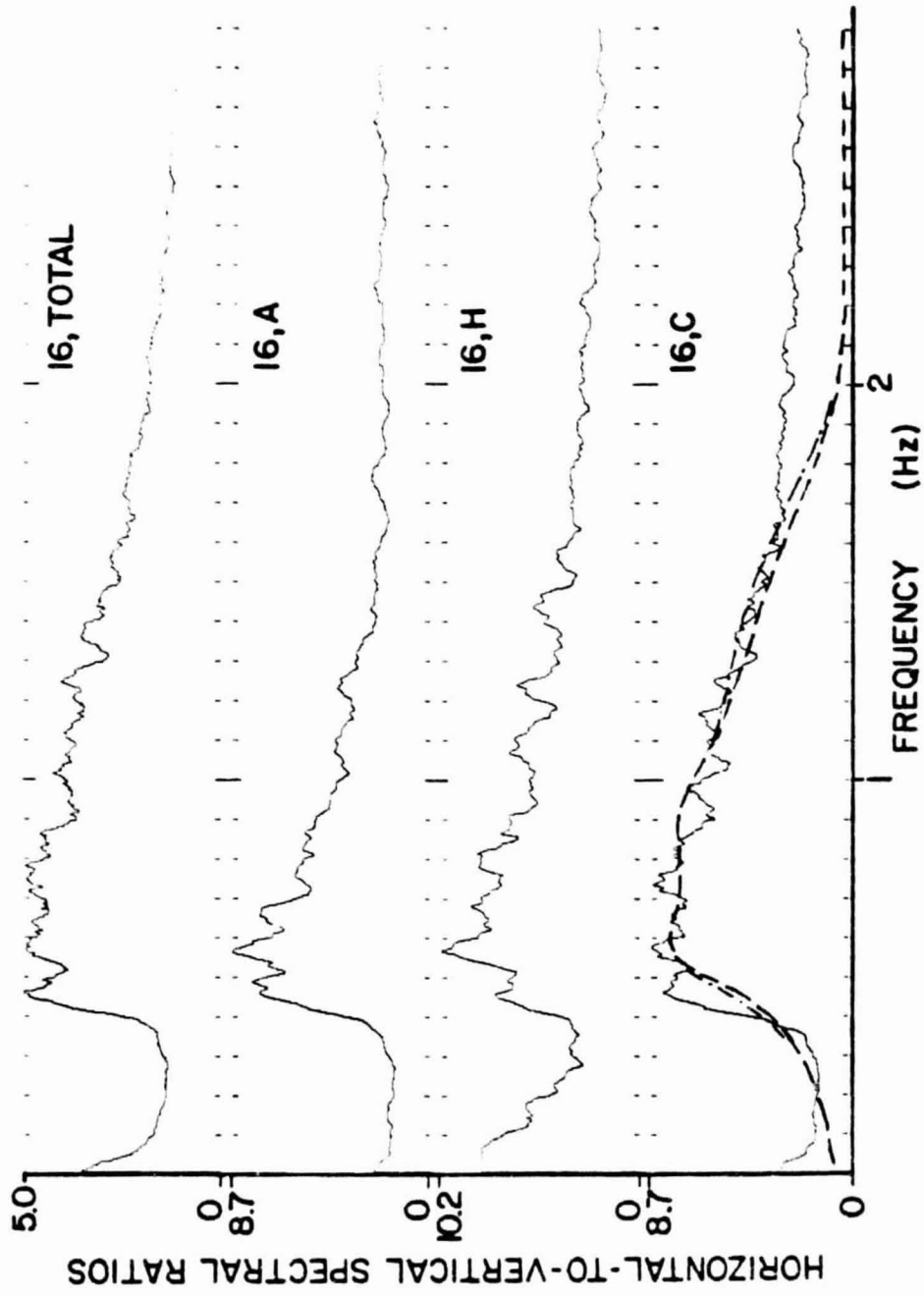


FIGURE 38.

Figure 39. Near-surface shear velocity profiles obtained for the Apollo 12, 14, 15, and 16 landing sites. The model parameters are given in Table 13. The center of the layers is marked with a cross. The dashed line is the piecewise linear shear velocity function described in Table 14.

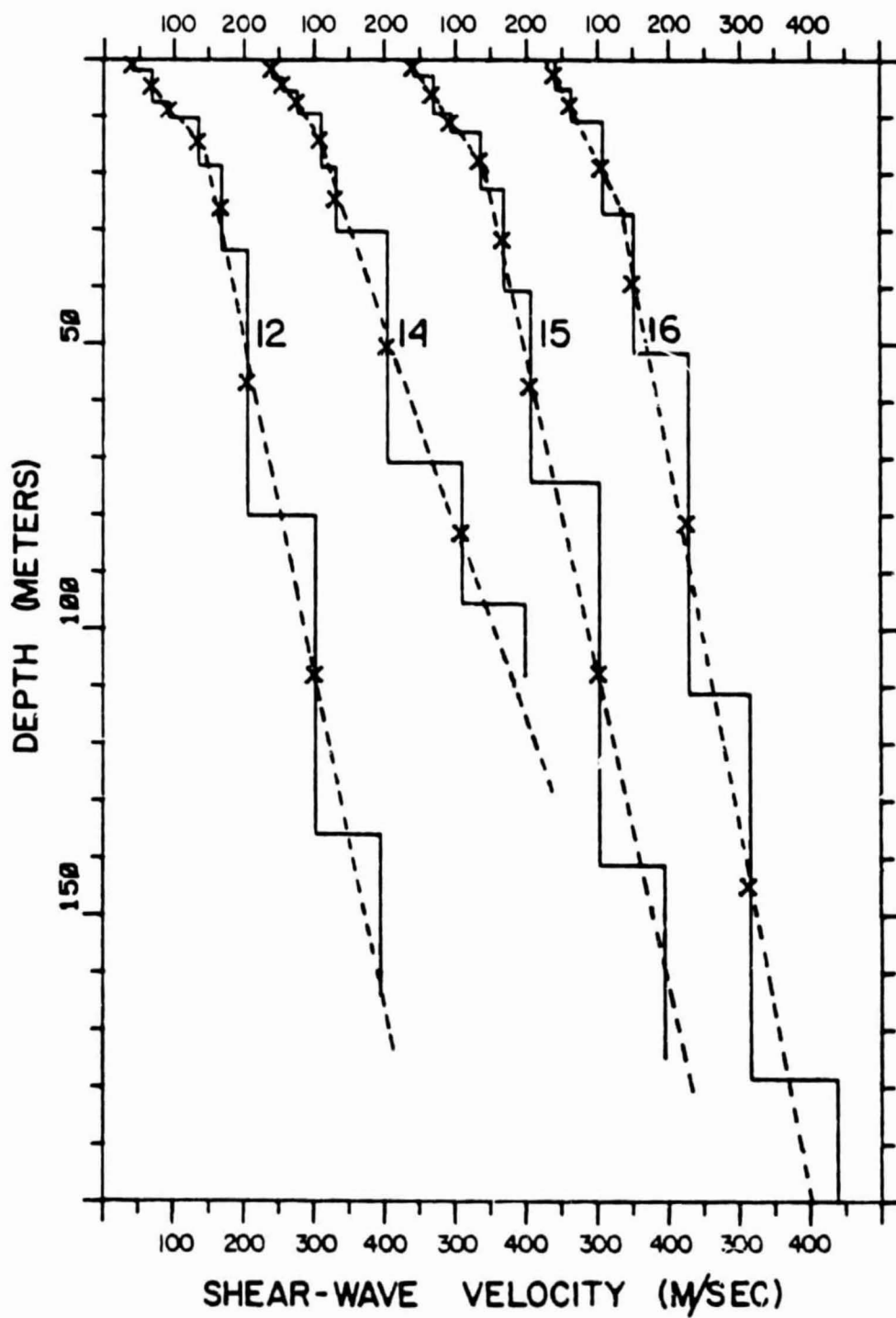


FIGURE 39.

Figure 40. Travel time curves of the refracted compressional waves for station 12. The model parameters are given in Table 13. The first arrival from the Lunar Module lift-off is indicated with a star.

Figure 41. Travel time curves of the refracted compressional waves for station 14. See Figure 39 for explanation.

FIGURE 40.

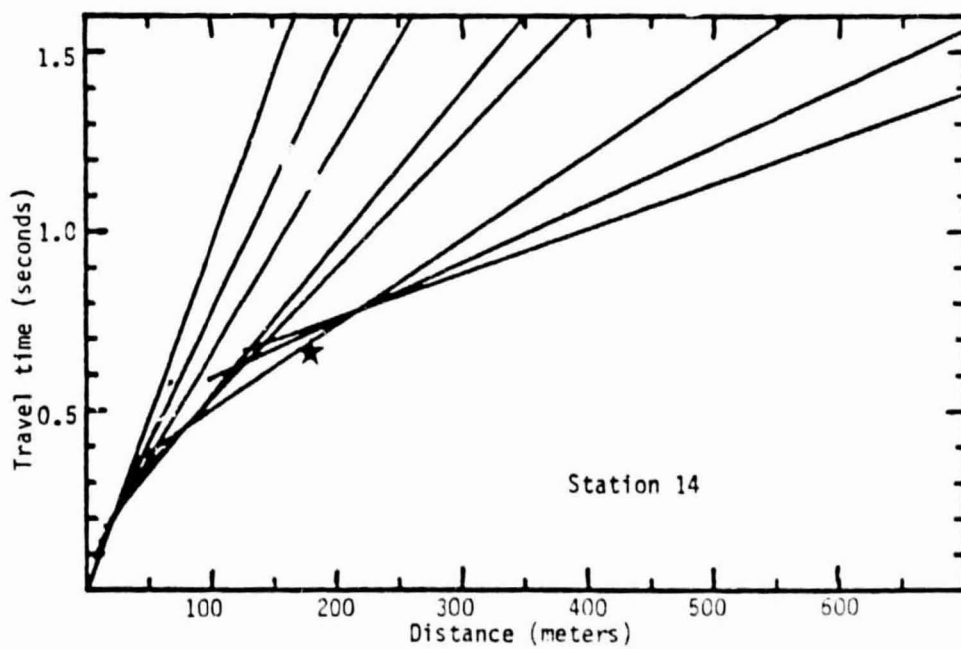
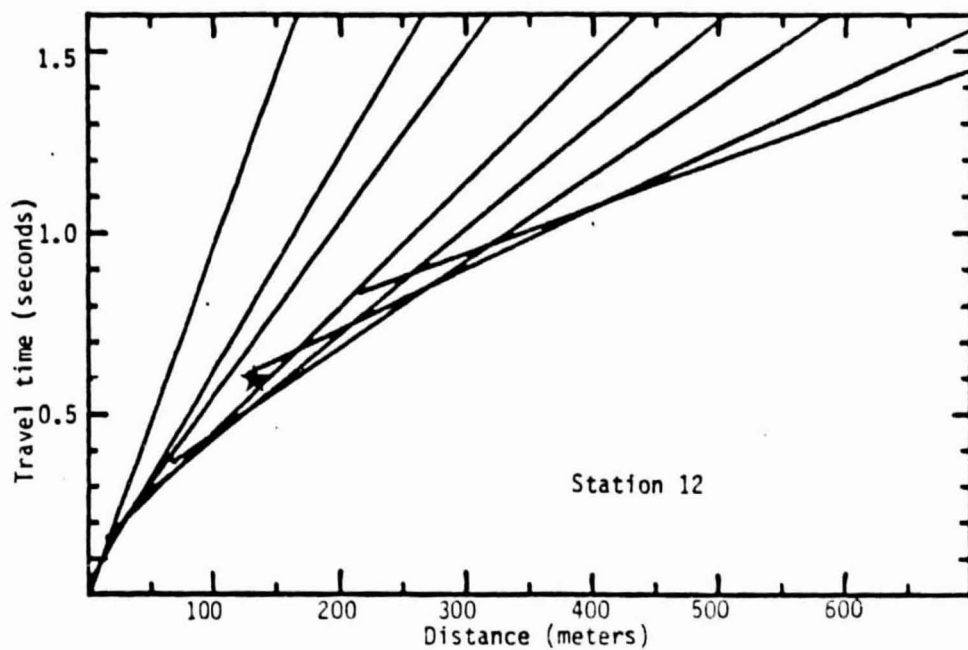


FIGURE 41.

Figure 42. Travel time curves of the refracted compressional waves for station 15. See Figure 39 for explanation.

Figure 43. Travel time curves of the refracted compressional waves for station 16. The model parameters are given in Table 13.

FIGURE 42.

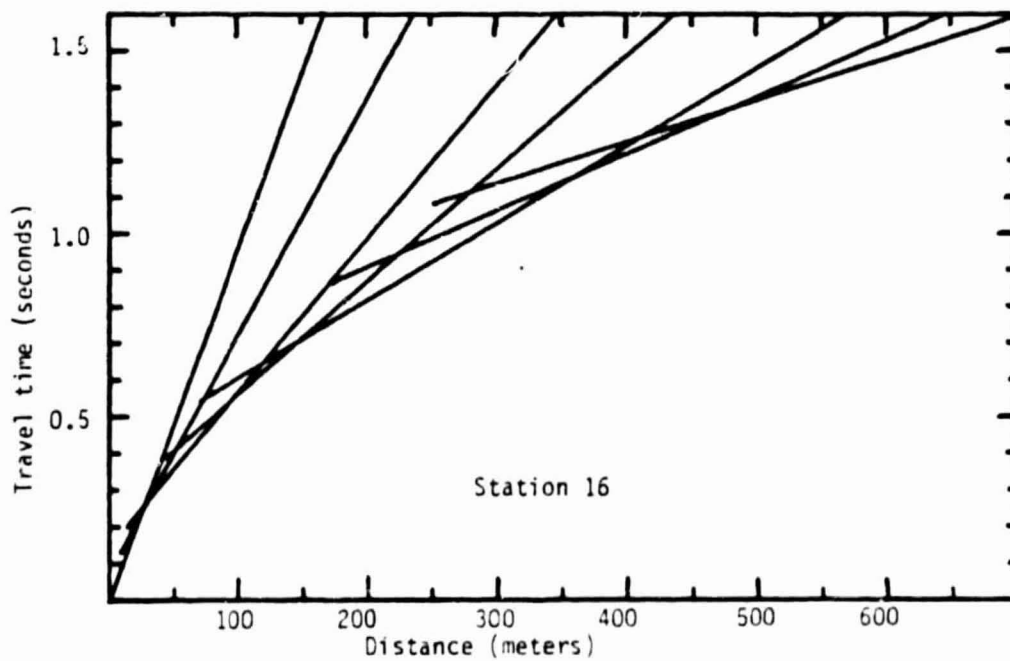
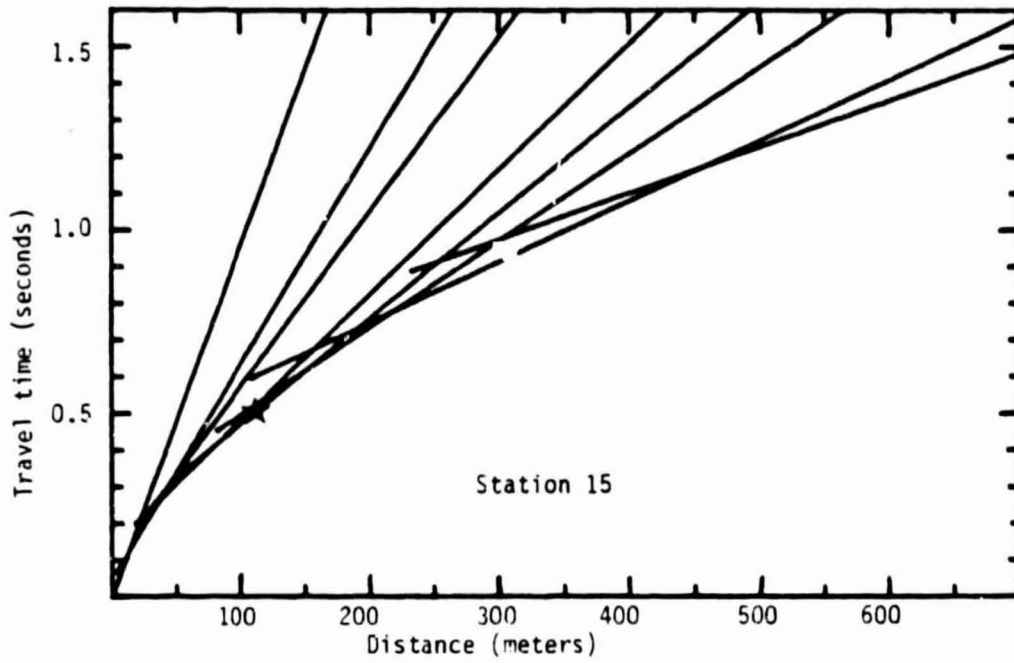


FIGURE 43.

Figure 44. Velocity models used in this study for the whole moon. The velocities of the model with thicker crust and higher mantle velocities (continuous line) are given in Table 16. The velocities of the model with thinner crust and lower mantle velocities (dashed line) are given in Table 17.

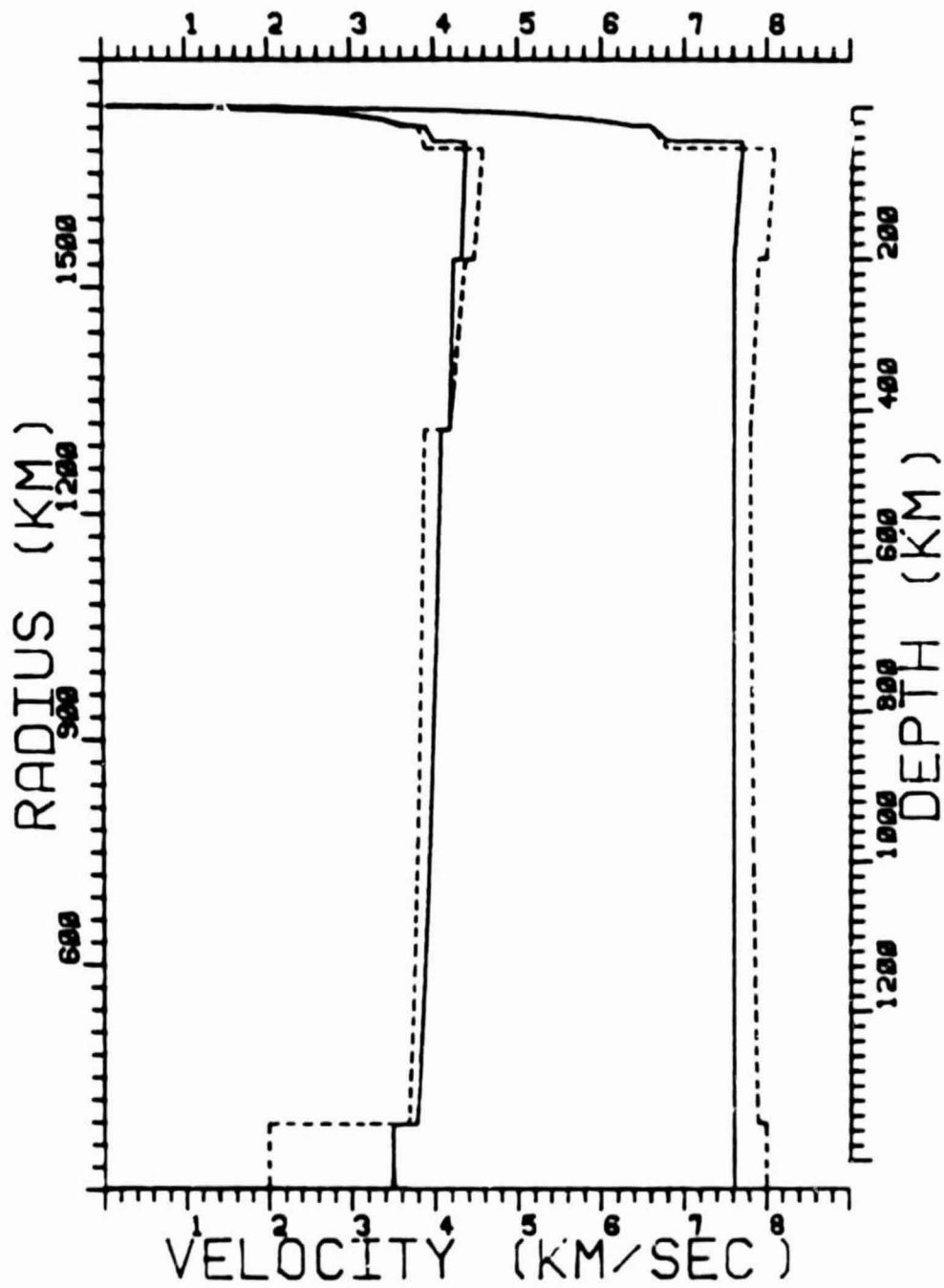


FIGURE 44.

Figure 45. Velocity models used in this study for the lunar crust and upper mantle only. See Figure 43 for explanation.

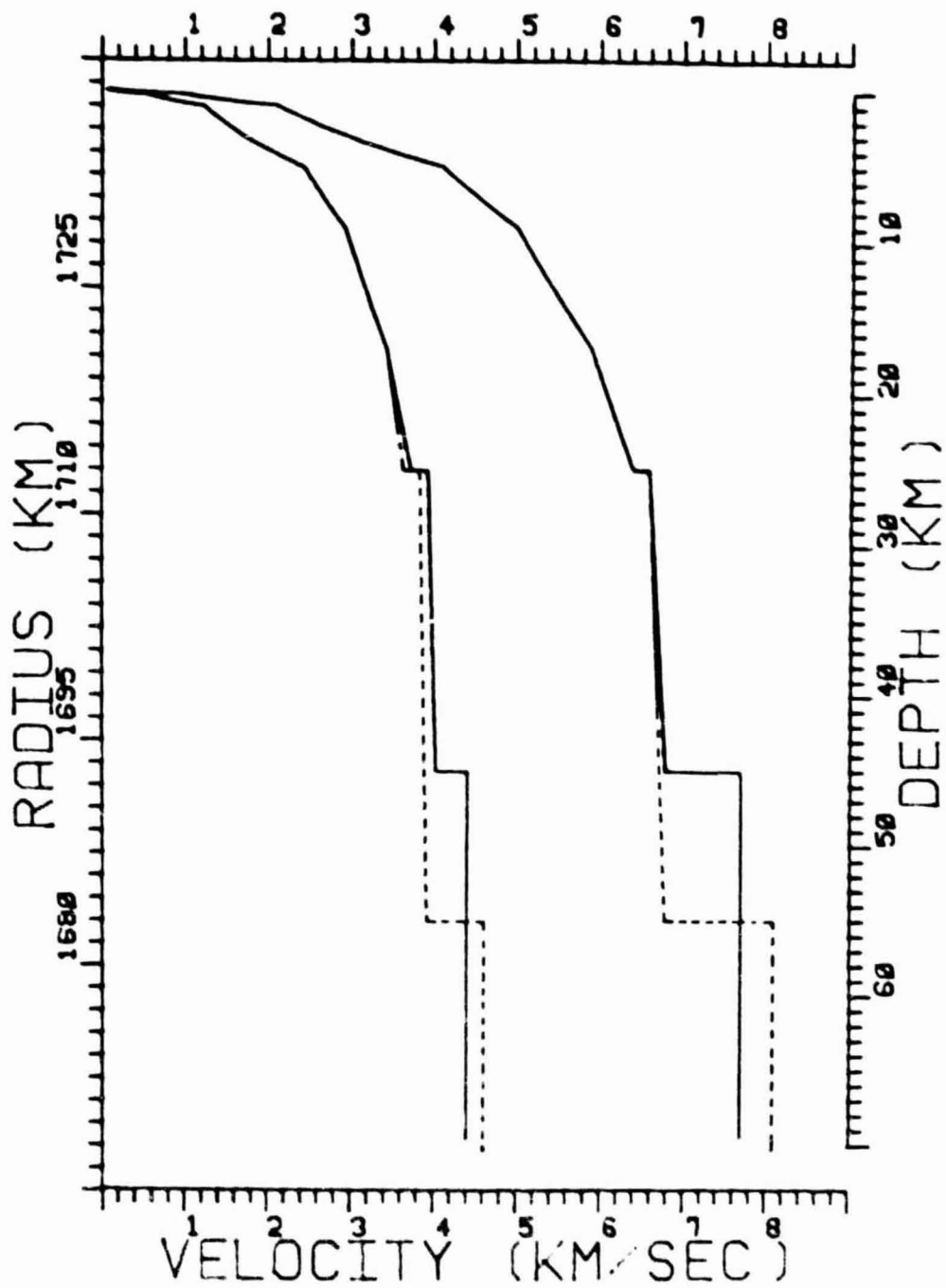


FIGURE 45.

Figure 46. Locations of impacts as determined in this study. The base map is the whole moon in an equal area projection. Table 17 lists these events. The location of the seismic stations are also given.

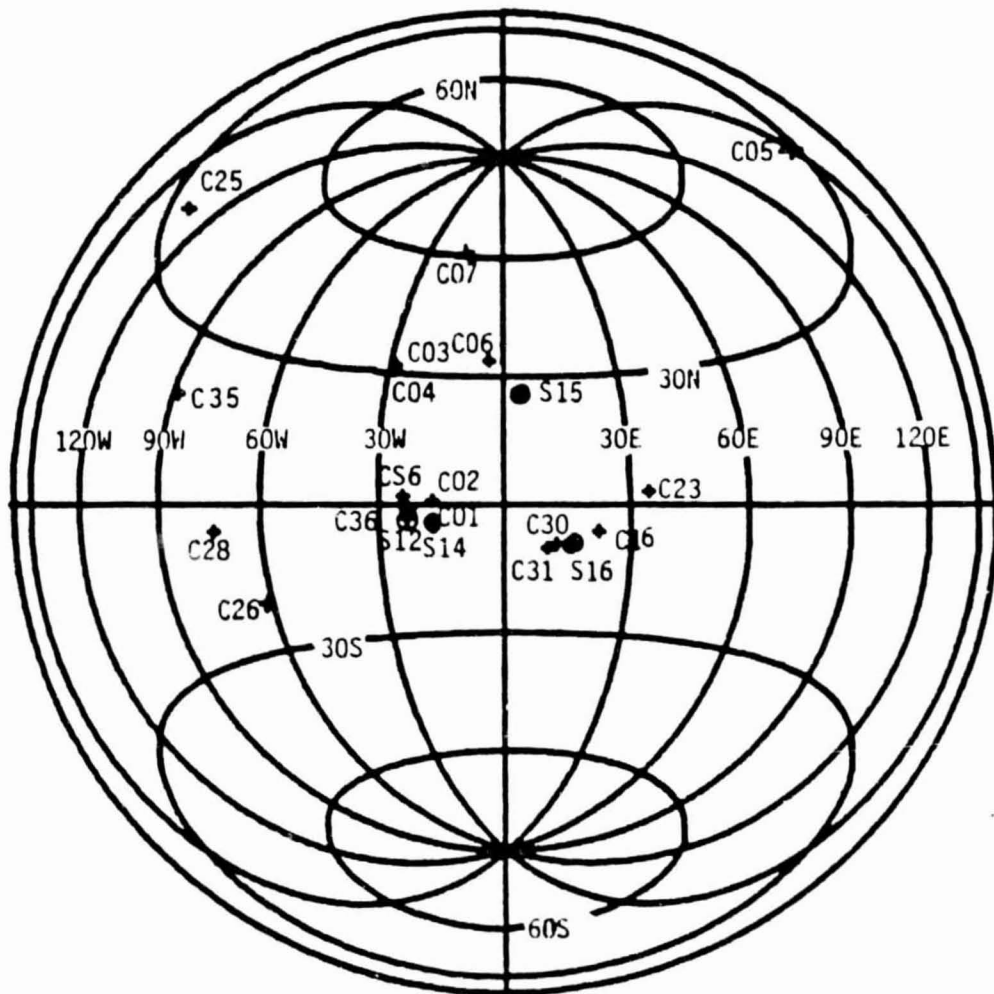


FIGURE 46.

Figure 47. Epicenters of shallow moonquakes as determined in this study. See Figure 45 for explanation.

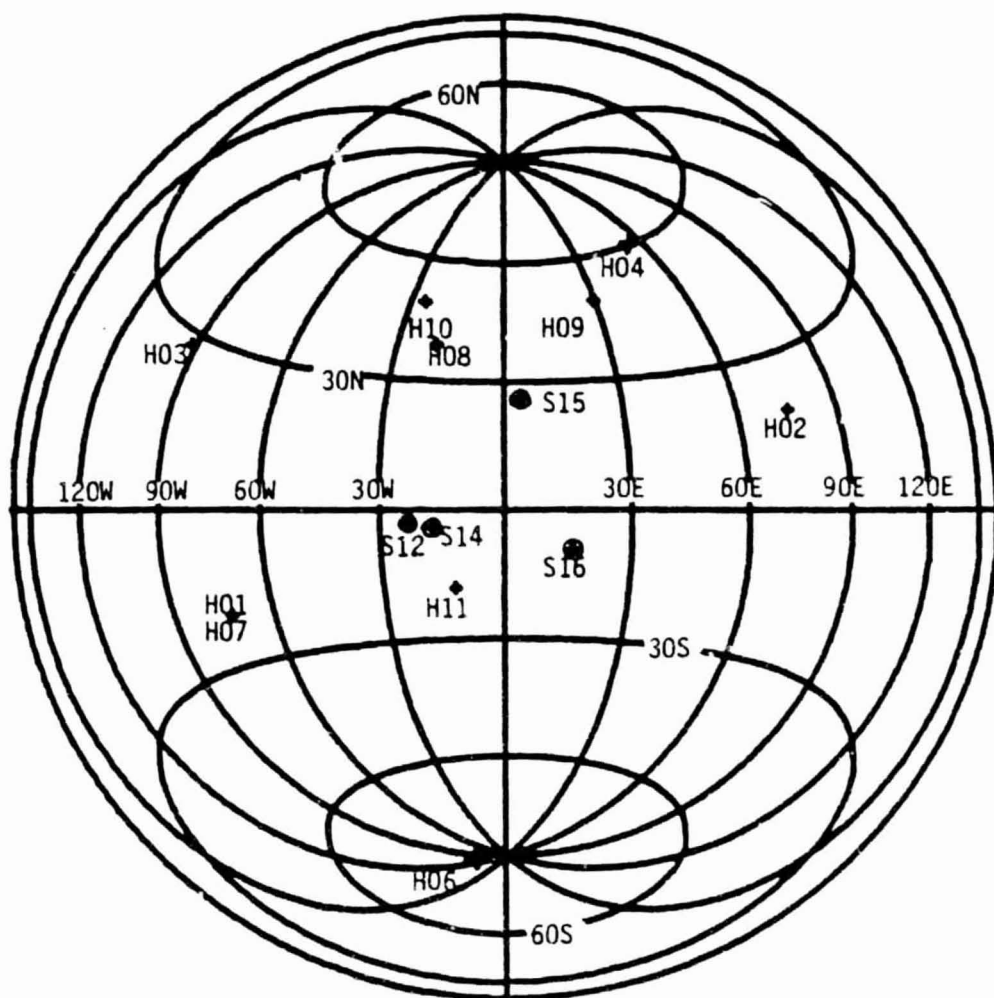


FIGURE 47.

SEISMIC SECTION CAPTIONS

'IMFACTS (R,0.4-1.5HZ)' Radial component of ground motion, distance range is 0 to 50⁰. Seismograms were corrected for instrument response and near-surface effects, filtered with a 3-pole Butterworth filter, and rotated into the above direction with azimuths given in Table 18. The distances, at which the records are aligned, are given in Table 18. and are indicated by drawing a line from the given distance to the beginning of the seismic record. The arrival times of the direct waves, compressional (P) or shear (S), at which the seismic records are lined up, are given in Table 19. The seismic records are identified with a sequence number, with a four-character word (first three characters are the codes given in Tables 9 and 18, the fourth character is the second digit of the station number), and with a number giving the scale factor which was used to normalize the amplitudes by division. Glitches were zeroed. If a component was not operating normally (see Table 9), then the seismogram was zeroed. The part of the seismic records where the amplitudes are clipped were not plotted. The following arrival times were calculated with velocity distributions given in Table 17 and in Figures 43 and 44 and were drawn with continuous lines: S - direct shear wave arrival; PS-P to S reflection at the free surface; SS, 3S and 4S - shear wave is reflected once, twice and three times at the free surface; S25-peg leg multiple in the upper crust; S45-peg leg multiple in the whole crust; SLC - peg leg multiple in the lower crust; S²⁰⁰_p - S to P conversion at 200 km.

'IMFACTS (T,0.4-1.5HZ)' Transverse component of ground motion, distance range is 0 to 50⁰. See Seismic Section 'IMFACTS (R,0.4-1.5HZ)'

for explanation.

'IMPACTS (Z,0.4-1.5HZ)' Vertical component of ground motion, distance range is 0 to 50⁰. See Seismic Section 'IMPACTS (R,0.4-1.5HZ)' for explanation.

'IMPACTS (R,0.4-1.5HZ)' Radial component of ground motion, distance range is 60 to 160⁰. See Seismic Section 'IMPACTS (R,0.4-1.5HZ)' for explanation.

'IMPACTS (T,0.4-1.5HZ)' Transverse component of ground motion, distance range is 60 to 160⁰. See Seismic Record Section 'IMPACTS (R,0.4-1.5HZ)' for explanation.

'IMPACTS (Z,0.4-1.5HZ)' Vertical component of ground motion, distance range is 60 to 160⁰. See Seismic Section 'IMPACTS (R,0.4-1.5HZ)' for explanation.

'SHALLOW MOONQUAKES (R,0.4-1.5HZ)' Radial component of ground motion; distance range is 0 to 120⁰. See Seismic Section 'IMPACTS (R,0.4-1.5HZ)' for explanation.

'SHALLOW MOONQUAKES (Z,0.4-1.5HZ)' Vertical component of ground motion, distance range is 0 to 120⁰. See Seismic Section 'IMPACTS (R,0.4-1.5HZ)' for explanation.

'DEEP MOONQUAKES (R,0.4-1.5HZ)' Radial component of ground motion, distance range is 0 to 100⁰. See Seismic Section 'IMPACTS (R,0.4-1.5HZ)' for explanation.

'DEEP MOONQUAKES (T,0.4-1.5HZ)' Transverse component of ground motion, distance range is 0 to 100⁰. See Seismic Section 'IMPACTS (R,0.4-1.5HZ)' for explanation.

'DEEP MOONQUAKES (Z)' Vertical component of ground motion as recorded with seismographs operated in the peaked mode, distance range is 0 to 100⁰. See Seismic Section 'IMPACTS (R,0.4-1.5HZ)' for explanation.

VITA

Peter Horvath was born in [REDACTED], a son of Horváth Pál and Gracza Erzébet. After completing his secondary school training at the Kolcsey Ferenc Gimnazium, Budapest, Hungary, in 1965, he studied Geophysics and Astronomy at the School of Natural Sciences, Eötvös Loránd University, Budapest, Hungary. He completed all the requirements for the Diploma in Geophysics and Astronomy with a thesis titled "Designing criteria for induction well logging devices" in July, 1970. During the following years he was employed as a geophysicist at Eötvös Loránd Geophysical Institute, Budapest, Hungary, at Western Geophysical Company, Houston, Texas, at Sun Oil Co., Dallas, Texas, and at The University of Texas, Marine Science Institute, Galveston, Texas. In January, 1975, he entered the Graduate School of The University of Texas at Dallas.

Permanent address: 304 University Blvd., #C-11
Galveston, Texas 77550

IMPACTS (Z, 0.4)

TIME - P

0.

60.

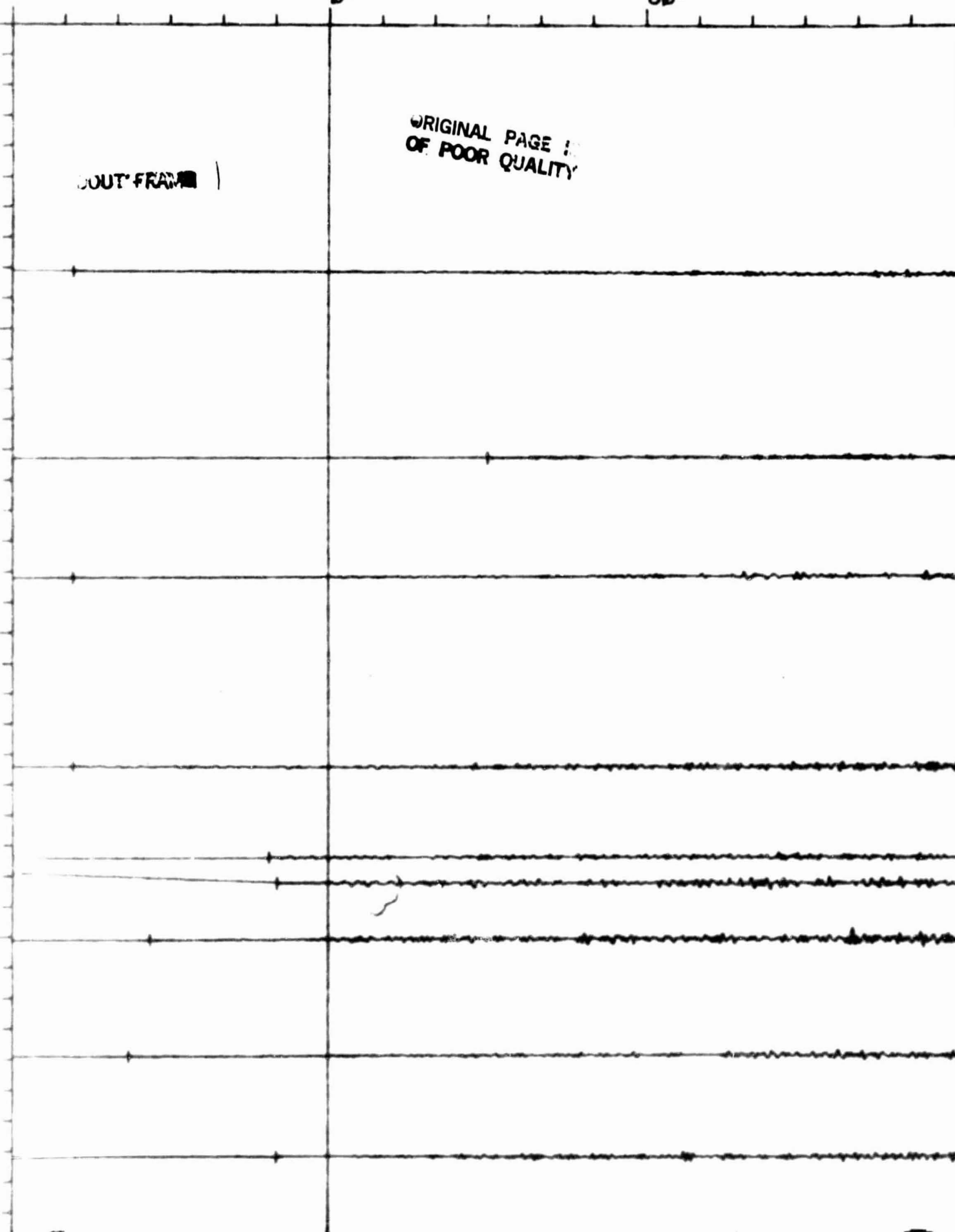
OUT FRAME |

ORIGINAL PAGE IS
OF POOR QUALITY

.09

.04

.08



P (SECONDS)

120°

180°

240°

OLDOUT FRAME 2

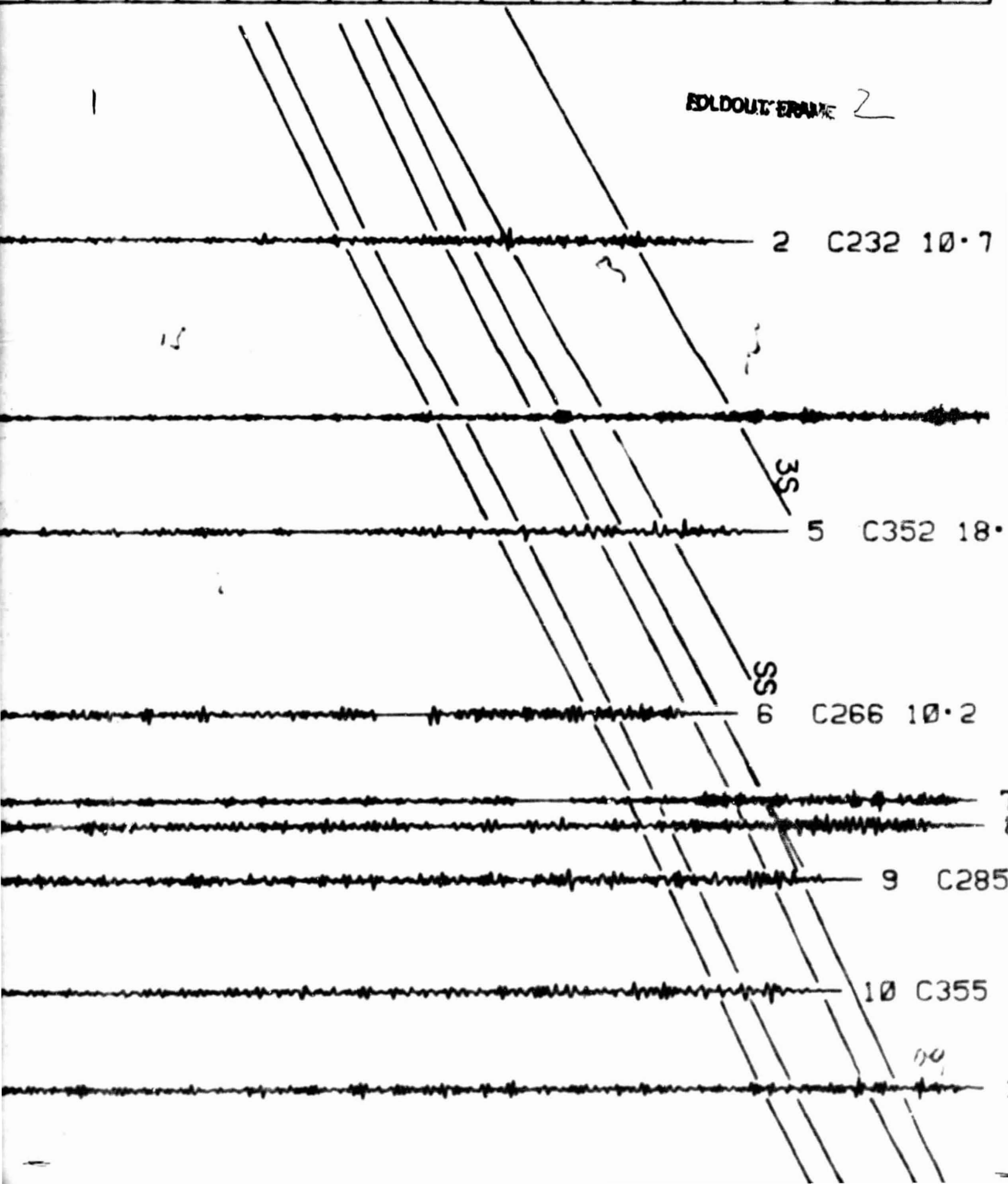
2 C232 10.7

5 C352 18.

6 C266 10.2

9 C285

10 C355



FOLDOUT FRAME

3

32 10.7

3 C072 4.0

352 18.0

5 10.2

7 C076 6.1
8 C265 8.4

9 C285 16.8

0 C355 19.4

10
11 C286 32.0

DISTANCE (DEGREE)

100.

110.

120.

130.

2

ORIGINAL PAGE IS
OF POOR QUALITY

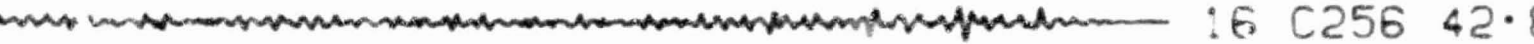
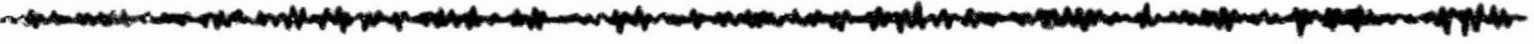
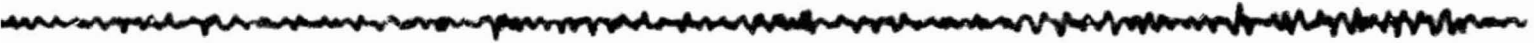
OUTLINE 3

1

S45
S25

PS

FOLDOUT: ~~XXXX~~ 4

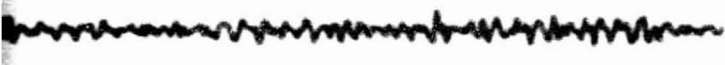


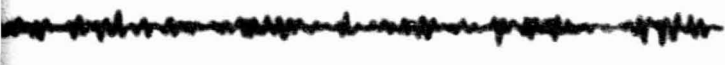
16 C256 42.8

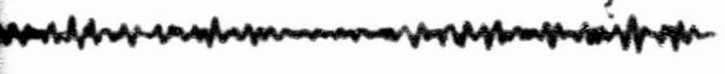


S45
S25

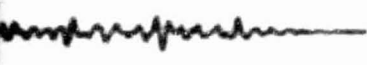
PS

 12 C252 18.2

 13 C356 16.5

 15 C055 18.2

END OF FRAME 5

 16 C256 42.8

 17 C056 26.2

130.

140.

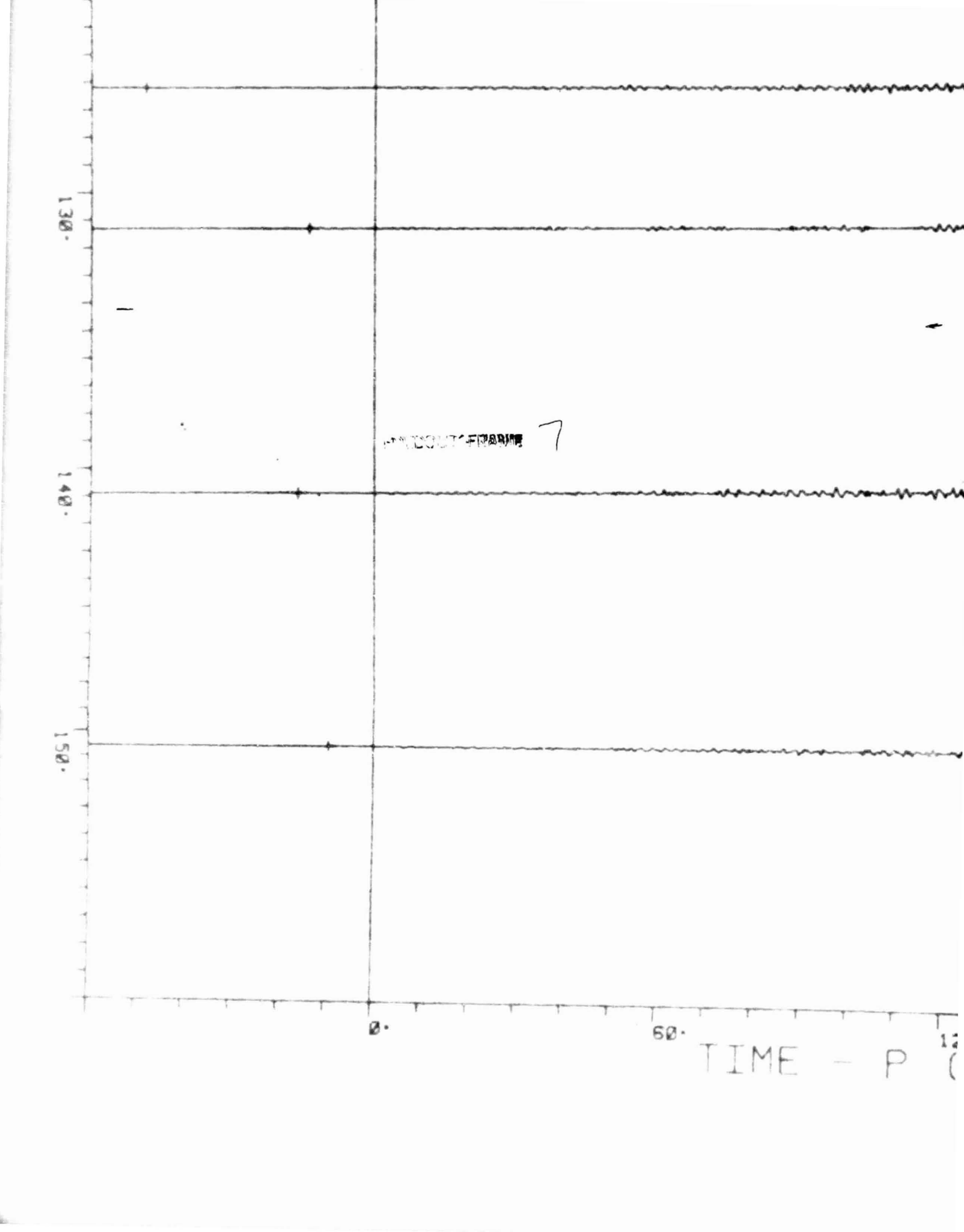
150.

0.

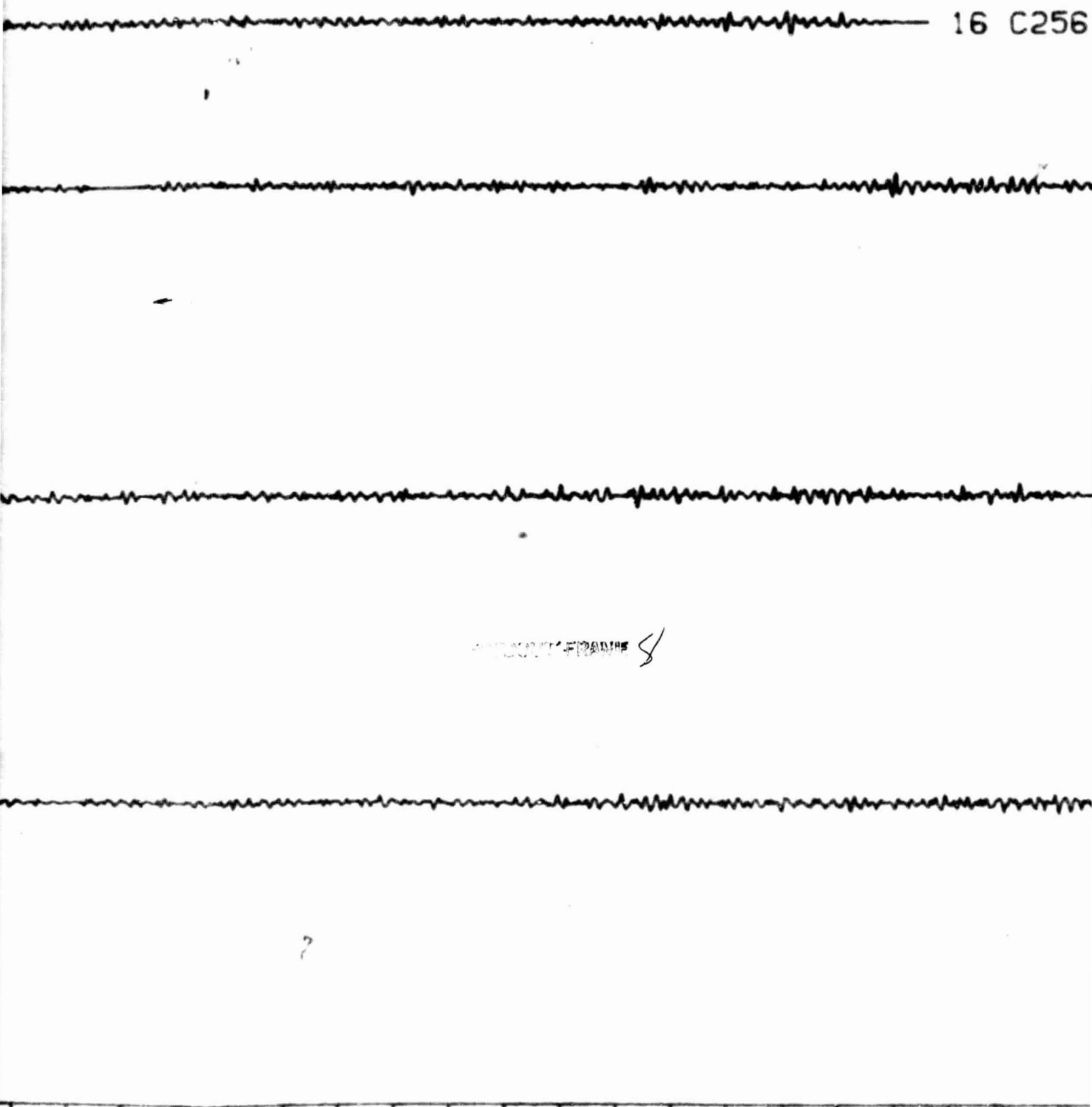
60.

TIME - P (

STANDARD FRAME 7



16 C256



ANTISCROLL FRAME S

E - P (SECONDS) 120. 180. 240.

16 C256 42.8

17 C056 26.2

18 C255 17.9

20 C052 6.7

ENCLOSURE FRAME 9

240.

AKES (Z, ' 0.4-1.5HZ)

P (SECONDS)

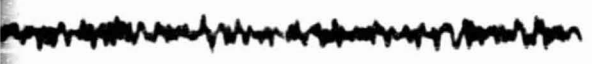
120.

180.

240.



OLDOUT FRAME 2

 2 H112 1.6

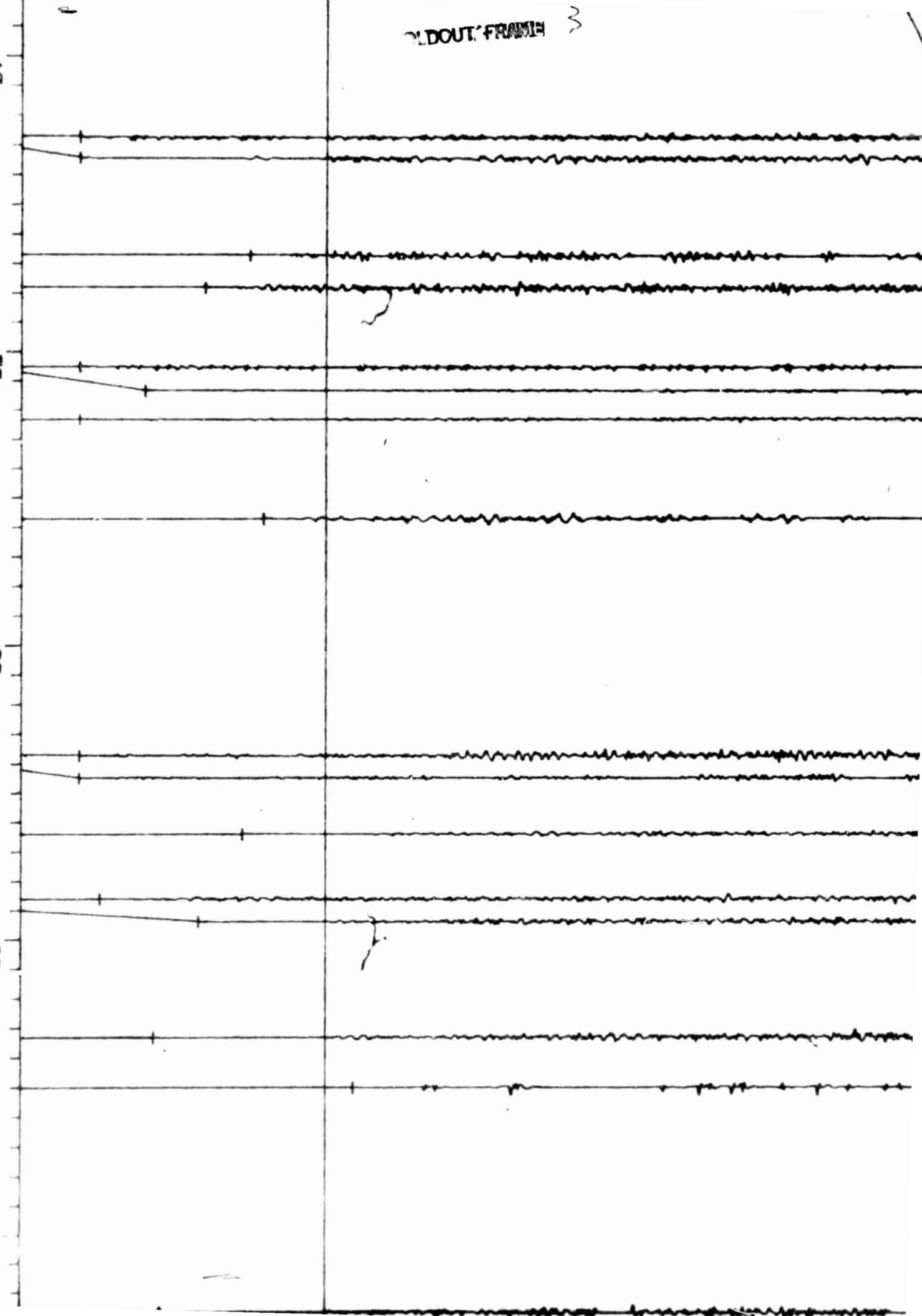
 3 H116 5.5

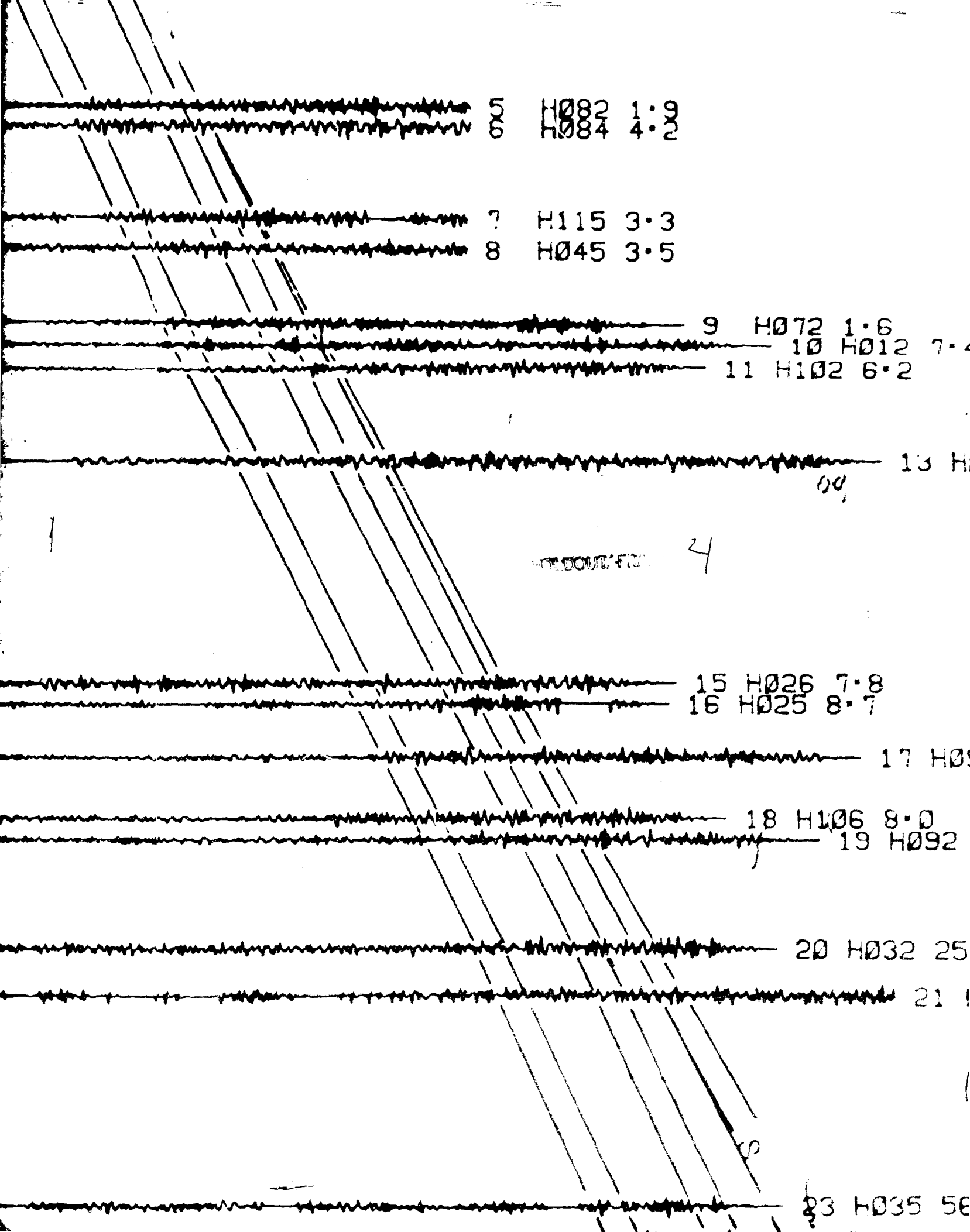
 4 H105 7.8

OLD OUT FRAME

DISTANCE (DEGREE)

40.
50.
60.
70.
80.





5 H082 1.9
6 H084 4.2

7 H115 3.3
8 H045 3.5

9 H072 1.6
10 H012 7.4
11 H102 6.2

13 H00

WITHOUT FILE 4

15 H026 7.8
16 H025 8.7

17 H0

18 H106 8.0
19 H092

20 H032 25

21

23 H035 56

9 H072 1.6
10 H012 7.4
11 H102 6.2

13 H074 2.8
00,

FOLDOUT FRAME

5 H026 7.8
6 H025 8.7

17 H094 16.5

18 H106 8.0
19 H092 8.9

20 H032 25.1

21 H048 2.1

23 H035 56.2

0.28

0.26

0.24

0.22

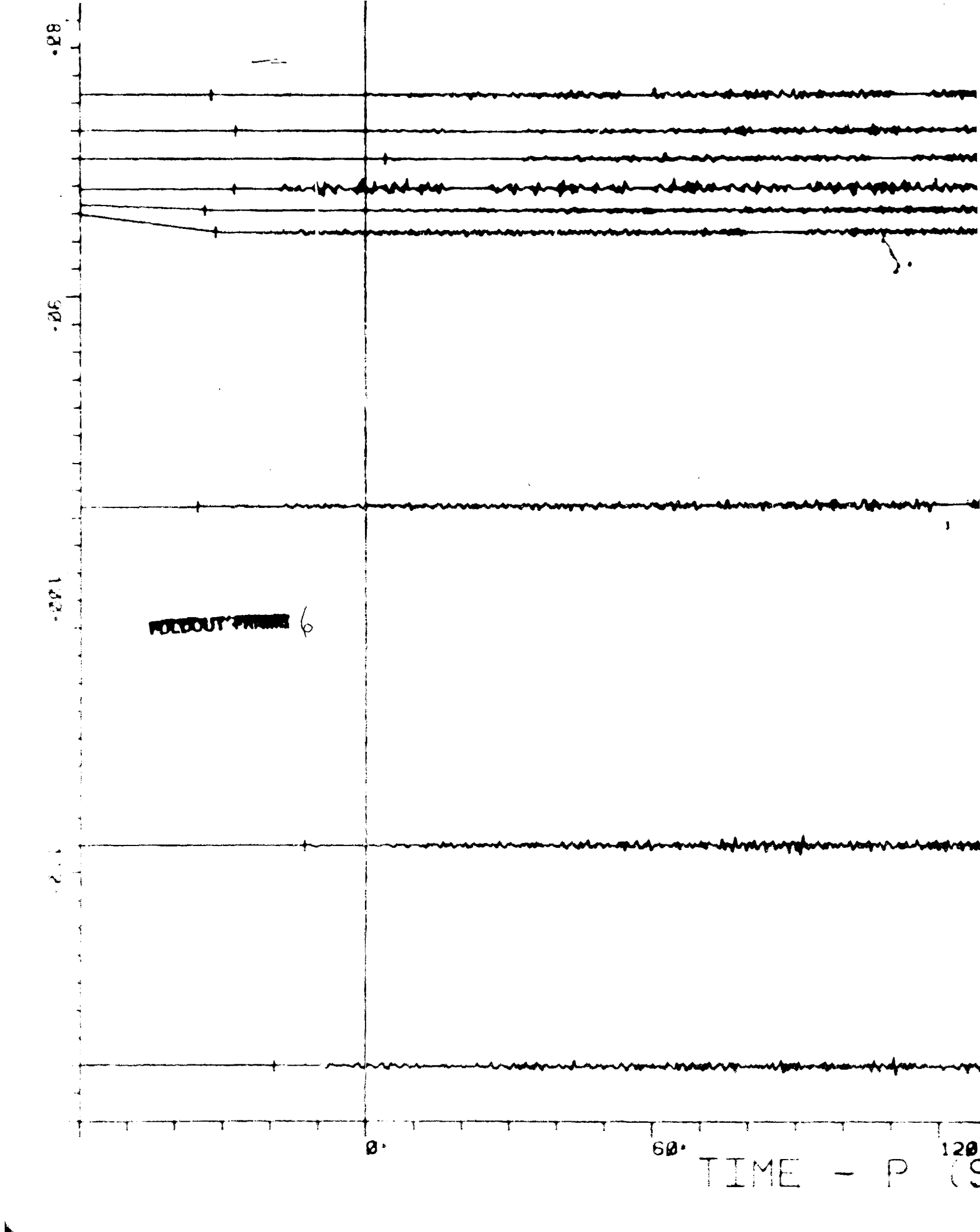
0

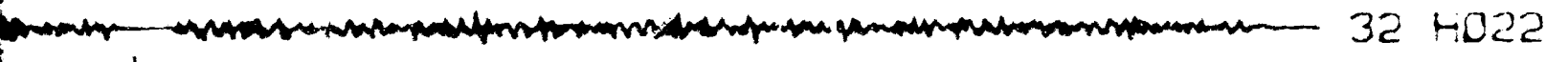
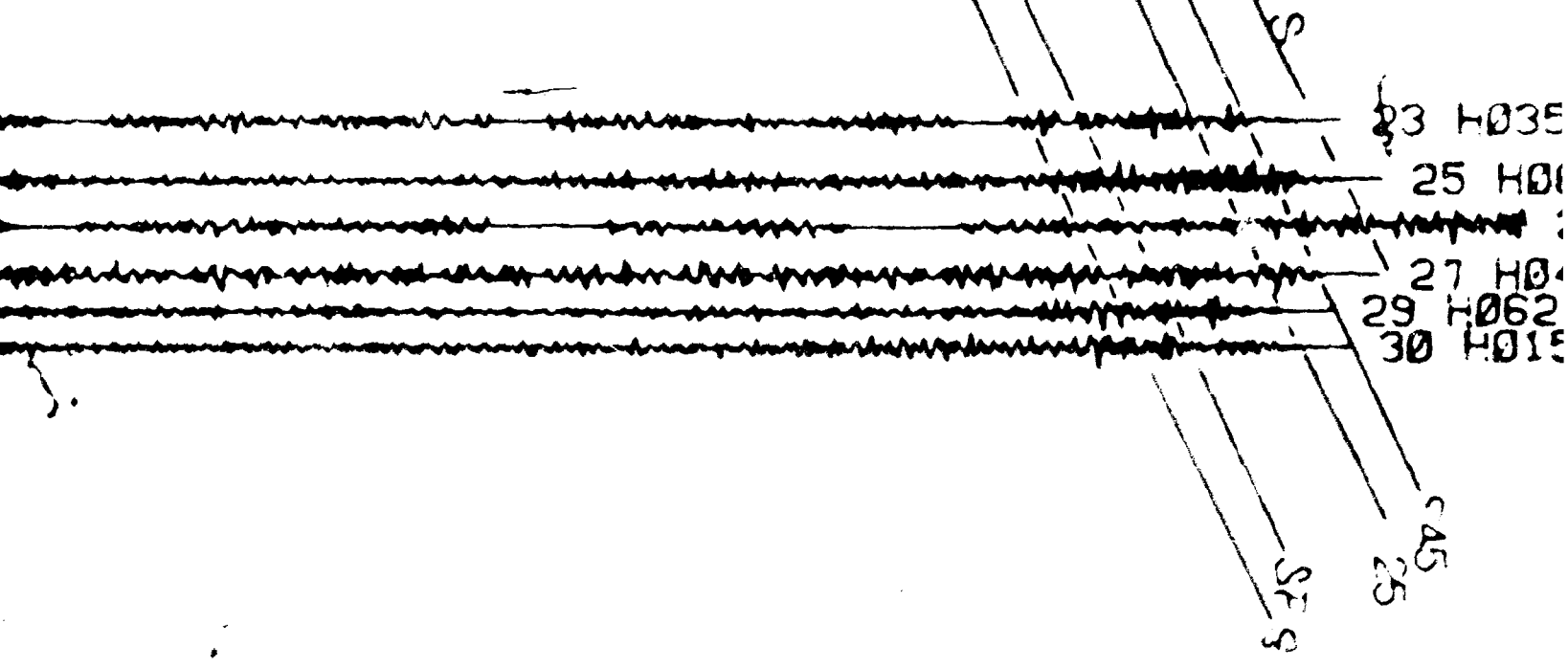
60

120

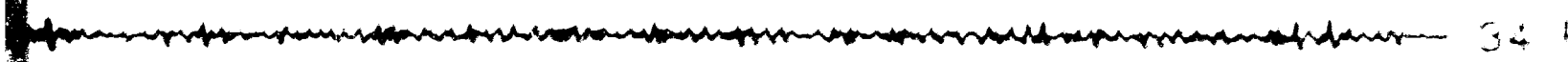
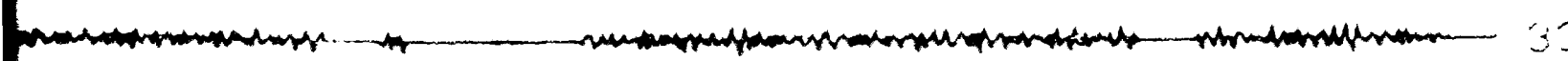
TIME - P (S)

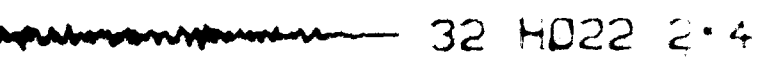
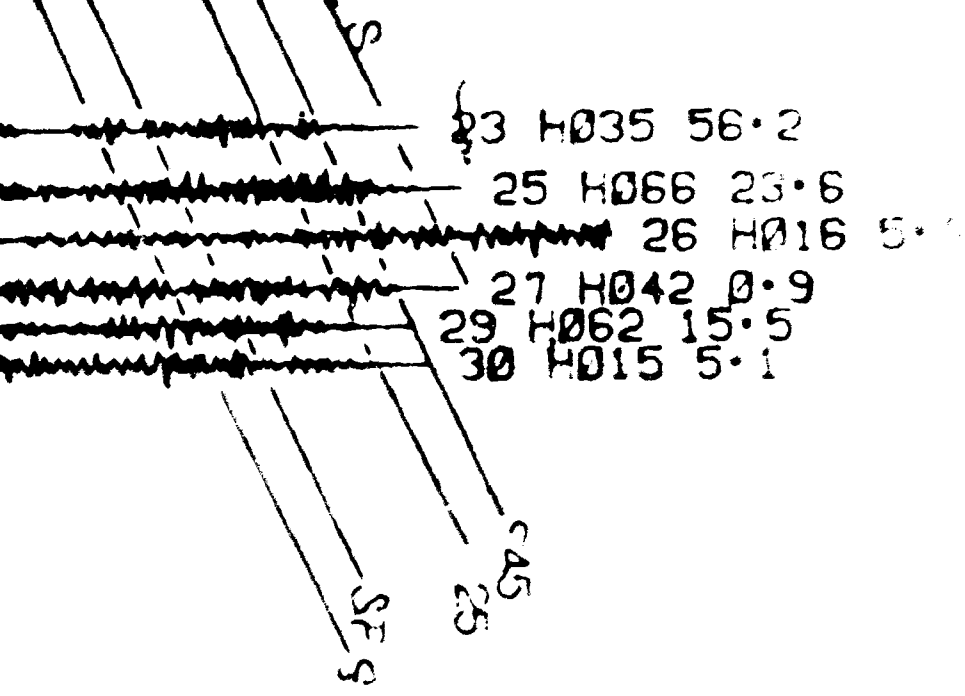
FOLDOUT FRAME 6



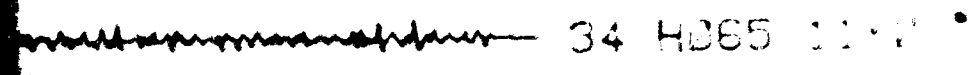
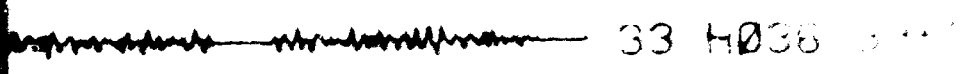


FOLDOUT FRAME 7





FOODOUT ERASER 8

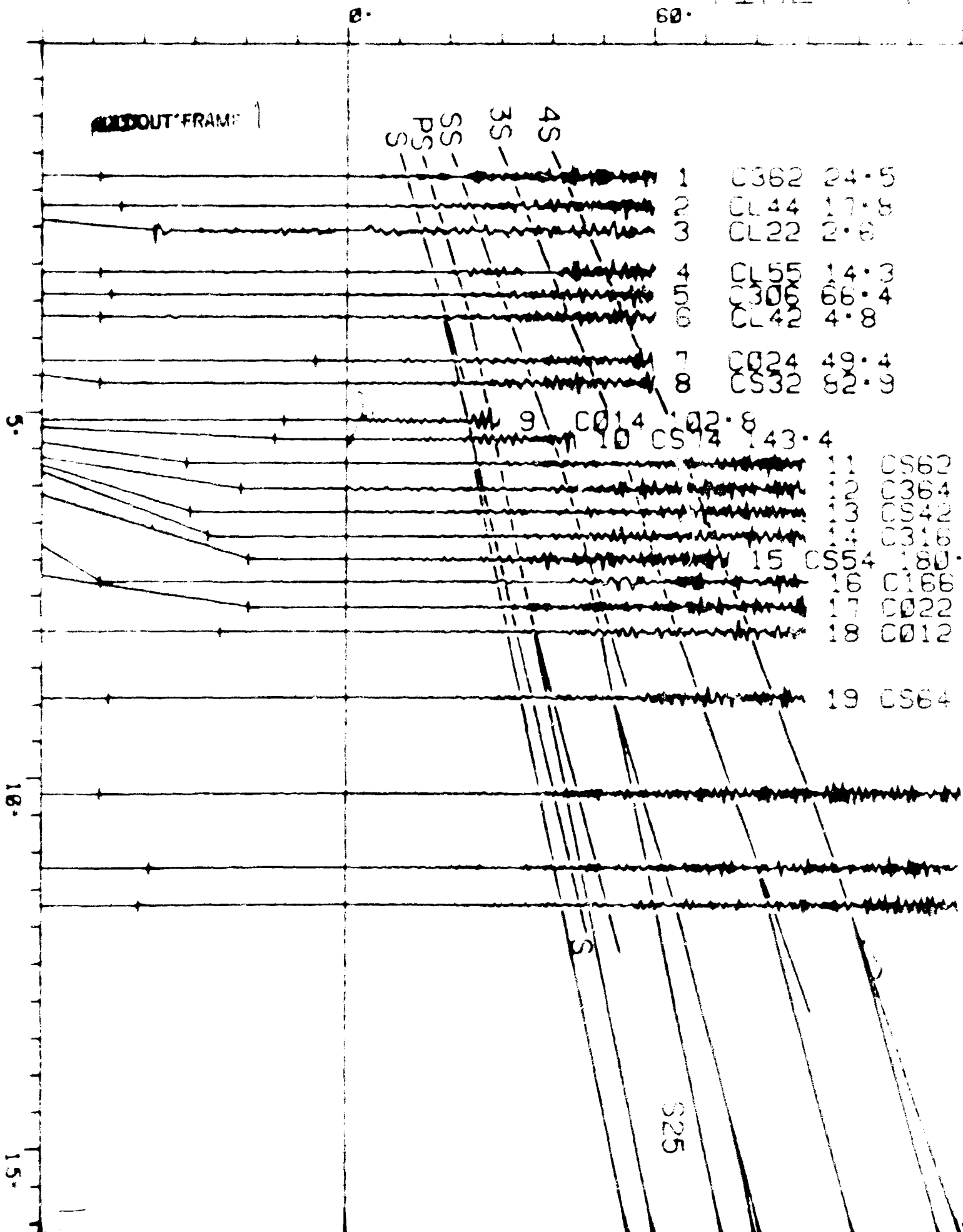


240

ORIGINAL PAGE IS
 OF POOR QUALITY

IMPACTS U, U - 4

TIME - P



1.5HZ

SECONDS



EXCLUDED FRAMES

37.6
 .5
 56.2
 0.9
 4.9
 4.2
 37.4

1.3

0 0065 72.4

1 CS72 36.2

2 CS52 33.7

DISTANCE (DEGREE)

5°

20°

25°

30°

SS

ECDDOUT FRAME 3

1

1

45

SS

23 C236 29.9

FOLDOUT FRAME

4

SS

24 CS76 23.5

25 C045 21.0

26 C015 67.4

35.

40.

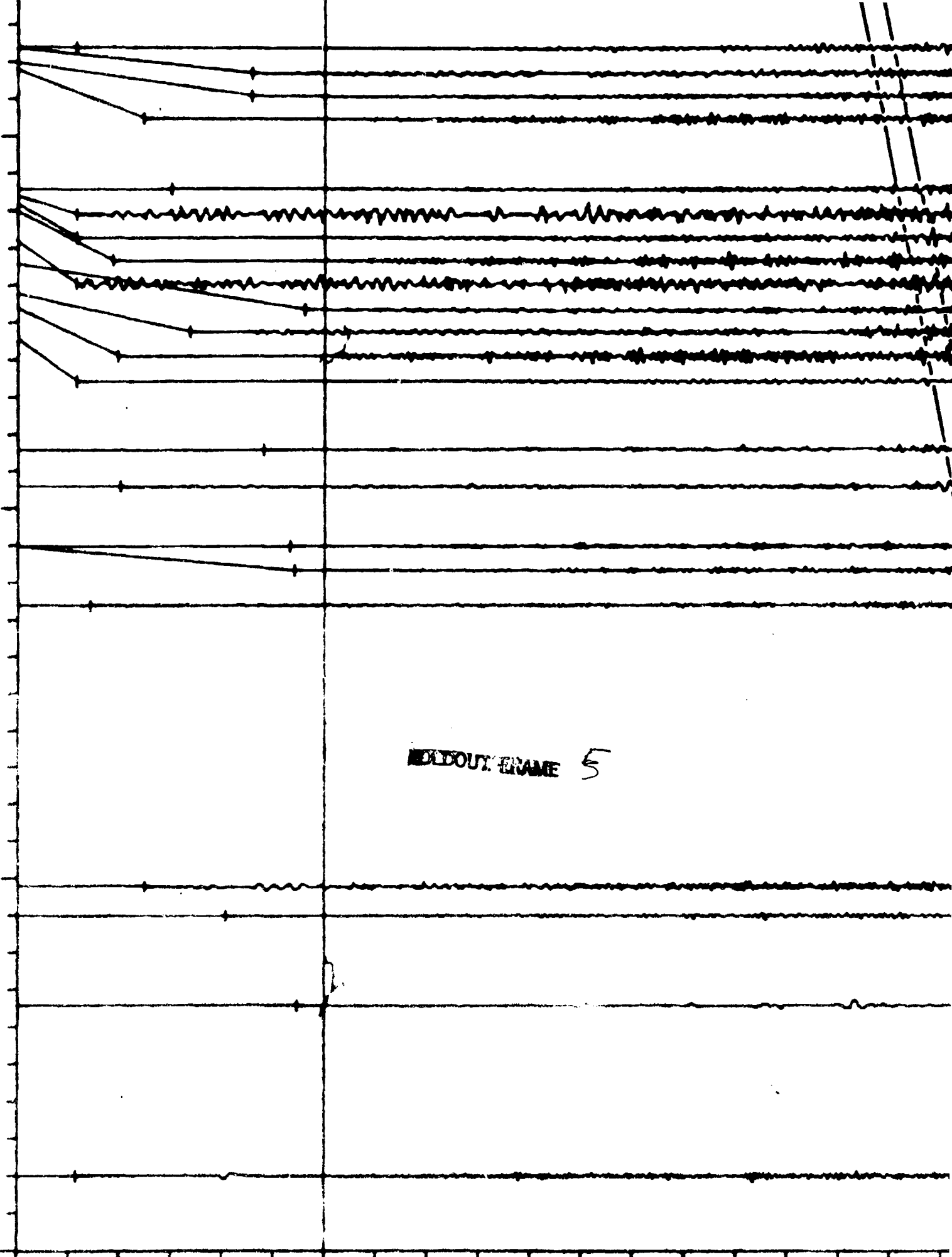
45.

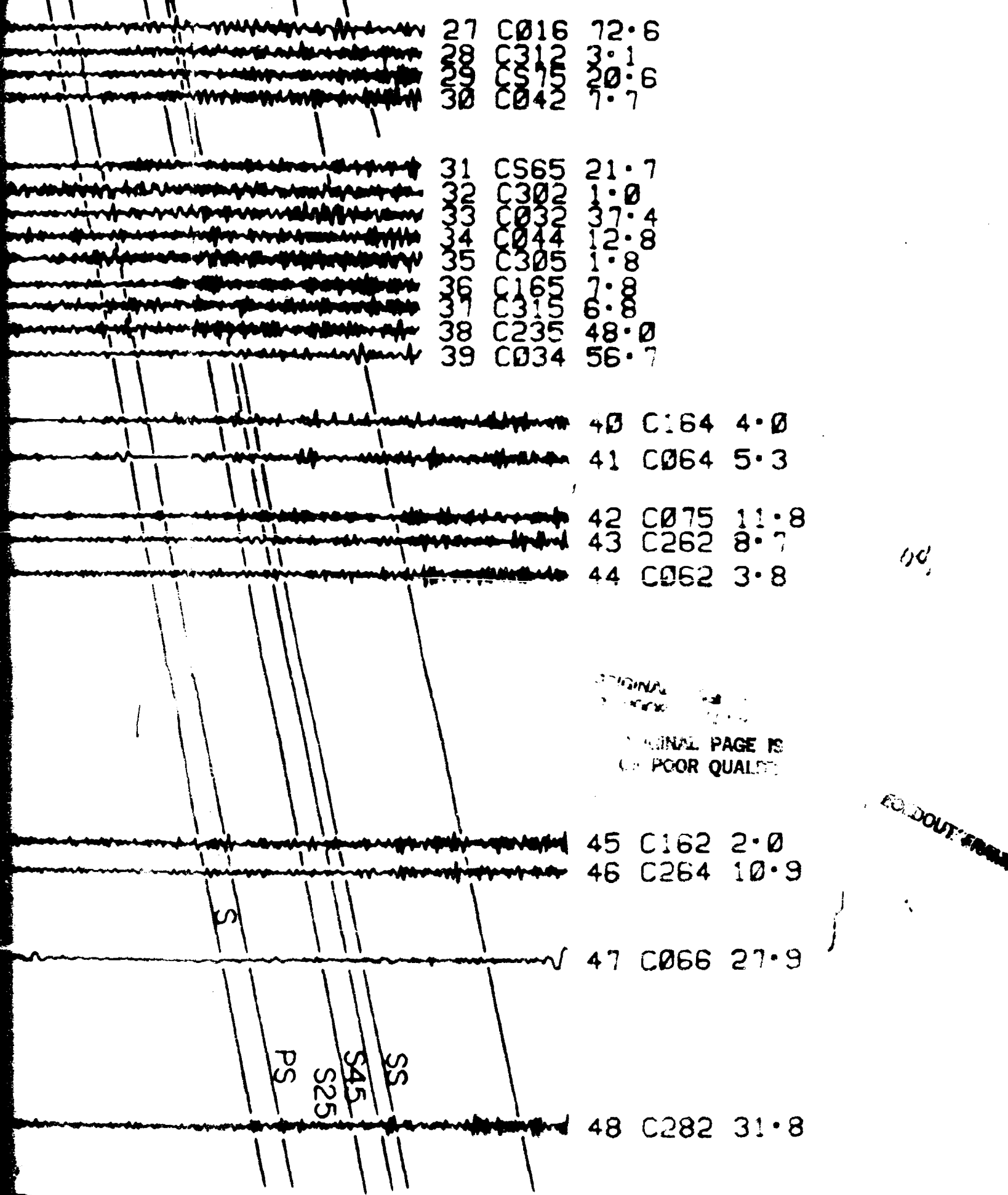
0.

60.

WELDOUT FRAME 5

TIME - P





27	C016	72.6
28	C312	3.1
29	C315	20.6
30	C042	7.7
31	CS65	21.7
32	C302	1.0
33	C032	37.4
34	C044	12.8
35	C305	1.8
36	C165	7.8
37	C315	6.8
38	C235	48.0
39	C034	56.7

40	C164	4.0
41	C064	5.3
42	C075	11.8
43	C262	8.7
44	C062	3.8

45	C162	2.0
46	C264	10.9
47	C066	27.9
48	C282	31.8

P (SECONDS)

120.

180.

240.

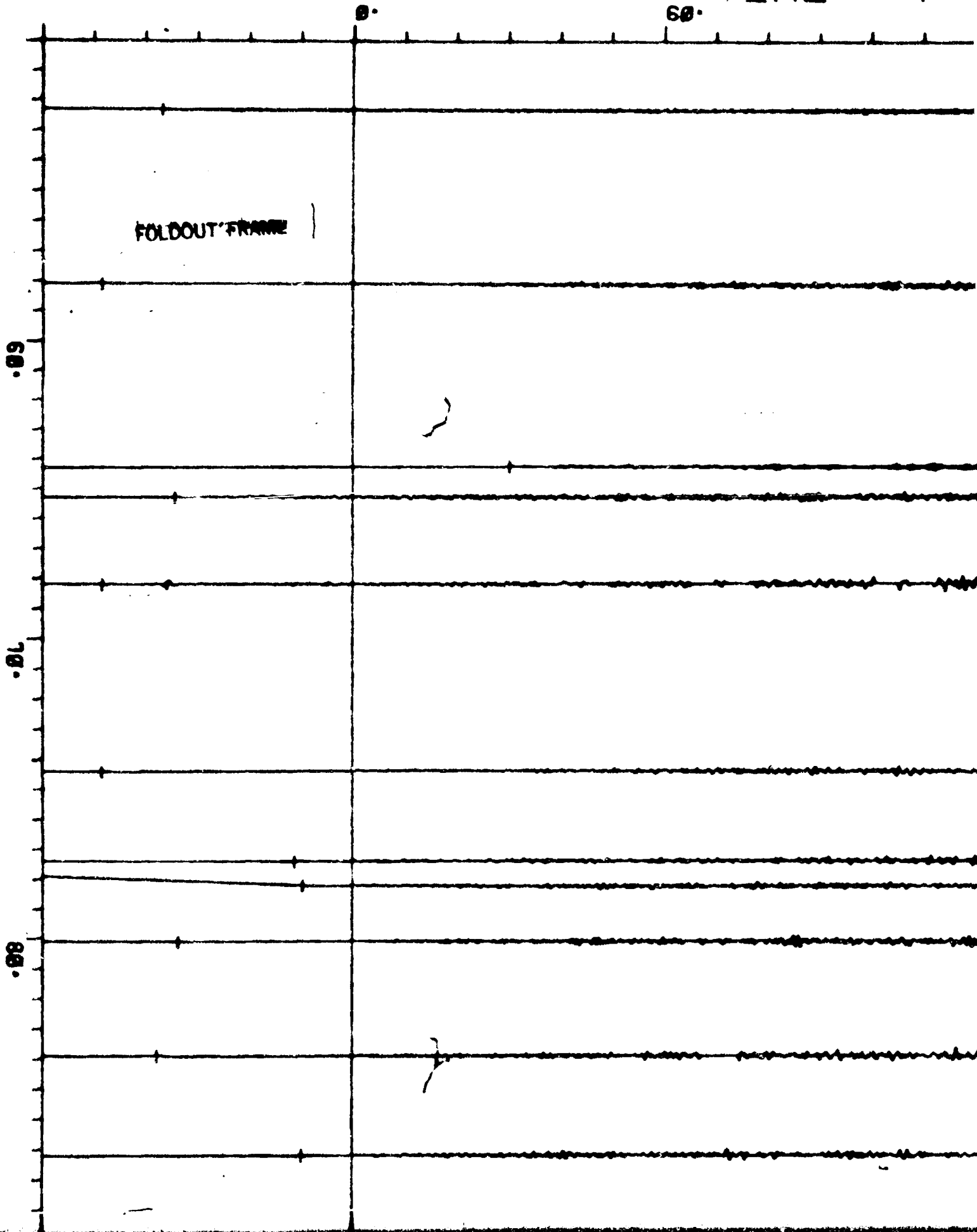
PS
S25
S45
SS

ORIGINAL
PAGE IS
OF POOR QUALITY

REPRODUCED FROM

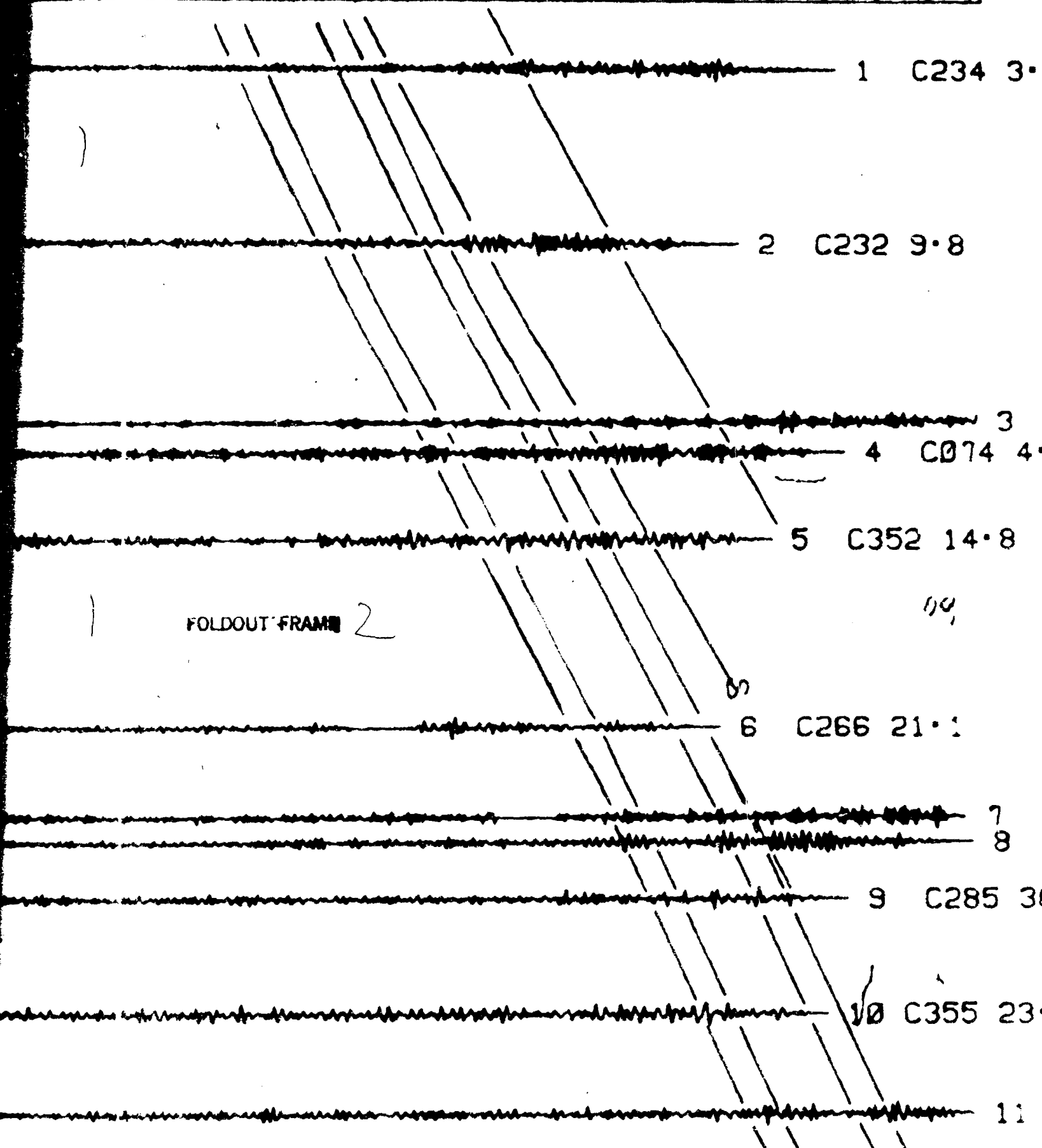
IMPACTS (T, 0.4-

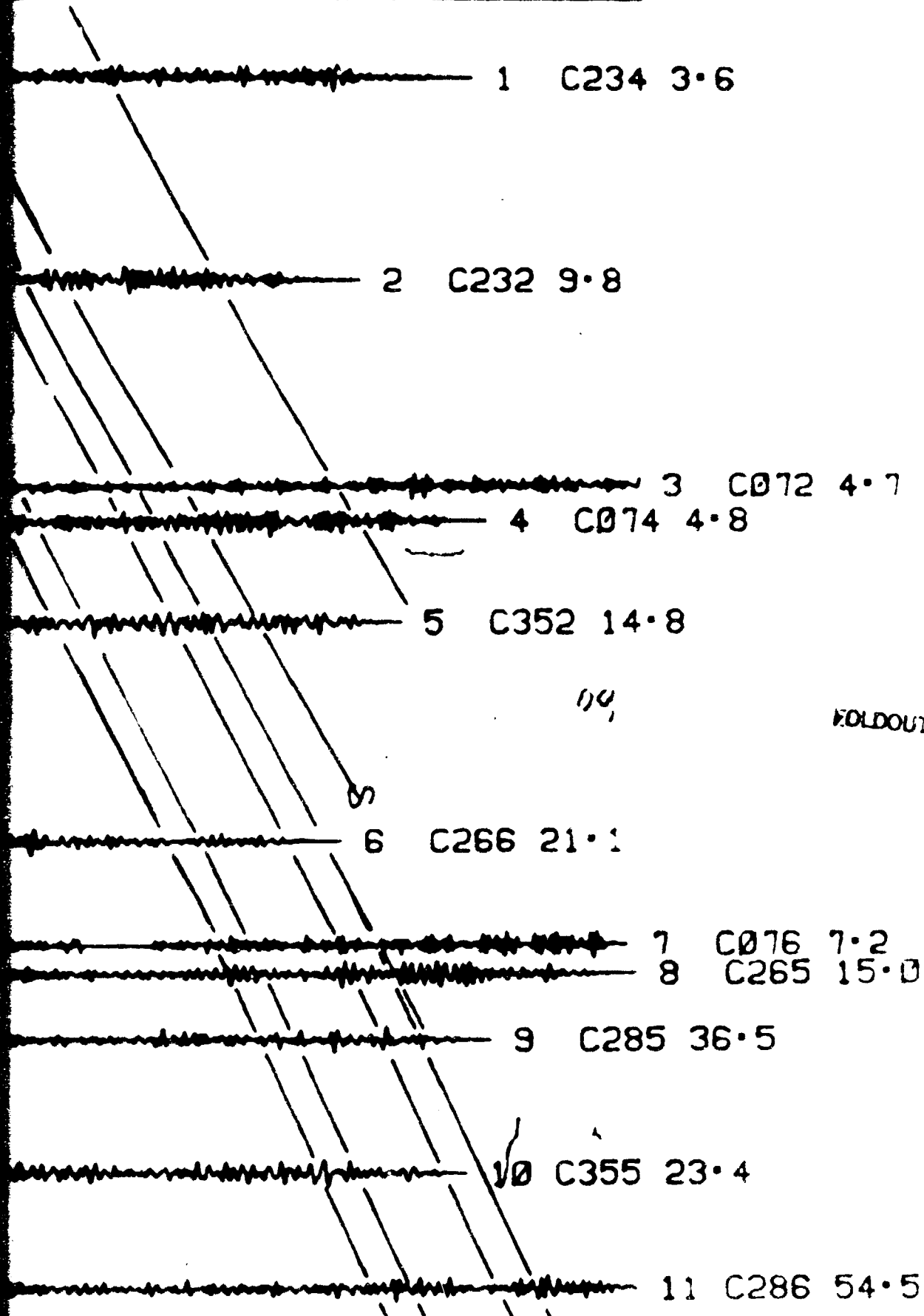
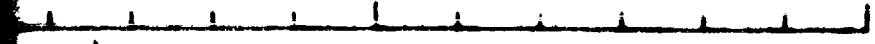
TIME - P



(SECONDS)

120 180 240





00,

FOLDOUT FRAME 

0

10

DISTANCE (DEGREE)

90°

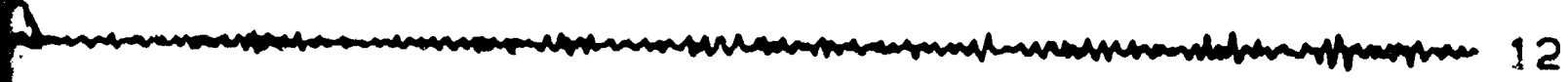
100°

110°

120°

130°

PORT OUT FRONT 4

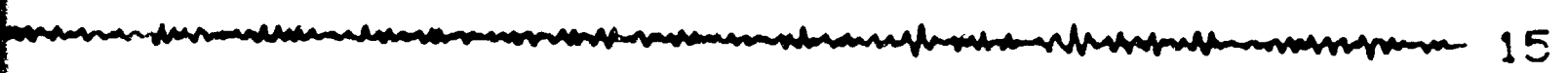


12



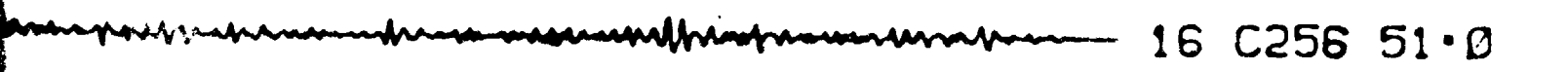
13

14 C

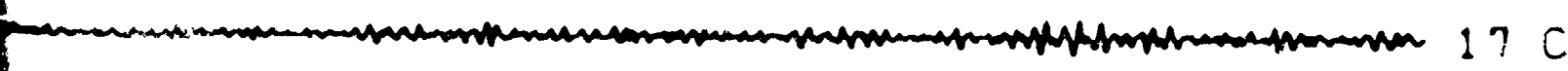


15

FOLDOUT FIGURE 5



16 C256 51.0



17 C

25
26

12 C252 25.6

13 C356 26.4

14 C254 30.1

15 C055 32.2

FOLDOUT FRAME 4

16 C256 51.0

17 C056 46.2

0.

130.

140.

150.

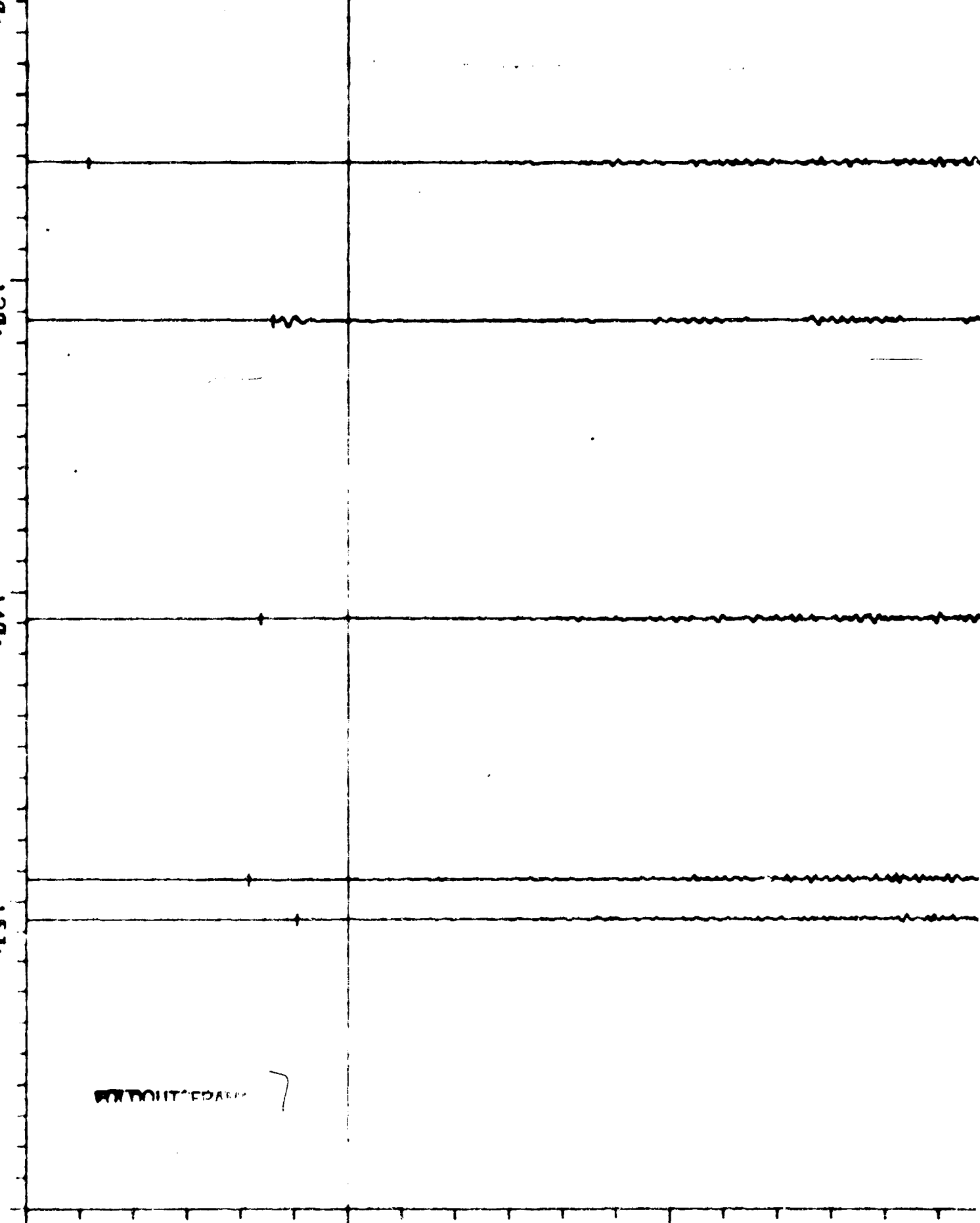
0.

60.

TIME - P

WITHOUT FEEDBACK

7



16 C256 51

FOLDOUT FRAME 8

19

- P (SECONDS) 120 180 240

16 C256 51.0

17 C056 46.2

18 C255 27.3

19 C054 13.0

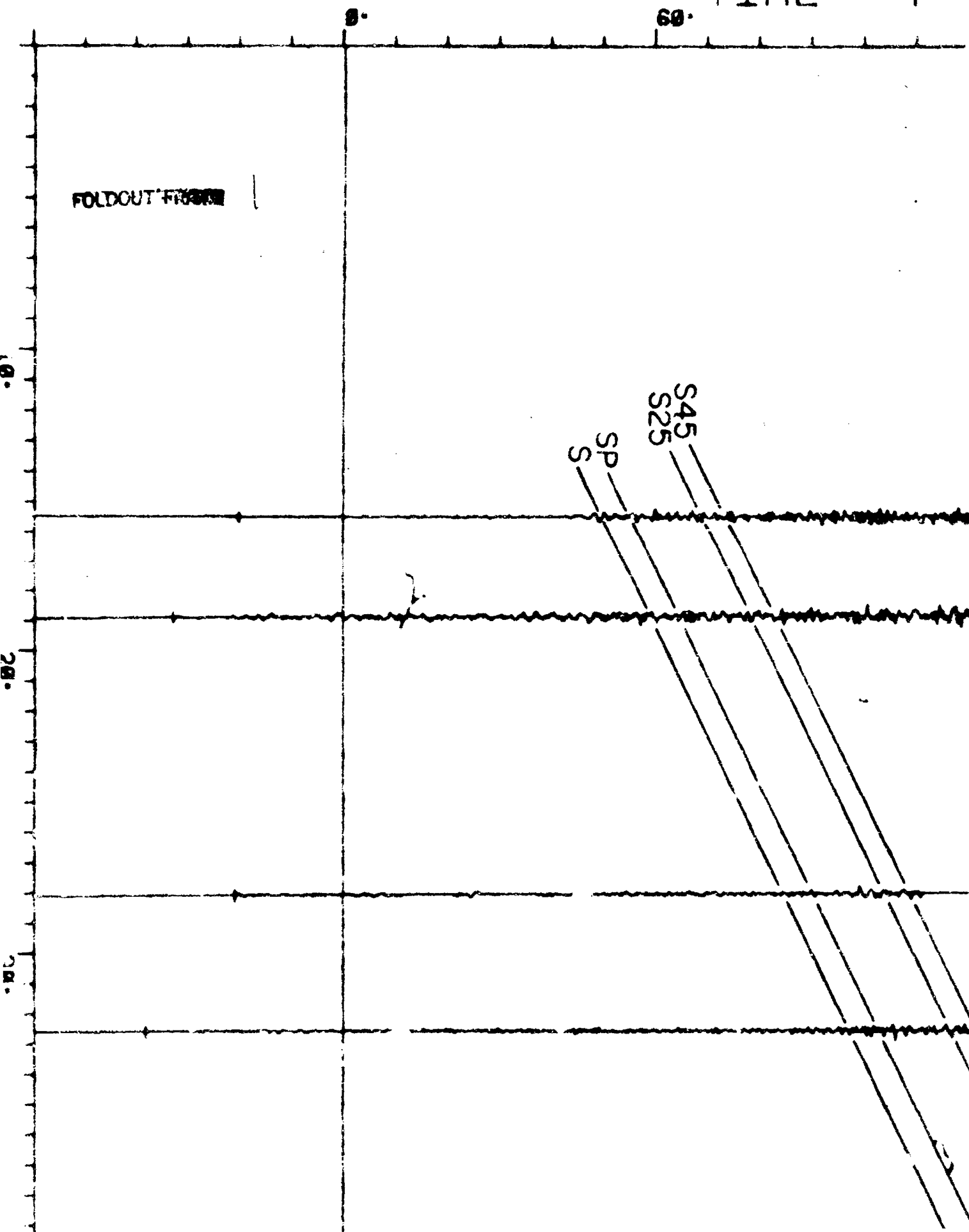
20 C052 8.0

FOLDOUT FILE 9

240

SHALLOW MOONQUAKES

TIME - P



WAKES (T, ' 0.4-1.5HZ)

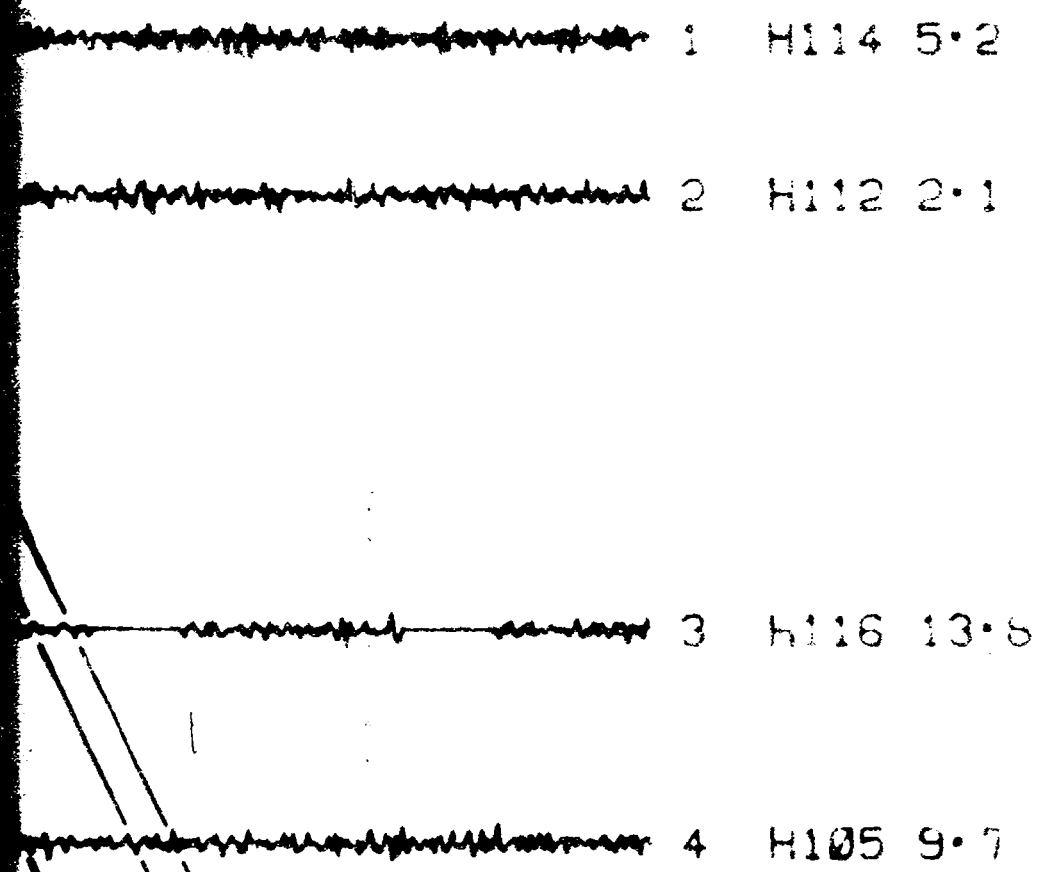
P (SECONDS)

120.

180.

240.

00,



EDUCATION CENTER 2

DISTANCE (DEGREE)

49°

59°

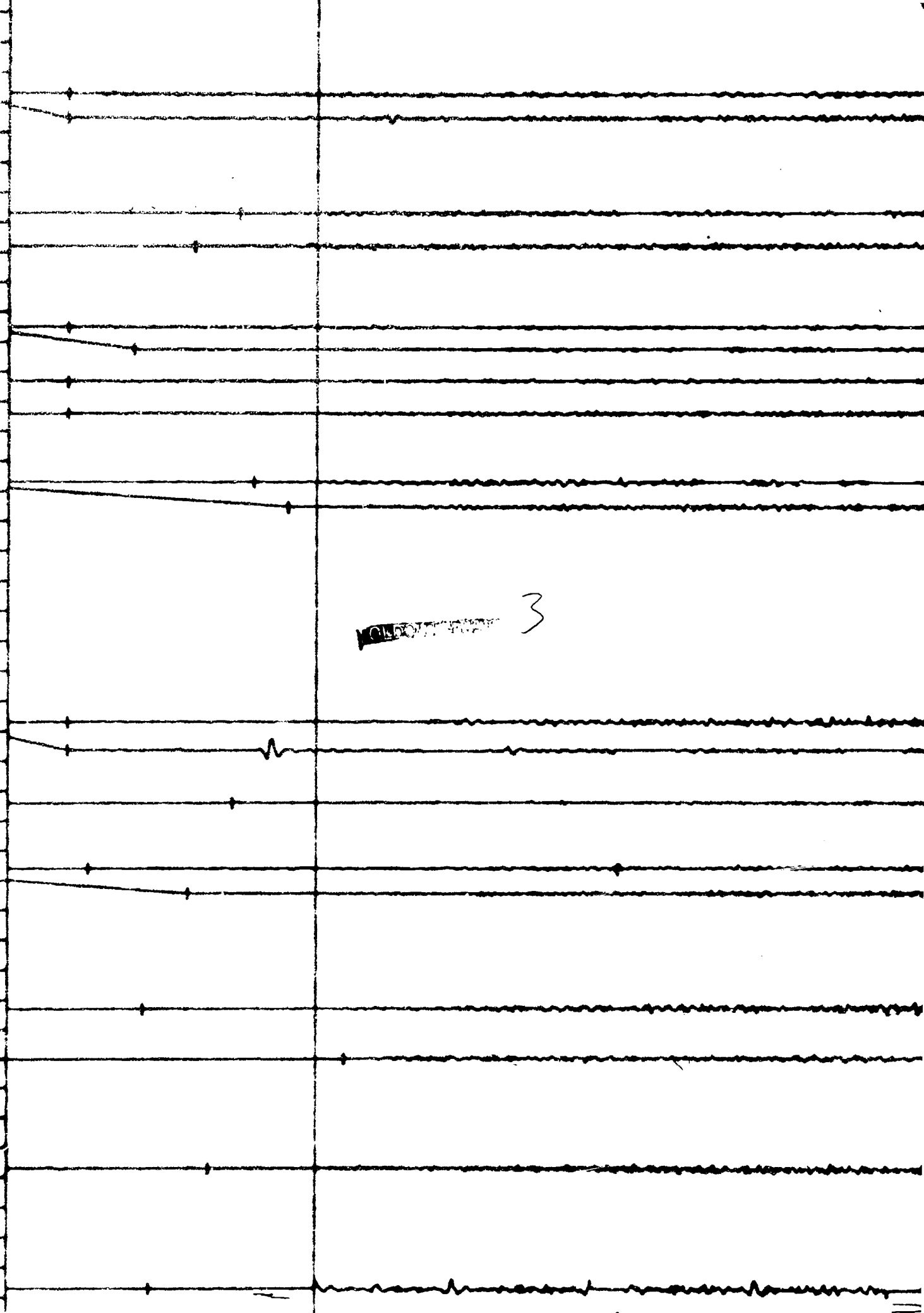
69°

79°

89°

~~NO. 100777~~

3



SS

5 H082 2.7
6 H084 4.3

7 H115 5.3
8 H045 4.1

9 H072 3.4
10 H012
11 H102 7.4
12 H104 13.8

FOLDOUT FRAME 4

15 H026 15.8
16 H025 18.4

17
18 H106 11
19 H0

20 H032

22 H

23 H035

SS

3.4
H012 9.4
2 7.4
13.8

13 H074 2.4
14 H014 8.7

FOLDOUT FRAME



15.8
18.4

17 H094 24.2

06 11.5
19 H092 15.1

H032 33.8

21 H046 2.8

22 H034 39.4

H025 100.0

.00

.06

1.00

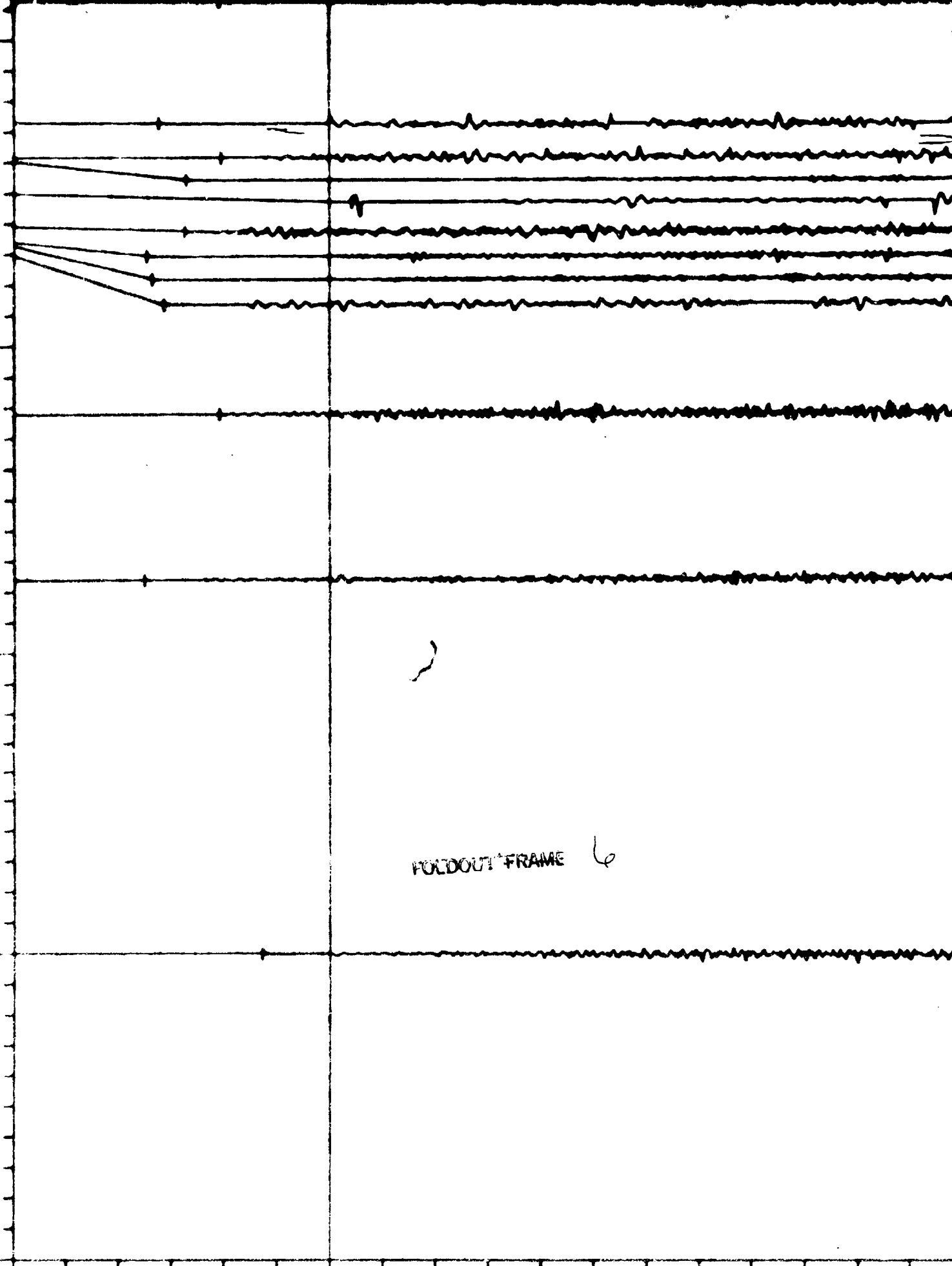
11.0

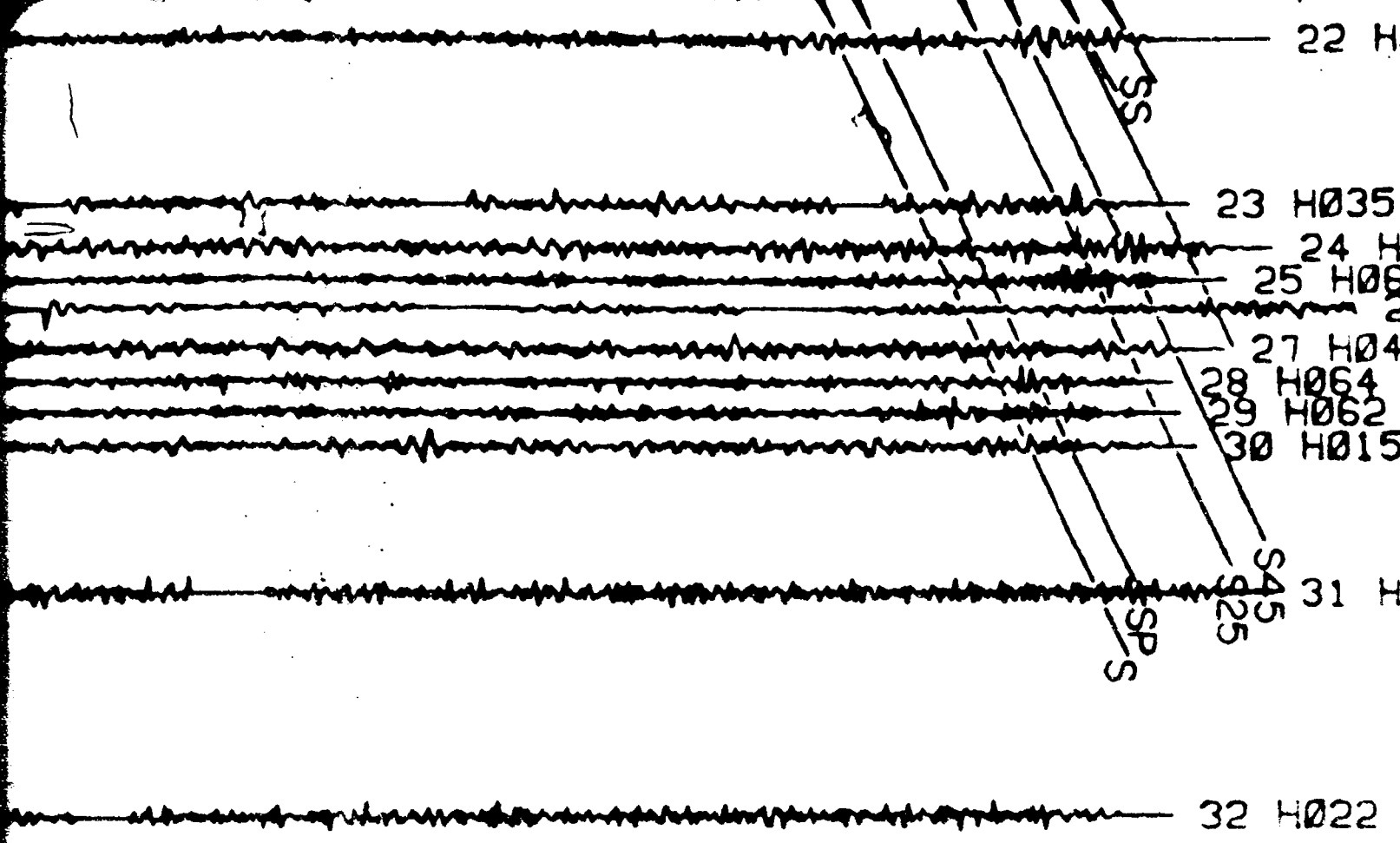
0°

60°

TIME - P

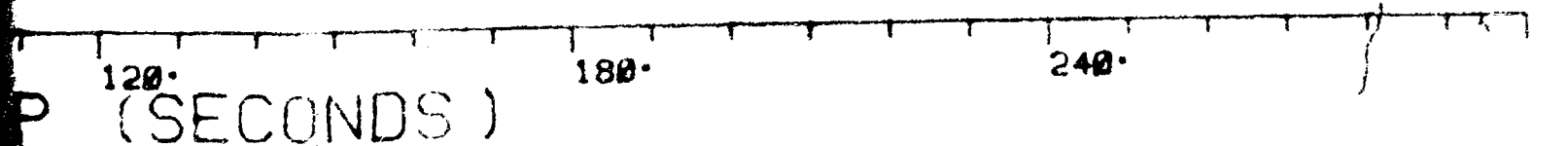
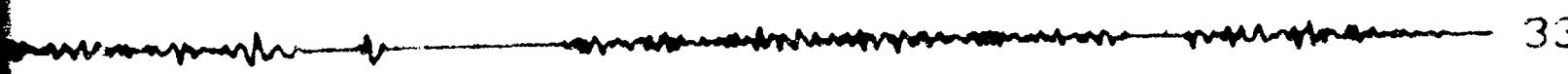
FOLDOUT FRAME 6





BOREHOLE FRAME 7

04



22 H034 39.4

23 H035 100.9

24 H044 1.0

25 H056 44.4

26 H016 17.8

27 H042 1.2

28 H064 2.0

29 H062 20.1

30 H015 10.6

31 H024 4.6

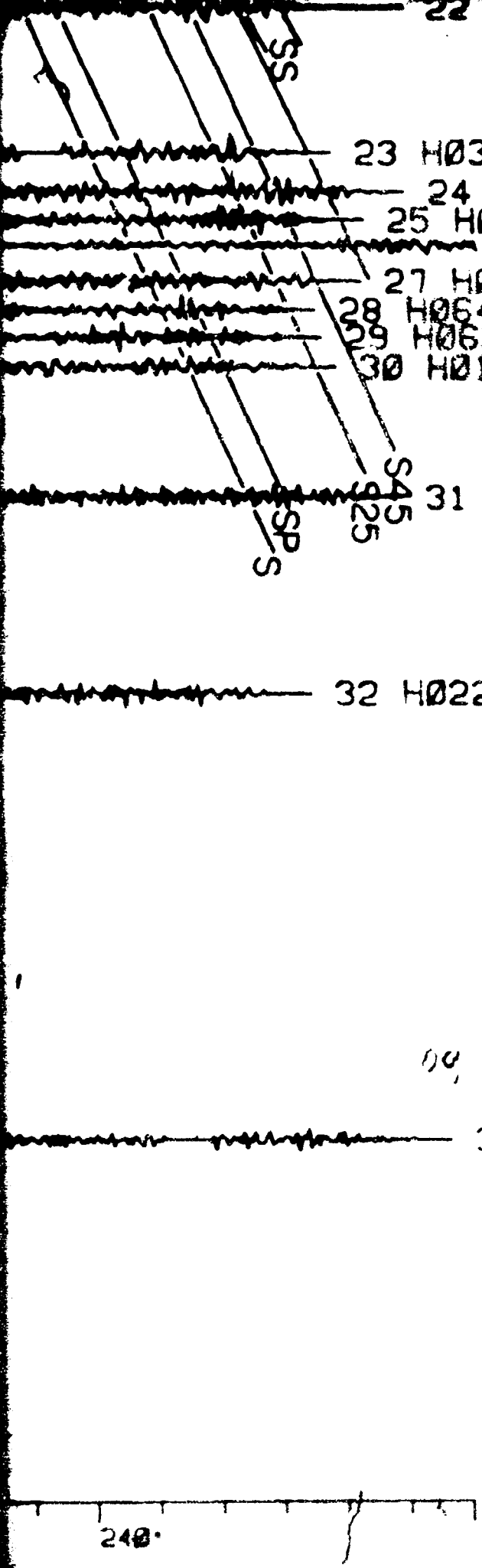
32 H022 3.0

RECORDED BY 8

00

33 H036 69.8

240

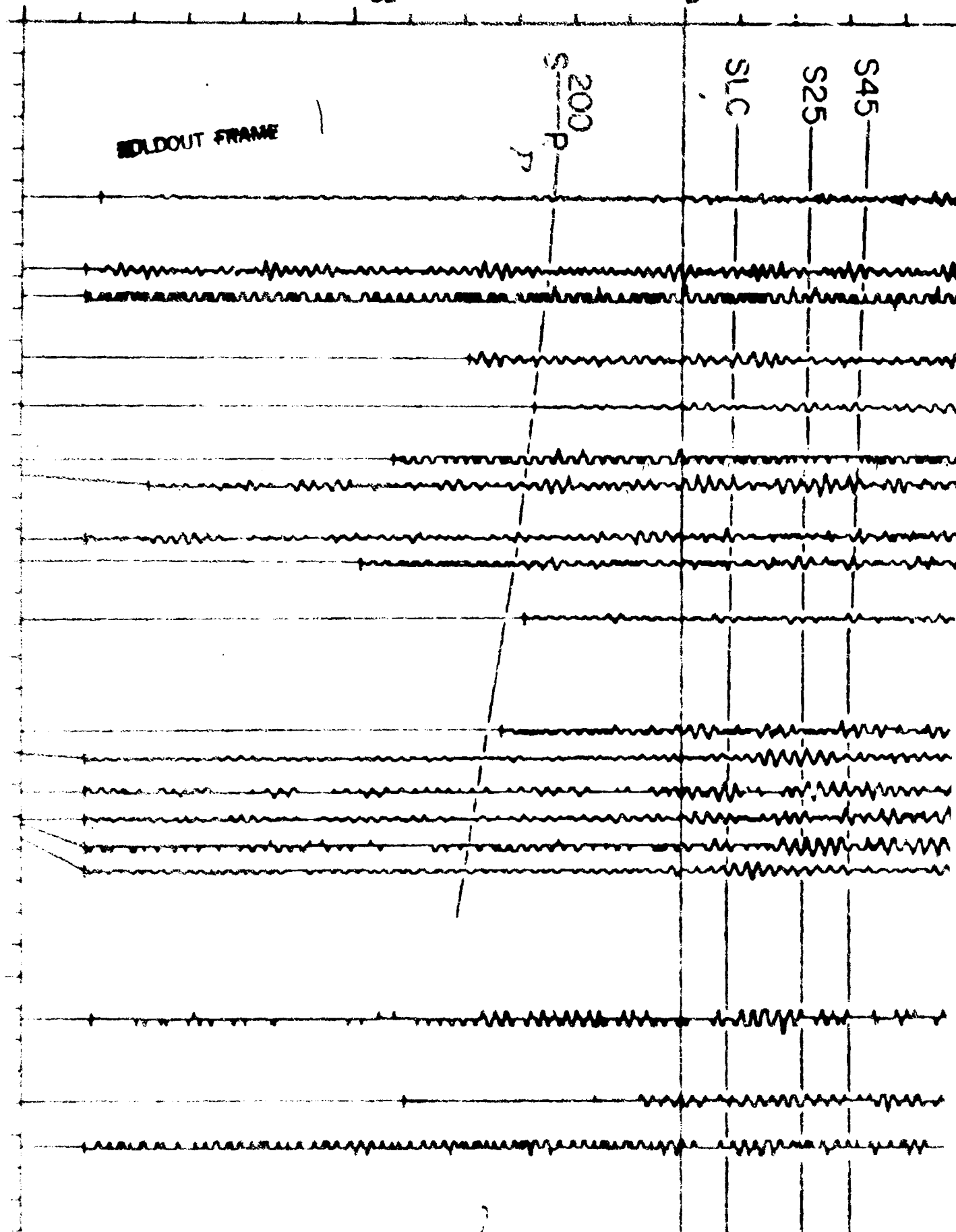


DEEP MOONQUAKES

TIME -

-82-

8.



BOLDOUT FRAME

S 200 P

SLC

S25

S45

S (SECONDS)

60.

120.

180.

1 A012 145

2 A014 35.0

3 A166 15.0

4

5

7

8 A205

9 A175 40.0

1

1

16 A016 120.0

17 A736 25.0

18 A015 50.0

19 A146 20.0

20 A206 35.0

21 A176 15.0

2

24 A446 15.0

1 A012 145.0

2 A014 35.0

4 A345 30.0

5 A202 30.0

7 A346 15.0

8 A205 30.0

9 A175 40.0

10 A422 25.0

11 A172 35.0

15 A425 25.0

A016 120.0

17 A736 25.0

30.0

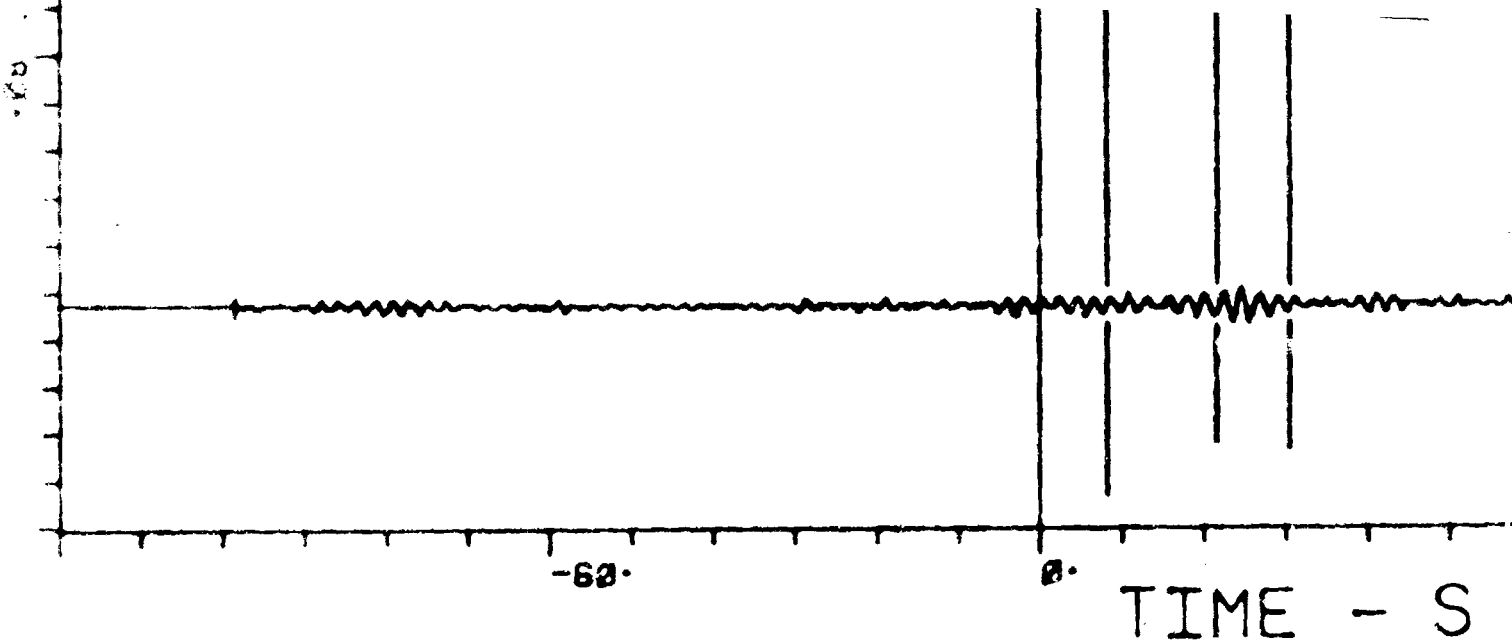
46 20.0

VOID OUT FRAME 3

21 A176 15.0

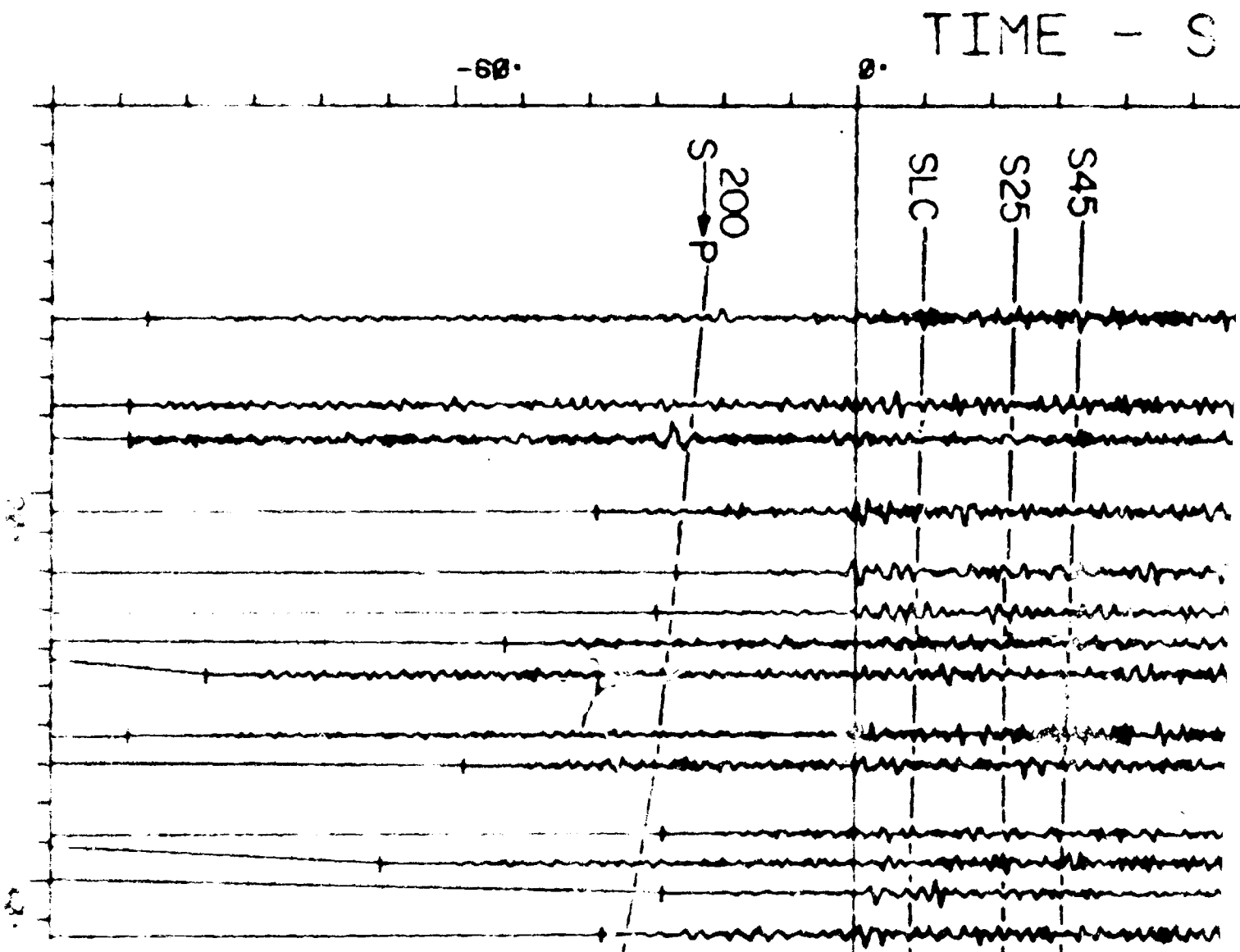
22 A426 20.0

24 A446 15.0

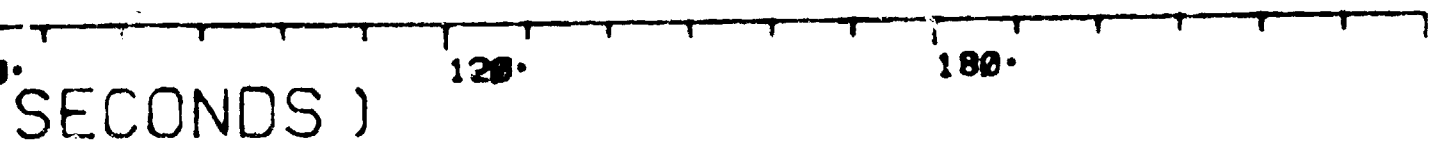


FOLDOUT FRAME 4

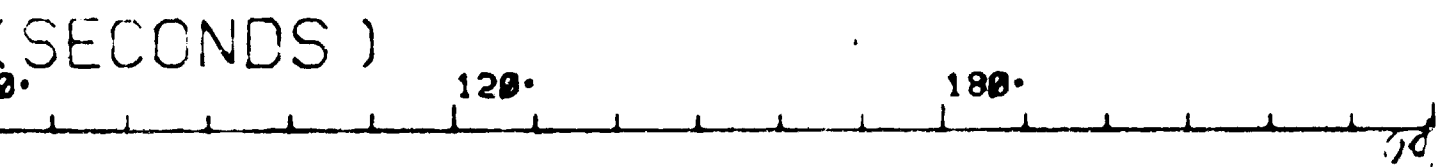
DEEP MOONQUAKES



25 A336^{3d} 35.0



(R, 0.4-1.5HZ)



FOR DOIT FRAME 5

1 A012 6.0

2 A014 2.7

3 A166 4.2

4 A3

5 A2

6 A2

7 A3

8 A205 3.4

9 A175 4.5

10 A4

11 A1

12 A42

13 A1

14 A2

15 A1

25 A336^{3d} 35.0

180.

HZ)

180.

FM. DOUT FRAMES 6

1 A012 6.0

2 A014 2.7
4.2

4 A345 1.7

5 A202 2.3

6 A204 2.4

7 A346 2.1

8 A205 3.4

9 A175 4.5

10 A422 0.8

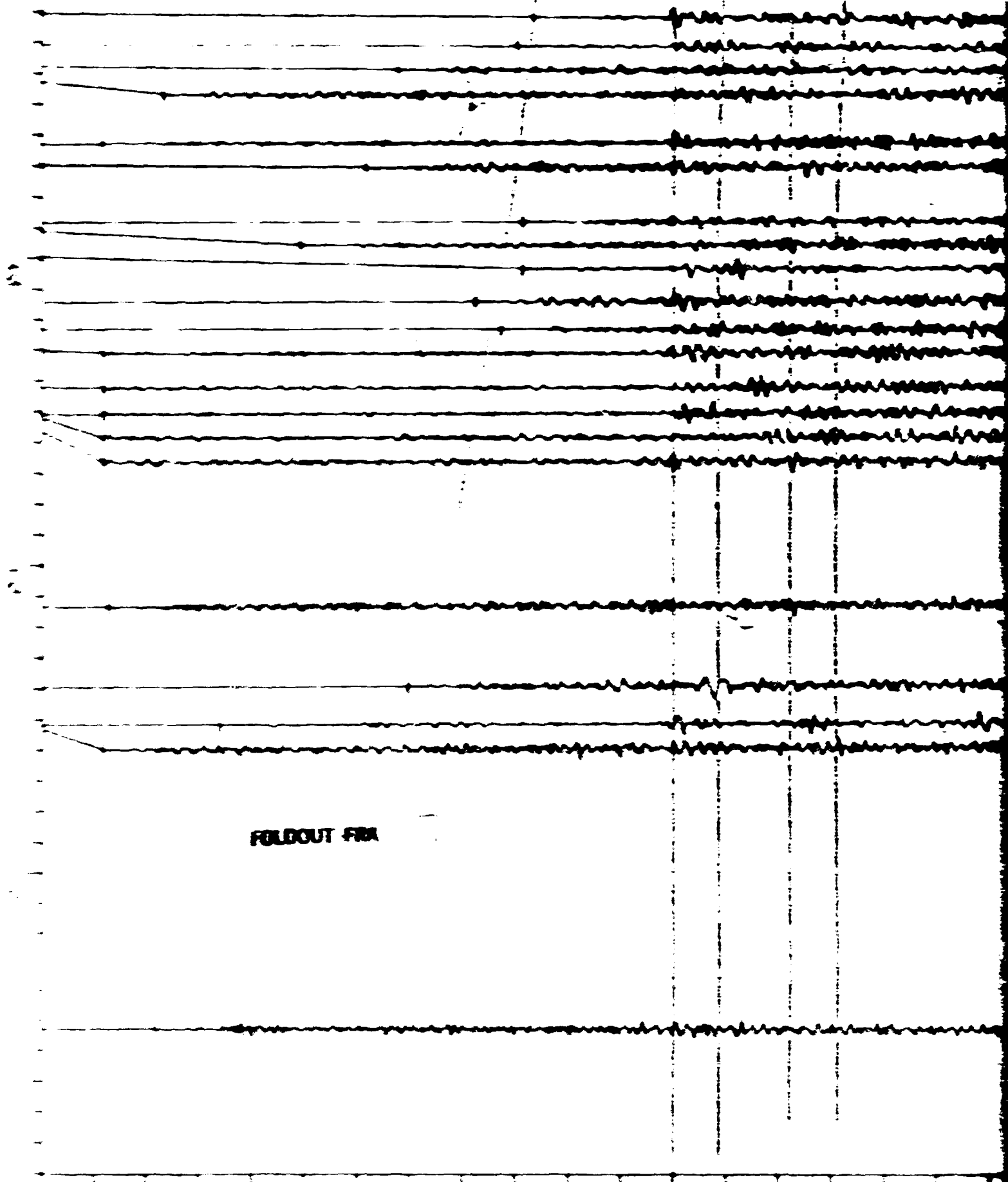
11 A172 1.3

12 A424 2.1

13 A174 2.1

14 A284 1.2

15 A425 2.4

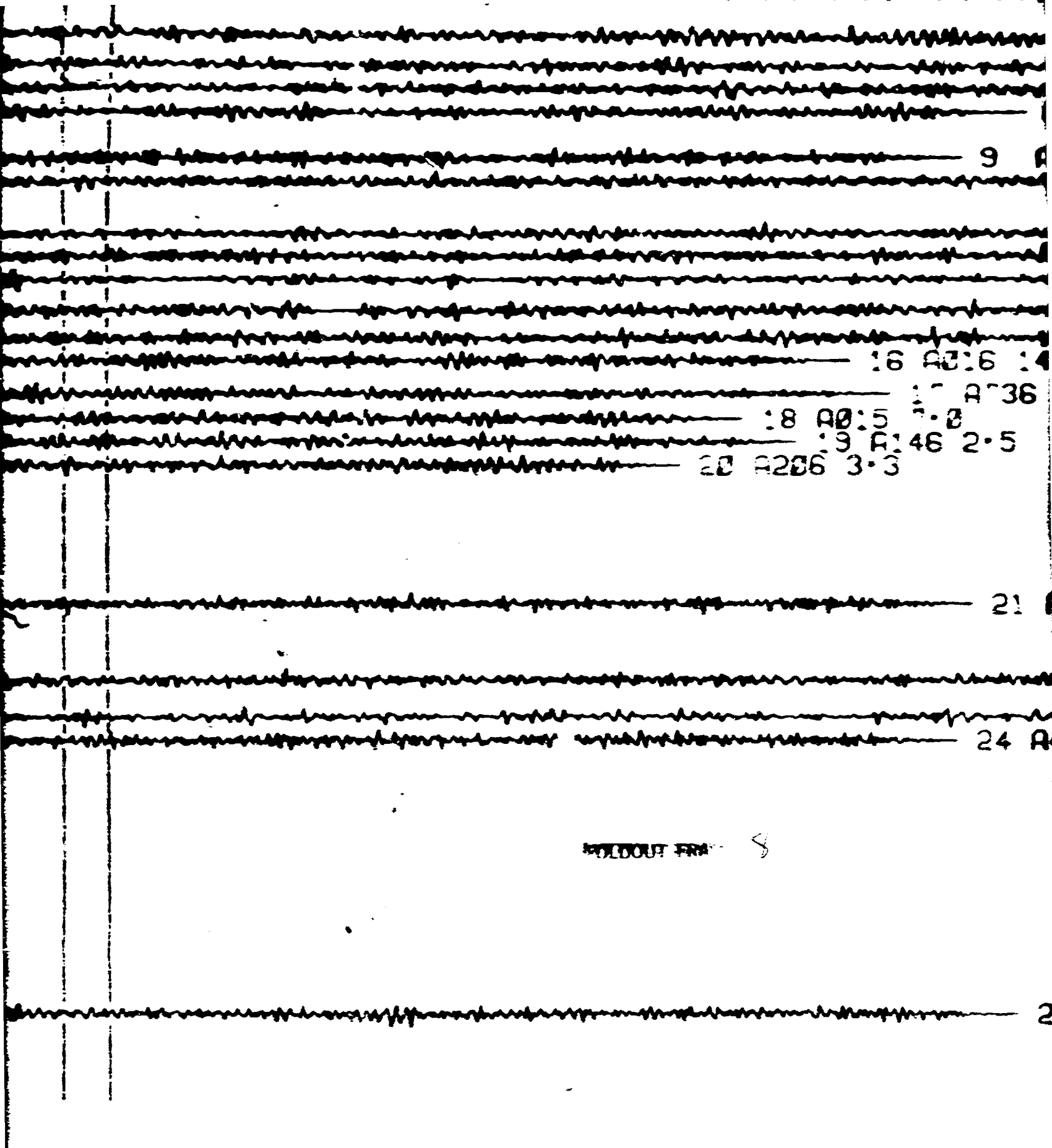


FOLDOUT FIB

-22-

2.

TIME - S



9

16 A216 14

17 A36

18 A0:5 2.8

19 A146 2.5

20 A286 3.3

21

24 A

2

WILDOUT FRA 8

TIME - S (SECONDS)

60

120

180

4 A345 1.7
 5 A202 2.3
 6 A204 2.4
 7 A346 2.1
 8 A205 3.4
 9 A175 4.5
 10 A422 0.8
 11 A172 1.3
 12 A424 2.1
 13 A174 2.1
 14 A284 1.2
 15 A425 2.4
 16 A216 14.8
 17 A136 2.7
 18 A15 2.2
 19 A146 2.5
 20 3.3

21 A176 3.6

22 A426 2.5

23 A444 1.1

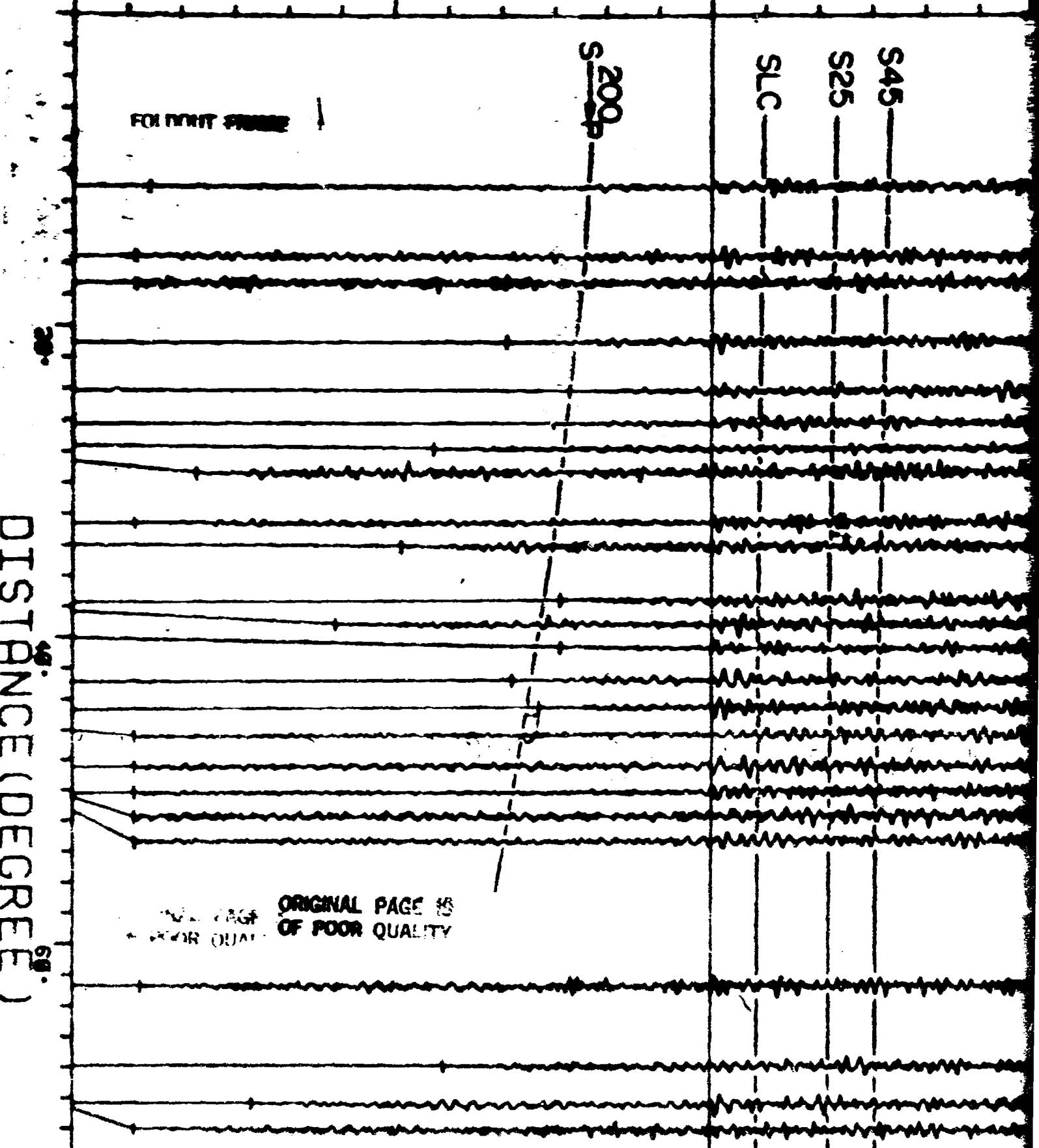
24 A446 2.8

25 A336 3.4

FOLDOUT FRA 9

DEEP MOONQUAKES

TIME - S



FOURTH PAGE

S200

SLC

S25

S45

DISTANCE (DEGREE)

ORIGINAL PAGE IS
OF POOR QUALITY

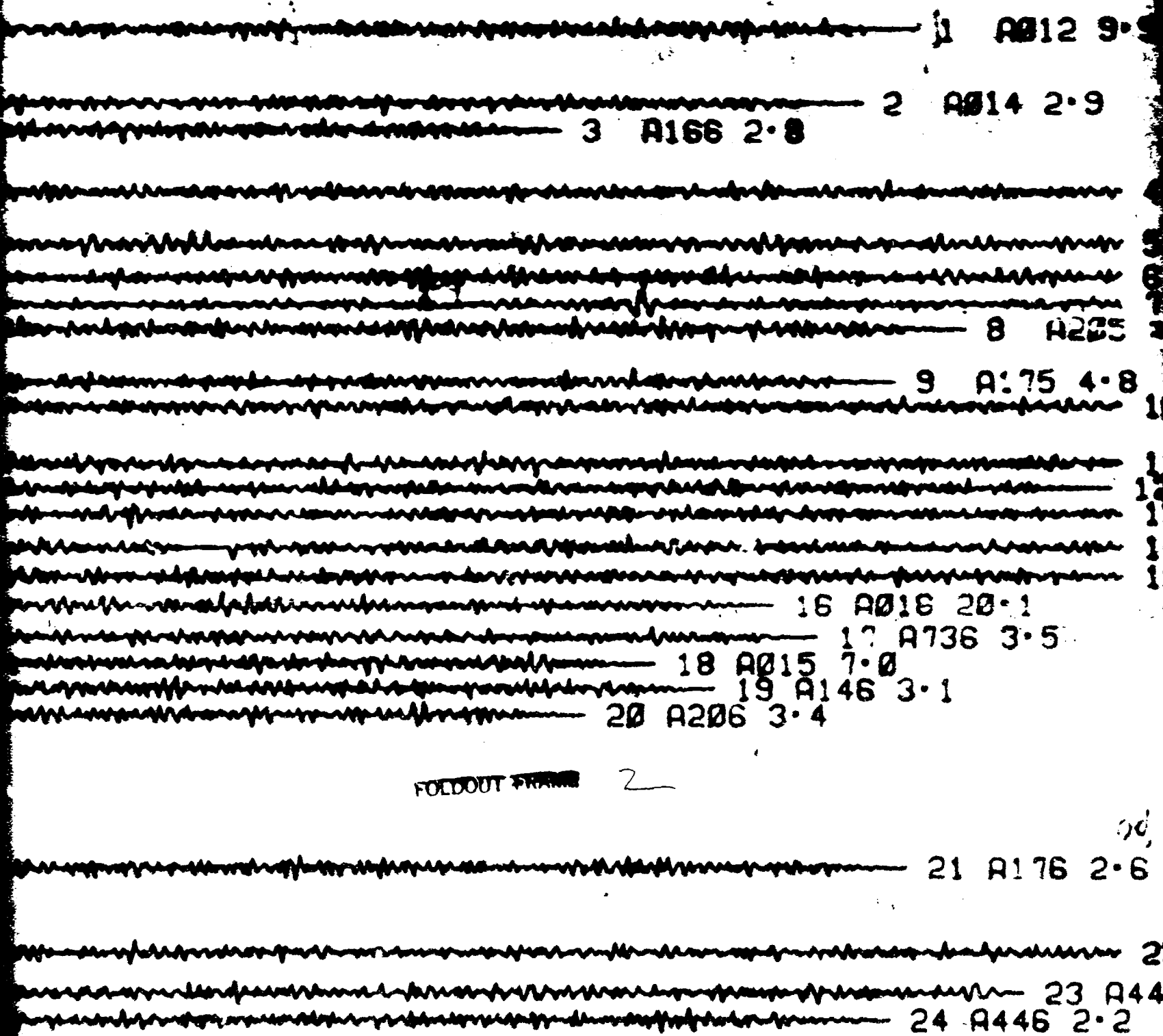
S (1,000.4-1.5HZ)

S (SECONDS)

90°

120°

180°



FOLDED OUT FRAME 2

12 9.5

2.9

4 A345 2.1

5 A202 2.5

6 A204 2.3

7 A346 3.0

A205 3.0

5 4.8

10 A422 1.1

11 A172 1.2

12 A424 1.9

13 A174 2.0

14 A284 1.5

15 A425 2.9

5

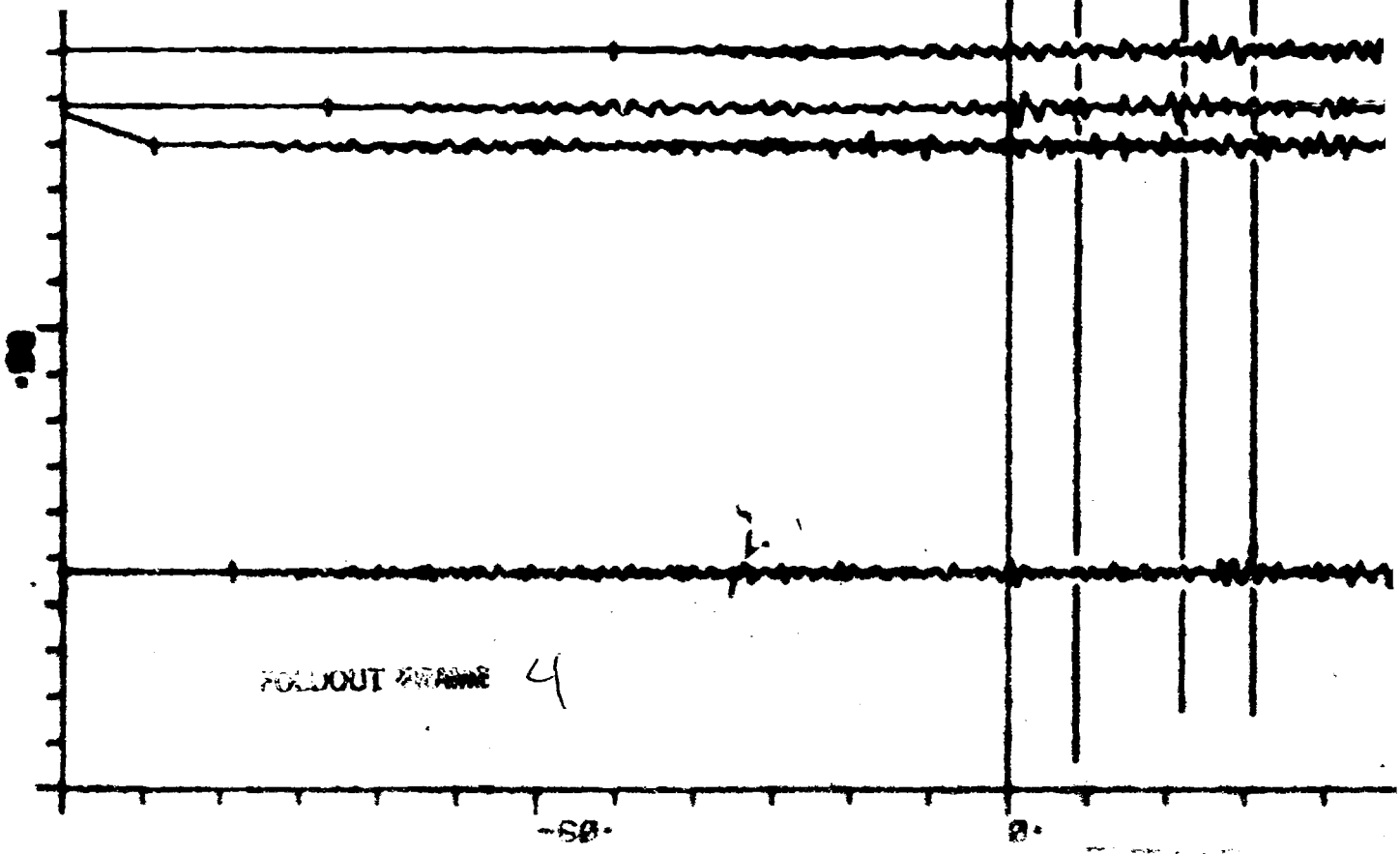
FOLDOUT FRAME

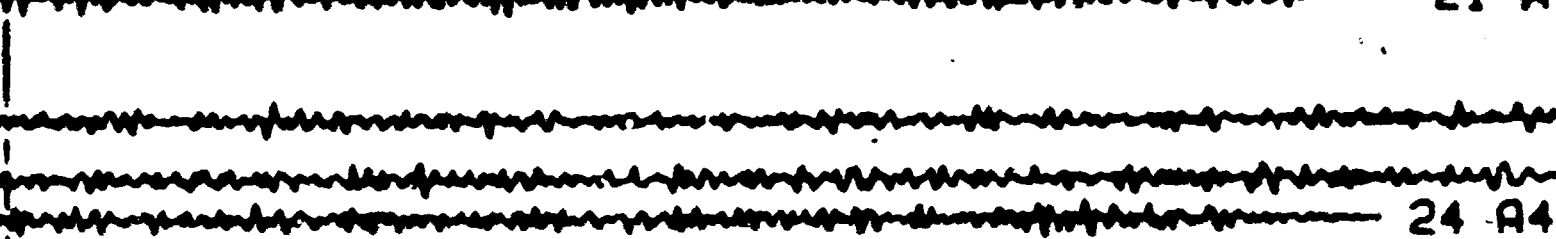
6 2.6

22 A426 2.5

23 A444 1.3

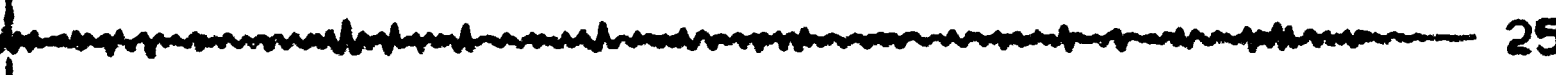
2.2



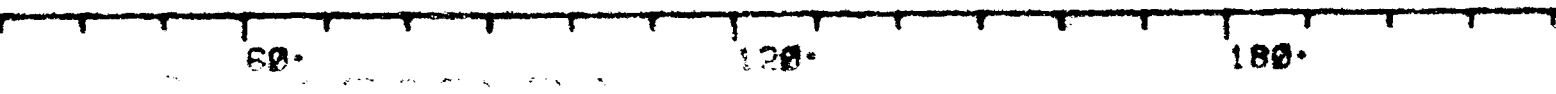


24 A4

EMERALD LINDSEY S



25



60

120

180

21 A176 2-6

22 A426 2-5

23 A444 1-3

24 A446 2-2

POSSIBLE FRAMES

30

25 A336 4-4

180-

4--1.5HZ)

P (SECONDS)

120.

180.

240.

7
2
6
3

CS62 122.2
C364 4.4
CS42 129.8
C316 65.4
147.1
C166 50.4
C022 20.7
C012 172.4

CS64 57.8

~~20~~ C065 71.1

~~21~~ CS72 37.3

~~22~~ CS52 36.7

EXHIBIT INDEX 2

15.

20.

25.

30.

M T W T F S S

35

3

5

5 35

23 C236 39.5

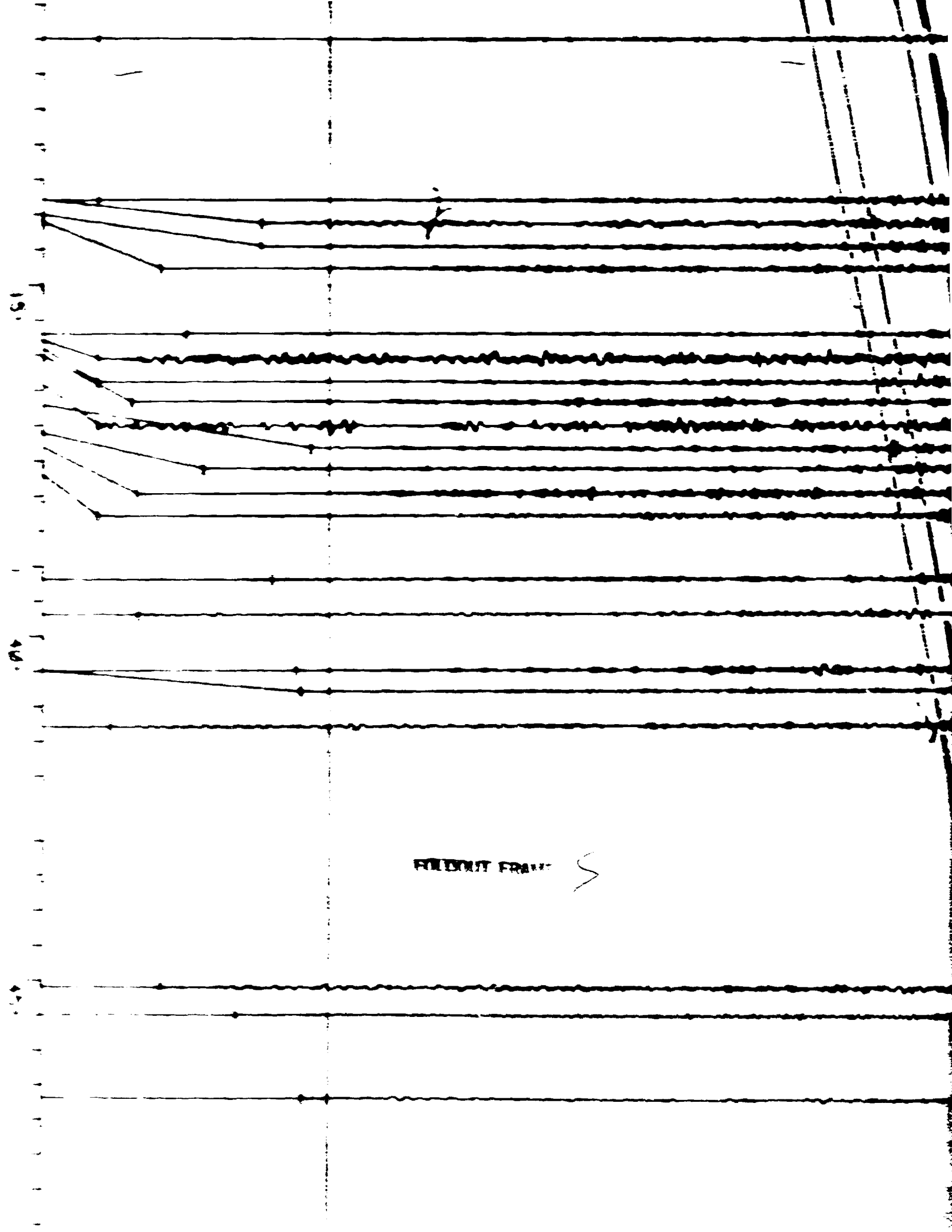
FOLDOUT FRAME

4

24 CS76 15.5

25 C045 25.6

26 C015 93.3



FILMOUT FRAME



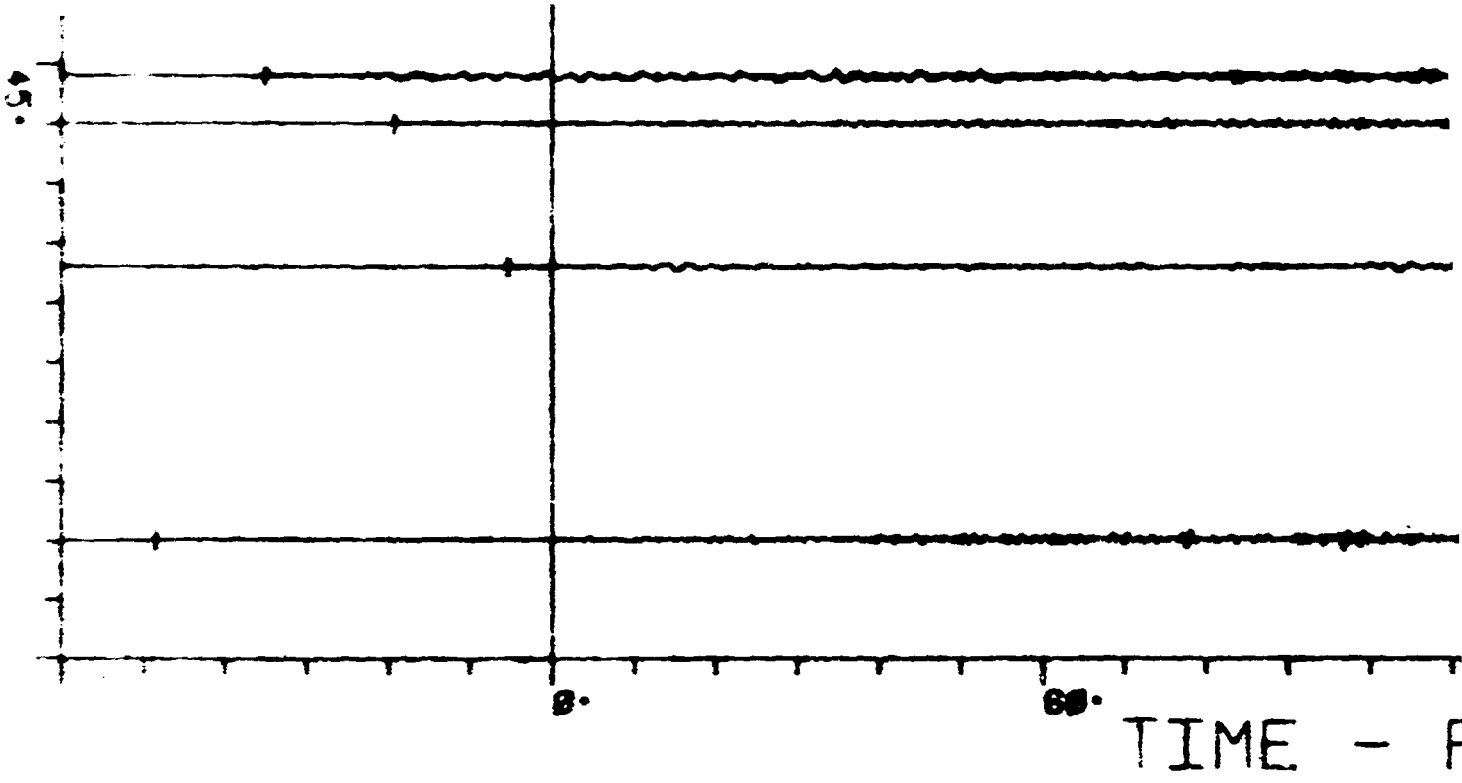
27	C016	64-1
28	C312	3-0
29	CS75	17-7
30	C042	7-6

31	CS65	22-5
32	C302	1-1
33	C032	42-2
34	C044	16-3
35	C305	2-3
36	C165	7-1
37	C315	9-3
38	C235	63-9
39	C034	45-9

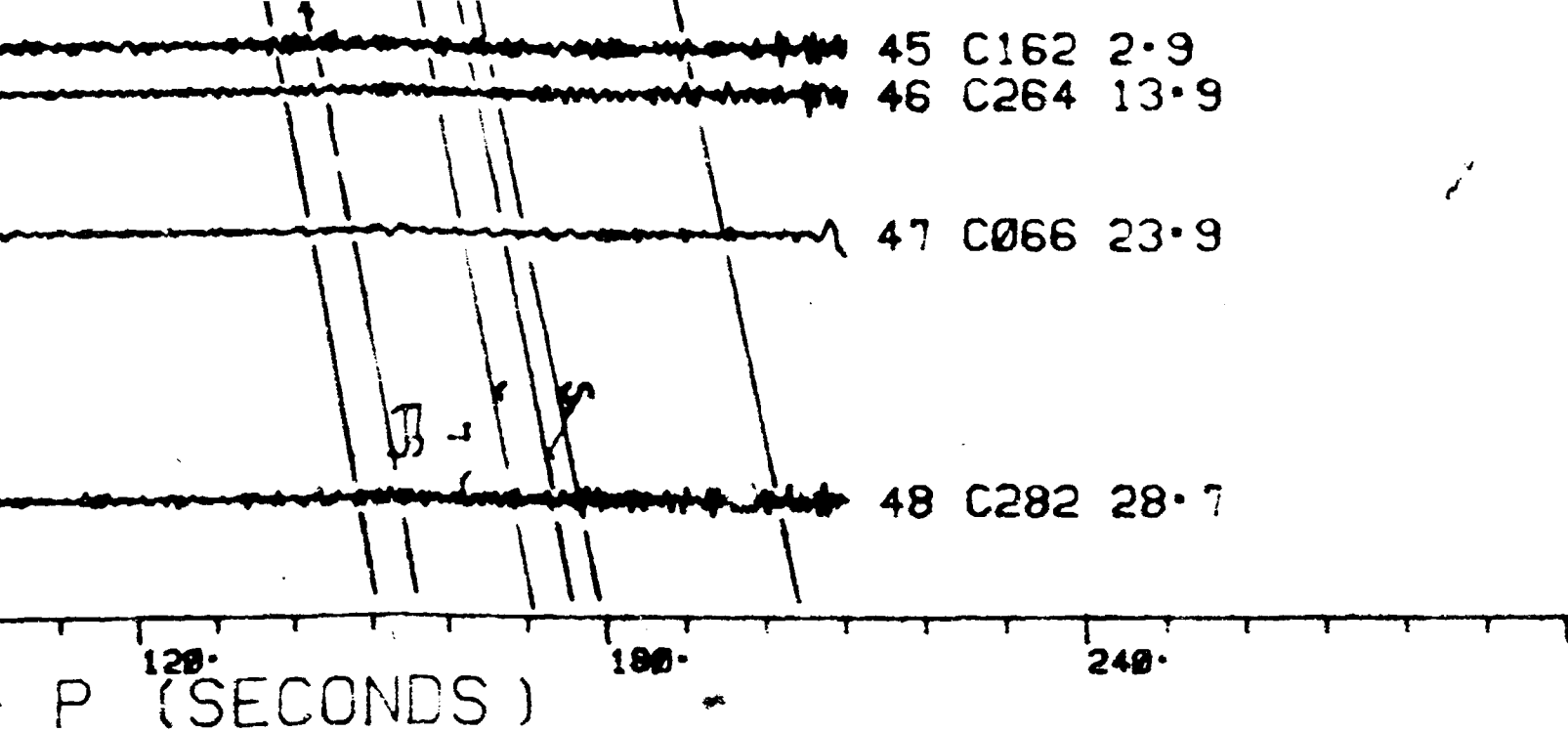
40	C164	5-2
41	C064	4-5
42	C075	11-1
43	C262	9-8
44	C062	3-0

FOLDOUT FRAME 6

45	C162	2-9
46	C264	13-9
47	C066	23-9
48	C282	28-7



FOLDOUT FRAME 7



FOURTH FRAME 8

SHALLOW MOONQUAKE

TIME - P (S)

0.

60.

120.

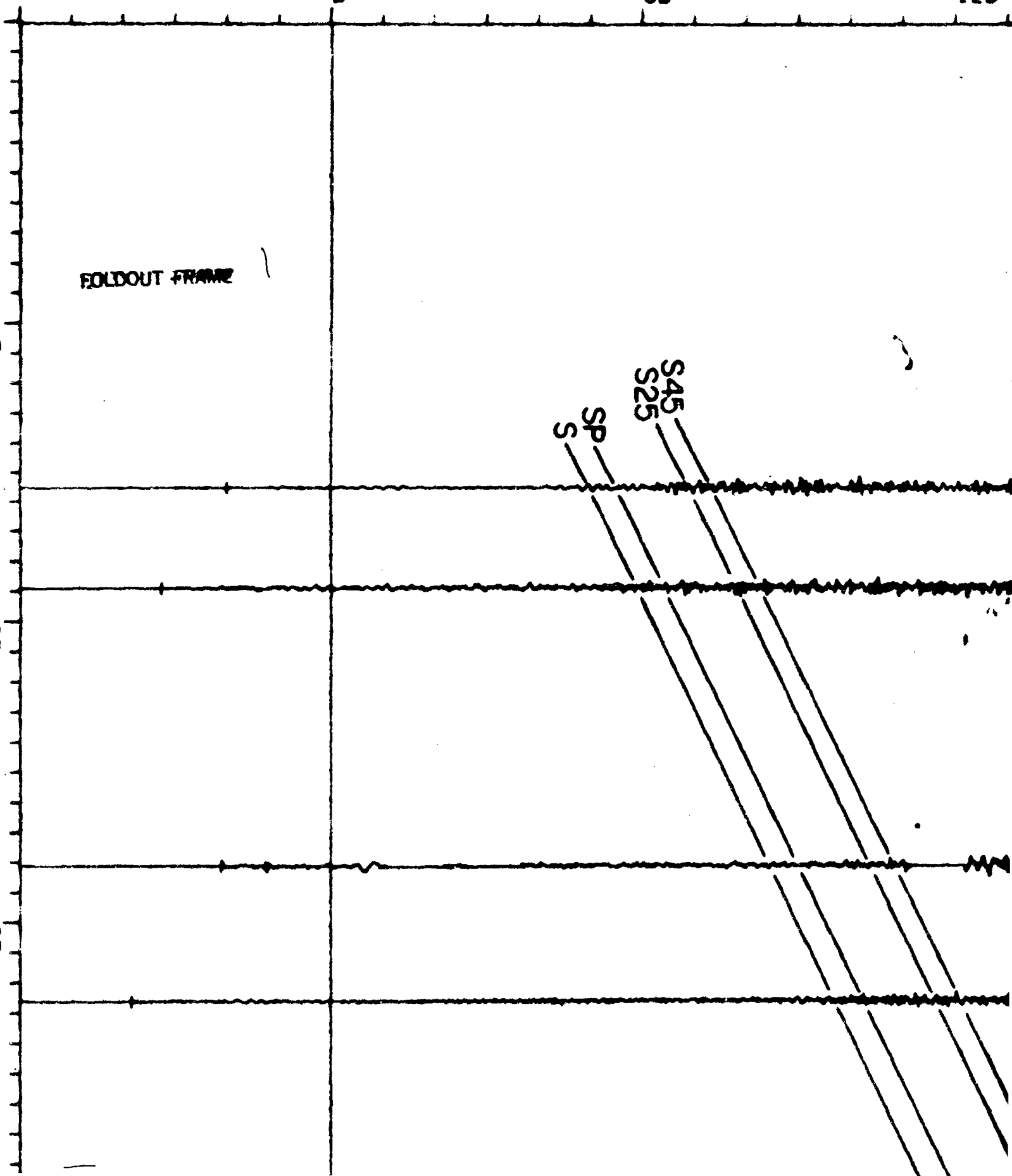
FOLDOUT FRAME

10.

20.

30.

S
SP
S25
S45



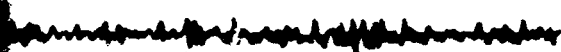
AKES (R, ' 0.4-1.5HZ)

(SECONDS)

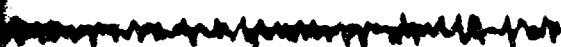
120.

180.

240.



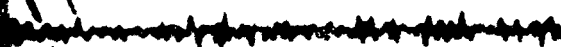
1 H114 4.6



2 H112 2.4



3 H116 9.0



4 H105 10.4

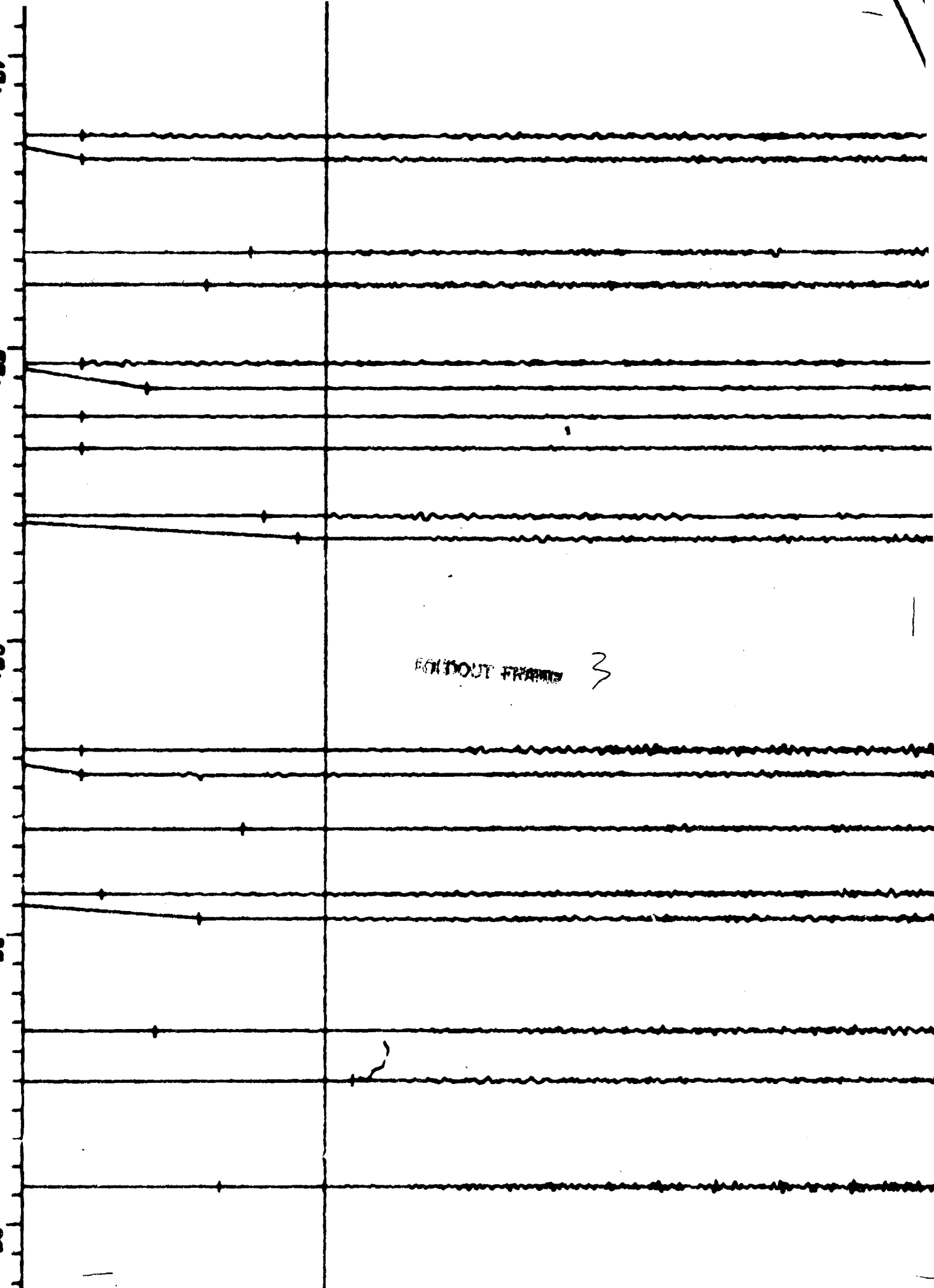
FOOTOUT FRAME

21

DISTANCE (DEGREE)

40.
50.
60.
70.
80.

EXCLUDED FRAMES 3



SS

5 H082 2.3
6 H084 4.1

7 H115 5.4
8 H045 4.4

9 H072 2.5
10 H012 9.4
11 H102 8.2
12 H104 15.3

13 H
14

RODOUT FRAME 4

15 H026 9.6
16 H025 16.1

17 H0

18 H106 10.0
19 H092

20 H032 40

21

22 H03

23⁰⁰ H035 9

SS

72 2.5
10 H012 9.4
H102 8.2
104 15.3

13 H074 2.5
14 H014 8.3

26 9.6
25 16.1

17 H094 17.4

H106 10.0
19 H092 12.6

20 H032 40.4

21 H046 3.7

22 H034 36.7

23 H035 93.6

24 H044 1.0

25 H066 44.4

26 H016 7.1

FOLDOUT FRAME S

98.

100.

110.

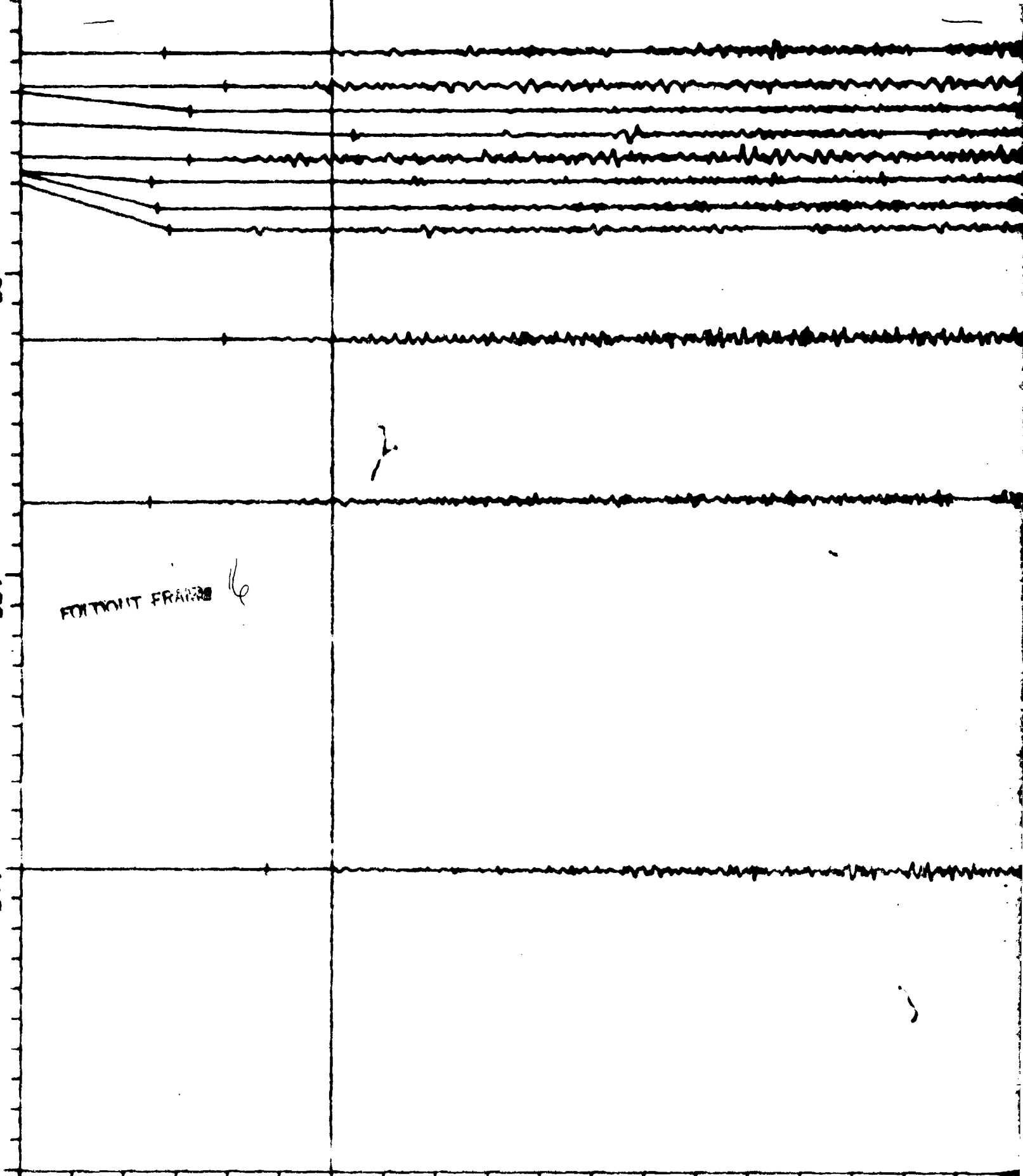
0.

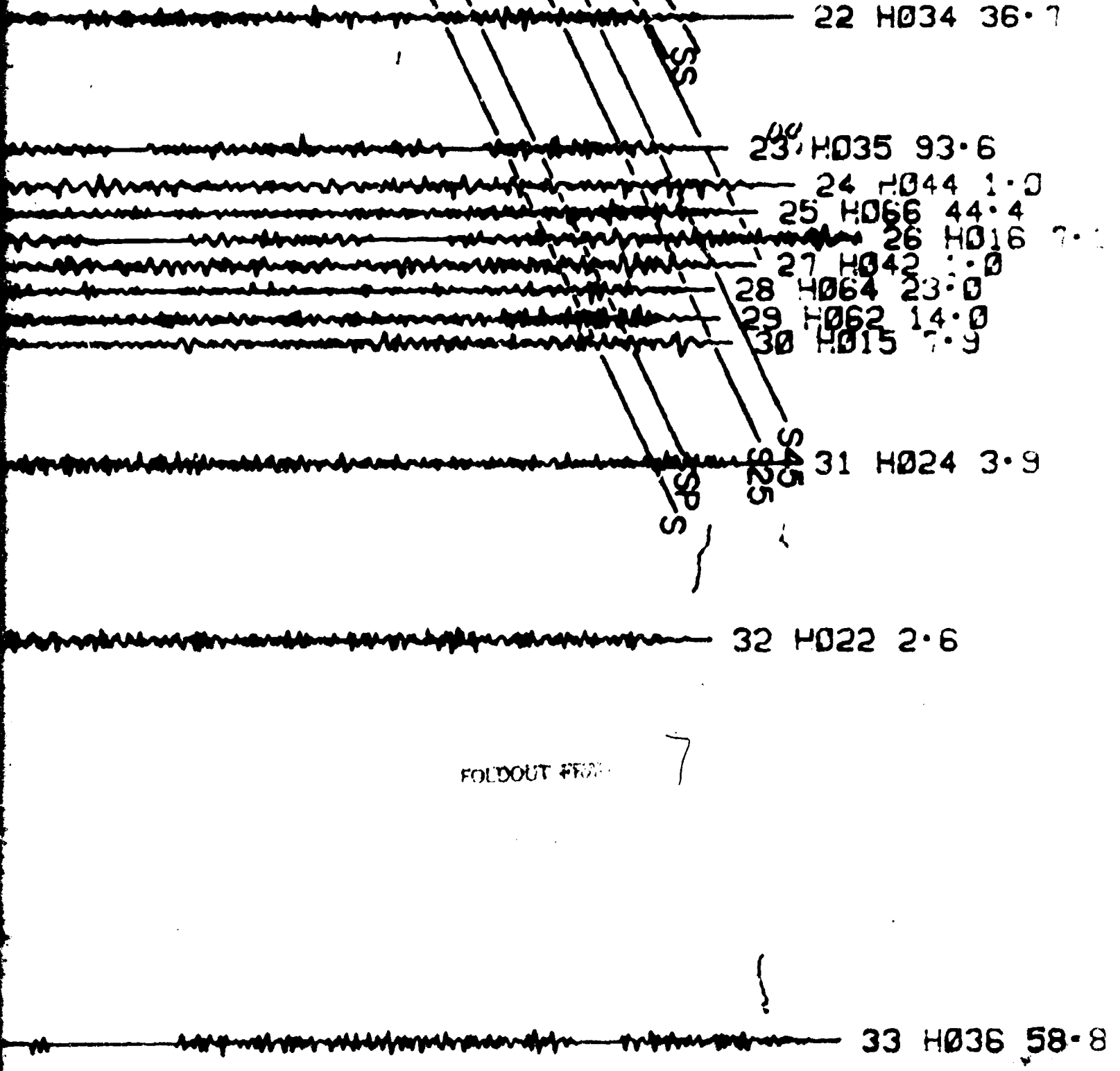
60.

120.

FOLDOUT FRAME 16

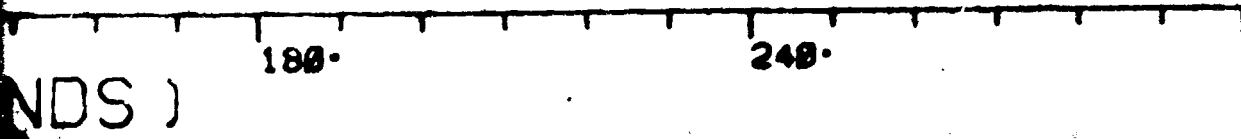
TIME - P (S)





FOLDOUT FROM

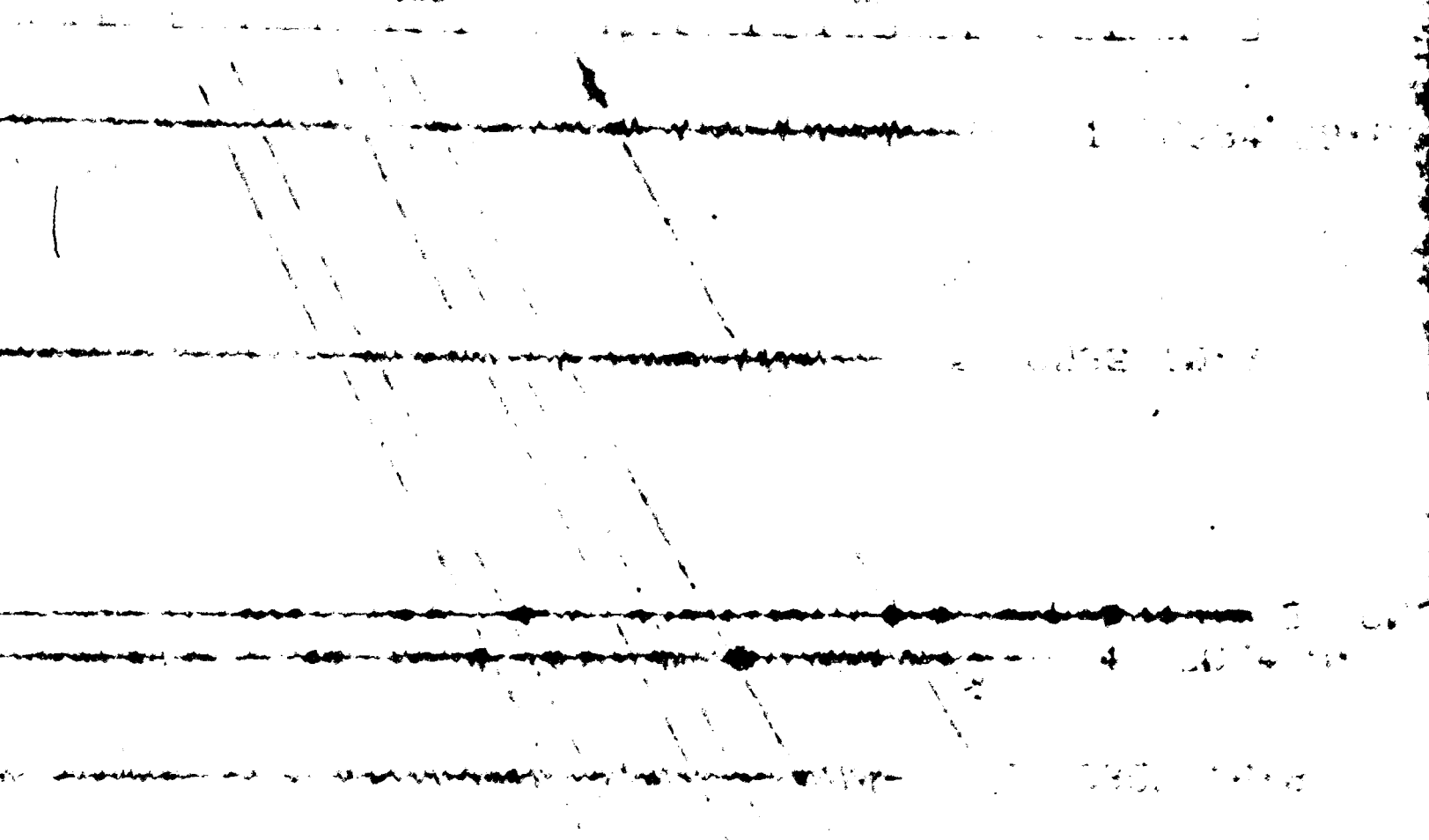
7



100-1017
SERIES

180

100



1
WITHOUT FRAMES

2

ORIGINAL PAGE IS
OF POOR QUALITY

1 0234 10-0

2 0232 10-3

4 0234 10-0

5 0234 10-0

FOURTH FLOOR

3

8 0234 10-0

9 0234 10-0

TABLE 4

TABLE 4 IS
A PART OF THE

ORIGINAL FILE
IN THE QUALITY

100
000

12

13

14

15

FOLDOUT SIDE

3

16 (256 51-7

17

11 C286 58.8

SAS
SAS

12 C252 16.6

13 C956 27.8

14 C254 37.9

15 C055 32.8

WITHOUT FRAME

16 C258 51.7

86°

TIME - P (SECONDS)

120°

FOLDOUT FRAME

7

17 0

ORIGINAL PAGE IS
OF POOR QUALITY

18 0

19 0

20

120- 180- 240-
(SECONDS)

ORIGINAL PAGE IS
OF POOR QUALITY

EOLDOUT FRAME 9

17 C056 32.5

ORIGINAL PAGE IS
OF POOR QUALITY

18 C255 26.4

19 C054 9.0

20 C052 6.6

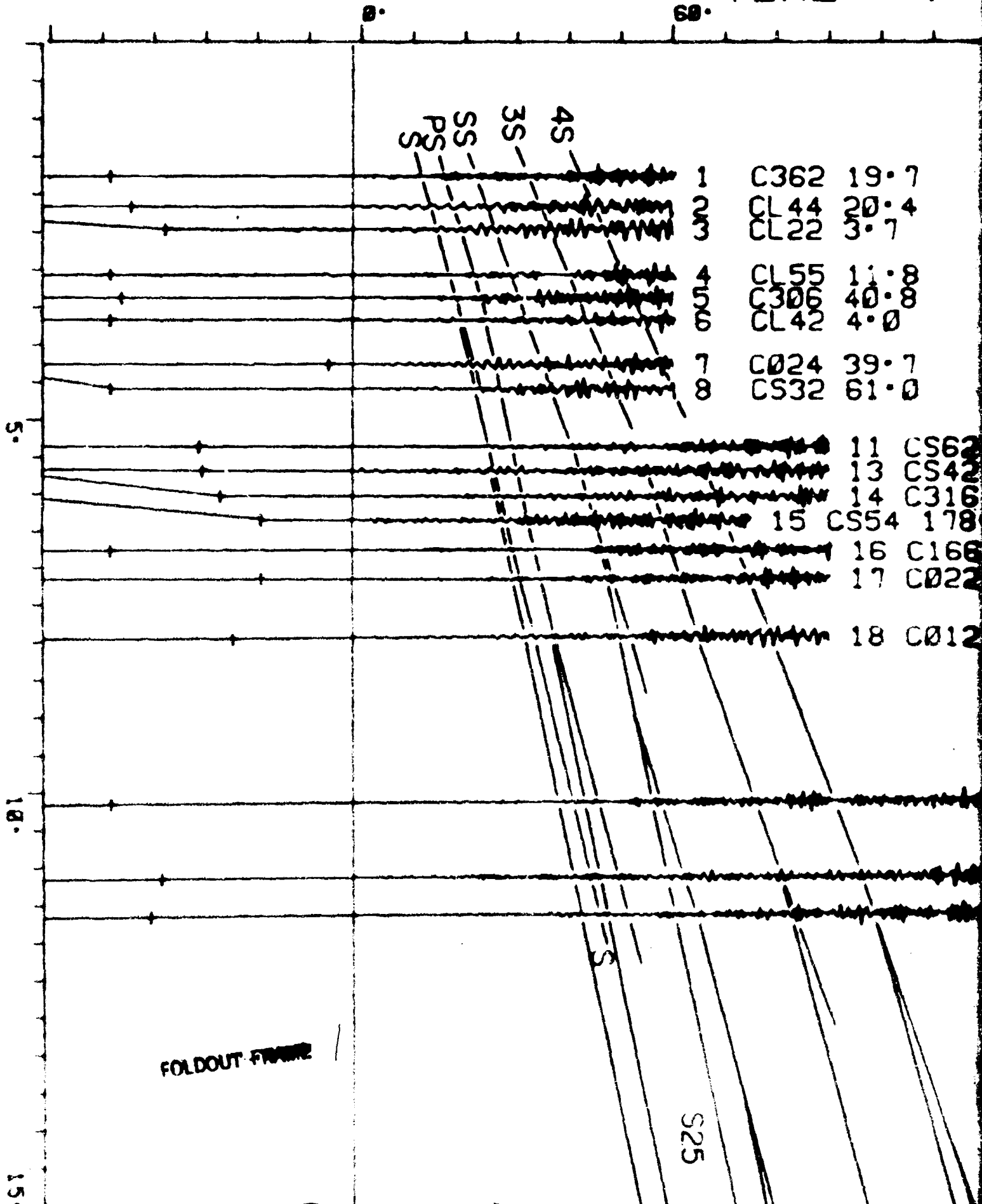
248.

FREIGHT FRAME

9

IMPACTS (Z, 0.4)

TIME - P



-1.5HZ)

(SECONDS)



120.7
84.3
48.6
9
49.1
23.6
119.7

20 C065 55.8

21 CS72 37.6

22 CS52 27.1

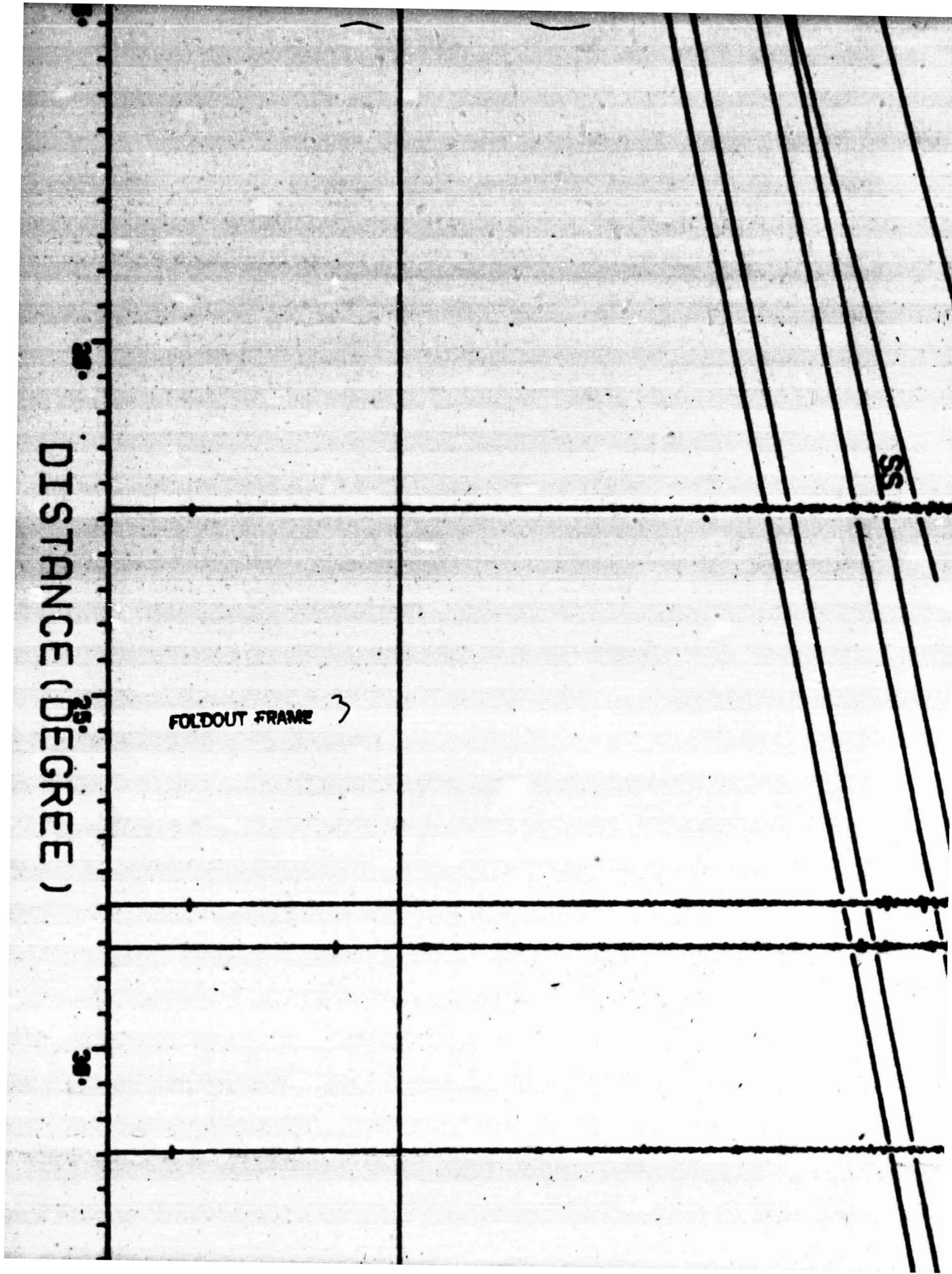
FOLDOUT FRAME

2

DISTANCE (DEGREE)

FOLDOUT FRAME 3

SS



45

52

23 C236 22.9

FOLDOUT FRAME

4

52

24 CS76 17.4

25 C045 15.9

26 C015 46.9

35.

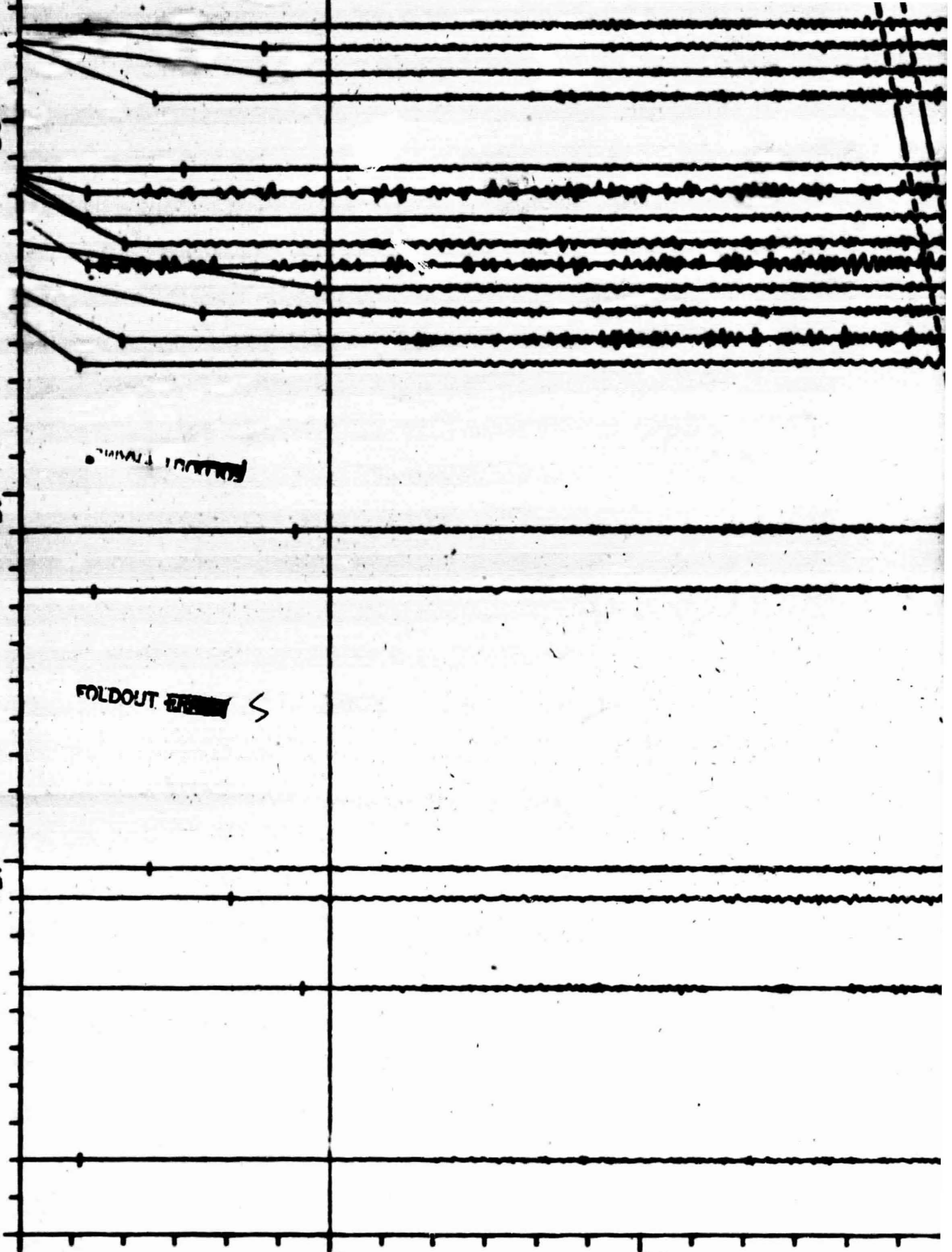
40.

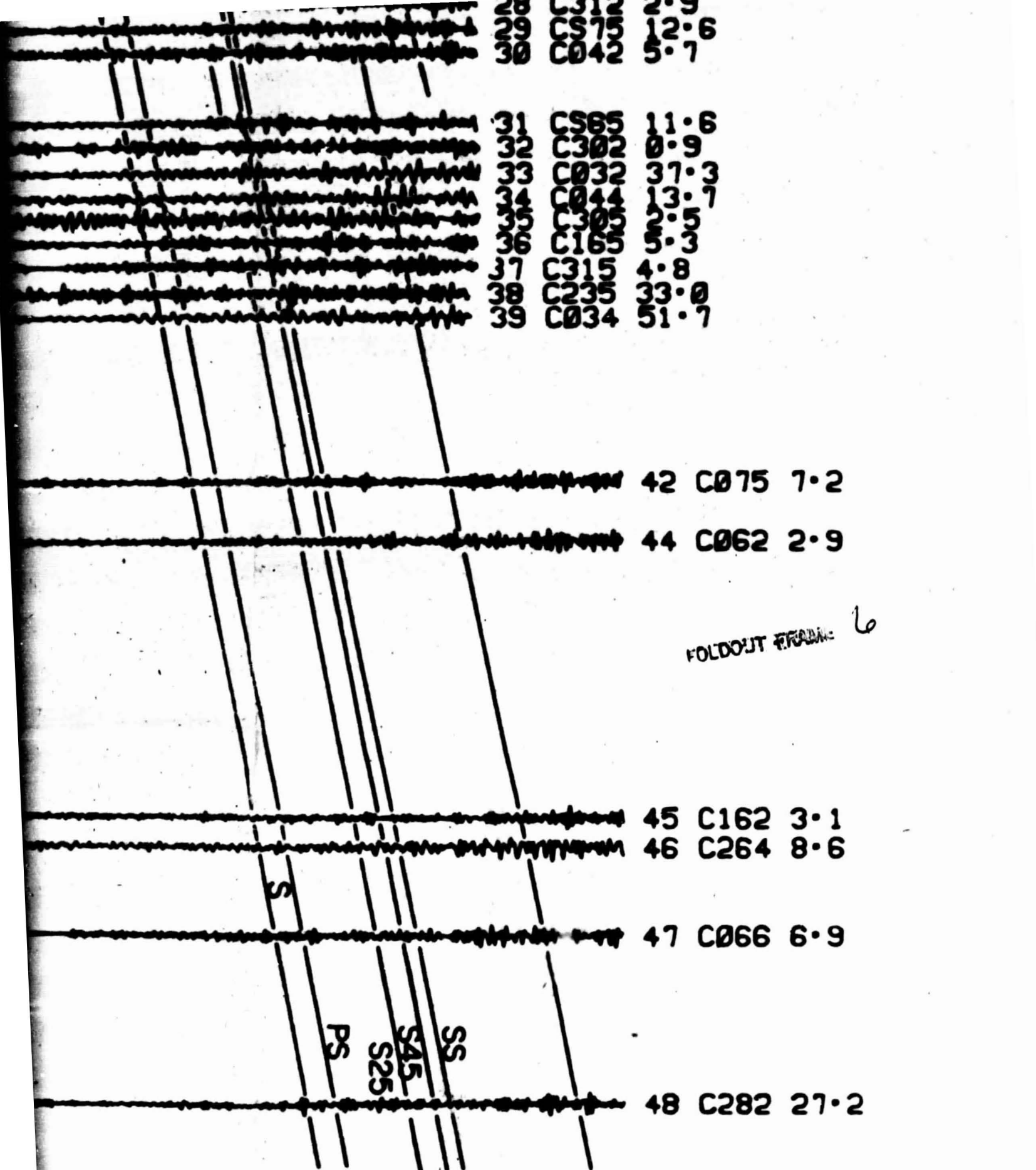
45.

FOLDOUT TIME

FOLDOUT TIME \leq

TIME - P





29 CS75 12.6
 30 C042 5.7
 31 CS65 11.6
 32 C302 0.9
 33 C032 37.3
 34 C044 13.7
 35 C305 5.5
 36 C165 5.3
 37 C315 4.8
 38 C235 33.0
 39 C034 51.7

42 C075 7.2

44 C062 2.9

FOLDOUT FROM: 6

45 C162 3.1

46 C264 8.6

47 C066 6.9

48 C282 27.2

S
 PS
 SAS
 SS

- P (SECONDS)

120.

180.

240.